



<https://theses.gla.ac.uk/>

Theses Digitisation:

<https://www.gla.ac.uk/myglasgow/research/enlighten/theses/digitisation/>

This is a digitised version of the original print thesis.

Copyright and moral rights for this work are retained by the author

A copy can be downloaded for personal non-commercial research or study,
without prior permission or charge

This work cannot be reproduced or quoted extensively from without first
obtaining permission in writing from the author

The content must not be changed in any way or sold commercially in any
format or medium without the formal permission of the author

When referring to this work, full bibliographic details including the author,
title, awarding institution and date of the thesis must be given

Enlighten: Theses

<https://theses.gla.ac.uk/>
research-enlighten@glasgow.ac.uk

OPTOELECTRONIC DEVICES EXPLOITING
THE GUNN EFFECT

A Thesis

Submitted to the Faculty of Engineering
of the University of Glasgow
for the Degree of

Doctor of Philosophy

by

David Moreland

October, 1989

ProQuest Number: 11007331

All rights reserved

INFORMATION TO ALL USERS

The quality of this reproduction is dependent upon the quality of the copy submitted.

In the unlikely event that the author did not send a complete manuscript and there are missing pages, these will be noted. Also, if material had to be removed, a note will indicate the deletion.



ProQuest 11007331

Published by ProQuest LLC (2018). Copyright of the Dissertation is held by the Author.

All rights reserved.

This work is protected against unauthorized copying under Title 17, United States Code
Microform Edition © ProQuest LLC.

ProQuest LLC.
789 East Eisenhower Parkway
P.O. Box 1346
Ann Arbor, MI 48106 – 1346

To my Parents

ACKNOWLEDGEMENTS

I wish to express my thanks to Professor J. Lamb for the provision of the research facilities of the Department of Electronics and Electrical Engineering.

I am particularly grateful to Dr. S.P. Beaumont for his academic supervision of this work, and to Dr. A. MacDonach for his industrial supervision. I would also like to thank Mr. M.R.S. Taylor for many valuable discussions, particularly relating to the microwave aspects of the project, and to Professor J.R. Barker for his help with the Gunn simulation program. The provision of material from the SERC III-V Semiconductor Facility, at the University of Sheffield, is also acknowledged.

I should also like to acknowledge the technical assistance which was available under the leadership of Mr. G.W.T. Boyle, with special thanks to Mr. A. Stark and Mr. D. Gourlay for their assistance with the scanning electron microscopy. Thanks are also given to Mr. R. Harkins, Mr. J. Young, and Mr. J. Cochrane. The help and support of many staff members and fellow research students was greatly appreciated, especially that from Mr. R.H. Hutchins and Mr. D.K. Lau.

I would like to especially direct my thanks to Miss Caroline T. Lang for her support and interest throughout the project, and her patience and understanding during the preparation of the manuscript.

Finally I would like to thank my parents for their continual support and encouragement.

This work was supported by an SERC CASE Award, in conjunction with Barr and Stroud Ltd., and also by the IEE through a Postgraduate Scholarship financed by the Joseph William Beauchamp Bequest Fund.

PUBLISHED WORK

1. MORELAND, D., ROBERTS, J.S., and BEAUMONT, S.P.: 'Optical Modulation within a Rib Waveguide by Propagating Gunn Domains', Submitted to *Elect. Lett.*, July 1989
2. LAU, D.K., IRONSIDE, C.N., MORELAND, D., and BEAUMONT, S.P.: 'Optically Triggered and Detected Gunn Domains', Semiconductor and Integrated Opto-Electronics (SIOE'89), Cardiff, March 1989
3. LAU, D.K., BEAUMONT, S.P., IRONSIDE, C.N., MORELAND, D., and STANLEY, C.R.: 'High Speed Optoelectronic Properties of Gunn Domains', Ninth National Quantum Electronics Conference, Oxford, September 1989

CONTENTS	Page No.
Acknowledgements	i
Published Work	ii
Contents	iii
Summary	vii
Chapter 1: Introduction	1
1.1 Gallium Arsenide Technology	1
1.2 Areas of, and Reasons for Interest	4
1.3 Integrated Device Structures	6
1.4 Summary of Thesis Contents	7
Chapter 2: Optical Waveguiding	9
2.1 The Dielectric Slab Guide	9
2.1.1 Ray Optical Treatment	10
2.1.2 Electromagnetic Theory	12
2.2 Three-Dimensional Waveguides	14
2.2.1 The Effective Index Method	14
2.2.2 The Variational Analysis Technique	15
2.2.3 The Finite Difference Technique	17
2.3 Photoelastic Waveguides	19
2.3.1 Stresses in Thin Films	19
2.3.2 The Photoelastic Effect	21
2.4 Loss Mechanisms in Dielectric Waveguides	22

Chapter 3:	The Gunn Effect	25
3.1	The Mechanism of the Gunn Effect	25
3.2	Space Charge Instabilities	28
3.2.1	Domain Formation	28
3.2.2	Domain Dynamics	30
3.3	Conventional Gunn Diode Structures	34
3.4	Modes of Operation	36
3.4.1	Constant Voltage Modes	36
3.4.2	Constant Current Modes	37
Chapter 4:	Optical Modulation	40
4.1	Electro-Optic Modulation	40
4.2	Optical Effects due to a Propagating Gunn Domain	40
4.2.1	The Linear Electro-Optic Effect	41
4.2.2	The Electro-Absorption Effect	44
4.2.3	Free Carrier Contributions	46
4.3	Optoelectronic Interaction Mechanisms	49
4.3.1	Exploitation of Domain Induced Optical Changes	49
4.3.2	Exploitation of Optically Induced Electrical Changes	51
Chapter 5:	Devices and their Design	53
5.1	Device Structures	53
5.2	Optical Design	54
5.2.1	Refractive Index Calculations	54
5.2.2	Slab Waveguide Calculations	56

5.2.3	Rib Waveguide Calculations	57
5.2.4	Photoelastic Waveguide Calculations	59
5.3	Electrical Design	60
5.3.1	Electrical Performance	60
5.3.2	Thermal Considerations	64
5.4	Electro-Optical Considerations	65
5.4.1	Calculation of Domain Characteristics	65
5.4.2	Influence on Optical Guiding by the Gunn Domain	74
5.4.3	Comparison of Modulator Designs	77
5.4.4	Influence on Threshold Field of Stress due to the Photoelastic Effect	78
5.5	Devices Designed in Other Materials	78
Chapter 6:	Devices, their Fabrication and Characterisation	80
6.1	Procedural Aspects	80
6.1.1	Material Growth	80
6.1.2	Material Characterisation	81
6.1.3	Device Fabrication	85
6.2	Spot Contact Gunn Diodes	87
6.3	Vertical/Rib Devices	90
6.4	Planar/Photoelastic Devices	95
6.5	Cleaving, Mounting, and Bonding of Devices	98
Chapter 7:	Experimental Results and Discussion	101
7.1	Optical Experiments	101
7.1.1	Guiding Characteristics	101
7.1.2	Loss Measurements	103

7.2	Microwave Experiments	105
7.2.1	Microstrip Circuit Design and Fabrication	105
7.2.2	Experimental Results	108
7.3	Electro-Optic Experiments	110
7.3.1	Experiments at a Wavelength of $1.15\mu\text{m}$	113
7.3.2	Experiments at a Wavelength of 905nm	116
7.3.3	Calculation of Electro-Optic and Electro-Absorption Coefficients	118
Chapter 8:	Summary of Results, and Future Work	120
8.1	Conclusions	120
8.2	Future Investigations	123
8.3	Integrated Devices	126
Appendices		128
A.	The Equal Areas Rule	128
B.	Listing of GUNNSIM, the Gunn Effect Simulator	131
C.	Documentation for GUNNSIM	143
D.	Optical Apparatus	146
E.	Slow Diode Analysis	147
References		151

SUMMARY

Semiconductor integrated Electro–Optic modulators which exploit the Gunn effect, have been produced in gallium arsenide.

Both vertical and planar diode structures incorporating a form of optical waveguide were investigated. Optical, electrical, and Electro–Optical, design calculations were carried out for each of the proposed device designs. The vertical Gunn diode structures incorporated either a slab or a rib waveguide, whereas the planar Gunn diode structure incorporated a photoelastic waveguide.

Various methods, such as the Effective Index Method, the Variational Analysis technique, and the Finite Difference method, were used to assess the propagation characteristics of the rib guide structures. The results of this assessment provided a comparison between the different techniques available, and revealed the advantages and disadvantages of each method. The propagation characteristics of the photoelastic waveguides were analysed by the Finite Difference method.

A computer program was developed to analyse the electrical characteristics of the integrated devices. The program solves Poisson's equation and the Current Continuity equation under the conditions for a stable propagating dipole Gunn domain, for: an approximate velocity–field characteristic, $v(E)$, and field independent diffusion coefficient, D ; an analytical $v(E)$ characteristic and field independent D ; or an analytical $v(E)$ and a field dependent D . The program supplies an estimate of the maximum electric field within the domain, and also of the domain length. The results for the three possible analysis situations were compared.

The perturbations induced in the optical guiding characteristics, at above bandgap optical wavelengths, due to the presence of a domain, have been studied. A knowledge of the characteristics of the domain, as it propagates through the device, leads to an estimate of the magnitude of the induced optical changes, eg. in the refractive index, or in the optical absorption. A measure of the Electro–Optic interaction between the propagating domain and the guided optical wave was therefore obtained.

In order to test the electrical characteristics of the vertical devices, spot contact diodes, varying in diameter from $20\mu\text{m}$ to $90\mu\text{m}$, were fabricated. Also, for the purpose of testing both the optical and Electro–Optical properties of the vertical devices, rib guides, varying in width from $4\mu\text{m}$ to $15\mu\text{m}$, were fabricated by optical photolithography and dry etching techniques.

Unique devices incorporating a vertical Gunn diode and a rib waveguide were consequently designed and fabricated, and assessed for their modulation depth. Optical modulation, at a frequency of 24GHz, was observed in the vertical diode structure. While at a wavelength of $1.15\mu\text{m}$ modulation was solely due to the Linear Electro–Optic effect, at a wavelength of 905nm modulation was seen to be due to both the Linear Electro–Optic effect, and the Electro–Absorption effect.

Estimated values of the observed Electro–Optic coefficient, r_{41} , at wavelengths of $1.15\mu\text{m}$ and 905nm were obtained, along with an estimate of the observed Electro–Absorption coefficient, α , at 905nm.

CHAPTER 1

INTRODUCTION

1.1 GALLIUM ARSENIDE TECHNOLOGY

Interest in gallium arsenide (GaAs), as a material suitable for the fabrication of electrical devices, has existed since the invention of the bipolar transistor in the late 1940's. Gallium arsenide provides a number of distinctive and desirable properties not present in silicon.

One such property is the Transferred Electron effect. For example one of the first commercial applications found for gallium arsenide was as a Gunn diode. This two terminal device exploits the Transferred Electron effect, and can be used to generate RF power at frequencies up to and around 100GHz. Gunn diodes have thus been used as local oscillators, power amplifiers and solid-state sources for microwave applications such as radars, intrusion alarms, and microwave test instruments.

A second property of gallium arsenide, which is important in the consideration of materials for electrical devices, is the relatively high electron mobility exhibited by the material; gallium arsenide having a low-field electron mobility of around $8500\text{cm}^2\text{V}^{-1}\text{s}^{-1}$ compared to $1300\text{cm}^2\text{V}^{-1}\text{s}^{-1}$ for silicon. However, silicon has till now remained the preferred material because of advantages in device fabrication such as an easily grown, high quality native oxide, having good interfacial characteristics with the substrate. Silicon also offers the easy availability of large, high purity, low defect density substrates.

Many fabrication problems associated with gallium arsenide are, however, being overcome, and useful discrete Metal Semiconductor Field Effect Transistors (MESFET's), operating at frequencies of up to 30GHz, have been produced. These transistors are suitable for use as the basic elements of analogue or digital integrated circuits fabricated in gallium arsenide, or in related III-V compounds. Presently other potentially faster devices are also being studied such as the High Electron

Mobility Transistor (HEMT) and the Heterojunction Bipolar Transistor (HBT) [1].

In the late 1950's proposals were put forward suggesting semiconductors as materials capable of resulting in laser action, and in 1962 it was shown [2] that laser action was indeed possible in direct bandgap semiconductors. It was not, however, until 1969 that room temperature CW operation of a semiconductor laser diode was achieved [3]. This structure was based on the lattice matched heterojunction GaAs/AlGaAs, and provided both optical and carrier confinement, although at this time the importance of the heterostructure in confining light was not fully understood.

Concurrent with the work on gallium arsenide laser diodes has been progress in the field of integrated optics which deals with the study of discrete components as well as optoelectronic integrated circuits (OEIC's). These are suitable for use in optical communications systems, signal processing, instrumentation or sensors. In integrated optical systems the information signal is carried by means of an optical beam rather than by an electrical current. Also, the various circuit elements are interconnected by optical waveguides on a substrate wafer rather than by metal tracks. The advantages of integrated optical systems are similar to those afforded by optical fibres, ie. increased bandwidth, immunity to electro-magnetic interference, low-loss transmission and reduced weight.

The ability to control the guided optical radiation, by some external signal, requires the control of local perturbations in the optical characteristics of the material, such as the absorption or the refractive index. For example, the refractive index may be perturbed via the Acousto-Optic, Magneto-Optic or the Linear Electro-Optic effects. The latter effect has to date been the most popular.

Two groups of materials have so far been used in integrated optics; the ferroelectric materials, in particular lithium niobate (LiNbO_3), and the III-V semiconductors, in particular gallium arsenide. Lithium niobate has the advantage over gallium arsenide of having a larger Electro-Optic coefficient, ie. $r_{33} = 30.0 \times 10^{-12} \text{mV}^{-1}$ for lithium niobate, at a wavelength of 633nm, compared with $r_{41} = 1.2 \times 10^{-12} \text{mV}^{-1}$ for gallium arsenide, at a wavelength of 900nm. Also

lithium niobate has a lower refractive index, thus producing lower reflection losses at the interface between fibre and device. III–V materials however offer the distinct advantage of potential monolithic integration of all the components necessary for a complete OEIC, including source, detector, and control electronics, on the same substrate.

Gallium arsenide has also become the basic material for microwave integrated circuits where both active and passive elements are combined on the same chip. This choice is due to two properties of the material [4]. First, it is available in semi-insulating form which provides natural low-capacitance isolation between circuit components. Second, the electrons move with higher velocities than in silicon, so reducing parasitic resistance and transit time effects. Fabrication techniques, such as ion-implantation, air-bridges, and through-GaAs vias, have been specially developed to exploit these properties. This has led to the demonstration and commercial availability of a number of Monolithic Microwave Integrated Circuits (MMIC's) operating in the range 1–100GHz.

The passive components in MMIC's take the form of either distributed or lumped elements. The two most popular transmission lines used on gallium arsenide to date are microstrip and coplanar waveguide. Of these two, microstrip has been the most exploited medium, since the advantage of coplanar waveguide (that of accessible ground planes on the top surface of the chip) is useful only for simple circuits. Lumped elements may also be included, producing a greater design flexibility, provided that the equivalent circuit of such components can be accurately modelled.

From the foregoing, it can be seen that gallium arsenide has found four separate areas of application as a material suitable for fabrication of devices: (i) in electronic circuits (eg. Gunn diodes, and MESFET's); (ii) in optical transducers (eg. light emitting diodes, LED's, laser diodes, LD's, and avalanche photodiodes, APD's); (iii) in integrated optics; and (iv) in guided wave devices (eg. MMIC's).

Until now these areas have remained separate. However, more recently work has begun in order to exploit the potential advantages of monolithically integrated

circuits incorporating dissimilar device types, eg. electrical and optical components. Such circuits would not only be smaller than electrically connected discrete devices, but also more rugged, reliable and inexpensive. Furthermore, the integrated device would be faster and less noisy, due to the reduction in parasitic reactances from electrical interconnections [5].

1.2 AREAS OF, AND REASONS FOR INTEREST

Efforts to exploit the potential bandwidth of light as an information carrier have brought about a renewed interest in the use of microwave techniques for optical systems. Whereas in the late 1960's primary interest was directed towards analysing propagation in optical waveguides and fibres, using methods originally developed for microwave waveguides, present activity is directed towards the design of microwave control circuitry compatible with high-speed optical devices. Investigations are also being made into the use of optical techniques for the transmission, generation and control of microwave signals [6].

The overall aim of this project was to explore the problems involved in the monolithic integration of microwave electronic devices (sources, waveguides, etc) with integrated optical structures (lasers, waveguides, modulators and detectors). To this end, it was the original objective of the project to design and fabricate an integrated active optoelectronic microwave receiver. Such a receiver would detect a radiant microwave signal, and use this microwave signal to directly modulate a guided optical wave.

As a first attempt at the practical realisation of such an integrated receiver, it became the specific intention to design and fabricate a device which combined a Gunn diode and an optical waveguide within the same device design. Such a device exhibits true monolithic integration of an electronic and an optical device, not only on the same substrate, but also within the same structure, both contributing to the overall device action. It was also proposed that the work be extended to include the design of an electrode structure for the receiver which would detect radiant

microwave energy. It was envisaged that the electrode pattern would resemble a dipole antenna array.

After initial literature surveys relating to optical modulation by propagating Gunn domains, it was found that no work had previously been done to investigate the possibility of Gunn domains being used to modulate an optical signal within an integrated optical guiding structure. It was therefore decided after the first year of research to limit the scope of the work to the investigation of modulation effects occurring within an integrated optical guiding structure due to the presence of propagating Gunn domains. This was felt to be a realistic aim to be achieved within the given time, taking due account of the resources available.

Prior work by Cohen *et al* [7], and Ohta *et al* [8], showed that light could be modulated by propagating Gunn domains in bulk GaAs samples. In these reports the interaction was however found to be weak, and of little practical value. Further, these bulk samples required high bias voltages, and provided no means of guiding the optical radiation. This suggested that a much stronger interaction, between the propagating Gunn domain and the optical radiation, might be obtained if the domain propagated through an integrated optical waveguide. Investigations therefore included:

- (a) The design of optical waveguides compatible with the structure of a super-critical Gunn diode. Design criteria were two-fold, since the device should exhibit monomode optical guiding, as well as the formation and propagation of dipole Gunn domains under the correct bias conditions.
- (b) The optical properties of Gunn devices under super-critical conditions, ie. the influence of the electric field pulse associated with a propagating Gunn domain on the optical waveguiding characteristics of the material through which it passes, due to Electro-Optic effects. Considerations not only included the magnitude of the optical perturbation induced within the device, but also the shape of the electric field profile, as well as practical limitations of the length of the propagating domain.
- (c) The optimum fabrication conditions for the proposed devices and their testing, optically, electrically, and as integrated devices.

Optically active but electronically passive materials such as lithium niobate have

already been used to produce active Electro-Optic modulators. This technology may, and indeed has, been directly transferred to semiconductor materials such as gallium arsenide. The translation fails however to exploit the electronic properties of the semiconductor material.

The proposed device was therefore original in operation in that it depended not only on the presence or absence of a local perturbation in the optical characteristics (produced by the microwave action), but also that this perturbation would propagate. Further, the magnitude and positions of nucleation and destruction of the perturbation within the device could be controlled. This was unlike conventional Electro-Optic modulators designed in either electronically passive, or electronically active materials.

1.3 INTEGRATED DEVICE STRUCTURES

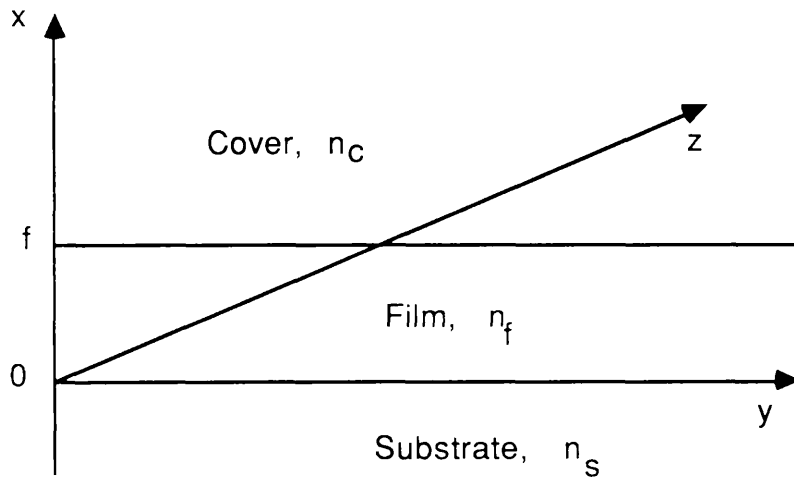
The ability to guide radiation in an integrated optical waveguide requires the refractive index of the guiding region to be greater than that of the surrounding regions. In the III-V semiconductor system this is most popularly achieved by a combination of geometry and material compositional or dopant changes, such as in the slab or rib guide [9]. However, strain induced effects may also be utilised as in the photoelastic guide [10].

The simplest dielectric guide is the three-layer slab guide shown in fig(1.1)(a). The refractive indices of the substrate and cover are less than that of the film, due either to compositional or dopant changes. The result is a planar film of refractive index n_f sandwiched between two regions of lower refractive index n_s and n_c . The light is therefore confined by total internal reflection at the film-substrate and film-cover interfaces. A four-layer slab guide, shown in fig(1.1)(b), may also be formed where the refractive indices are such that $n_f > n_s$, n_b , n_c , and $n_b > n_c$.

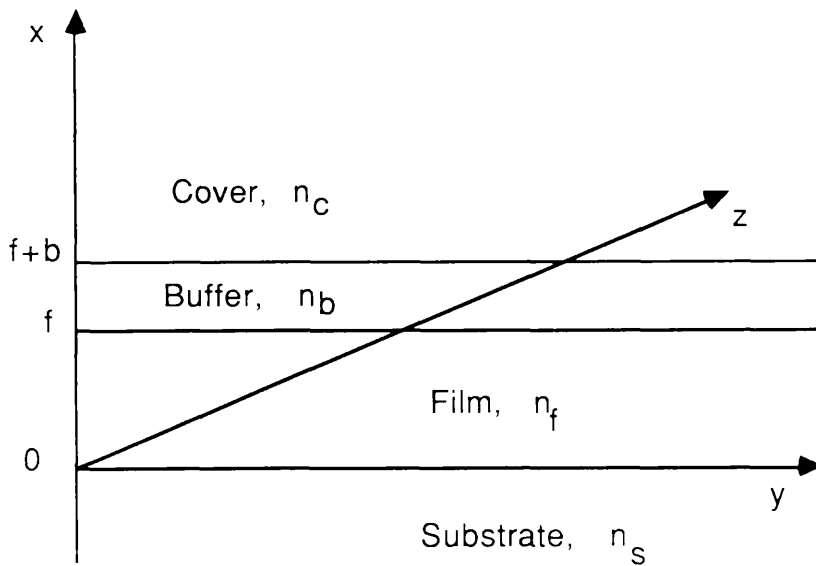
However, the simple planar dielectric guide provides no confinement of the light within the film plane, ie. the $y-z$ plane; confinement occurring in the

Fig (1.1) Optical Waveguiding Structures in III-V Materials

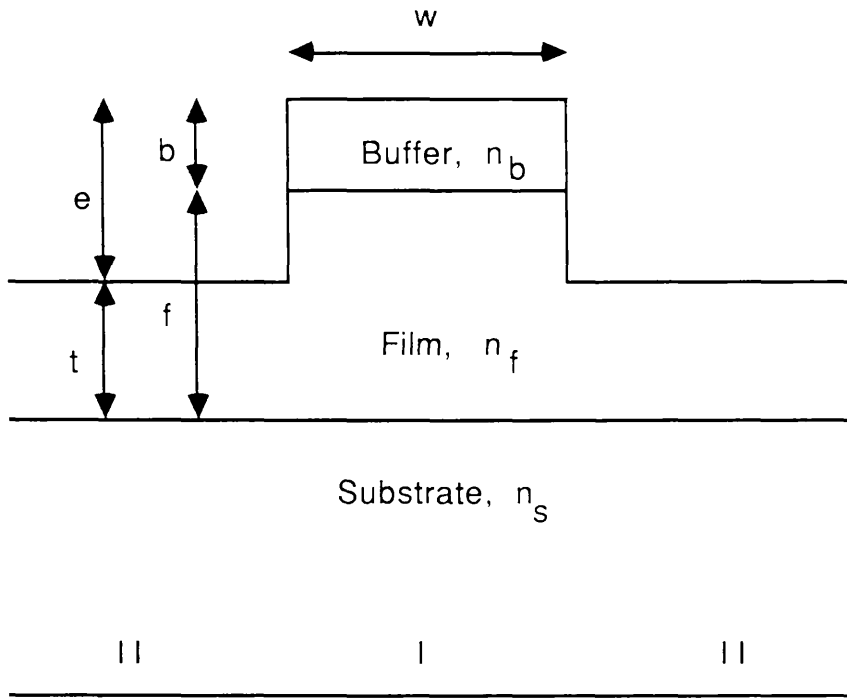
(a) The Three-Layer Slab Guide



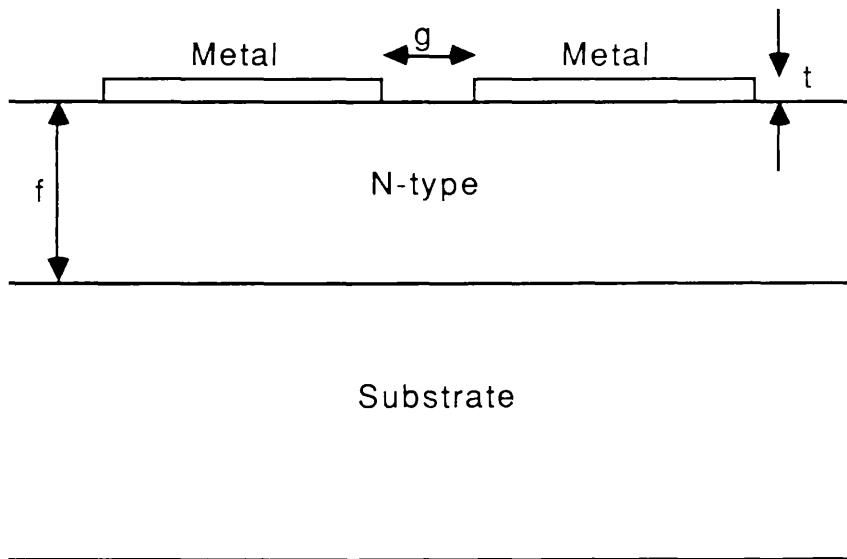
(b) The Four-Layer Slab Guide



(c) The Rib Waveguide



(d) The Photoelastic Waveguide



x– dimension only. Confinement in the y– dimension can be achieved by forming rib structures as shown in fig(1.1)(c). These ribs may be formed by etching away parts of the substrate between mask lines formed photolithographically. Thus, careful thought prior to fabrication means that an etch mask, formed using metallisation, can subsequently form the control electrode, so ensuring self alignment. The dielectric bias field will therefore be largely confined to the unetched rib region, so minimising the effects due to crystal damage.

Strain induced optical waveguides can be formed in gallium arsenide, and other III– V compound semiconductors, simply by opening windows or defining stripes in an applied surface film which is under compression or tension, as shown in fig(1.1)(d). Since most applied films are likely to be under stress as a result of thermal expansion mismatch, as well as the deposition process, photoelastic waveguiding or antiwaveguiding may be present in many stripe– geometry III– V semiconductor optical devices.

Two common device structures for Gunn diodes may be identified. These are the vertical diode, wherein current flow is perpendicular to a highly conductive substrate, and the less common planar diode, wherein current flow is parallel to an insulating substrate. These structures are shown in fig(1.2)(a) and (b) respectively.

Integrating the optical waveguiding structures with a compatible Gunn diode structure, the following combinations can be identified:

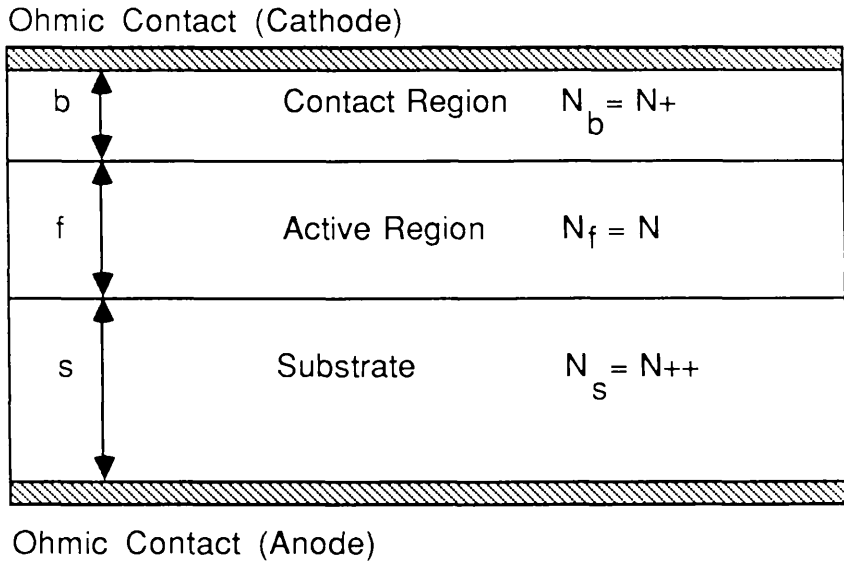
- (a) a slab guide and a vertical diode, shown in fig(1.3)(a);
- (b) a rib guide and a vertical diode, shown in fig(1.3)(b); and
- (c) a photoelastic guide and a planar diode, shown in fig(1.3)(c).

1.4 SUMMARY OF THESIS CONTENTS

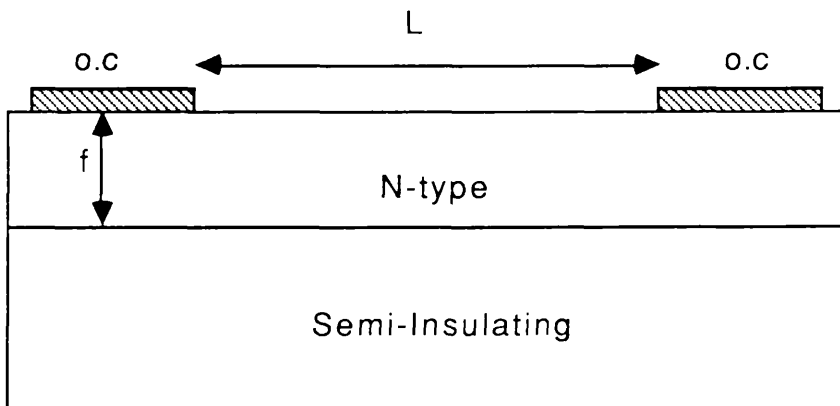
The preceding sections of this Chapter have identified the areas of investigation, and reasons for undertaking this work. Also presented are the integrated device structures which will be dealt with in greater depth in succeeding Chapters.

Fig (1.2) Conventional Gunn Diode Structures

(a) The Vertical Gunn Diode



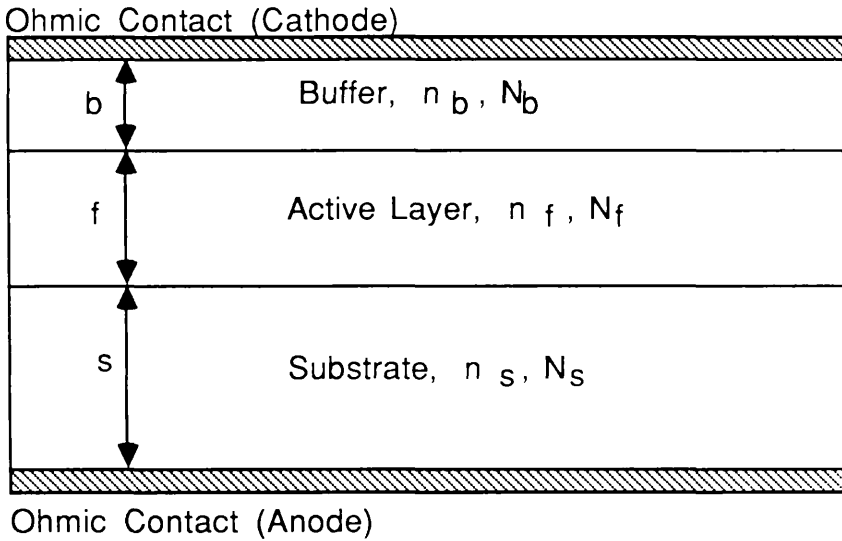
(b) The Planar Gunn Diode



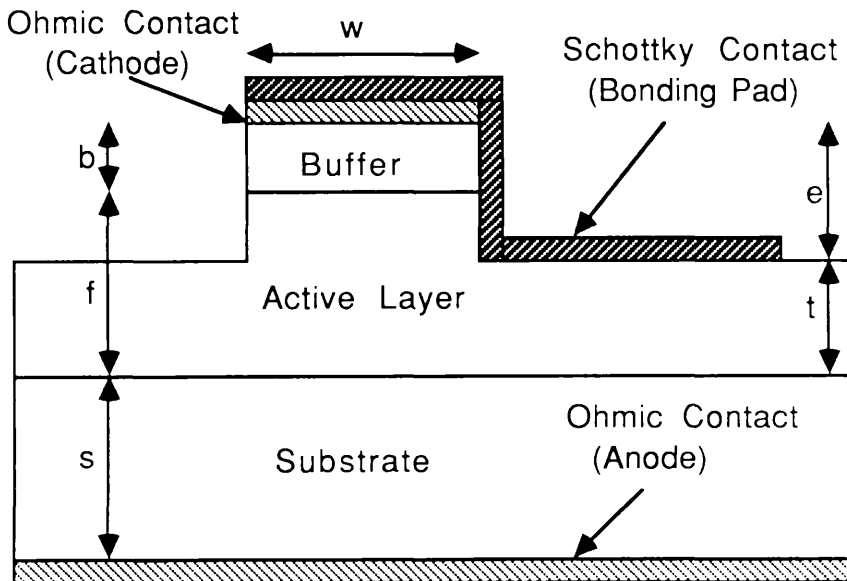
o.c = Ohmic Contact

Fig(1.3) Integrated Device Structures

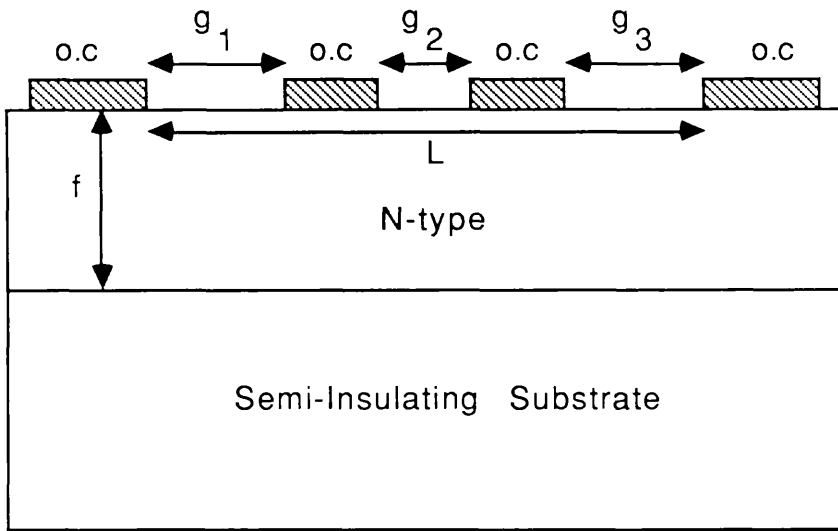
(a) Four-Layer Slab Waveguide / Vertical Gunn Diode



(b) Rib Waveguide / Vertical Gunn Diode



(c) Photoelastic Waveguide / Planar Gunn Diode



o.c = ohmic contact

Chapter 2 describes the theory of optical propagation in slab, rib and photoelastic waveguides, in addition to the various methods of analysis which may be used to calculate the guiding characteristics.

The mechanism of the Gunn effect is explained in Chapter 3, along with a more detailed description of the cyclic formation and propagation of Gunn domains, and an explanation of the possible modes of operation of such devices.

The theoretical basis of Electro–Optical modulation is explained in Chapter 4, along with the analysis of the precise interaction between a propagating Gunn domain and an optical field distribution at wavelengths greater than that of the band gap energy of the material.

In Chapter 5 the techniques which were employed in device design are explained. Since the device must act in the correct way both optically and electrically, the precise design criterion are explained and the necessary trade–offs identified. The design of such devices in materials other than gallium arsenide is mentioned.

In Chapter 6 the methods of growth and characterisation of the material used in making these devices is given, as well as the methods of device fabrication and characterisation. The cleaving, bonding and mounting of completed devices is also addressed.

Experimental observations and results are presented and discussed in Chapter 7, for wavelengths of $1.15\mu\text{m}$ and 905nm . Values of the observed Electro–Optic coefficient, r_{41} , at both of these wavelengths are given, along with the observed Electro–Absorption coefficient, α , at 905nm .

Finally, Chapter 8 summarises the overall conclusions reached, and identifies various areas which may be of interest in future investigations. This Chapter concludes by suggesting possible structures for an integrated active optoelectronic microwave receiver, capable of detecting radiant microwave energy and directly modulating a guided optical carrier wave.

CHAPTER 2

OPTICAL WAVEGUIDING

Optical guiding in integrated optics is produced by the use of dielectric waveguides [9],[10],[11]. This Chapter explains the mechanism of optical propagation, and the method of analysis, for three and four-layer planar dielectric guiding structures, propagation within such structures being used to develop the analysis of optical propagation within more complex guiding structures.

Three methods of analysis for optical propagation within rib waveguides are presented, ie. the approximate Effective Index Method, and the analytical Variational Analysis Technique, and Finite Difference Method. The advantages and disadvantages of these methods are compared.

The approximate method inherently gives a higher value of the modal effective index, n_{eff} than is correct. Since for the homojunction rib waveguides analysed herein n_{eff} is normally near cut-off, it is important in designing these guides that n_{eff} is not overestimated. Hence the need to employ the Variational Analysis Technique or the Finite Difference Method.

The contributions to optical losses in dielectric waveguides are also briefly considered.

2.1 THE DIELECTRIC SLAB GUIDE

In the simple three layer slab guide previously shown in fig(1.1)(a) light is confined, and propagates by total internal reflection at the film-substrate and film-cover interfaces.

Section(2.1.1) therefore introduces the ray-optical picture of light propagation in slab waveguides. Although this is the simplest picture to use, it is helpful in gaining an understanding of the properties of more complicated dielectric waveguides. It also introduces many concepts used in dielectric guides including the nature of the modes of propagation, waveguide cut-off and the propagation constant, β .

Section(2.1.2) goes on to describe the fundamentals of the electromagnetic theory of dielectric waveguides.

2.1.1 Ray Optical Treatment

The ray picture of light guided in a dielectric slab waveguide is one in which light rays trace a zig-zag path within the film, total internal reflection of the light occurring at the film-substrate and film-cover interfaces, as shown in fig(2.1). Now, if $\theta > \theta_c$, where $\theta_c =$ the critical angle, we have that the reflection coefficient, R is such that $|R|=1$, and total internal reflection of the light occurs [11]. R is now complex and the reflected light is phase shifted.

Further, using the Fresnel formulaes [12], the following expressions for the phase shifts ψ_{TE} and ψ_{TM} , corresponding to the two polarisation states, may be found to be

$$\tan\psi_{TE} = \frac{(n_1^2 \sin^2 \theta - n_2^2)^{1/2}}{n_1 \cos \theta} \quad \dots\dots 2.1$$

$$\tan\psi_{TM} = \frac{n_1^2 (n_1^2 \sin^2 \theta - n_2^2)}{n_2^2 n_1 \cos \theta}$$

where, the expressions used in the above equations are as defined in fig(2.1).

With reference to fig(1.1)(a) introducing normalisations which combine several guide parameters, we have that

Normalised frequency $V = kf(n_f^2 - n_s^2) \quad \dots\dots 2.2$
 and film thickness,

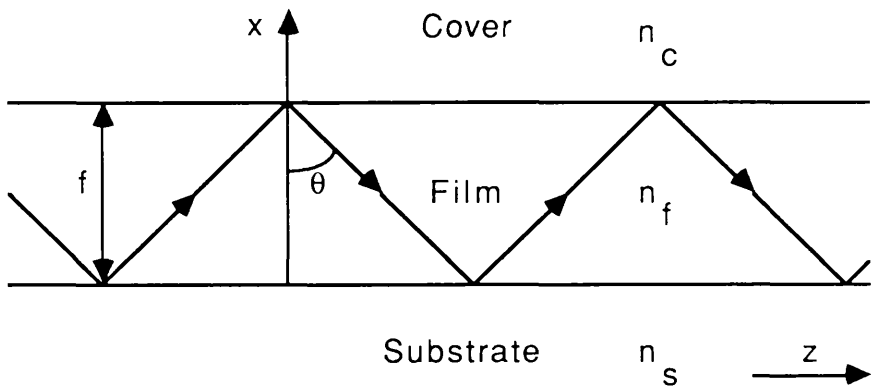
where, $k =$ wavevector $= 2\pi/\lambda$

$\lambda =$ wavelength of propagation

$f =$ film thickness

Normalised guide index, $b' = \frac{(n_{eff}^2 - n_s^2)}{(n_f^2 - n_s^2)} \quad \dots\dots 2.3$

Fig (2.1) Ray Optical Propagation



$$= 0 \quad \text{at cut-off when } n_{\text{eff}} = n_s$$

where, n_{eff} = effective index of mode = $\beta/k = n_f \sin\theta$

β = propagation constant

$$\begin{aligned} \text{Asymmetry of the guide, } a &= \frac{(n_s^2 - n_c^2)}{(n_f^2 - n_s^2)} && \text{for TE modes} \\ & && \dots\dots 2.4 \\ &= \frac{n_f^4}{n_c^4} \frac{(n_s^2 - n_c^2)}{(n_f^2 - n_s^2)} && \text{for TM modes} \end{aligned}$$

Now, adding up the phase shifts between like points in the ray path, and remembering that for self consistency the sum of all these phase shifts must be a multiple of 2π , it can be shown that the Dispersion relation may be represented as

$$2kn_f h \cos\theta - 2\psi_s - 2\psi_c = 2\nu\pi \quad \dots\dots 2.5$$

where, ν = mode number = 0,1,2,.....

ψ_s = phase shift introduced on reflection from the film-substrate interface

ψ_c = phase shift introduced on reflection from the film-cover interface

Now, for TE modes, equation(2.1) may be used in conjunction with the normalisations of equations(2.2), (2.3), and (2.4) to rewrite the Dispersion relation, ie. equation(2.5), in the form [9]

$$V(1-b')^{1/2} = \nu\pi + \tan^{-1} \left[\frac{b'}{1-b'} \right] + \tan^{-1} \left[\frac{b'+a}{1-b'} \right] \quad \dots\dots 2.6$$

For a four-layer slab guide, as shown in fig(1.1)(b), the Dispersion relation is given by [13]

$$V(1-b')^{1/2} = \nu\pi + \tan^{-1} \left[\frac{b'}{1-b'} \right]^{1/2} + \tan^{-1} \left\{ \eta \left[\frac{b'+a_1}{1-b'} \right]^{1/2} \right\} \quad \dots\dots 2.7$$

where, $\eta = S_3/S_4 \cdot (1+T)/(1-T)$

$$T = e^{-2S_3 b} \cdot (S_4 - S_3) / (S_4 + S_3)$$

$$S_3 = (a_2 + b')^{1/2} \cdot r/f$$

$$S_4 = (a_2 + b')^{1/2} \cdot r/f$$

$$a_1 = (n_S^2 - n_C^2) / (n_F^2 - n_S^2) \quad \text{for TE modes}$$

$$a_2 = (n_S^2 - n_B^2) / (n_F^2 - n_S^2)$$

$b =$ buffer thickness

2.1.2 Electromagnetic Theory

For a time dependent field, Maxwell's equations may be represented as

$$\nabla \times \mathbf{E} = -\partial \mathbf{B} / \partial t \quad \dots\dots\dots 2.8$$

$$\nabla \times \mathbf{H} = \partial \mathbf{D} / \partial t$$

where, $t =$ time

$$\nabla = i \frac{\partial}{\partial x} + j \frac{\partial}{\partial y} + k \frac{\partial}{\partial z}$$

$\mathbf{E}(t) =$ electric field

$\mathbf{H}(t) =$ magnetic field

$\mathbf{D}(t) =$ electric displacement

$\mathbf{B}(t) =$ magnetic induction

All fields are assumed to have a periodic time dependent form such as

$$\mathbf{E}(t) = \mathbf{E} \exp(j\omega t) + \mathbf{E}^* \exp(-j\omega t) \quad \dots\dots\dots 2.9$$

where, $\mathbf{E} =$ a complex amplitude

$\mathbf{E}^* =$ the complex conjugate

Further, assuming a lossless medium, then

$$\mathbf{D} = \epsilon \mathbf{E}, \text{ and } \mathbf{B} = \mu \mathbf{H} \quad \dots\dots\dots 2.10$$

Thus we have that

$$\nabla \times \mathbf{E} = -j\omega\mu\mathbf{H}, \text{ and } \nabla \times \mathbf{H} = j\omega\epsilon\mathbf{E} \quad \dots\dots\dots 2.11$$

Separating the components of equation(2.11) shows that

$$\begin{aligned} \nabla_t \times \mathbf{E}_t &= -j\omega\mu\mathbf{H}_z & \dots\dots\dots 2.12 \\ \nabla_t \times \mathbf{H}_t &= j\omega\epsilon\mathbf{E}_z \\ \nabla_t \times \mathbf{E}_z + e_z \times \partial \mathbf{E}_t / \partial z &= -j\omega\mu\mathbf{H}_t \\ \nabla_t \times \mathbf{H}_z + e_z \times \partial \mathbf{H}_t / \partial z &= j\omega\epsilon\mathbf{E}_t \end{aligned}$$

where, $\nabla_t = (\partial/\partial x, \partial/\partial y, 0)$

$e_z =$ unit vector in the z direction

$x, y, z =$ the coordinate system defined in figs(1.1)(a) and (2.1)

Now, a waveguide mode is defined as a field solution having the form

$$\begin{aligned} \mathbf{E}(x, y, z) &= \mathbf{E}_p(x, y)\exp(-j\beta_p z) & \dots\dots\dots 2.13 \\ \mathbf{H}(x, y, z) &= \mathbf{H}_p(x, y)\exp(-j\beta_p z) \end{aligned}$$

where, $p =$ the mode number

$\beta_p =$ the propagation constant of mode p

Thus, combining equation(2.13) with equations(2.12) shows that

$$\begin{aligned} \nabla_t \times \mathbf{E}_{t,p} &= -j\omega\mu\mathbf{H}_{z,p} & \dots\dots\dots 2.14 \\ \nabla_t \times \mathbf{H}_{t,p} &= j\omega\epsilon\mathbf{E}_{z,p} \\ \nabla_t \times \mathbf{E}_{z,p} - j\beta_p e_z \times \mathbf{E}_{t,p} &= -j\omega\mu\mathbf{H}_{t,p} \\ \nabla_t \times \mathbf{H}_{z,p} - j\beta_p e_z \times \mathbf{H}_{t,p} &= j\omega\epsilon\mathbf{E}_{t,p} \end{aligned}$$

Equations(2.14) are for slab guide structures incorporating guiding in only one axial direction. For two dimensional guides two mode numbers (or labels) would be needed.

The above equations have two types of solution: those corresponding to guided modes where the energy is confined near the axis of propagation, and radiation modes where the energy spreads out through the medium around the guide. The guided modes have a discrete number of solutions with corresponding propagation constants, β_p , and are analogous to the bound state solutions of the Schrodinger

equation. The radiation modes are, however, analogous to unbound state solutions, and therefore represent a continuum of possible solutions.

For planar guides equations(2.14) may be simplified by setting $\partial/\partial y=0$. A planar guide may therefore support transverse electric (TE) modes for which $E_{x'}=0$, and transverse magnetic (TM) modes for which $H_{x'}=0$. For TE modes $H_{y'}=0$, and for TM modes $E_{y'}=0$. Thus, for TE modes, from equations(2.14)

$$\begin{aligned} E_{x'} &= 0 & \dots\dots\dots 2.15 \\ \beta_{y'} E_{y'} &= -\omega\mu H_{x'} \\ \partial E_{y'}/\partial x &= -j\omega\mu H_{z'} \\ \partial H_{y'}/\partial x + j\beta_{y'} H_{x'} &= -j\omega\epsilon E_{y'} \end{aligned}$$

Combining the above equations yields that for E_y the wave equation is given by

$$\partial^2 E_y / \partial x^2 = (\beta^2 - n^2 k^2) E_y \dots\dots\dots 2.16$$

Further, by setting $E_y=0$ in equation(2.14), an analogous approach may be adopted to find the wave equation for TM- modes.

2.2 THREE-DIMENSIONAL WAVEGUIDES

The analysis of dielectric stripe guides is much more complex than that of planar guides, the modes of the guide having no exact analytic solutions. Approximate methods (eg. the Effective Index Method, or the Modified Effective Index Method) or numerical analysis techniques (eg. the Variational Analysis Technique, or the Finite Difference Method) must therefore be employed [9],[10],[14],[15].

2.2.1 The Effective Index Method

In this technique, propagation constants are calculated semi-analytically using equations(2.6) and (2.7) for two slab guides: the slab formed if the rib width were infinite (I), and the slab formed if the rib width were zero (II), as shown in

fig(1.1)(c) [9]. These propagation constants are taken as corresponding to the effective refractive indices inside and outside the rib, ie. n_{I} and n_{II} respectively, in the horizontal direction. Region II must therefore be able to support at least one mode. These values are then used to define a symmetric slab, with n_{I} confined by n_{II} on either side, the solution of which gives the resulting propagation constant.

The approximation inherent in this method is that when the waveguide is initially considered as three distinct regions, field continuity conditions at the interface are not met. This method is therefore most accurate when the rib step height is small and the rib width much larger than the rib height. The value of the effective index, n_{eff} of the mode calculated in this way is consequently greater than the true value.

This overestimation of n_{eff} can be unfortunate in the design of homojunction $N^{+}/N/N^{++}$ rib waveguides as herein under discussion. This is because in such waveguides n_{eff} of the first order mode is normally not much greater than n_s , ie. the waveguide operates near to cut-off. Hence, using the Effective Index Method to design such guides may lead to the fabrication of waveguides which do not actually guide. Other more accurate methods must therefore be used in designing these guides in order to obviate this problem.

A partial solution to this problem is found in the Modified Effective Index Method, which applies an equivalent network approach to the problem of finding the guided modes in a dielectric thin film waveguide. The application of the so-called transverse resonance technique yields approximate analytical expressions for the Dispersion relations [14].

2.2.2 The Variational Analysis Technique

This method finds the modal field profiles and propagation constants using the Rayleigh-Ritz procedure. The method may be implemented using a computer program called .NWAVE. The wave-equation to be solved, in some region of arbitrary refractive index distribution, is the Helmholtz scalar wave-equation given

by [15]

$$\nabla_{xy}^2 E_x + k^2 E_x = \beta^2 E_x \quad \dots\dots\dots 2.17$$

where, $E(x,y)$ = electric field

$$k = k(x,y)$$

Since equation(2.17) must be true over all space and is orthogonal, then

$$\beta^2 = F(E) = \frac{\iint_{-\infty}^{\infty} (\nabla^2 E + k^2 E) \cdot E dx dy}{\iint_{-\infty}^{\infty} E \cdot E dx dy} \quad \dots\dots\dots 2.18$$

Now, in order to solve equation(2.18) a form of trial function, capable of approximating to $E(x,y)$ as closely as required, must be used. A linear combination of parabolic cylinder (Hermite–Gaussian) functions is therefore chosen because: (i) they resemble the modes of a waveguide; (ii) they are orthogonal; and (iii) they are continuous and tend to zero at $\pm\infty$.

The parabolic cylinder function of order n is defined as

$$D_n(z) = (-1)^n \exp\left[\frac{z^2}{4}\right] \frac{d^n}{dz^n} \left[\exp\left[\frac{-z^2}{2}\right] \right] \quad \dots\dots\dots 2.19$$

The guide is assumed symmetric about the y -axis but not the x -axis. Therefore a zero shift parameter, x_0 equal to the estimated height of the mode centre from the origin, is introduced. Also, the functions must be scaled using the parameters η and ξ , the estimated half width in the x and y directions respectively. Further, the functions must be normalised, where the norm of the function $D_i(y/\xi)$ is given by $(2\pi)^{1/2} i! \xi$. We therefore have that

$$E(x,y) = \sum_{j=0}^n \sum_{i=0}^m a_{ij} \left[2\pi \eta \xi i! j! \right]^{-1/2} \cdot D_j \left[\frac{y}{\xi} \right] \cdot D_i \left[\frac{x-x_0}{\eta} \right] \quad \dots\dots\dots 2.20$$

which is a product of x and y direction parabolic cylinder functions. Thus, by substituting equation(2.20) into equation(2.18), and setting $\partial F/\partial a_{ij}$ to zero, we obtain

the matrix eigenvalue equation

$$[N - \beta^2 I] \mathbf{a} \mathbf{a} = 0 \quad \dots\dots 2.21$$

where, N = a symmetric square matrix ($nm \times nm$)

The matrix N has nm possible eigenvalues, β^2 , each with its corresponding eigenvector \mathbf{a} . The main task of the program .NWAVE is therefore to assemble the matrix N , and calculate the eigenvalues and eigenvectors. The number of eigenvalues resulting from the program is specified at the beginning within a data file, these eigenvalues corresponding to the effective indices of the modes of the guide (odd or even – whichever was originally specified within the data file).

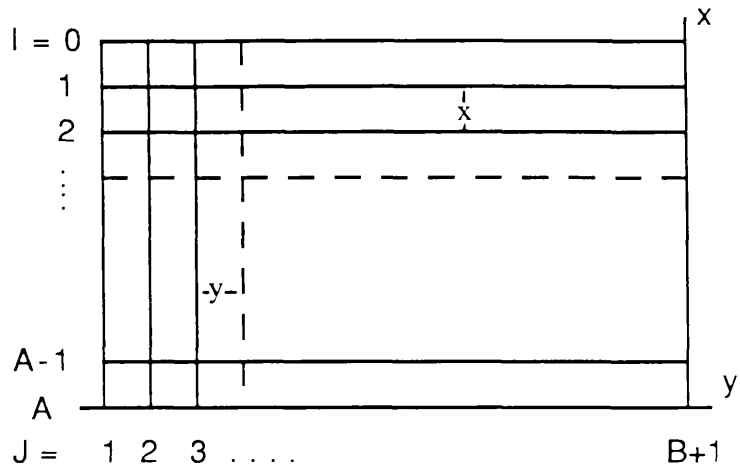
Thus if $n_{\text{eff}} < n_{II}$, where n_{II} = the effective refractive index of the region outside the rib (as defined in section(2.2.1)), then the mode will be cut-off, whereas if $n_{\text{eff}} > n_{II}$, the mode will be guided.

2.2.3 The Finite Difference Technique

The basis of this method is the substitution of the wave equation by finite difference relations in terms of the fields at discrete mesh points, boundary conditions being enforced by enclosing the guide within an arbitrarily determined electric wall [10]. This technique thus leads to a matrix eigenvalue problem, and the iterative calculation of the field distribution and eigenvalue of the modal effective index, n_{eff} .

As shown in fig(2.2) the application of the finite difference technique requires the waveguide cross section to be divided into a rectangular mesh, which suggests that the field $E_y(x,y)$ at discrete mesh points may be expressed in terms of finite difference expressions [10]. For TE modes the finite difference expression has the form

Fig (2.2) Solution of the Wave Equation by the Finite Difference Technique: Definition of Axes and Mesh Points



$$E(I, J) = \frac{E(I+1, J)+E(I-1, J)+R^2(E(I, J+1)+E(I, J-1))}{2[1+R^2]-k^2X^2-(n^2(I, J)-n_{eff}^2)} \quad \dots\dots\dots 2.22$$

where, $R = X/Y$

$n(I, J) =$ refractive index at point (IX, JY)

The waveguide dimensions are therefore AX by $2BY$, with a centre line, $J=1$, and the boundary conditions that $E(0, J) = E(A, J) = E(I, B+1) = 0$.

A variational expression for the propagation constant, β , of the waveguide can then be formed [10]. This produces a lower bound for β^2 , which improves as E_y tends toward the actual mode distribution. This variational expression, which can also be expressed in Finite Difference form, is the Rayleigh Quotient, given by

$$\beta^2 = k^2 N^2 > \frac{\iint_{x\text{-sect}} \left[\frac{\partial^2 E_y}{\partial x^2} + \frac{\partial^2 E_y}{\partial y^2} + k^2 n^2 E_y \right] E_y dx dy}{\iint_{x\text{-sect}} E_y^2 dx dy} \quad \dots\dots\dots 2.23$$

The method operates by drawing up the mesh and assigning a refractive index value to each mesh point, the eigenvalue of n_{eff} then being estimated. Equation(2.22) is subsequently applied to each point and new field values calculated, these being substituted into the Rayleigh Quotient from which a better approximation to β , and hence n_{eff} , may be calculated. The process is then repeated by substituting these values into equation(2.22) until the eigenvalue of n_{eff} converges satisfactorily.

The rate of convergence may be increased by implementing the method of Successive Over-Relaxation (SOR). This overcorrects at each stage by a factor, S ($0 < S < 2$). If SOR is used then equation(2.22) takes the form [10].

$$E(I, J) = \frac{S \left[E(I+1, J)+E(I-1, J)+R^2(E(I, J+1)+E(I, J-1)) \right]}{2(1+R^2)+k^2X^2(n^2(I, J)-n_{eff}^2)} \quad \dots\dots\dots 2.24$$

$$- (S-1)E(I, J)$$

2.3 PHOTOELASTIC WAVEGUIDES

2.3.1 Stresses in Thin Films

Strain-induced optical waveguides can be formed in GaAs, and other III-V compound semiconductors, simply by opening windows or defining stripes in an applied surface film which is under compression or tension [10],[16],[17],[18],[19]. Since most applied films are likely to be under stress as a result of thermal expansion mismatch, as well as the deposition process, photoelastic waveguiding or antiwaveguiding may be present in many stripe-geometry III-V semiconductor optical devices. These simply formed waveguides may therefore be suitable for integrated optical applications.

The treatment of the stress field beneath a film window, given below, uses an isotropic average value of Young's modulus, E' , and Poisson's ratio, ν , for GaAs, even though GaAs has an anisotropic elastic compliance tensor. Now, from Kirby *et al* [18], and according to the definitions of fig(2.3)

$$\sigma_{ox}t = \frac{E' s^2}{6\rho(1-\nu)} = \text{force per unit length} \quad \dots\dots 2.25$$

where, σ_{ox} = compressive stress of film

t = film thickness

$E/(1-\nu) = 1.23 \times 10^{12} \text{ dyn cm}^{-2}$ in the {100} plane (GaAs)

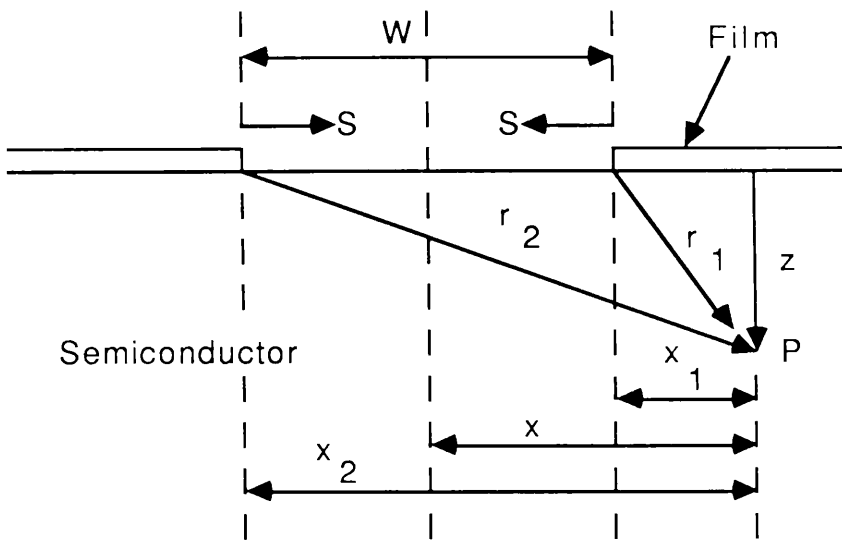
s = substrate thickness

ρ = radius of curvature of substrate

Thus σ_{ox} may be found for any given film thickness by measuring the radius of curvature, ρ , of the substrate which is under compression or tension. ρ may itself be measured using a sodium-interference-microscope objective [10].

As shown in fig(2.3), if a stripe window is present in the film then a force per unit length, $S = \sigma_{ox}t$ (dyn cm^{-1}), is exerted on the GaAs substrate by the film

Fig(2.3) Configuration of Stripe Photoelastic Waveguide for Stress Calculations



edge. The applied force S causes the coordinates of point P to change from (x,z) to (x+u,z+w). The displacements are given by [18]

$$u = 2S \left[(AB-C) \ln(r_1/r_2) + A(x_1^2/r_1^2 - x_2^2/r_2^2) \right] \quad \dots\dots\dots 2.26$$

$$w = S \left\{ 2A \left[(x_1 z/r_1^2) - (x_2 z/r_2^2) \right] + 2C \left[\cos^{-1}(z/r_1) - \cos^{-1}(z/r_2) \right] \right\} \quad \dots\dots\dots 2.27$$

where, x_1 , x_2 , r_1 , and r_2 are shown in fig(2.3), and

$$\begin{aligned} A &= (1+\nu)/2E' = 1.63 \times 10^{-3} \text{cm}^2 \text{dyn}^{-1} \\ B &= (3-4\nu) = 2.08 \quad \dots\dots\dots 2.28 \\ C &= (1+\nu)(1-2\nu)/2\pi E' = 8.81 \times 10^{-14} \text{cm}^2 \text{dyn}^{-1} \end{aligned}$$

The three independent elastic constants of GaAs are $C_{11} = 11.88 \times 10^{11}$, $C_{12} = 5.38 \times 10^{11}$, and $C_{44} = 5.94 \times 10^{11} \text{dyncm}^{-2}$. Also, the Voight average shear modulus $= \mu = C_{44} - H/5 = 4.86 \times 10^{11} \text{dyncm}^{-2}$, and the Lamé constant $= \lambda = C_{12} - H/5 = 4.30 \times 10^{11} \text{dyncm}^{-2}$ where, $H = 2C_{44} + C_{12} - C_{11}$.

Also,

$$E' = \mu(3\lambda+2\mu)/(\mu+\lambda) = 1.2 \times 10^{12} \text{dyncm}^{-2} \quad \dots\dots\dots 2.29$$

$$\nu = \lambda/2(\mu+\lambda) = 0.23 \quad \dots\dots\dots 2.30$$

These averaged elastic constants can thus be used in equations(2.26), (2.27) and (2.28). Further, the stresses and strains at any point (x,y) are defined as follows [10]

$$\text{Non-zero elastic strains, } e_{xx} = du/dx, \text{ and } e_{zz} = dw/dz \quad \dots\dots\dots 2.31$$

$$\text{Shear strain, } e_{xz} = e_{zx} = 0.5(du/dz + dw/dx) \quad \dots\dots\dots 2.32$$

$$\begin{aligned} \text{Stresses, } \sigma_{xx} &= (\lambda+2\mu)e_{xx} + \lambda e_{zz} \\ \sigma_{yy} &= \lambda e_{xx} + \lambda e_{zz} \quad \dots\dots\dots 2.33 \end{aligned}$$

$$\begin{aligned} \sigma_{zz} &= \lambda e_{xx} + (\lambda+2\mu)e_{zz} \\ \text{Shear stress, } \sigma_{xz} &= \sigma_{zx} = 2\mu e_{xz} \quad \dots\dots\dots 2.34 \end{aligned}$$

Explicit expressions for the strains e_{xx} and e_{zz} of equation(2.31) in the x and z directions respectively, may therefore be obtained by differentiating equations(2.26) and (2.27) with respect to x and z respectively, ie.

$$\begin{aligned}
e_{xx} &= \frac{du}{dx} = 2S \left[(AB-C) \left[\frac{x_2}{r_2^2} - \frac{x_1}{r_1^2} \right] - 2Az^2 \left[\frac{x_2}{r_2^4} - \frac{x_1}{r_1^4} \right] \right] \quad \dots\dots\dots 2.35 \\
e_{zz} &= \frac{dw}{dz} = 2S \left[A \left[\frac{x_1(r_1^2 - 2z^2)}{r_1^4} - \frac{x_2(r_2^2 - 2z^2)}{r_2^4} \right] \right. \\
&\quad \left. - C \left[\frac{x_1}{r_1^2} - \frac{x_2}{r_2^2} \right] \right]
\end{aligned}$$

2.3.2 The Photoelastic Effect

The Photoelastic effect describes the dependence of the dielectric constant, ϵ , and hence the refractive index, n , of a crystal on the stress (or strain) within the crystal. The dielectric constant profile produced by the strain field in the active layer may be found from [10]

$$B_{ij} = P_{ijrs} e_{rs} \quad (ijrs = x,y,z) \quad \dots\dots\dots 2.36$$

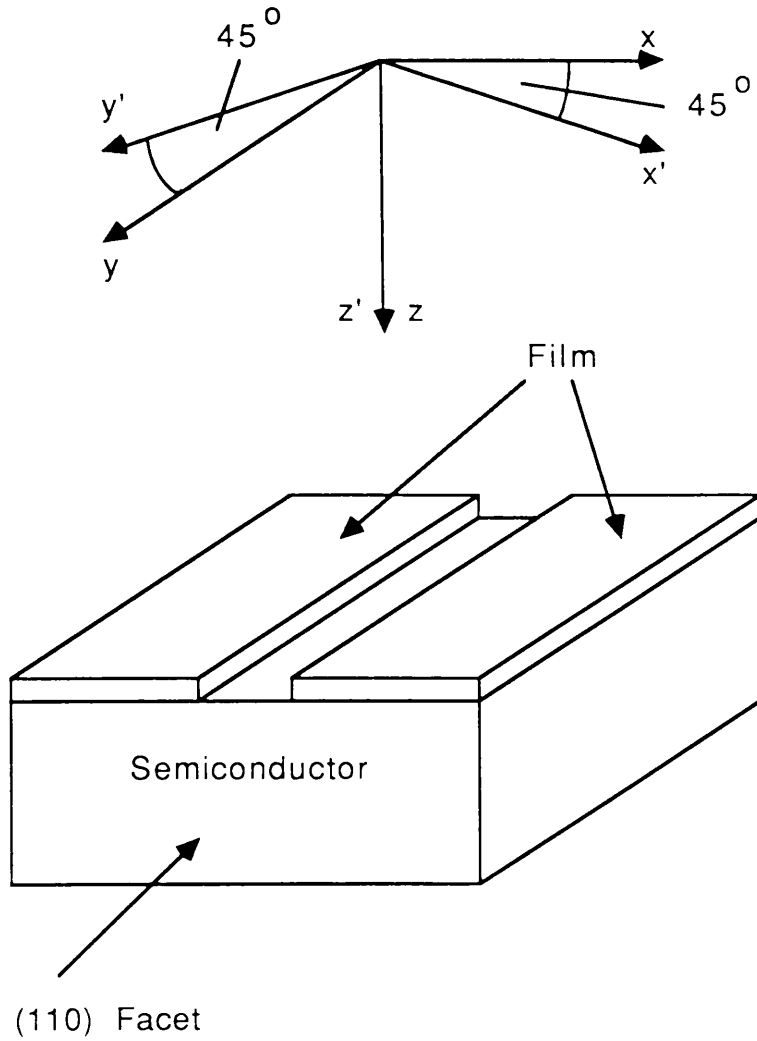
where, B_{ij} = change in the relative impermeability tensor B_{ij} (where the relative impermeability is the inverse of the dielectric constant)

P_{ijrs} = Photoelastic coefficients (forming a fourth rank tensor)
 e_{rs} = strain tensor

Now, for crystals of class $\bar{4}3m$, such as GaAs, there exist only three independent photoelastic constants p_{11} , p_{12} , and p_{44} , which are given with respect to the primary crystal axes $x'y'z'$, shown in fig(2.4), and not those used in the previous stress calculation of section(2.3.1). Thus, to find the matrix B_{ij} it is necessary to transform the strain field axes from xyz to $x'y'z'$, multiply by the photoelastic tensor, then transform the axes of the resulting B_{ij} matrix back to the xyz axes. This gives [10]

$$B_{ij} = \begin{bmatrix} e_{xx}[0.5(p_{11}+p_{12})+p_{44}] + e_{zz}p_{12} & 0 & 2e_{xz}p_{44} \\ 0 & e_{xx}[0.5(p_{11}+p_{12})-p_{44}] + e_{zz}p_{12} & 0 \\ 2e_{xz}p_{44} & 0 & e_{xx}p_{12} + e_{zz}p_{11} \end{bmatrix} \quad \dots\dots\dots 2.37$$

Fig(2.4) Relationship between the Primary Crystal Axes $x'y'z'$, and the xyz Axes used for Strain and Refractive Index Profile Calculations



Since the change in the relative dielectric impermeability, ΔB , is small in comparison to B , then by series expansion to a first approximation the change in dielectric constant can be found from

$$\begin{aligned} \Delta\epsilon_{XX} &= -\epsilon^2 B_{XX} = -\epsilon^2 \left\{ e_{XX} [0.5(p_{11} + p_{12}) + p_{44}] + e_{ZZ} p_{12} \right\} && \text{for TE waves} \\ &&& \dots\dots\dots 2.38 \\ \Delta\epsilon_{ZZ} &= -\epsilon^2 B_{ZZ} = -\epsilon^2 \left\{ e_{XX} p_{12} + e_{ZZ} p_{11} \right\} && \text{for TM waves} \end{aligned}$$

Equations(2.38) can consequently be used, in conjunction with equations(2.25), (2.28) and (2.35), to calculate the refractive index distribution for any proposed photoelastic waveguide.

2.4 LOSS MECHANISMS IN DIELECTRIC WAVEGUIDES

While the preceding sections of this Chapter have dealt with mode propagation in slab, rib, and photoelastic type waveguides, and the analysis of such propagation, this section introduces the concept of optical attenuation or loss within the guide.

Whereas optical propagation may be thought of as the propagation of optical rays or waves, loss mechanisms may be more readily described by viewing the optical radiation as a flux of photons. The total optical power will thus decrease as the optical radiation propagates along the waveguide, due to photons being scattered, absorbed, or radiated. Scattering losses usually predominate in glass or dielectric waveguides, while in semiconductor waveguides thickness variations of the order of $0.01 \mu\text{m}$ suggest that scattering losses are not important, absorption losses being much larger.

A measure of the optical loss may be derived through the exponential attenuation coefficient, α (cm^{-1}), where

$$I(z) = I_0 e^{-\alpha z} \dots\dots\dots 2.39$$

where, I = the optical intensity at any point, z along the waveguide length

I_0 = the initial optical intensity

z = propagation distance as defined in fig(2.1)

Further, the loss, L in dBcm^{-1} may be given by

$$\begin{aligned} L &= 10 \log_{10} \left[\frac{I_0}{I} \right] && \dots\dots\dots 2.40 \\ &= 10 \log_{10} (e^{-\alpha z}) \\ &= 4.3\alpha \end{aligned}$$

Two types of scattering loss may be identified: surface scattering due to surface roughness, and volume scattering due to defects, contaminant atoms, and voids within the crystal structure. Provided that the optical wavelength is larger than any crystal imperfections, losses due to surface scattering are normally much greater than those due to volume scattering.

In semiconductor waveguides significant loss may also occur due to both interband and intraband absorption. Interband absorption is due to photons with energy larger than the bandgap of the material giving up their energy to raise electrons from the valence band to the conduction band. Interband absorption may therefore be avoided by choosing a wavelength longer than that of the absorption edge of the waveguide material.

Intraband, or Free Carrier absorption is that occurring due to a photon giving its energy up to an electron which is already in the conduction band, or a hole already in the valence band. Further, Free Carrier absorption may occur due to the existence of shallow donor states near the conduction band edge, or shallow acceptor states near the valence band edge.

In Chapter 4, classical electromagnetic theory is used to find a relation between the doping density, N , and the corresponding Free Carrier absorption, α_{FC} . From this analysis one can also derive the change in the refractive index due to the presence of free carriers. This effect is obviously of importance to the homojunction waveguide structures proposed in the devices studied herein.

Losses may also result from radiation, where photons are no longer guided, and radiate into the media surrounding the waveguide structure. Radiation losses can, however, be neglected in comparison to scattering – or absorption – losses in sections of straight waveguide in which the modes are well confined. Radiation losses are usually significant only in sections of curved, or bent waveguide.

CHAPTER 3

THE GUNN EFFECT

3.1 THE MECHANISM OF THE GUNN EFFECT

In 1963 Gunn [20],[21] discovered that a coherent microwave output was generated when a DC electric field, exceeding a critical threshold value, E_T , of several thousand volts per cm, was applied across a randomly oriented sample of N-type GaAs or InP. The frequency of oscillation was approximately equal to the reciprocal of the carrier transit time across the length of the sample. Subsequently, Gunn made capacitance probe measurements of the spatial variation of the electric field within the material [22]. These measurements showed that a moving distribution of potential, propagating from the cathode to the anode, accompanied each current oscillation.

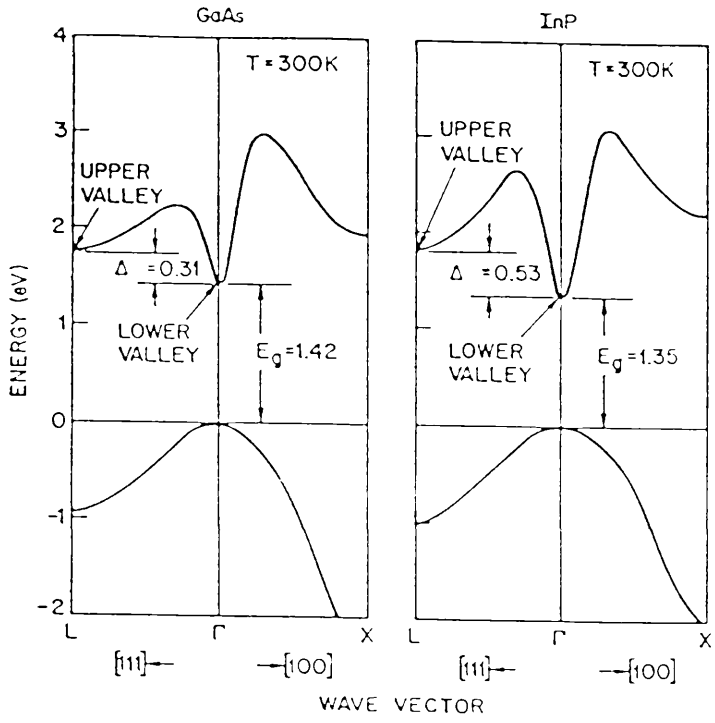
Kroemer [23] pointed out that the observed properties of the microwave oscillation were consistent with a theory of negative differential resistance (NDR) proposed by Ridley and Watkins [24], and independently by Hilsum [25],[26]. Ridley and Watkins had shown that the presence of NDR could result in the formation and propagation of high field dipole domains, ie. that a homogeneous material could become electrically heterogeneous.

Hilsum meanwhile had predicted that the phenomenon of the Transferred Electron effect could lead to NDR and produce amplification and oscillation.

The Transferred Electron effect is a direct result of the band structures of these semiconductors, which are shown in fig(3.1). It essentially consists of making the normally highly mobile conduction electrons in the lowest conduction band valley (Γ), transfer to higher energy, lower mobility states in the higher energy conduction band valleys (L). The action of the transfer is to reduce the average electron mobility within the semiconductor as the electron energy increases.

At low electric fields the conduction electrons occupy the bottom of the central valley, and are distributed over the thermal energy range. Energy is thus

Fig(3.1) Band Structures of GaAs and InP



delivered to the electrons during their acceleration until they collide with imperfections of the crystal lattice, eg. thermal lattice vibrations of a polar-optical character. As the electric field is increased further the equilibrium state of electrons exists at a higher mean energy, and the electrons will occupy a broader range of energies in the central valley of the conduction band.

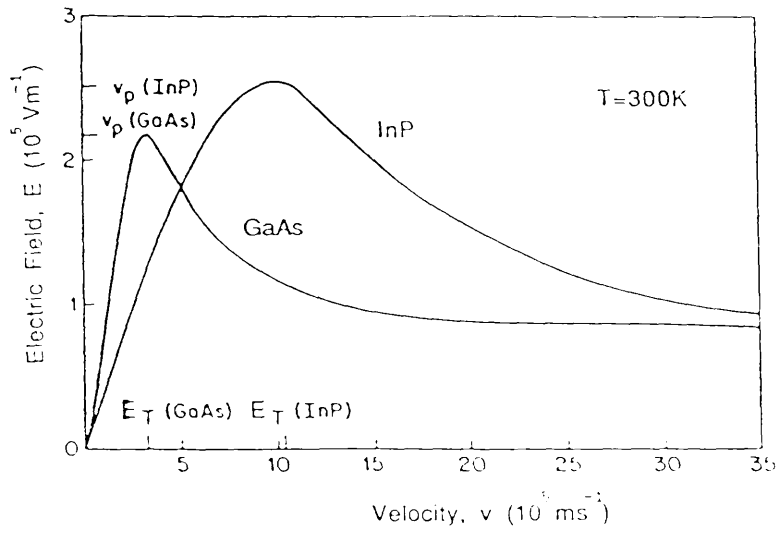
When the kinetic energy of the electrons exceeds the intervalley separation, Δ , there is a probability that they will occupy one of the satellite valleys of the conduction band. In these valleys electrons have a higher effective mass, and so the density of states of the satellite valleys is much greater than that of the central valley. Further, the electron mobility of the satellite valley is therefore smaller than that of the central valley. Thus, even though an incremental increase in the applied electric field will produce a separate increase of drift velocity in each valley, the combined effects of electron transfer may cause NDR. The resulting velocity-field characteristics for GaAs and InP are shown in fig(3.2) [27].

Convincing evidence that the Transferred Electron effect was responsible for the oscillations observed by Gunn was supplied by the pressure experiments of Hutson *et al* [28] carried out on GaAs, and the GaAsP alloy experiments of Allen *et al* [29]. These experiments varied the separation between the Γ and L valley minima, and demonstrated that the threshold electric field for oscillation, E_T , decreases with decreasing Δ .

In the case of Hutson *et al* the variation in Δ was brought about by the application of hydrostatic pressure. It was found that Δ had a sensitivity of around $9.0 \times 10^{-3} \text{eV/kbar}^{-1}$, and that the threshold voltage decreased with increasing pressure, such that at a pressure of 26kbar the instability vanished completely. This seemed reasonable since the accepted value of $\Delta(\text{GaAs})$, ie. the separation between the central Γ_5 valley and the first satellite valley, L_6 , is 0.2845eV [30], and should therefore be zero at such a pressure.

Without the application of hydrostatic pressure, Allen *et al* showed that by forming mixed compounds of $\text{GaAs}_x\text{P}_{1-x}$ with the compositional fraction, x , varying from 1.0 to 0.52, Δ could be seen to vary from 0.36eV to zero, with a

Fig(3.2) Velocity-Field Characteristics for GaAs and InP



corresponding variation of the threshold field, E_T .

More recent experimental work [31] has shown an increase with pressure of the electron effective mass in the Γ valley, thus resulting in an increase in the threshold field for pressures of up to 15kbar. It has been suggested that this effect was masked in earlier studies due to the imperfect ohmic action of the device contacts, resulting in the presence of high fields at the cathode contact.

It can be deduced from the above that the manifestation of current instabilities in a Gunn device is dependent upon the following:

(a) The electrical characteristics of the semiconductor, ie.: (i) the intervalley separation, Δ , which must be several times greater than the thermal energy, kT/e ($\approx 0.025\text{eV}$) so that the satellite valleys are not populated at low values of electric field. (ii) the fundamental energy gap, E_g ($\approx 1.58\text{eV}$ for GaAs) must be greater than Δ so that intervalley transfer occurs before impact ionisation of electrons across the band gap. (iii) the electron effective mass in the satellite valleys must be larger than that in the central valley. Electrons with sufficient energy will then more probably occupy the satellite valleys with their higher density of states. For GaAs, $m_\Gamma = 0.0632m_e$ and $m_L = 0.55m_e$, where $m_e = \text{electron mass} = 9.10956 \times 10^{-31}\text{kg}$. (iv) the electron mobility in the satellite valley should be less than that in the central valley, eg. for GaAs, $\mu_\Gamma = 8000\text{cm}^2\text{V}^{-1}\text{s}^{-1}$ and $\mu_L = 900\text{cm}^2\text{V}^{-1}\text{s}^{-1}$, the mobility in the L valley being lower owing to the higher effective mass of electrons, and also the stronger scattering processes which are observed in the satellite valleys.

(b) The circuit within which the device operates.

(c) The boundary conditions imposed on the active region of the device, particularly those at the cathode.

Points (b) and (c) are dealt with further in section(3.4) of this Chapter.

3.2 SPACE CHARGE INSTABILITIES

3.2.1 Domain Formation

A noise process, or defect in the doping uniformity, within a uniformly doped device may cause a spontaneous fluctuation of the electron density, N , within the device. There will also be a corresponding electric field non-uniformity, related to the space-charge fluctuation by Poisson's equation

$$\epsilon \frac{\partial E}{\partial x} = q(N - N_D) \quad \dots\dots\dots 3.1$$

where, ϵ = material dielectric constant

E = electric field

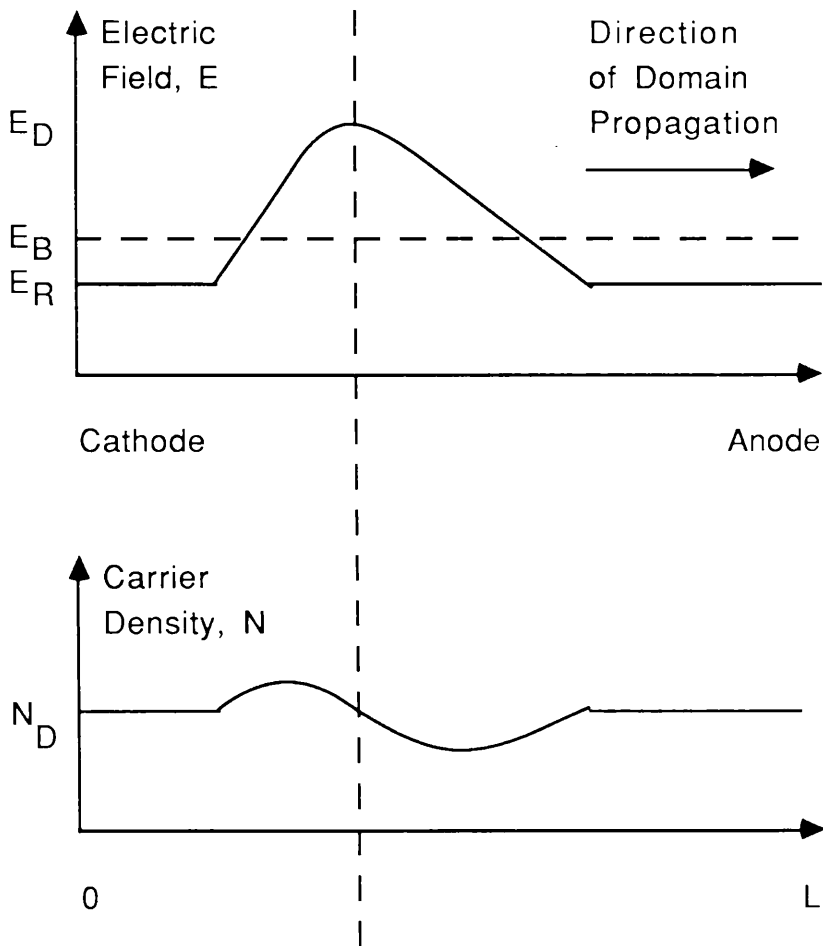
q = electronic charge

N_D = doping density

If the average electric field is below the threshold field, E_T , then electrons in the region of higher field will move more quickly than those outside, and so the electrons in the region of space-charge accumulation will tend to fill in the depleted region. If, however, the average electric field is above E_T , then there will be a reduction in the electron velocity within the region of higher field. Electrons outside this region will therefore travel faster than those within, leading to a further accumulation of electrons on the cathode side of the fluctuation, and depletion of electrons on the anode side.

Following equation(3.1) there will also be an increase in the electric field associated with the fluctuation, and a corresponding reduction in the drift velocity. The fluctuation thus continues to grow exponentially until the electric field outside the fluctuation, E_R , has fallen below E_T and the electron drift velocity is equal inside and outside the fluctuation. In this way, a dipole domain, as shown in fig(3.3), nucleates and propagates from anode to cathode. The fully matured domain

Fig(3.3) The Generalised Profile of a Dipole Domain



will then drift through the device from cathode to anode at a constant velocity. The

Current Density equation is given by

$$J = \frac{E}{\rho} - qD \frac{\partial N}{\partial x} \quad \dots\dots\dots 3.2$$

where, J = electron current density

ρ = resistivity = $1/Nq\mu$

μ = electron mobility

D = diffusion coefficient

Further, the one-dimensional continuity equation is given by

$$\frac{\partial N}{\partial t} + \frac{1}{q} \frac{\partial J}{\partial x} = 0 \quad \dots\dots\dots 3.3$$

Now, differentiating equation(3.2) with respect to x, and substituting in Poisson's equation yields that

$$\frac{1}{q} \frac{\partial J}{\partial x} = \frac{1}{\rho \epsilon} (N - N_D) - D \frac{\partial^2 N}{\partial x^2} \quad \dots\dots\dots 3.4$$

Substituting this into equation(3.3) gives that

$$\frac{\partial N}{\partial t} + \frac{(N - N_D)}{\rho \epsilon} - D \frac{\partial^2 N}{\partial x^2} = 0 \quad \dots\dots\dots 3.5$$

For the temporal response equation(3.6) has the solution

$$N - N_D = (N - N_D)_{t=0} \exp\left[\frac{-t}{\tau_R} \right] \quad \dots\dots\dots 3.6$$

where, τ_R = the dielectric relaxation time

$$\equiv \rho \epsilon = \epsilon / q\mu N$$

$$\approx \epsilon / q\mu N_D$$

The dielectric relaxation time represents the time constant for the decay of the space-charge to neutrality for a material with a positive differential resistivity, or the rate of growth of any charge imbalance for a material with negative differential resistivity. It should, however, be noted that the above is a simplified model of the behaviour of a space-charge instability

The formation of a strong space-charge instability is dependent upon the condition that enough charge is available in the semiconductor, and that the device is long enough to allow the necessary amount of space-charge to build up within the transit time of the electrons. If equation(3.6) is true throughout the entire transit time of the space-charge layer, then the maximum growth factor will be given by $\exp(L/v_D|\tau_R|)$ where, v_D = the average drift velocity of the space-charge layer, and L = the active layer length. This growth factor must be greater than unity for large space-charge growth, ie. $L/v_D|\tau_R| > 1$. Thus

$$N_D L > \frac{\epsilon v}{q|\mu_-|} \approx 10^{12} \text{cm}^{-2} \quad \text{for N-type GaAs and InP} \quad \dots\dots\dots 3.7$$

where, μ_- = maximum negative differential mobility
 $\approx -2400 \text{cm}^2 \text{V}^{-1} \text{s}^{-1} \quad \text{for GaAs}$

This condition defines the boundary between so-called sub-critical and super-critical Transferred Electron devices, ie. those in which domains do not form, and those in which domains do form.

3.2.2 Domain Dynamics

The analysis of stable uniform domain propagation was first proposed by Butcher [32] in the mid 1960's, the relevant equations determining the behaviour of the electron system being Poisson's equation (equation(3.1)) and the Current Continuity equation

$$J(t) = Nqv(E) - q \frac{\partial}{\partial x} \{D(E)N\} + \epsilon \frac{\partial E}{\partial t} \quad \dots\dots 3.8$$

= conduction + diffusion + displacement

We therefore seek a solution of equations(3.1) and (3.8) representing a high-field domain which propagates without change of shape from cathode to anode at a constant drift velocity, v_D . Further, E and N are functions of $y = x - v_D t$, such that $E \rightarrow E_R$, where $E_R =$ a constant value of electric field outwith the domain, and $N \rightarrow N_D$ as $x \rightarrow \pm\infty$.

It can be seen from fig(3.3) that within the domain N is a two-valued function of E, and that the domain consists of a depletion branch with $N < N_D$ which comes from the leading edge of the domain, and an accumulation branch with $N > N_D$ which comes from the trailing edge. The two branches come together with $N = N_D$ when $E = E_R$ - the field outside the domain - and also when $E = E_D$ - the peak domain field. The relation between E and y may be represented as [33]

$$y = y_m + \frac{\epsilon}{q} \int_{E_D}^E \frac{dE}{(N - N_D)} \quad \dots\dots 3.9$$

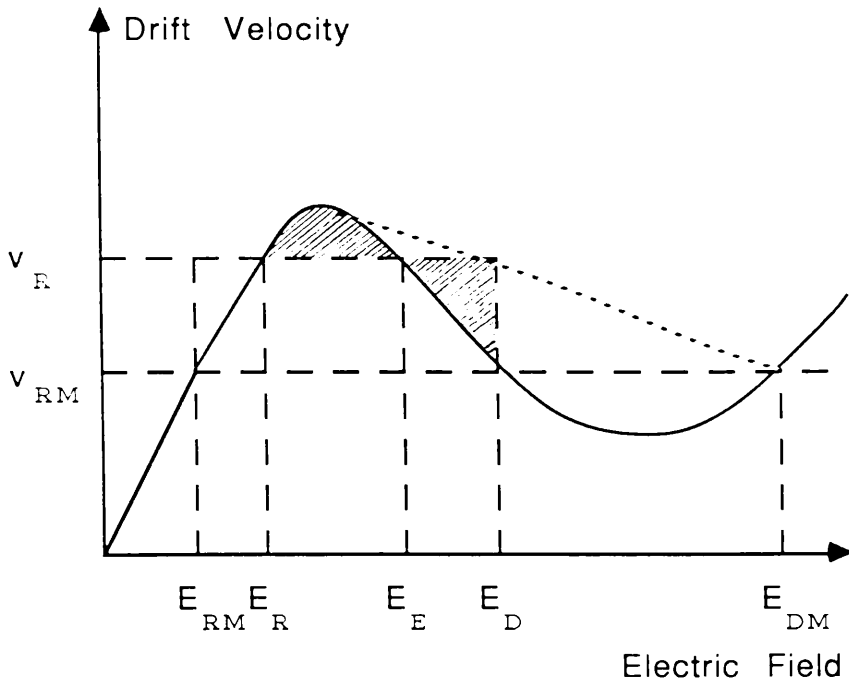
where, $y_m =$ an arbitrary constant

It can also be shown that when $D(E) = D$ a constant independent of E, the formal solution of equations(3.1) and (3.8) is [32]

$$\frac{N}{N_D} - \ln \left[\frac{N}{N_D} \right] - 1 = \frac{\epsilon}{qN_D D} \int_{E_R}^E \left[\{v(E) - v_D\} - \left[\frac{N_D}{N} \right] \{v_R - v_D\} \right] dE \quad \dots\dots 3.10$$

Now, $N = N_D$ at $E = E_R$ or $E = E_D$. Thus, from equation(3.10) $v_D = v_R$. Moreover, E_D is such as to make the integral in equation(3.10) vanish when $v_D = v_R$, ie. E_D is determined by the simple geometrical condition that the two shaded areas in fig(3.4) should be equal in magnitude. This condition is known as the Equal Areas Rule and holds, along with the identity $v_D = v_R$, for any value of

Fig(3.4) Schematic of Drift Velocity-Field (Full Curve), and Drift Velocity-Peak Domain Field (Broken Curve)



D so long as it is independent of E (see Appendix A).

Further, referring to equation(3.10), it can be seen that in the limit of zero diffusion the domain shape becomes very simple [33], ie. the domain will consist of a triangular field pulse to which is added a flat-topped region in long, low resistivity samples at high bias voltages. This can be seen since $N = N_D$ when $E = E_R$ or E_D for all values of D. However, when E lies between E_R and E_D the right hand side of equation(3.10) increases indefinitely as $D \rightarrow 0$, and so $N \rightarrow 0$ on the depletion branch, and $N \rightarrow \infty$ on the accumulation branch. Further, as E_R decreases towards the minimum value of the field outwith the domain, E_{RM} , the peak domain field increases to a maximum value of E_{DM} . Moreover, for higher applied fields $v(E_{DM}) = v(E_{RM})$, as predicted by the Equal Areas Rule, and so a flat-topped region of arbitrary width may be inserted between the accumulation and depletion layers.

The primary requirement for domain formation is a velocity-field characteristic with a region of negative differential resistivity; the field dependence of D is of secondary significance. The above analysis which assumes a field independent diffusion coefficient may therefore be expected to yield a useful semi-quantitative description of domain behaviour.

Butcher refined his theory further by introducing:

- (a) an analytical approximation to the static velocity-field characteristic for GaAs which takes into account all the relevant scattering mechanisms [34]; and
- (b) a constant diffusion coefficient, $D = 178 \text{ cm}^2\text{sec}^{-1}$ [35].

With the analytical velocity-field characteristic used by Butcher, which saturates at high fields, E_D increases without limit as $E_R \rightarrow E_{RM}$. Consequently the height and width of the depletion layer triangle also increase without limit, and flat-topped domains of the type discussed above will never arise.

When D is finite the domain shape is more complicated and must be calculated numerically from equations(3.9) and (3.10). It has been observed that when E_D is close to E_T , ie. when E_R is close to E_T , the domain assumes a symmetrical rounded shape, since the domain is then nearly neutral throughout its

width. However, as E_D increases, ie. E_R decreases, the domain assumes an assymetrical rounded triangular shape, due to the fact that the magnitude of the space-charge density in the depletion layer cannot exceed qN_D , while in the accumulation layer it can be much larger.

The final refinement which Butcher made to the theory was to introduce a field dependent diffusion coefficient, $D(E)$ [36],[37]. The field dependence of $D(E)$ can be found from the two-term Einstein relation

$$D(E) = \frac{k}{q} \frac{(N_1 \mu_1 T_1 + N_2 \mu_2 T_2)}{(N_1 + N_2)} \quad \dots\dots 3.11$$

where, N_1 = the electron density in the (000) valley

N_2 = the electron density in the (100) valley

μ_1, μ_2 = electron mobilities in (000) and (100) valleys
respectively

T_1, T_2 = electron temperatures in (000) and (100) valleys
respectively

The domain motion is still governed by equations(3.1) and (3.8). However, introducing a field dependent diffusion coefficient, the solution becomes [36]

$$\begin{aligned} \frac{N}{N_D} - \ln \left(\frac{N}{N_D} \right) - 1 &= \frac{\epsilon}{qN_D} \int_{E_R}^E \frac{(v(E) - v_D)}{D(E)} dE \quad \dots\dots 3.12 \\ &+ \frac{\epsilon}{qN_D} (v_D - v_R) \int_{E_R}^E \frac{N_D}{N(E)D(E)} dE \\ &- \int_{E_R}^E \frac{D'(E)}{D(E)} \left[\frac{N(E)}{N_D} - 1 \right] dE \end{aligned}$$

where, $D'(E)$ = the gradient of the diffusion coefficient - field
characteristic

It can thus be shown that the electron velocity inside the domain, v_D , is

larger than the electron velocity outside the domain, v_R , and that the difference between v_D and v_R may be determined by a weighted average of the derivative of D over the domain [36],[37]. The true dynamic characteristic will therefore lie somewhat above that determined by the Equal Areas Rule.

3.3 CONVENTIONAL GUNN DIODE STRUCTURES

Possible Gunn diode chip configurations are shown in fig(3.5)(a)–(f). The diodes represented in (a)–(d) depict vertical sandwich–type structures, wherein the direction of current flow is perpendicular to the conducting substrate. Types (e) and (f) are of a coplanar–contact structure, ie. a 'surface–oriented' or 'transverse'–type device, wherein the current flow is parallel to an insulating substrate.

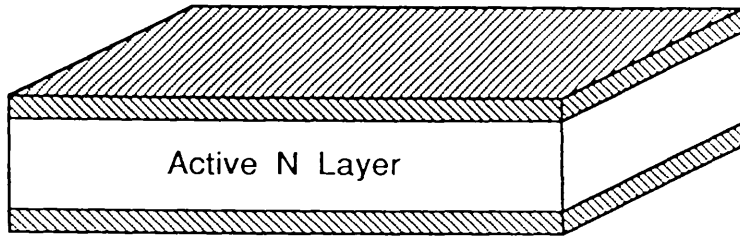
Type (a) consists of an active material sandwiched between two metal layers forming ohmic contacts. This is the simplest form of Gunn diode used frequently during the earlier stage of the experimental study of the Gunn effect.

Structures (b)–(d) are similar to structure (a) in that the contacts again form a sandwich structure, the active layer being grown epitaxially on a highly doped substrate. These are currently the most favoured configurations for commercial Gunn devices. In the case of device (b) the top metal contact is small in order to reduce the active device area, and therefore reduce the current drawn by the device, as well as to minimise surface breakdown. Devices (c) and (d) have been etched into a mesa structure in order to achieve the same reduction.

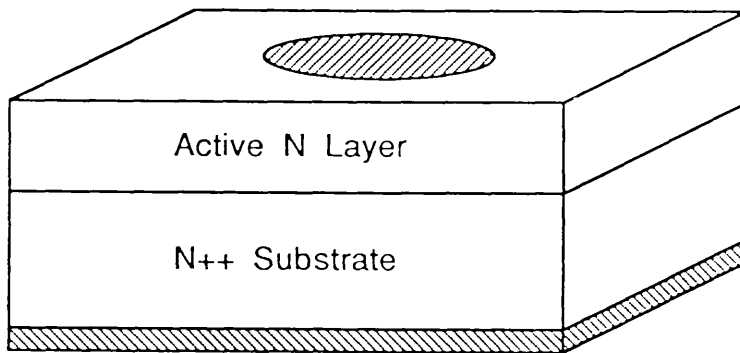
The planar structures of devices (e) and (f) are particularly useful for the incorporation of Gunn devices into integrated circuits, since their insulating substrate allows for the electrical isolation of adjacent discrete devices. Device (e), which still essentially forms a sandwich structure, is produced by selective and successive etching and epitaxial regrowth of N^+ , N and N^+ layers, with SiO_2 or Si_3N_4 films acting as a lithographic mask. Device (f) is however fundamentally different from the other structures since the active layer is grown directly onto a semi–insulating substrate. The ohmic contacts may be either applied directly to the surface of the active layer,

Fig(3.5) Gunn Diode Chip Configurations

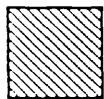
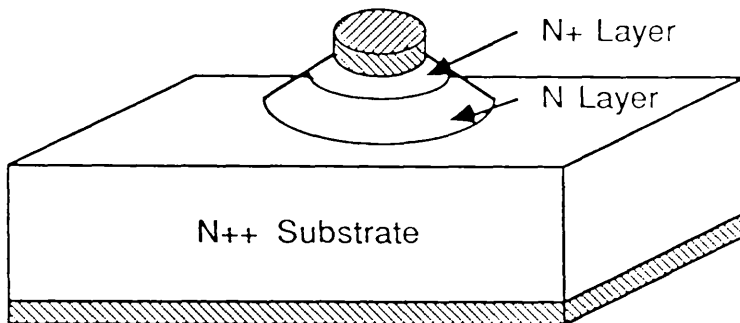
(a)



(b)

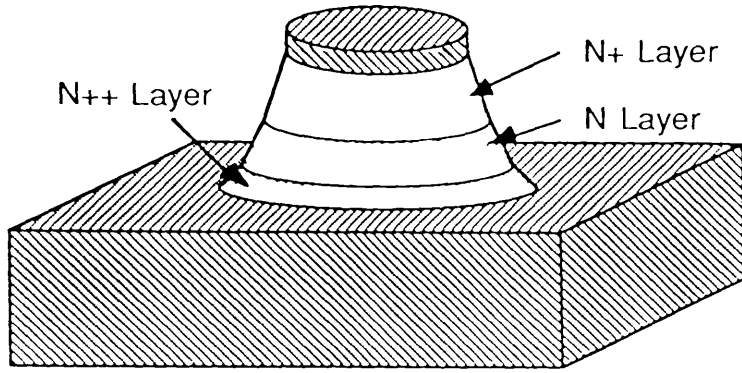


(c)

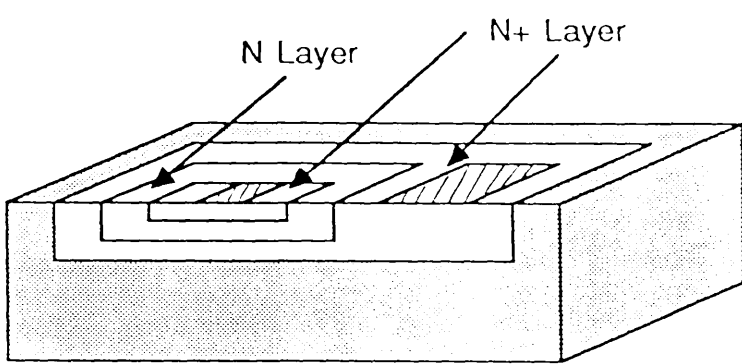


Ohmic Contact

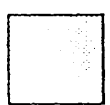
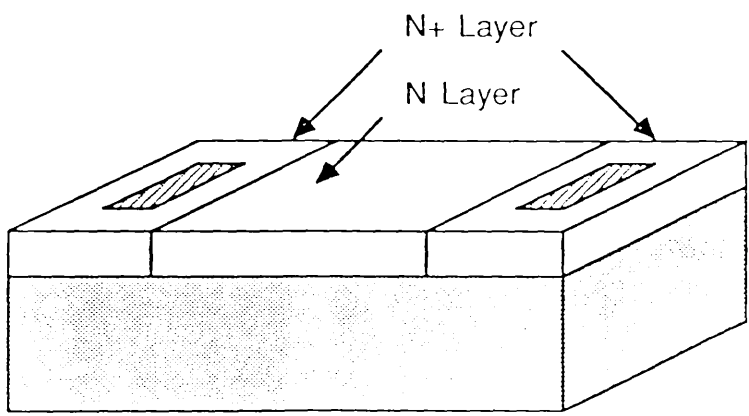
(d)



(e)



(f)



Semi-Insulating Material

or to the top of N^+ contact regions defined by selective etching and/or epitaxial regrowth. The surface of planar structures is often protected by an insulating film, eg. a SiO_2 film, sputtered onto the GaAs.

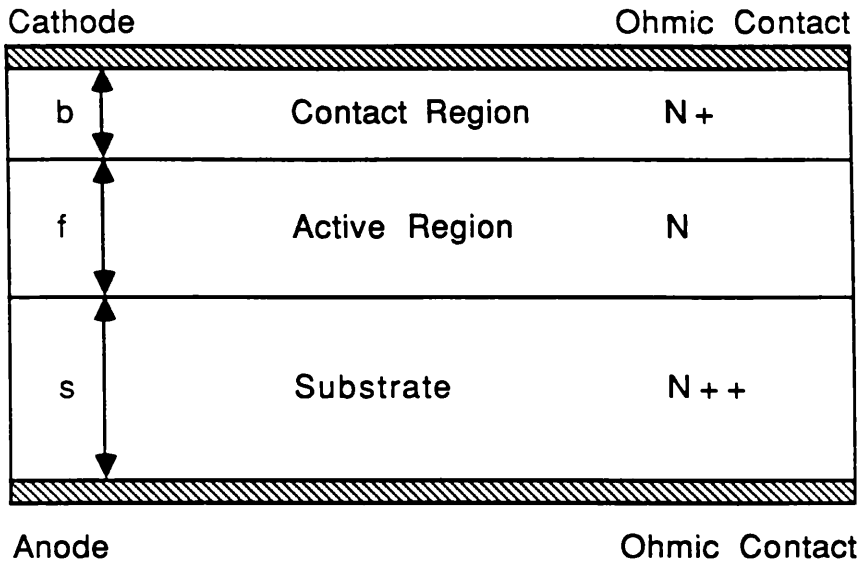
Plessey Microwave Ltd. supplied a number of X-Band and J-Band Gunn diode chips, the structures of which are shown in fig(3.6)(a). Shown in fig(3.6)(b) are electron micrographs of a typical J-Band diode chip, which is approximately $200\mu m \times 200\mu m \times 50\mu m$ in size. As can be seen from these micrographs, the J-Band chip has on its top surface a mesa-type structure approximately $53\mu m$ in diameter, and a spot ohmic contact approximately $41\mu m$ in diameter. The X-Band diode is of a similar structure, having a mesa diameter of approximately $77\mu m$ and a contact diameter of approximately $66\mu m$.

Shown in fig(3.7) is a Gunn oscillator microwave source, supplied by MESL Ltd.. As can be seen, the source consists of a hollow cavity machined from solid metal in which are separately housed a Gunn diode and a varactor diode. The efficiency of the process of conversion of DC energy into microwave energy is fairly small, eg. the device of fig(3.7) requires about 5Watts of DC power to produce 50mW of microwave power, ie. the device has a conversion efficiency of around 1%. This efficiency may decrease if the source is operated over a range of frequencies.

The function of the varactor (variable-reactor) diode is to provide electronic tuning of the Gunn diode source, and may be used to produce a frequency change of around 100MHz for a change in applied voltage from 0 to 30V. Mechanical tuning of the oscillator from about 8GHz to 10GHz is achieved by means of a knurled head screw, which may be used to vary the resonant frequency of the cavity.

Fig(3.6) Commercial Gunn Diodes

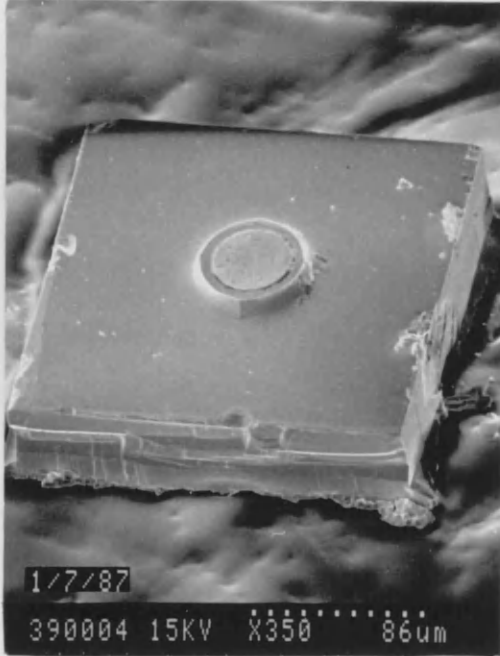
(a) Diode Structures



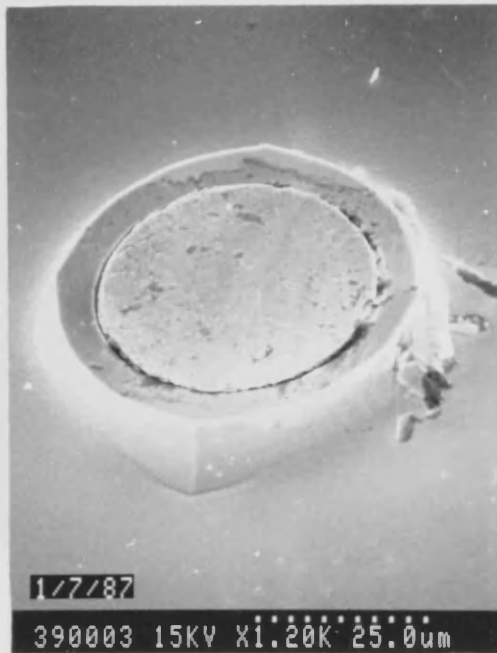
	X-Band	J-Band
b (μm)	2.8	2.0
N_b (cm^{-3})	6.5×10^{17}	2.0×10^{17}
f (μm)	9.2	5.0
N_f (cm^{-3})	8.0×10^{15}	3.8×10^{15}
$N_f \cdot f$ (m^{-2})	7.2×10^{16}	1.9×10^{16}
s (μm)	50	50
N_s (cm^{-3})	1.0×10^{18}	1.0×10^{18}

(b) Electron Micrographs of a J-Band Diode

(i) The Diode Chip

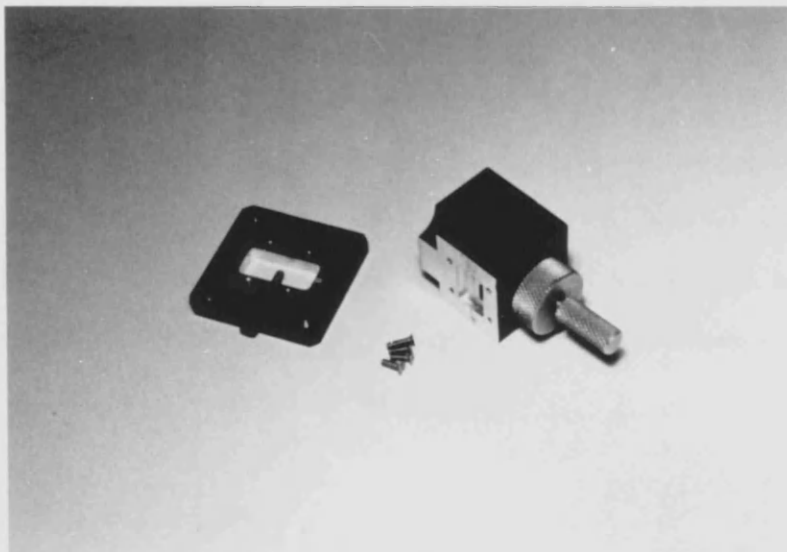


(ii) The Etched Mesa Structure

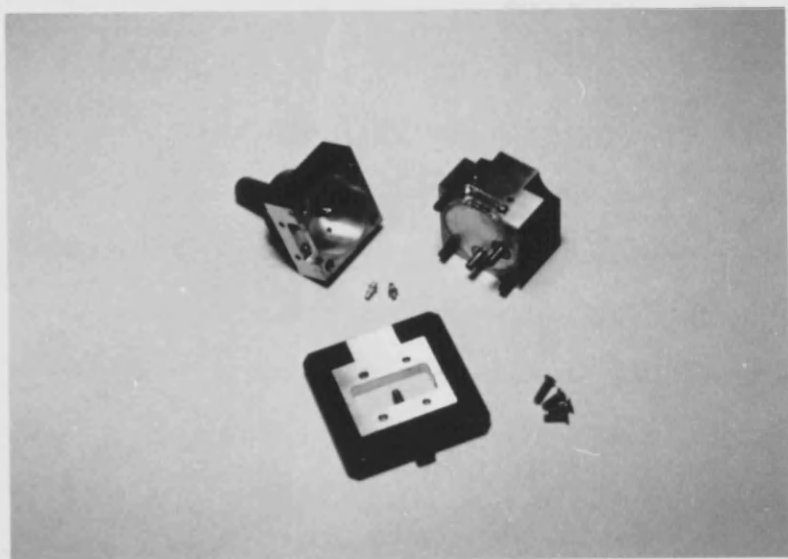


Fig(3.7) The M.E.S.L. Gunn Oscillator

(a) Assembled



(b) Disassembled



3.4 MODES OF OPERATION

If a Gunn diode is placed within a resonant circuit or cavity, one of several modes of oscillation may result. The equivalent circuit of a Gunn oscillator is represented in fig(3.8). The inductance, L_1 , and capacitance, C_1 , comprise the resonant circuit or cavity, and G is the circuit load corresponding to useful RF dissipation and to power loss.

The mode of oscillation depends upon: (a) the relative values of the domain transit time, T_D , and the circuit resonant period, T_R ; (b) the relative values of the dielectric relaxation time, τ_R , within the Gunn diode and T_R ; and (c) the circuit loading G . Under these conditions several modes of oscillation are possible when the bias voltage across the Gunn device, V_{bias} , is greater than the threshold voltage, V_T . These modes are explained in greater detail below.

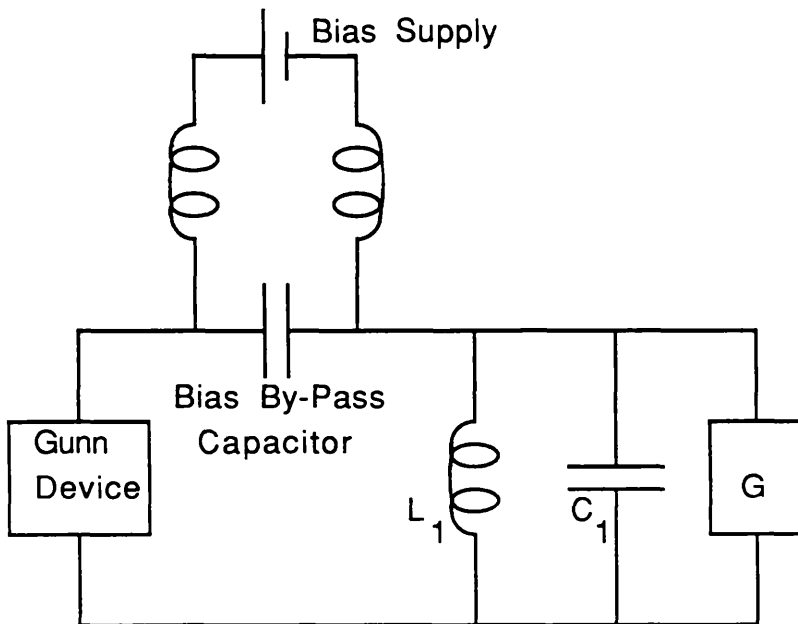
3.4.1 Constant Voltage Modes

There are three common Constant Voltage Modes, wherein domains will form and propagate. These are normally referred to as Transit Time Mode, Delayed Domain Mode and Quenched Domain Mode [38],[39],[40],[41].

In the case of Transit Time Mode a DC bias is applied to the Gunn device. The circuit is therefore purely resistive, and the frequency of oscillation is determined by the reciprocal of the space-charge transit time across the device. For this mode a current spike will occur when a domain enters the anode and re-nucleates at the cathode. A disadvantage of this mode is that the frequency of oscillation is defined by the domain transit time. The mode is therefore not frequency tuneable.

In Delayed Domain Mode, the resonant circuit applies a sinusoidal voltage of period T_e to the Gunn device, the amplitude of the waveform being large enough to cause the applied voltage to fall below the threshold voltage, V_T , over a portion of each cycle. If the domain transit time, T_D , is less than T_e , then when a domain

Fig(3.8) Equivalent Circuit of a Gunn Oscillator



disappears into the anode the bias voltage will be below threshold. The next domain cannot therefore nucleate until the voltage once again rises above threshold. In this way the frequency of oscillation, f_R , may be controlled and tuned within the range $f_D > f_R > f_D/2$, where $f_D =$ the Transit Time Mode frequency.

In Quenched Domain Mode the voltage across the Gunn device falls below the domain sustaining voltage, V_S , for part of each cycle, where $V_S = E_{RM} \cdot L$, and $L =$ the active length of the device. In this way frequencies higher than that of the Transit Time frequency may be generated since, as the bias voltage falls below V_S , the domain is quenched as it propagates between cathode and anode, and cannot renucleate until the bias voltage again rises above the threshold voltage, V_T . The upper frequency obtainable by this method is limited by the domain relaxation time, τ_R [39], ie. the time taken for a domain to nucleate or extinguish.

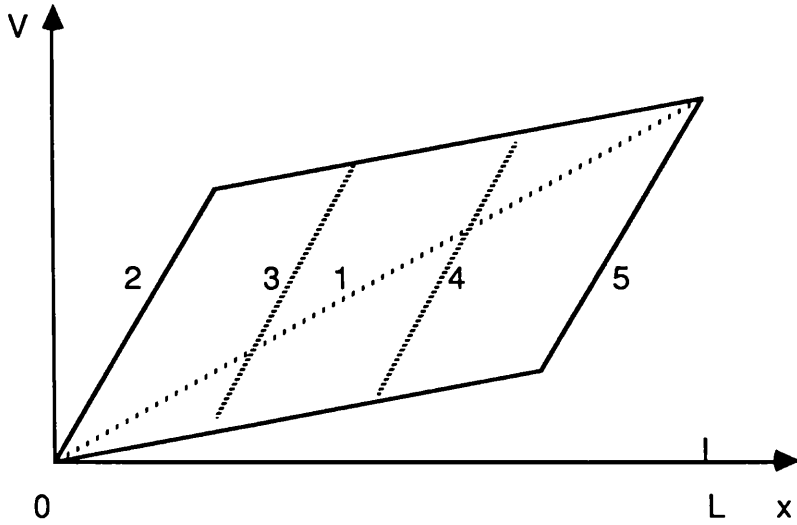
The formation of dipole domains basically masks the negative differential resistivity (NDR) responsible for their formation. Attempts have therefore been made to find methods to completely prevent the formation of space charge domains, and in so doing make use of the NDR as manifested by the static velocity-field characteristic. One such domain free mode is the Limited Space-Charge Accumulation Mode (LSA), in which the electric field across the device rises from below the threshold voltage, V_T , and falls back again quickly enough that the space charge distribution associated with the dipole domain does not have time to form. In this way only the primary accumulation layer forms near the cathode. Such a domain free mode is however of no use in the devices under consideration here.

3.4.2 Constant Current Modes

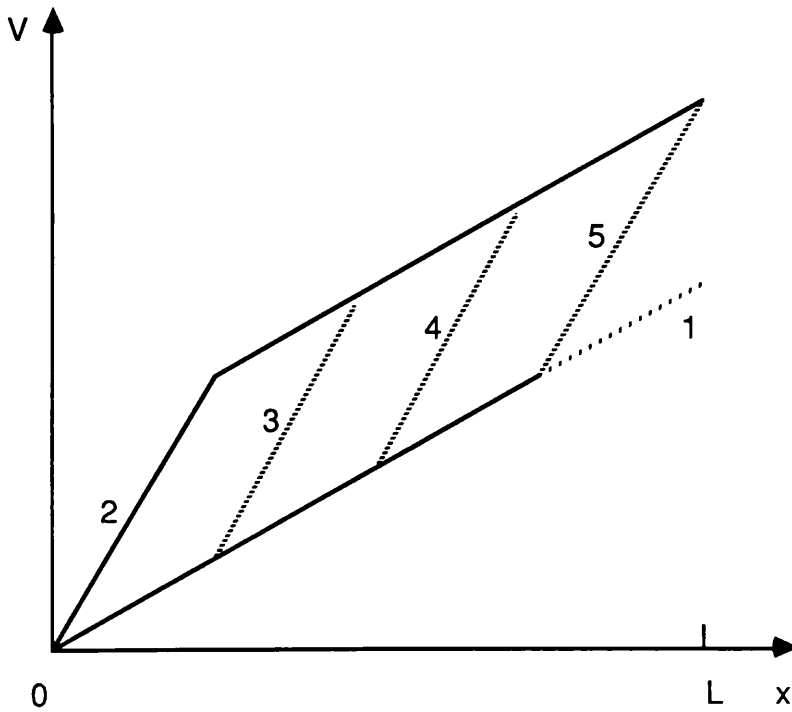
To this point only so called Constant Voltage Modes have been discussed, wherein the action of the domain is defined by the voltage applied across the contacts of the diode. As shown in fig(3.9)(a) for Constant Voltage Modes, the potential at points $x=0$ and $x=L$ are fixed, and the growth of a high-field dipole domain will cause the field outwith the domain to be reduced. When the voltage is

Fig(3.9) Potential Distribution within a Gunn Diode

(a) Under Constant Voltage Conditions



(b) Under Constant Current Conditions



applied to the diode, initially a linear (ohmic) distribution of potential exists (curve(1)). However, thereafter the domain nucleates at the cathode (curve(2)) and begins to propagate towards the anode (curves(3), (4) and (5)). As the domain propagates it can be seen that the field at the cathode becomes less than the value, corresponding to curve(1), which was sufficient to nucleate the domain. Thus, for Constant Voltage Modes, the existence of one domain within the diode inhibits the formation of a further domain, until the first domain reaches the anode and the potential distribution momentarily reverts to that of curve(1).

By contrast under Constant Current conditions [22], as shown in fig(3.9)(b), the field at the cathode is independent of the presence or absence of a domain elsewhere in the diode, and so further domains may be formed at any time. In Constant Current Modes a fixed current is forced through the specimen, the current being such that the threshold for instability is exceeded. Initially, as for Constant Voltage Modes, a linear distribution of potential exists (curve(1)). Thereafter, a domain forms (curve(2)) and propagates through the specimen (curves(3), (4) and (5)), the field outside the domain remaining approximately constant. Finally, the domain reaches the anode and passes out of the diode. Gunn [22] achieved approximately Constant Current conditions by applying to a GaAs sample above threshold, positive rectangular voltage pulses of a few nanoseconds duration via a circuit having a 50Ω impedance.

From the above description of Constant Voltage and Constant Current Modes an important distinction can be drawn between the two, ie. for any given point x along the length of the diode, under Constant Voltage conditions there will be two occasions when there is a change in the electric field: (a) when the domain forms; and (b) when the domain passes over the point x . This differs from what happens under Constant Current conditions, wherein there will be only one perturbation in the field at point x , ie. when the domain propagates across it.

This distinction is important to the operation of the devices under consideration herein, since a change in the electric field at a point will give rise to a corresponding change in the optical characteristics at that point.

Constant Current operation may therefore be more suitable for an optical modulator exploiting the Gunn effect, since for Constant Current operation: (a) no redistribution of the electric field throughout the device occurs during the time (equal to the dielectric relaxation time, $\tau_R \approx 20\text{pS}$) which exists between the extinction of a domain at the anode and the nucleation of a new domain at the cathode; and (b) more than one domain can exist within the diode at any given time, and so modulation frequencies greater than those possible in Constant Voltage Modes may be obtainable.

CHAPTER 4

OPTICAL MODULATION

4.1 ELECTRO-OPTIC MODULATION

Thin-film optical waveguide modulators are important in the development of integrated optical circuits, due to their high potential bandwidths, low electrical power requirements, and compatibility with other thin-film components such as laser diodes or waveguides [42].

Optical modulators may be classified according to the physical effect employed in their operation. These have most commonly been, to date, either the Electro-Optic, Acousto-Optic, or Magneto-Optic effects. Materials used in the fabrication of Electro-Optic modulators have been III-V and II-VI semiconducting compounds, as well as LiNbO_3 and the liquid nitrobenzene. Glass films on quartz, or LiNbO_3 substrates, have been used in Acousto-Optic devices, while garnets have been used in the production of Magneto-Optic devices.

Electro-Optic modulation depends upon one, or a combination of: (a) a change in the index of refraction; (b) a change in the optical absorption; and (c) a change in the scattering, of the material through which the light propagates. These changes are due to the application of an electric field across the material. Effect (c) is seen in some liquid crystals.

4.2 OPTICAL EFFECTS DUE TO A PROPAGATING GUNN DOMAIN

With reference to the generalised domain profile of fig(3.3), it can be seen that there are four possible contributions which may perturb the optical characteristics of the material through which a Gunn domain propagates. These contributions are due to:

- (a) the Linear Electro-Optic (Pockel's) effect;
- (b) the Electro-Absorption (Franz-Keldysh) effect;

- (c) the Free Carrier Plasma effect; and
- (d) the Free Carrier Absorption effect.

Contributions (a) and (b) are due to the electric field profile associated with the domain, while (c) and (d) are due to the variation in the carrier density. Further, contributions (a) and (c) perturb the refractive index of the material, whereas (b) and (d) perturb the optical absorption.

4.2.1 The Linear Electro-Optic Effect

The Linear Electro-Optic effect has to date been the most exploited physical effect used in the construction of light modulators. The effect is observed only in crystalline solids lacking a centre of symmetry. The change in the refractive index produced by the Linear Electro-Optic effect can be most conveniently characterised by the change in the components of the optical index ellipsoid [43]. In the absence of an electric field the index ellipsoid may be expressed as

$$\frac{x^2}{n_x^2} + \frac{y^2}{n_y^2} + \frac{z^2}{n_z^2} = 1 \quad \dots\dots 4.1$$

where, n_x , n_y , and n_z are the three principle refractive indices, with optical axes coincident with the crystallographic axes. In a zinblende crystal, such as GaAs, InP or CdTe, $n_x = n_y = n_z = n_o$. Thus, equation(4.1) becomes

$$\frac{x^2 + y^2 + z^2}{n_o^2} = 1 \quad \dots\dots 4.2$$

The effect of an applied electric field, $E(E_x, E_y, E_z)$, on a propagating optical signal may be conveniently expressed by giving the changes in the constants $1/n_x^2$, $1/n_y^2$, and $1/n_z^2$ of the index ellipsoid. By convention, in the presence of an electric field equation(4.1) may be written as [44]

$$\left(\frac{1}{n^2}\right)_1 x^2 + \left(\frac{1}{n^2}\right)_2 y^2 + \left(\frac{1}{n^2}\right)_3 z^2 + 2\left(\frac{1}{n^2}\right)_4 yz + 2\left(\frac{1}{n^2}\right)_5 xz + 2\left(\frac{1}{n^2}\right)_6 xy = 1 \quad \dots\dots\dots 4.3$$

Since equation(4.3) is equivalent to equation(4.1) in the absence of an electric field then, for E=0

$$\left(\frac{1}{n^2}\right)_1 = \frac{1}{n_x^2} \quad \left(\frac{1}{n^2}\right)_2 = \frac{1}{n_y^2} \quad \left(\frac{1}{n^2}\right)_3 = \frac{1}{n_z^2} \quad \dots\dots\dots 4.4$$

$$\left(\frac{1}{n^2}\right)_4 = \left(\frac{1}{n^2}\right)_5 = \left(\frac{1}{n^2}\right)_6 = 0$$

Also, the change in the coefficients $(1/n^2)_i$, where $i=1, 2, \dots, 6$, due to E is given by

$$\Delta\left(\frac{1}{n^2}\right)_i = \sum_{j=1}^3 r_{ij} E_j \quad \dots\dots\dots 4.5$$

where, $x=1, y=2$ and $z=3$ by convention. In matrix form equation(4.5) is shown as

$$\begin{bmatrix} \Delta\left(\frac{1}{n^2}\right)_1 \\ \Delta\left(\frac{1}{n^2}\right)_2 \\ \Delta\left(\frac{1}{n^2}\right)_3 \\ \Delta\left(\frac{1}{n^2}\right)_4 \\ \Delta\left(\frac{1}{n^2}\right)_5 \\ \Delta\left(\frac{1}{n^2}\right)_6 \end{bmatrix} = \begin{bmatrix} r_{11} & r_{12} & r_{13} \\ r_{21} & r_{22} & r_{23} \\ r_{31} & r_{32} & r_{33} \\ r_{41} & r_{42} & r_{43} \\ r_{51} & r_{52} & r_{53} \\ r_{61} & r_{62} & r_{63} \end{bmatrix} \begin{bmatrix} E_1 \\ E_2 \\ E_3 \end{bmatrix} \quad \dots\dots\dots 4.6$$

The 6x3 matrix of equation(4.6) with elements r_{ij} is known as the Electro-Optic tensor. The form of the tensor may be derived from symmetry considerations [45]. For crystals of the zinc-blende class the Electro-Optic tensor

has the form

$$\begin{bmatrix} 0 & 0 & 0 \\ 0 & 0 & 0 \\ 0 & 0 & 0 \\ r_{41} & 0 & 0 \\ 0 & r_{52} & 0 \\ 0 & 0 & r_{63} \end{bmatrix} \quad \dots\dots 4.7$$

ie. the three non-zero Electro-Optic tensor elements are r_{41} , $r_{52}=r_{41}$, and $r_{63}=r_{41}$. Now, using equation(4.2) with

$$\left[\frac{1}{n^2} \right]_1 = \left[\frac{1}{n^2} \right]_2 = \left[\frac{1}{n^2} \right]_3 = \frac{1}{n^2_0}$$

it can be shown that, if an electric field is applied to the crystal, the index ellipsoid is deformed according to

$$\frac{x^2 + y^2 + z^2}{n_0^2} + 2r_{41}(E_x yz + E_y zx + E_z xy) = 1 \quad \dots\dots 4.8$$

Equation(4.8) may be written with reference to a new coordinate system x', y', z' . The directions of this new system may be determined by rotating the original x, y, z system to coincide with those of equation(4.8), ie.

$$\frac{x'}{n_{x'}^2} + \frac{y'}{n_{y'}^2} + \frac{z'}{n_{z'}^2} = 1$$

and
$$\begin{bmatrix} x \\ y \\ z \end{bmatrix} = \begin{bmatrix} \alpha_1 & \beta_1 & \gamma_1 \\ \alpha_2 & \beta_2 & \gamma_2 \\ \alpha_3 & \beta_3 & \gamma_3 \end{bmatrix} \begin{bmatrix} x' \\ y' \\ z' \end{bmatrix} \quad \dots\dots 4.9$$

where, $n_{x'}, n_{y'}, n_{z'}$ = three principle indices when an electric field is applied

$\alpha_1, \beta_1, \gamma_1, \dots$ = direction cosines relating x, y, z and x', y', z'

Further, n'_x , n'_y , n'_z may be found from the roots of the discriminant [43]

$$\begin{vmatrix} \frac{1}{n_0^2} - \eta & r_{41}E_x & r_{41}E_y \\ r_{41}E_z & \frac{1}{n_0^2} - \eta & r_{41}E_x \\ r_{41}E_y & r_{41}E_x & \frac{1}{n_0^2} - \eta \end{vmatrix} = 0 \quad \dots\dots 4.10$$

For a zinc-blende crystal three electric field directions may be considered, i.e. a field perpendicular to a (100), (011) or (111) crystal planes. The natural cleavage planes of GaAs are the $\langle 011 \rangle$ set of planes. The devices under consideration (see fig(1.3)) are grown on or near to a (100) plane. It can therefore be seen, referring to fig(4.1)(a), that for the vertical/slab and vertical/rib devices of fig(1.3)(a) and (b) respectively, the domain propagates in the [100] direction. It can further be seen, referring to fig(4.1)(b), that for the planar/photoelastic device of fig(1.3)(c) the domain propagates in the [011] direction. The influence of an applied field in the [100] and [011] directions is summarised in table(4.1)

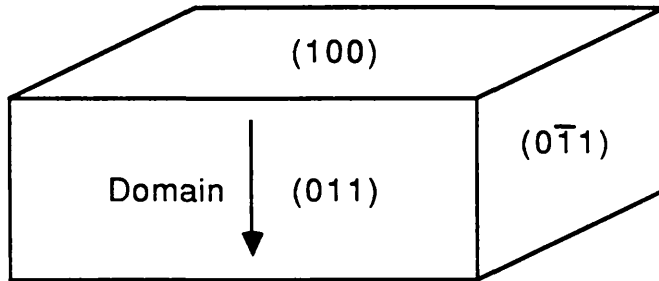
It should be noted from table(4.1) that for the vertical devices, optical radiation propagating in the [011] direction will undergo a positive phase shift, while radiation propagating in the $[0\bar{1}1]$ direction will undergo a negative phase shift. It can further be seen from table(4.1) that for the planar device, radiation propagating in the $[0\bar{1}1]$ direction will experience a phase shift, while radiation propagating in the [011] direction will experience no such shift.

4.2.2 The Electro-Absorption Effect

Optical modulation can also be produced by employing the Electro-Absorption (Franz-Keldysh) effect. In this effect the absorption edge of a semiconductor is shifted by the application of a strong electric field. The absorption coefficient, α , of photons whose energy is close to the energy gap depends very strongly on the

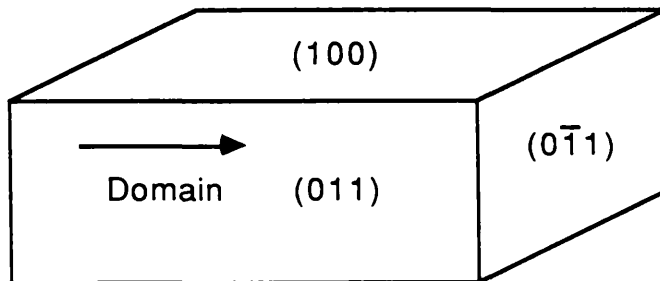
Fig(4.1) Crystallography of Vertical and Planar Devices

(a) Vertical Device



Direction of Domain Propagation = $[100]$

(b) Planar Device



Direction of Domain Propagation = $[011]$

Table(4.1) Influence on Optical Characteristics of an Applied Electric Field, E due to the Linear Electro-Optic Effect

	$E \perp (100)$	$E \perp (011)$
Applied Field	$E_x=E_y=0, E_z=E$	$E_x=E_y=E/\sqrt{2}, E_z=0$
n'_x	$n_o + \frac{1}{2}n_o^3 r_{41} E$	$n_o + \frac{1}{2}n_o^3 r_{41} E$
n'_y	$n_o - \frac{1}{2}n_o^3 r_{41} E$	$n_o - \frac{1}{2}n_o^3 r_{41} E$
n'_z	n_o	n_o
Phase Difference, Γ	$\Gamma[100] = \frac{2\pi}{\lambda} n_o^3 r_{41} V$ $\Gamma[001] = \Gamma[00\bar{1}] = 0$ $\Gamma[011] = \frac{\pi L}{\lambda d} n_o^3 r_{41} V$	$\Gamma[100] = 0$ $\Gamma[011] = 0$ $\Gamma[0\bar{1}1] = \frac{2\pi L}{\lambda d} n_o^3 r_{41} V$

where, V = applied voltage

L = thickness of crystal in direction of applied electric field

d = thickness of crystal in direction of optical propagation

difference between the photon energy and the energy gap. This is due to the steepness of the absorption edge in direct bandgap semiconductors, such as GaAs.

Illumination of the semiconductor material with photons of energy nearly equal to the bandgap energy, and the simultaneous application of a strong electric field, produces a large increase in the absorption of these photons. This is due to Electro-Absorption, which shifts the absorption edge in the direction of lower energies.

Electro-Absorption may be explained with reference to the energy band diagram of fig(4.2). As can be seen from this diagram, in the presence of a strong electric field the band edges bend. The presence of the electric field thus effectively broadens the states of the conduction band. There is then a finite probability of finding the electron within the energy gap. The effective bandgap is reduced, and hence the absorption edge is shifted to a longer wavelength. The effective change in bandgap energy is given by [46]

$$\Delta E = \frac{3}{2} (m^*)^{-1/3} (q\hbar E)^{2/3} \dots\dots 4.11$$

where, m^* = carrier effective mass

q = electronic charge

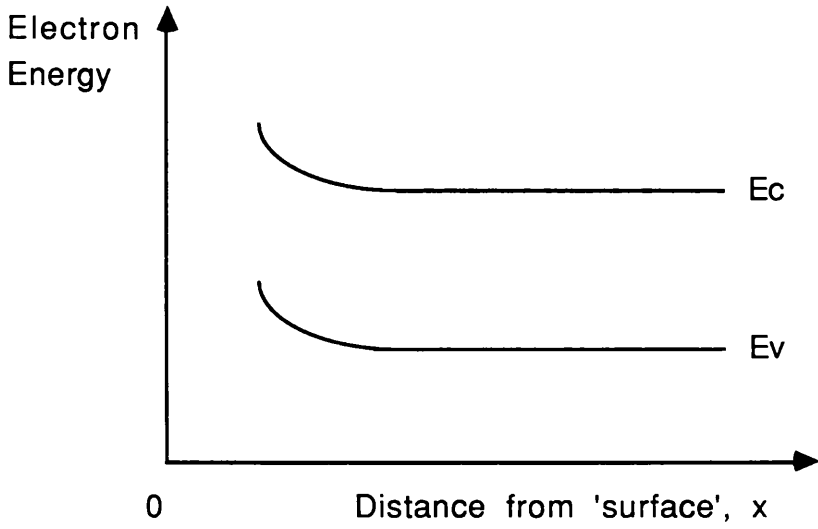
\hbar = $h/2\pi$

h = Planck's constant

E = electric field strength

In conventional Electro-Absorption modulators, increasing x represents increasing distance from the surface of the semiconductor, where there is a shallow p-n junction or Schottky contact. In such an arrangement a reverse bias voltage is applied at the device surface, resulting in increased band bending and hence absorption. In the devices proposed herein however, increasing x represents increasing distance from the propagating domain at any given time.

Fig(4.2) Energy Band Diagram



E_c = Conduction Band Edge
 E_v = Valence Band Edge

4.2.3 Free Carrier Contributions

Considering the generalised domain shape of fig(3.3), it can be seen that there is a variation in the carrier density throughout the extent of the domain. This variation may give rise to a change either in the absorption or the refractive index of the material across which the domain extends.

Free Carrier absorption (intraband absorption) occurs when a photon gives up its energy to an electron which is already in the conduction band, or a hole already in the valence band, thus raising it to a higher energy [11].

With reference to electromagnetic theory, in the presence of an electric field $E_0 \exp(i\omega t)$, the motion of an electron is given by the product of the electron mass times acceleration, plus any damping acting on the electron motion due to interaction with the lattice, ie.

$$m^* \frac{d^2x}{dt^2} + m^*g \frac{dx}{dt} = -qE_0 e^{i\omega t} \quad \dots\dots 4.12$$

where, x = displacement

g = damping factor

Solving equation(4.12) gives that

$$x = \frac{(q/E_0)/m^*}{\omega^2 - i\omega g} e^{i\omega t} \quad \dots\dots 4.13$$

Now, the material dielectric constant is

$$K = \frac{\epsilon}{\epsilon_0} = 1 + \frac{P}{\epsilon_0 E} \quad \dots\dots 4.14$$

where, P = polarisation

$$= P_0 + P_1$$

P_0 = polarisation without carriers

$$\begin{aligned}
P_1 &= \text{additional polarisation due to electron shift under} \\
&\quad \text{applied electric field} \\
&= -Nq\mathcal{E} \\
N &= \text{free carrier concentration}
\end{aligned}$$

Thus, employing equations(4.14) and (4.13), under an applied field

$$\begin{aligned}
K &= 1 + \frac{P}{\epsilon_0 E} + \frac{P_1}{\epsilon_0 E} \\
&= n_0^2 + \frac{P_1}{\epsilon_0 E} \\
&= n - \frac{(Nq^2)/(m^* \epsilon_0)}{\omega^2 - i\omega g} \dots\dots 4.15
\end{aligned}$$

Hence, the real and imaginary parts of the dielectric constant are given as

$$\begin{aligned}
K_r &= n_0^2 - \frac{(Nq^2)/(m^* \epsilon_0)}{\omega^2 + g^2} \dots\dots 4.16 \\
K_i &= \frac{(Nq^2 g)/(m^* \omega \epsilon_0)}{\omega^2 + g^2}
\end{aligned}$$

Now for steady state $d^2x/dt^2=0$. Thus, equation(4.12) becomes

$$m^* g \frac{dx}{dt} = qE$$

$$\text{ie. } g = \frac{q}{m^*} \frac{E}{(dx/dt)} = \frac{q}{\mu m^*} \dots\dots 4.17$$

Taking $q=1.60218 \times 10^{-19} \text{C}$, $\mu_{\Gamma}(\text{GaAs}) \approx 0.8 \text{m}^2 \text{V}^{-1} \text{s}^{-1}$ and $m_{\Gamma}^*(\text{GaAs}) \approx 0.0632 m_e$ gives that $g \approx 3.45 \times 10^{12} \text{s}^{-1}$. Also, at optical frequencies $\omega \approx 10^{15} \text{s}^{-1}$. Thus, approximating equation(4.16) gives

$$K_r = n_o^2 - \frac{Nq^2}{m^* \epsilon_o \omega^2} \quad \dots\dots 4.18$$

$$K_i = \frac{Nq^2 g}{m^* \epsilon_o \omega^3} = \frac{Nq^3}{(m^*)^2 \epsilon_o \mu} \quad (\text{by equation(4.17)})$$

Further, the absorption coefficient due to Free Carrier absorption, α_{FC} , is related to K_i by [11]

$$\alpha_{FC} = \frac{kK_i}{n}$$

where, k = magnitude of the wavevector = ω/c

n = refractive index

c = $f\lambda$

λ = free space wavelength

ω = $2\pi f$

f = frequency of the optical radiation

Thus,

$$\begin{aligned} \alpha_{FC} &= \frac{k}{n} \frac{Nq^3}{(m^*)^2 \epsilon_o \mu} = \frac{Nq^3}{(m^*)^2 n \epsilon_o \omega^2 \mu c} \quad \dots\dots 4.19 \\ &= \frac{Nq^3 \lambda_o^2}{4\pi^2 n (m^*)^2 \mu \epsilon_o c^3} \end{aligned}$$

Also, we may rewrite equation(4.18) as

$$K_r = n_o^2 - \Delta n^2$$

$$\text{where, } \Delta n^2 = 2n_o \Delta n = - \frac{Nq^2}{m^* \epsilon_o \omega^2} \quad \dots\dots 4.20$$

Further, by analogy with the change in index, Δn produced in a dielectric by a plasma of charged particles, wherein $\Delta n^2 = 2n_o \Delta n$, the change in the index of refraction resulting from the presence of free carriers may be given by [11]

$$\Delta n = - \frac{Nq^2}{2n_0 m^* \epsilon_0 \omega^2} = - \frac{Nq^2 \lambda_0^2}{8\pi^2 \epsilon_0 n_0 m^* c^2} \quad \dots\dots\dots 4.21$$

As was pointed out in Chapter 2, the depression in the refractive index due to the presence of free carriers is of extreme importance in the devices under discussion herein, as this is the mechanism used to form the homojunction slab and rib guides of the vertical devices.

4.3 OPTOELECTRONIC INTERACTION MECHANISMS

4.3.1 Exploitation of Domain Induced Optical Changes

The electric field intensity within a propagating Gunn domain is much higher than any electric field which can safely be produced within a wafer of GaAs by conventional methods. It can therefore be concluded that the optical perturbations induced within the wafer will be much more pronounced in the presence of a domain, and the optical beam influenced to a greater extent, than would otherwise be possible. Further, the amplitude and frequency of the optical perturbation may be controlled by variation of the voltage applied to the diode contacts by way of the various modes of operation already outlined in section(3.4).

The first publication referring to travelling Gunn domains being used to modulate a light beam, within a wafer comprising a Gunn diode, was by E.I. Gordon [47]. In this publication it was suggested that the high electric field intensity of the domain may radically alter the local refractive index and absorption edge of the material.

From section(4.2.1) it can be seen that if an electric field is applied along certain crystallographic directions in a zincblende crystal, such as GaAs or InP, the index of refraction is perturbed due to the Linear Electro-Optic effect. The perturbation in the refractive index, Δn is linearly proportional to the first power of the electric field, and for a field of approximately $40.0 \times 10^5 \text{Vm}^{-1}$, $\Delta n \approx 10^{-4}$.

Fundamental experimental work relating to this modulation mechanism was reported by Cohen *et al* [7] who observed the Electro-Optic modulation of a $1.15\mu\text{m}$ He:Ne laser within a long GaAs Gunn diode due to the presence of a propagating Gunn domain. The active region of the samples used by Cohen *et al* were around $25\mu\text{m}$ to $200\mu\text{m}$ long. Consequently oscillation frequencies varying from 0.5GHz to 4GHz were observed.

As was explained in section(4.2.2), light can also be modulated by high field domains via the Electro-Absorption effect. Ohta *et al* [8] reported on the modulation of light from a GaAs laser diode at a frequency of 0.1GHz, by a travelling high-field domain in a bulk GaAs element. It was shown in these experiments that optical modulation due to propagating Gunn domains occurred due to both the Linear Electro-Optic effect and the Electro-Absorption effect. Further, by measuring the Electro-Absorption contribution, a quantitative correction could be made to the observed Linear Electro-Optic effect. This correction showed that the retardation due to the Linear Electro-Optic effect was linearly proportional to the electric field within the high field domain. The samples used by Ohta *et al* were approximately $80\mu\text{m}$ thick, $600\mu\text{m}$ wide and 1mm long. Guetin and Boccon-Gibod [48] also independently observed a 25% increase in the optical absorption when a high field domain crossed a region illuminated with radiation of wavelength equal to the energy gap of GaAs.

The prior experimental work outlined above clearly indicated that optical modulation by propagating Gunn domains, due to both the Linear Electro-Optic effect and the Electro-Absorption effect, were possible in bulk GaAs samples. The interaction was however found to be weak, and of little practical value. Further, these samples required high bias voltages, and provided no means of guiding the optical radiation. This suggests that a much stronger interaction might be obtained if the domain propagated through an integrated optical waveguide, and it was the purpose of the devices outlined in fig(1.3) to provide such waveguiding means.

To this point the discussion has been restricted to devices wherein the direction of optical propagation is substantially perpendicular to the direction of

propagation of the travelling Gunn domain. If however the light beam strikes the domain at an acute angle, θ , then the domain may be thought of as a mirror moving at a velocity, $v_D \approx 10^5 \text{ms}^{-1}$. Optical modulation may therefore be produced by exploiting the variation in the reflection coefficient of the domain in comparison with the reflection coefficient of the material as a whole [49]. It can therefore be envisaged that the Doppler effect may be obtained from a propagating domain.

4.3.2 Exploitation of Optically Induced Electrical Changes

Section(4.3.1) essentially deals with the electrical control of an optical signal. However, the electrical behaviour of a Gunn diode may be controlled by illuminating all or part of the diode with optical radiation.

The influence of illumination on the Gunn effect depends on whether the whole or only part of the device is illuminated. If only the region near the anode is illuminated, and the intensity of the light is high enough to sufficiently increase the conductivity of that region, then two different effects may be observed. Since the field intensity near the anode will decrease due to the high illumination induced conductivity, a high field will be extinguished on entering the illumination region. The active length of the device will thus be reduced, and the oscillation frequency increased. This is the so-called 'virtual anode' situation [50].

A different effect is the switching of Gunn domains by illumination [51]. If the diode is biased just below the threshold voltage then an increase in the conductivity at the anode by illumination will result in an increase of the electric field near the cathode, thus leading to domain formation and Gunn oscillations. If the light pulse duration is longer than the domain transit time then oscillations will be observed for as long as the sample is illuminated. If however the light pulse duration is less than the domain transit time, then only a single domain and associated current pulse will be generated. On the other hand, the illumination of the cathode region reduces the field near the cathode, and thus suppresses the formation of domains at voltages greater than the threshold value.

If the whole sample is illuminated then again two cases can be distinguished. If the energy of the photons is greater than that of the energy gap then generated carriers will be distributed uniformly across the sample. Hence, the coherence and amplitude of the oscillations will be enhanced [52]. If however the photon energy is less than that of the energy gap, then the opposite behaviour may be observed, since electrons will be excited into the conduction band from deep lying impurity centres, and the coherence of the oscillations thus reduced [53].

CHAPTER 5

DEVICES AND THEIR DESIGN

Preceding Chapters have addressed the operation and the analysis of discrete optical waveguides and Gunn diodes, and the effects present within a device which integrates both. This Chapter presents the possible device designs which integrate some form of optical waveguiding with a super-critical Gunn diode. Also presented are detailed results of the optical design and the electrical design of these devices, along with a consideration of the magnitude of the Electro-Optic effects present.

5.1 DEVICE STRUCTURES

As was explained in Chapter 1, the optical waveguiding structures of potential use are the slab, rib, or photoelastic waveguides. Also, the Gunn diode structures of potential use are either the vertical or the planar diode structures. Any integrated device structure must incorporate the following device design criteria:

- (a) It must allow only one optical mode to propagate, ie. be a monomode waveguide. This is because different optical modes propagate within different parts of an optical guide. This means that the propagating Gunn domain would interact with different modes at different parts within the device, and also at different times. Further, different modes travel along the guide at different velocities of propagation.
- (b) As for all super-critical Gunn diodes, the N_0L product ($= N_f l$ for the vertical devices) must be greater than 10^{12}cm^{-2} for GaAs and InP, for dipole domains to form and propagate.
- (c) It must have a sensible operating voltage, in order that electrical power may easily be supplied to the device. This ensures that the device may be driven from available power sources and further, that the device does not overheat.

Adhering to the above criteria, the possible integrated device structures that may be envisaged are as follows:

- (a) a vertical Gunn diode incorporating a slab waveguide (as shown in

- fig(1.3)(a));
- (b) a vertical Gunn diode incorporating a rib waveguide (as shown in fig(1.3)(b)); and
- (c) a planar Gunn diode incorporating a photoelastic waveguide (as shown in fig(1.3)(c)).

The specific device designs which were proposed for both theoretical and experimental investigations are shown in table(5.1). As can be seen, seven such designs were put forward. These will hereafter be referred to as S41, S42, S43, R1, R2, R3, and P1.

Other structures incorporating a thin, low doped P-type layer on top of a highly doped N-type substrate may also be considered. These structures are shown in fig(5.1)(a) and (5.1)(b). For example, a device forming a planar Gunn diode incorporating a photoelastic waveguide, fabricated on an N-type substrate, could be considered. This device would resemble device P1 in operation. Alternatively, a planar Gunn diode incorporating a rib waveguide, on an N-type substrate, could be fabricated. However, the devices presented in fig(5.1) are presently not feasible, since current material growth technologies are unable to grow a thin enough low doped P-type region on top of the highly doped N-type substrate, and therefore play no further part in this work

5.2 OPTICAL DESIGN

5.2.1 Refractive Index Calculations

As was explained and derived in Chapter 4, homojunction optical waveguides may be produced in semiconductor materials by a combination of device geometry and device doping density. This is because increasing the doping density produces a corresponding decrease in the refractive index, Δn , of the material, due to the negative plasma contribution to the refractive index, n . This perturbation, Δn , is dependent upon the square of the wavelength of propagation, and inversely

Table(5.1) Proposed Device Designs

(a) Vertical Gunn Diode / Slab Waveguide Devices

Device	S41	S42	S43
Buffer Thickness, b (μm)	0.5	0.5	2.0
Buffer Doping, N_b (cm^{-3})	1.0×10^{18}	1.0×10^{18}	2.0×10^{17}
Film Thickness, f (μm)	7.0	5.0	5.0
Film Doping, N_f (cm^{-3})	5.0×10^{16}	5.0×10^{16}	5.0×10^{15}
$N_f \cdot f$ Product (m^{-2})	3.5×10^{17}	2.5×10^{17}	2.5×10^{16}
Substrate Thickness, s (μm)	425	425	425
Substrate Doping, N_s (μm)	1.0×10^{18}	1.0×10^{18}	1.0×10^{18}

(b) Vertical Gunn Diode / Rib Waveguide Devices

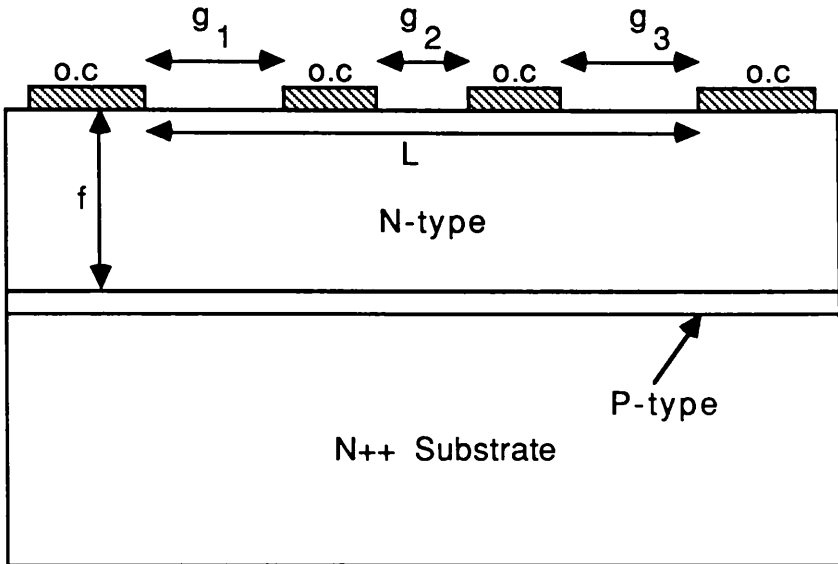
Device	R1	R2	R3
Guiding Region, I	S41	S42	S43
Etch Depth, e (μm)	4.5	3.0	4.0
Rib Width, w (μm)	10.0	5.0	5.0

(c) Planar Gunn Diode / Photoelastic Waveguide Devices

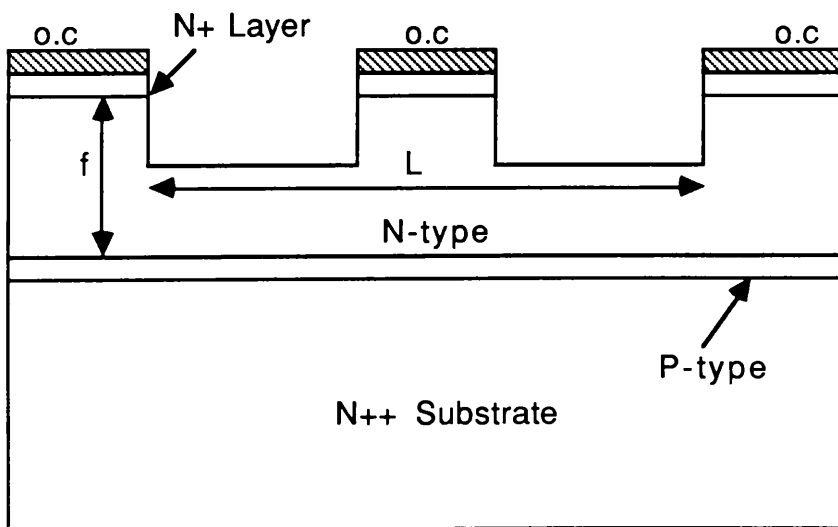
Device	P1
Metal Film Thickness, t (μm)	1.5
Epi-Layer Thickness, f (μm)	5.0
Epi-Layer Doping, N_f (cm^{-3})	5.0×10^{16}
Guide Width, g_1 (μm)	10.0
g_2 (μm)	6.0, 8.0, 10.0 or 12.0
g_3 (μm)	10.0
Active Length, L (μm)	50

Fig(5.1) Alternative Integrated Device Structures

(a) A Planar Gunn Diode incorporating a Photoelastic Waveguide, on an N-type Substrate



(b) A Planar Gunn Diode incorporating a Rib Waveguide, on an N-type Substrate



proportional to the refractive index in the absence of free carriers, n_0 (see equation(4.21)). The refractive index, n , of a semiconducting material is therefore dependent upon a number of factors. These are:

- (a) the compositional fraction, x , of the material in tertiary or quaternary alloys, eg. in $Al_xGa_{1-x}As$ or $Al_xGa_{1-x}As_yP_{1-y}$;
- (b) the wavelength of radiation used to illuminate the material; and
- (c) the doping concentration, N , within the material.

The refractive index in the absence of free carriers, $n_0(x,\lambda)$ of $Al_xGa_{1-x}As$, may be calculated by a number of methods [54],[55],[56],[57]. A method proposed by Yariv, based on the reflectivity experiments of Ilegems and Pearson, suggests that the refractive index in the absence of free carriers, $n_0(x,\lambda)$ is given by [55]

$$n_0(x,\lambda) = \left\{ 10.9 - 2.92x + \frac{0.9751}{[(\lambda^2 - C) - D\lambda^2]} \right\}^{1/2} \dots\dots 5.1$$

where, $C = 0.30386 - 0.105x$ if $x > 0.36$
 $= 0.52886 - 0.735x$ if $x \leq 0.36$
 $D = (1.41x + 1) \times 2.467 \times 10^{-3}$
 $\lambda =$ wavelength in microns

In contrast, a method proposed by Adachi [56],[57] suggests that the real part of the dielectric constant in a zincblende material, below the direct band edge, may be expressed as

$$\begin{aligned} \epsilon_1(\omega) &= n_0^2(x,\lambda) \dots\dots 5.2 \\ &= A_0 \left\{ f(\chi) + \frac{1}{2} \left[\frac{E_g}{E_g + \Delta} \right]^{3/2} f(\chi_{SO}) \right\} + B_0 \end{aligned}$$

where, E_g = direct band gap (eV)
 $= 1.425 + 1.155x + 0.37x^2$ for GaAs
 Δ = energy gap between the Γ and the L valleys
 $= 0.340 - 0.040x$

$$f(\chi) = \chi^{-2}(2-[1+\chi]^{1/2}-[1-\chi]^{1/2})$$

$$\chi = \hbar\omega/E_g$$

$$\chi_{so} = \hbar\omega/(E_g+\Delta)$$

$$\hbar\omega = \text{photon energy (wavelength, } \lambda)$$

$$A_o(x) = 6.0+17.8x$$

$$B_o(x) = 9.5+9.8x$$

Refractive index values calculated by Yarivs and Adachis methods for a wavelength, λ , of $1.15\mu\text{m}$ with varying compositional fraction, x , are shown in table(5.2)(a). Further, refractive index values calculated by Adachis method for varying wavelengths, λ and a constant compositional fraction, $x=0$ (ie. GaAs) are shown in table(5.2)(b). As can be seen from these results, n_o decreases with increasing x and with increasing λ . In all optical design calculations hereafter presented Adachis method has been employed, since this method post dates Yarivs, and is also fitted to more recent experimental data.

Now, considering the change, Δn , in the refractive index, n , brought about through doping of the semiconductor material, it can be seen that

$$n = n(x, N, \lambda) = n_o(x, \lambda) - \Delta n \quad \dots\dots\dots 5.3$$

where, n_o is given by either equation(5.1) or (5.2), and Δn is given by equation(4.21). The results of such a calculation using equation(5.3) for various doping densities are shown in table(5.3). The doping densities for which the corresponding refractive index has been calculated are those of importance for the preferred embodiments of the devices, the design procedure for which are outlined in succeeding sections of this Chapter.

5.2.2 Slab Waveguide Calculations

Using the Dispersion relation of equation(2.6), a short program was written to run on a GEC 4180 minicomputer in order to calculate the modal refractive index,

Table(5.2) Calculated Refractive Index values, n_0 in the absence of Free Carriers

(a)

Wavelength, λ	Method	x	n_0
1.15 μ m	Yariv	0	3.4406
	Adachi	0	3.467567
	Yariv	6%	3.4088
	Adachi	6%	3.438300

(b)

Wavelength, λ	Method	x	n_0
1.15 μ m	Adachi	0	3.467567
905nm	Adachi	0	3.587488

Table(5.3) Calculated Refractive Index values, n (by Adachis Method)

λ	n_0	$N \text{ (cm}^{-3}\text{)}$	Δn	$n = n_0 - \Delta n$
1.15 μm	3.467567	5.0×10^{15}	1.353×10^{-5}	3.467554
		5.0×10^{16}	1.353×10^{-4}	3.467432
		1.0×10^{17}	2.706×10^{-4}	3.467296
		2.0×10^{17}	5.412×10^{-4}	3.467026
		1.0×10^{18}	2.706×10^{-3}	3.464861
905nm	3.587488	5.0×10^{15}	8.011×10^{-6}	3.587480
		5.0×10^{16}	8.011×10^{-5}	3.587408
		1.0×10^{17}	1.602×10^{-4}	3.587328
		2.0×10^{17}	3.204×10^{-4}	3.587168
		1.0×10^{18}	1.602×10^{-3}	3.585886

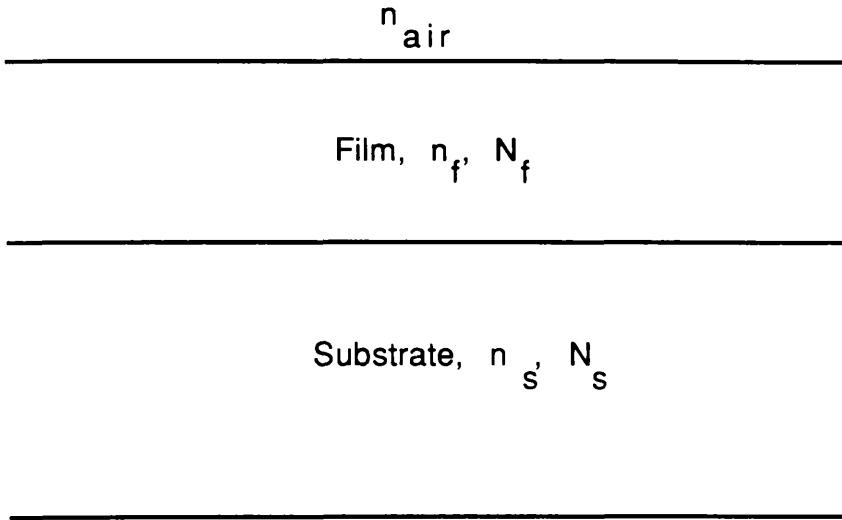
n_{eff} of three-layer slab guide structures. For the three-layer slab guides defined in fig(5.2), the modal refractive indices were calculated, as shown in fig(5.3), for various guide thicknesses, f . As can be seen from fig(5.3)(a), for a wavelength of $1.15\mu\text{m}$ the first-order mode of devices S31 and S32 cuts-off at a film thickness of $2.1\mu\text{m}$. Similarly, as can be seen from fig(5.3)(b), for a wavelength of $1.15\mu\text{m}$ the first-order mode of device S33 cuts-off at a film thickness of around $2.05\mu\text{m}$, and for a wavelength of 905nm at a film thickness of $2.075\mu\text{m}$.

Using the Dispersion relation of equation(2.7) for four-layer slab guides, a similar program as for the three-layer slab was written. In the same way as for the three-layer slab guides, the modal refractive indices of the four-layer slab guides shown in fig(5.4), were calculated. Fig(5.5) shows plots for varying guide thickness, f , for the wavelengths, λ , of interest. It was found by running the four-layer slab program that S41 and S42 had a first-order cut-off thickness of around $1.5\mu\text{m}$ at a wavelength of $1.15\mu\text{m}$, and $1.53\mu\text{m}$ at 905nm . At these thicknesses the effective index of the first-order mode became equal to the substrate refractive index (which is also equal to the buffer index in these guides). It was further found that S43 had a cut-off thickness of around $3.35\mu\text{m}$ at $1.15\mu\text{m}$, and $3.40\mu\text{m}$ at 905nm . It should be noted that by varying the buffer thickness, b , between $0.5\mu\text{m}$ and $2.5\mu\text{m}$ for device S43, with $f=5\mu\text{m}$, no significant variation in the modal effective index was observed.

5.2.3 Rib Waveguide Calculations

The rib guides of fig(5.6) were analysed by: (a) an Effective Index Method (EIM) program based on the Dispersion relation for the four-layer slab guide, running on the GEC 4180 minicomputer; (b) the .NWAVE program, running on the GEC 4180 minicomputer; and (c) a Finite Difference (FD) program, running on a BBC microcomputer. A comparison of these results is presented in figs(5.7)(a), (b) and (c) for ribs R1, R2, and R3 respectively at a wavelength of $1.15\mu\text{m}$. Also shown in fig(5.7)(d) are the corresponding plots for R3 for a wavelength of 905nm .

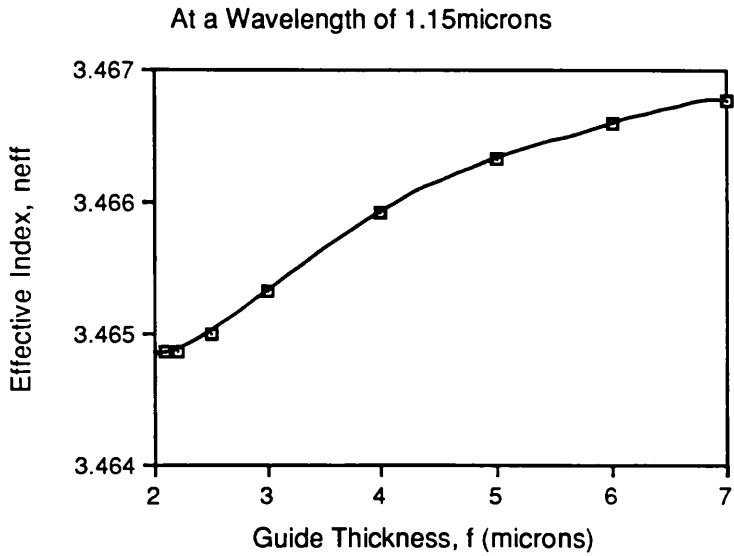
Fig(5.2) Structure and Composition of the Three-Layer Slab Guides under consideration



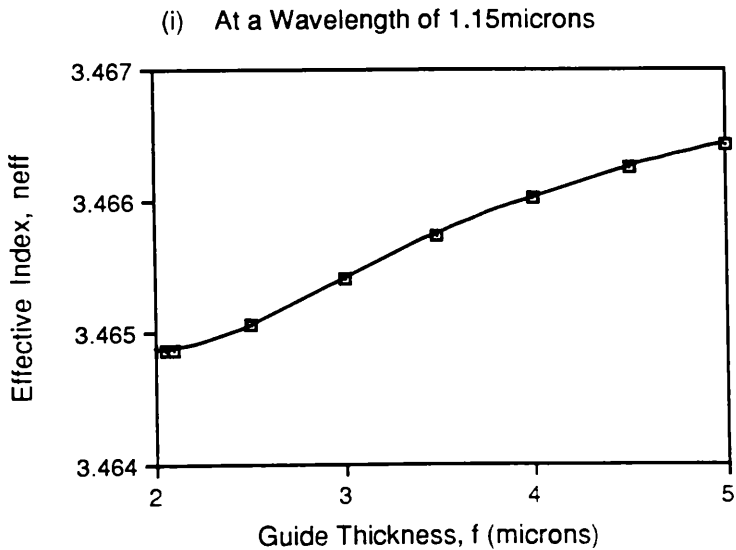
Device	S31 and S32	S33
f (μm)	0 - 7.0	0 - 5.0
N_f (cm^{-3})	5.0×10^{16}	5.0×10^{15}
s (μm)	425	425
N_s (cm^{-3})	1.0×10^{18}	1.0×10^{18}

Fig(5.3) Effective Refractive Index of First-Order Mode of Three-Layer Slab Guides versus Guide Layer Thickness

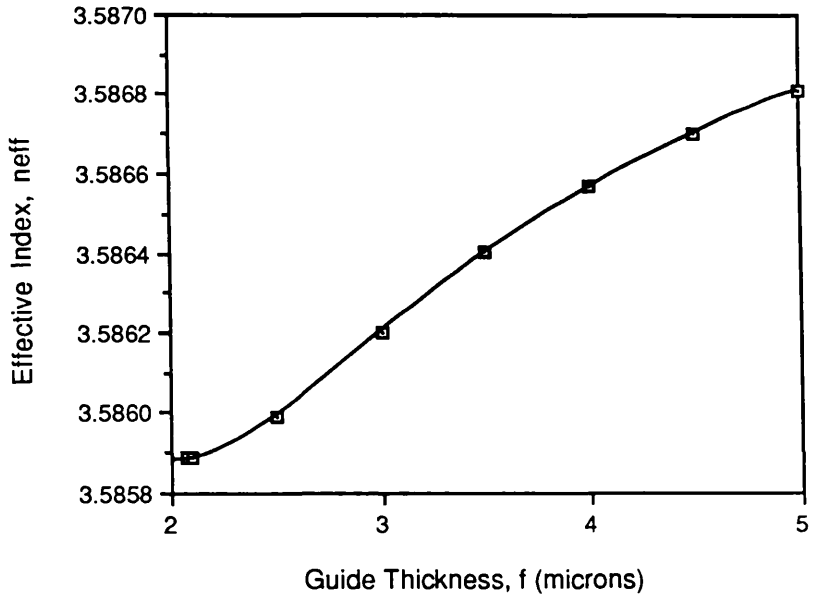
(a) For Slabs S31 and S32



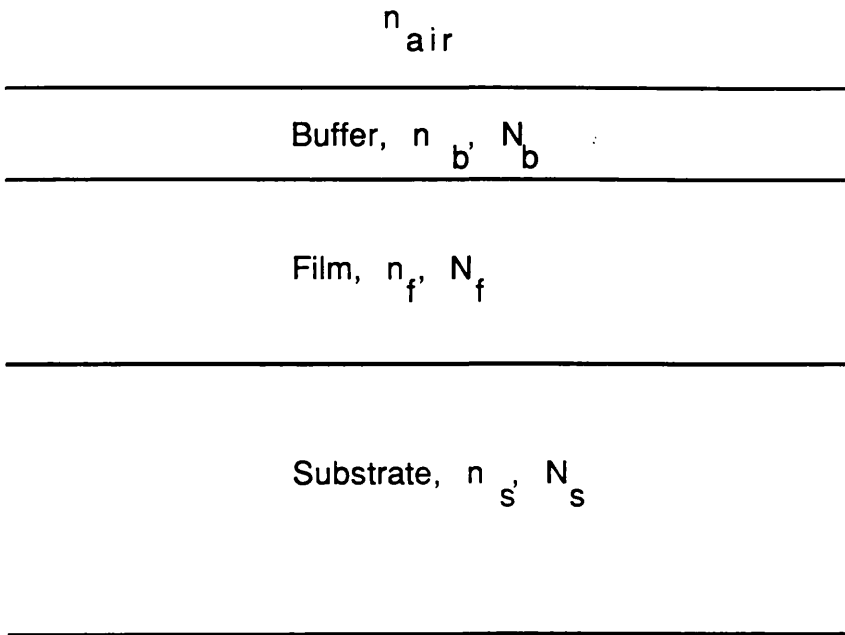
(b) For Slab S33



(ii) At a Wavelength of 905nm



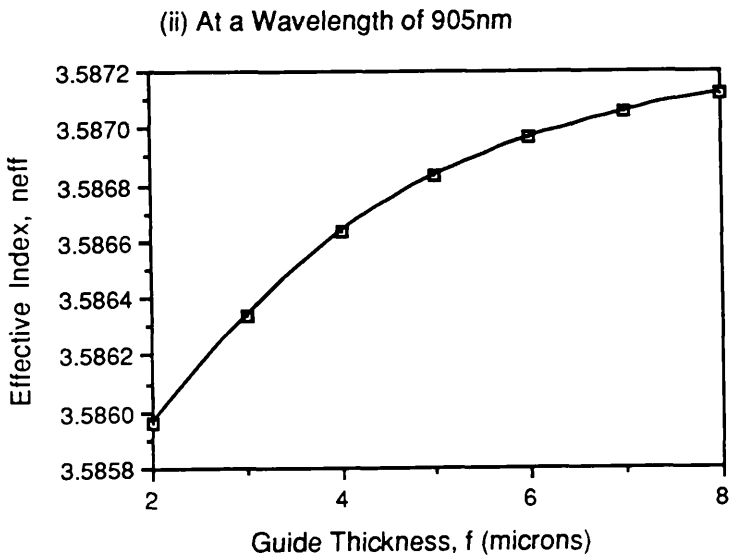
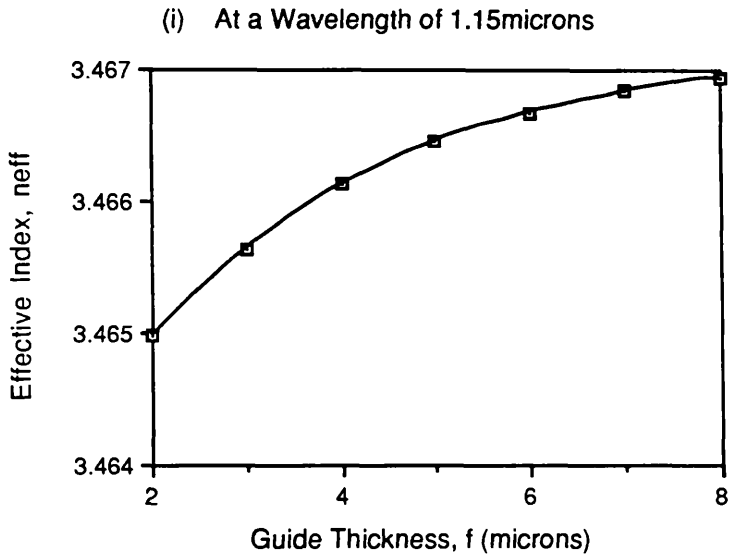
Fig(5.4) Structure and Composition of the Four-Layer Slab Guides under consideration



Device	S41	S42	S43
b (μm)	0.5	0.5	2.0
N_b (cm^{-3})	1.0×10^{18}	1.0×10^{18}	2.0×10^{17}
f (μm)	1.0 - 8.0	1.0 - 5.0	1.0 - 8.0
N_f (cm^{-3})	5.0×10^{16}	5.0×10^{16}	5.0×10^{15}
s (μm)	425	425	425
N_s (cm^{-3})	1.0×10^{18}	1.0×10^{18}	1.0×10^{16}

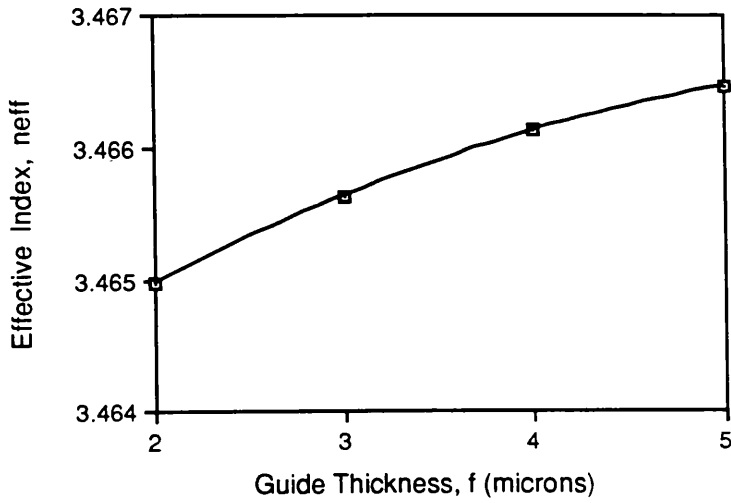
Fig(5.5) Effective Index of First-Order Mode of Four-Layer Slab Guides versus Guide Layer Thickness

(a) For Slab S41

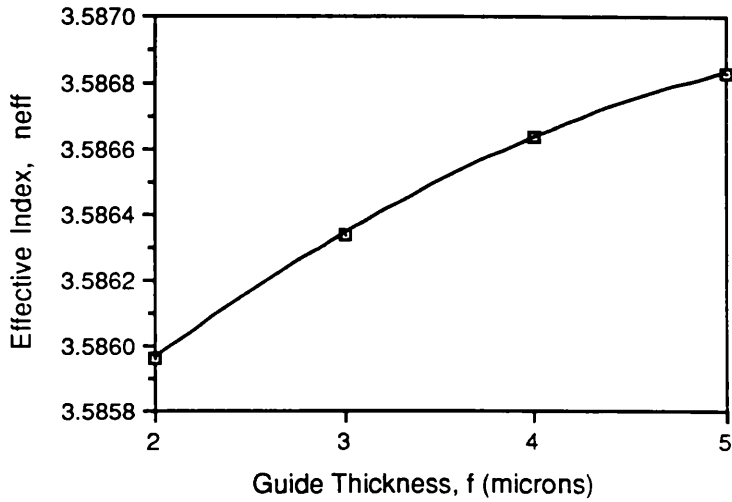


(b) For Slab S42

(i) At a Wavelength of 1.15microns

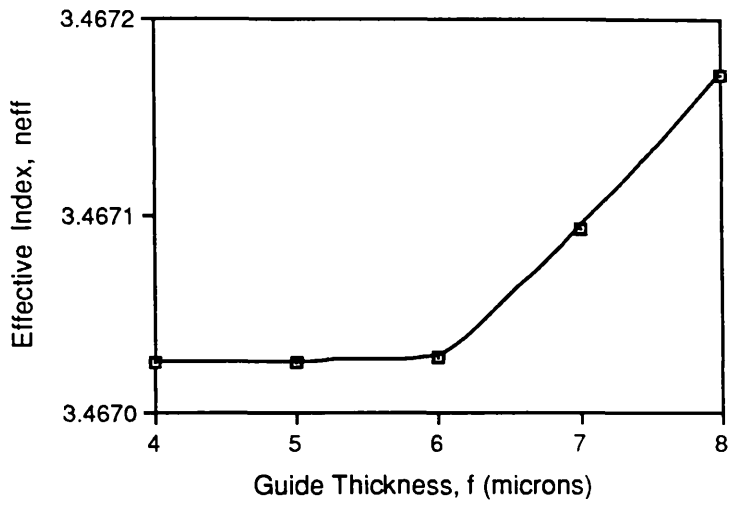


(ii) At a Wavelength of 905nm

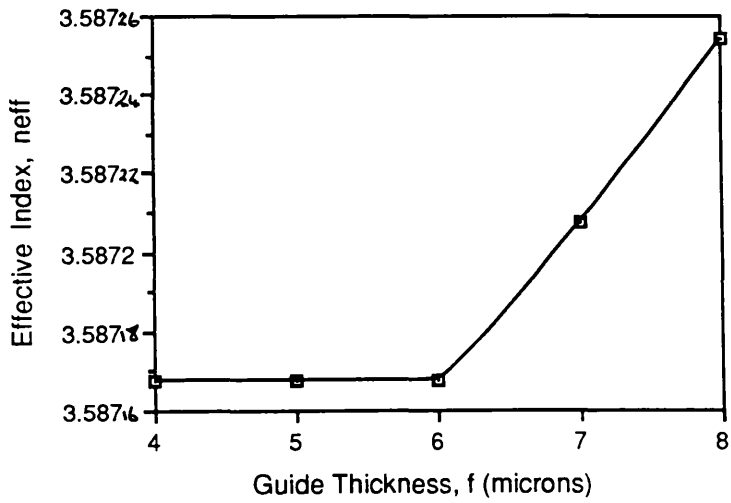


(c) For Slab S43

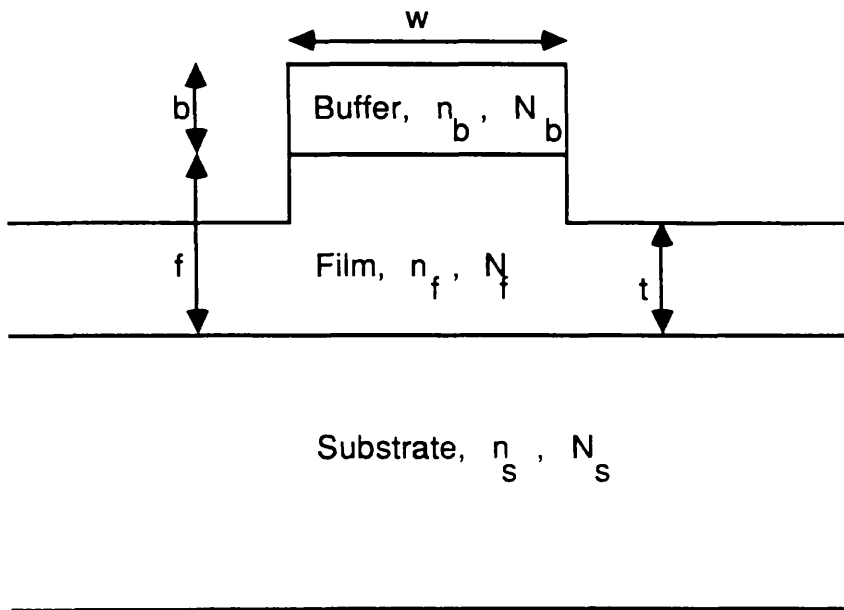
(i) At a Wavelength of 1.15microns



(ii) At a Wavelength of 905nm



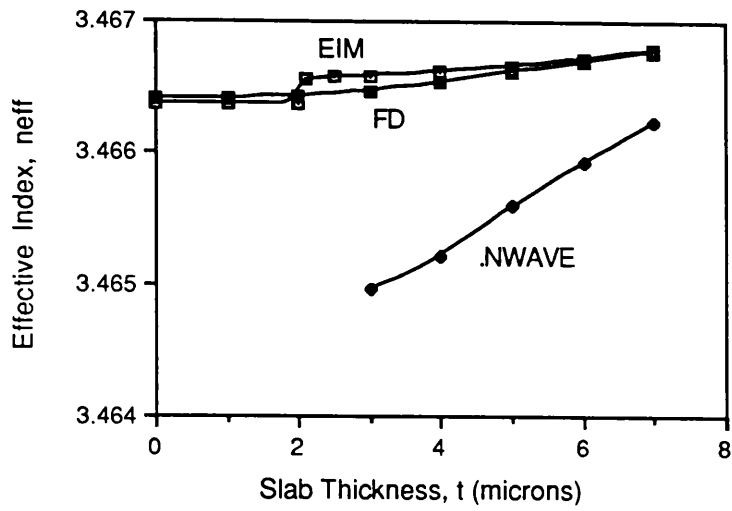
Fig(5.6) Structure and Composition of the Rib Guides under consideration



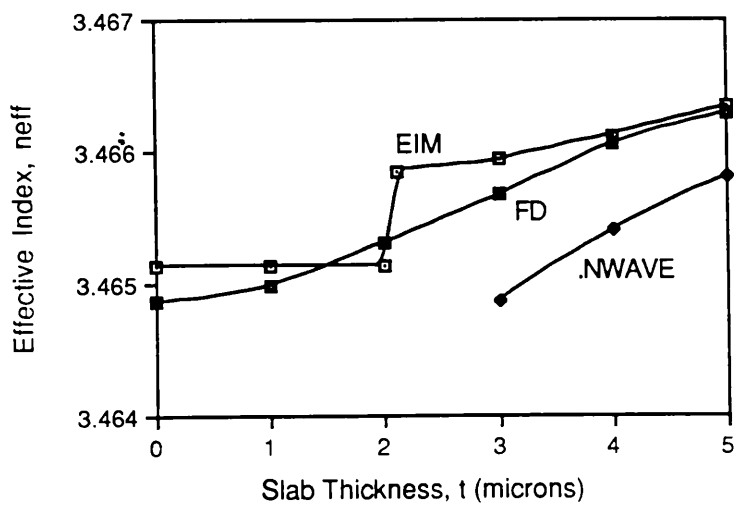
Device	R1	R2	R3
b (μm)	0.5	0.5	2.0
N_b (cm^{-3})	1.0×10^{16}	1.0×10^{16}	2.0×10^{17}
f (μm)	7.0	5.0	5.0
N_f (cm^{-3})	5.0×10^{16}	5.0×10^{16}	5.0×10^{15}
s (μm)	425	425	425
N_s (cm^{-3})	1.0×10^{16}	1.0×10^{18}	1.0×10^{16}
t (μm)	0 - 7.0	0 - 5.0	0 - 5.0
w (μm)	10.0	5.0	5.0

Fig(5.7) Effective Refractive Index of First-Order Mode of Rib Guides versus Outer Slab Thickness

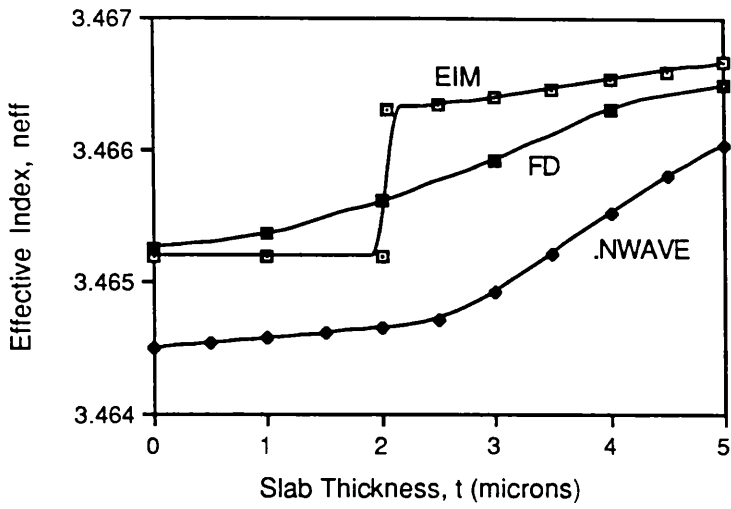
(a) For Rib R1, at a Wavelength of 1.15microns



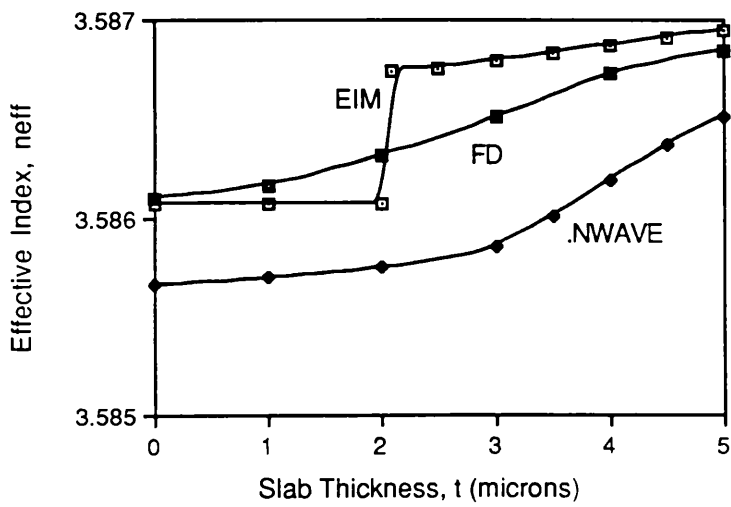
(b) For Rib R2, at a Wavelength of 1.15microns



(c) For Rib R3, at a Wavelength of 1.15microns



(d) For Rib R3, at a Wavelength of 905nm

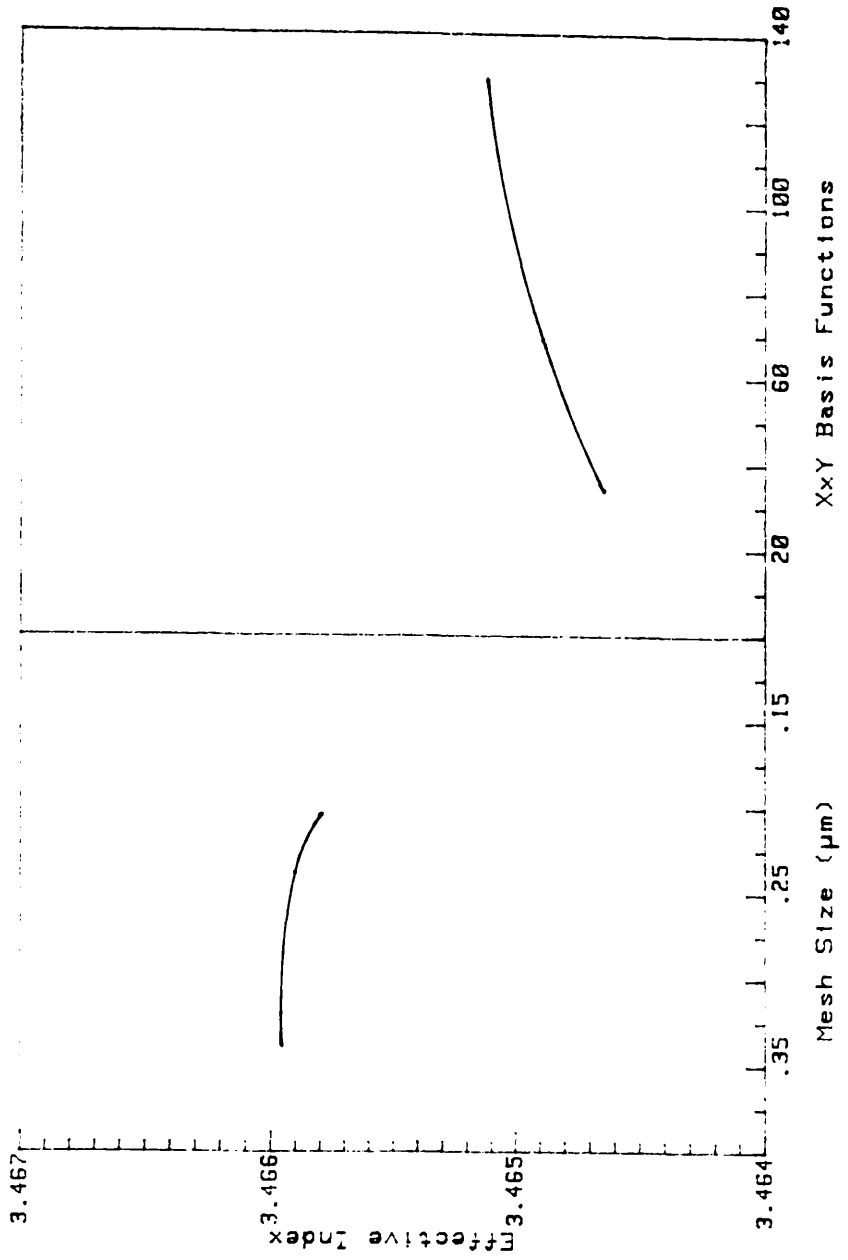


As can be seen from these results, above the cut-off thickness of the outer slab, the Effective Index Method produces an answer greater than that of both of the other methods, due to the limitations imposed on this method. These limitations have already been discussed in section(2.2.1). There can also be seen to be a discrepancy between the results produced by the .NWAVE program and by the FD program. This discrepancy can be explained as being a result of the limitations imposed on the accuracy of these methods set by the choice of the number of basis functions for the .NWAVE program, and the mesh-size for the FD method. In the results presented in fig(5.7), for .NWAVE, $f_1=10$ and $f_2=7$, where f_1 and f_2 are the number of basis functions in the x and y directions respectively, and for the FD method the mesh size is $0.2500\mu\text{m}$, $0.1833\mu\text{m}$ and $0.2333\mu\text{m}$ for guides R1, R2 and R3 respectively.

Further, for structure R3 (with $t=3.0\mu\text{m}$, and $w=5.0\mu\text{m}$) the device was analysed by both the .NWAVE program, varying the number of basis functions used, and by the FD method, varying the mesh size used. The pairs of basis functions used were $f_1=5$, $f_2=7$, and $f_1=7$, $f_2=10$, and $f_1=10$, $f_2=13$. The mesh sizes which were used were $0.2666\mu\text{m}$, $0.2333\mu\text{m}$ and $0.2000\mu\text{m}$. In the FD program the mesh, ie. grid, size was varied by varying the size of the analysis box within which the waveguide lay, and keeping the number of mesh points constant at 61. The corresponding variation in the resulting value of the effective index, n_{eff} , was as shown in fig(5.8).

As can be seen from this the results of the .NWAVE program and the FD method, tend to converge to the true value of n_{eff} , given a large enough number of basis functions and a large enough mesh size. The above result is in agreement with that found by Robertson *et al* [58] in so far as the answers given by the two methods will converge. However, Robertson *et al* found that the FD method converged with decreasing mesh size, not increasing as is the case here. This discrepancy is due to the fact that Robertson *et al* varied the mesh size by varying the number of mesh points, leaving the box size constant, whereas here the mesh size was varied by leaving the number of mesh points constant and varying the box

Fig(5.8) Variation in the Modal Effective Index with Number of Basis Functions, and with Mesh Size



size.

A graphics program .CONPLOT was used in conjunction with .NWAVE. The resulting mode profiles for the fundamental $\nu=0$ mode of devices R1, R2 and R3, with $f_1=10$ and $f_2=7$, for a wavelength of $\lambda=1.15\mu\text{m}$, is shown in fig(5.9). The corresponding mode profile of device R3, obtained by the FD program, is shown in fig(5.10).

5.2.4 Photoelastic Waveguide Calculations

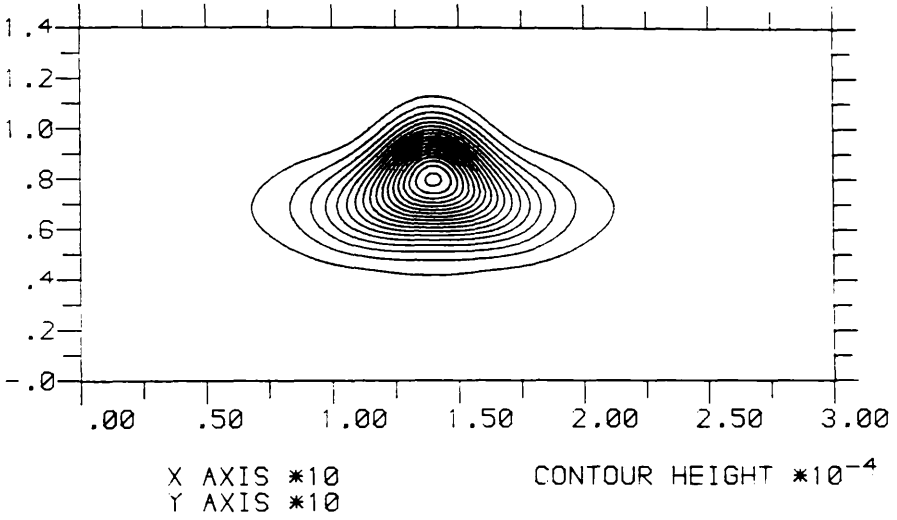
Design calculations for photoelastic waveguides were carried out using another program based on the FD technique, also running on a BBC microcomputer. The structures which were analysed are shown in fig(5.11). These structures consisted of: (a) a semi-insulating substrate, with no epilayer, for which: (1) the metal layer thickness was varied, and (2) the stripe width was varied; and (b) a semi-insulating substrate, with a $5\mu\text{m}$, $5.0 \times 10^{15} \text{cm}^{-3}$ N-type epilayer grown on the top surface, for which again: (1) the metal layer thickness was varied, and (2) the stripe width was varied. These designs were designated P11, P13, P12 and P14 respectively.

For all of these design calculations the refractive index of the semi-insulating substrate was taken to be $n=3.467567$, and the refractive index of the N-type epilayer to be $n=3.467554$, for a wavelength of $1.15\mu\text{m}$. Further, the box size was taken to be $15.0\mu\text{m}$, giving a mesh size of $0.2459\mu\text{m}$.

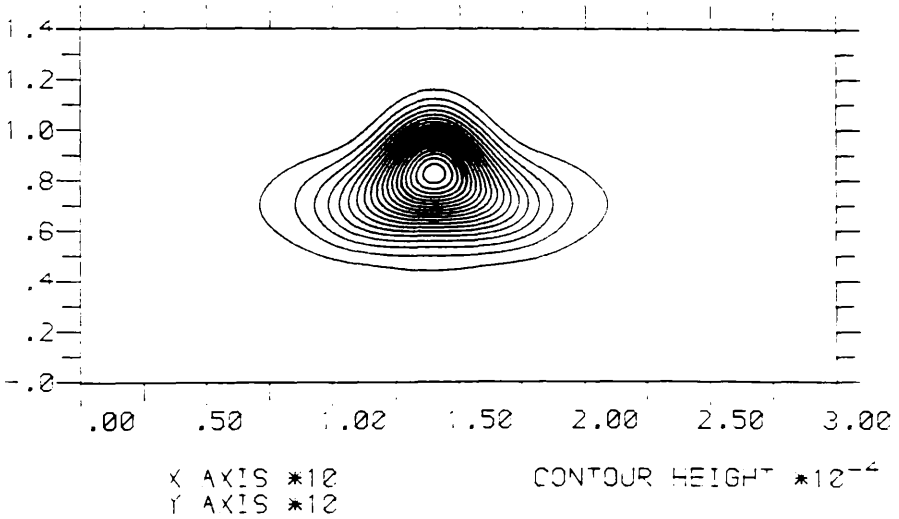
As can be seen from fig(5.12)(a), for both P11 and P12 the modal refractive index increases with increasing metal thickness. This is because the influence on the material refractive index, due to the photoelastic effect, increases with increasing metal thickness. Also, from fig(5.12)(b) it can be seen that the modal refractive index also increases with increasing guide width. This is as would be expected since, the wider the metal stripe spacing, the more modes the guide will be expected to support.

Fig(5.9) Mode Profiles Produced by .NWAVE for the First Order Mode

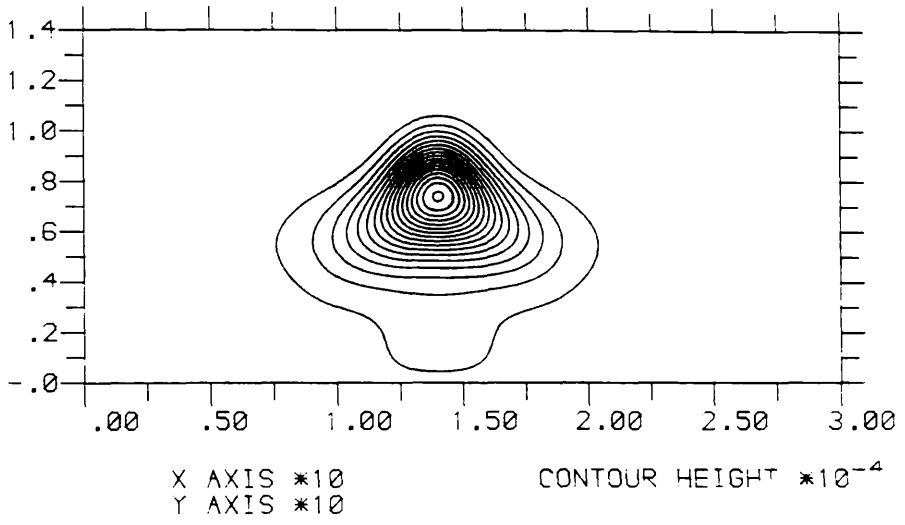
(a) For Device R1



(b) For Device R2

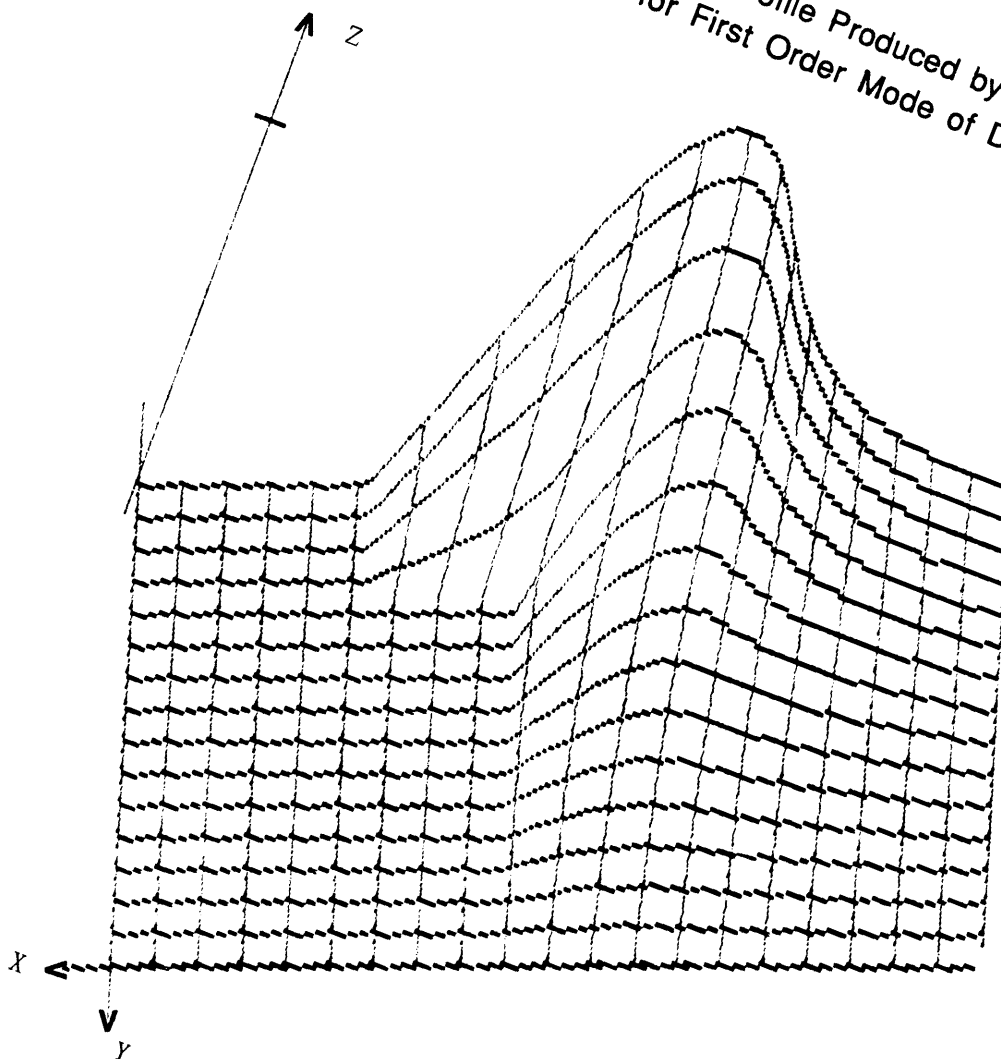


(c) For Device R3



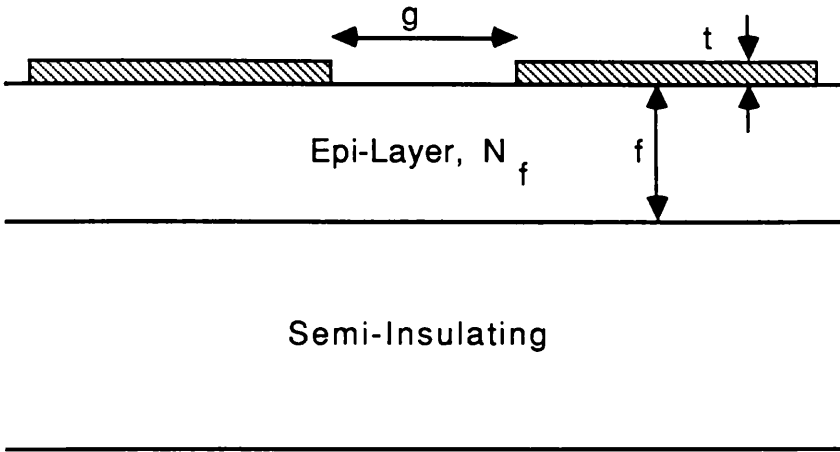
Fig(5.10)

Mode Profile Produced by the FD Program
for First Order Mode of Device R3



Box size=14.0 microns

Fig(5.11) Structure and Composition of the Photoelastic Guides under consideration

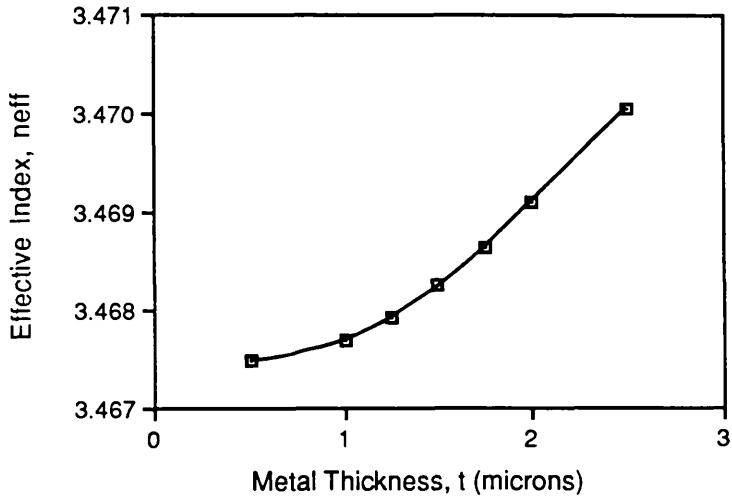


Device	N_f (cm^{-3})	f (μm)	t (μm)	g (μm)
P11	SI	-	0.5 - 2.5	5.0
P12	5.0×10^{15}	5.0	0.5 - 2.5	5.0
P13	SI	-	1.5	2.0 - 12.0
P14	5.0×10^{15}	5.0	1.5	2.0 - 12.0

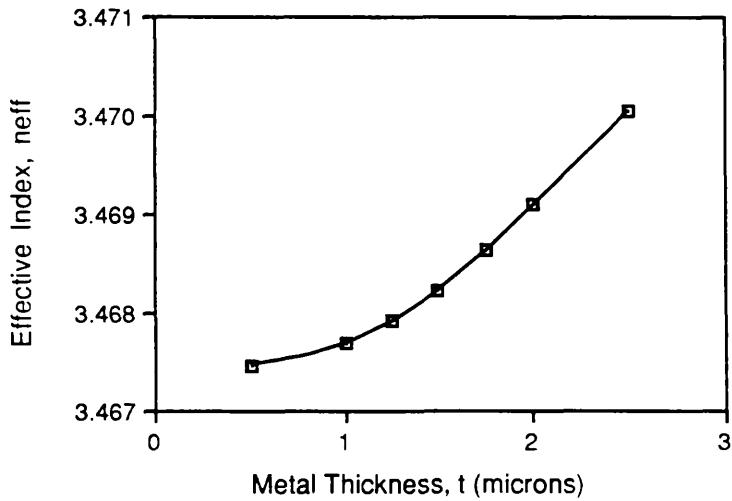
Fig(5.12) Effective Index of First Order Mode of Photoelastic Guides, $\lambda = 1.15\text{microns}$

(a) With varying Metal Thickness, t

(i) For Waveguide P11, $f=5.0\text{microns}$, $g=5.0\text{microns}$

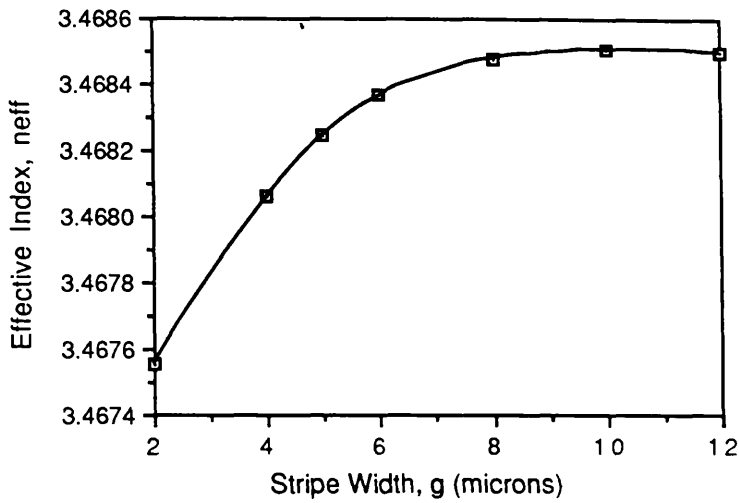


(ii) For Waveguide P12, $f=5.0\text{microns}$, $g=5.0\text{microns}$

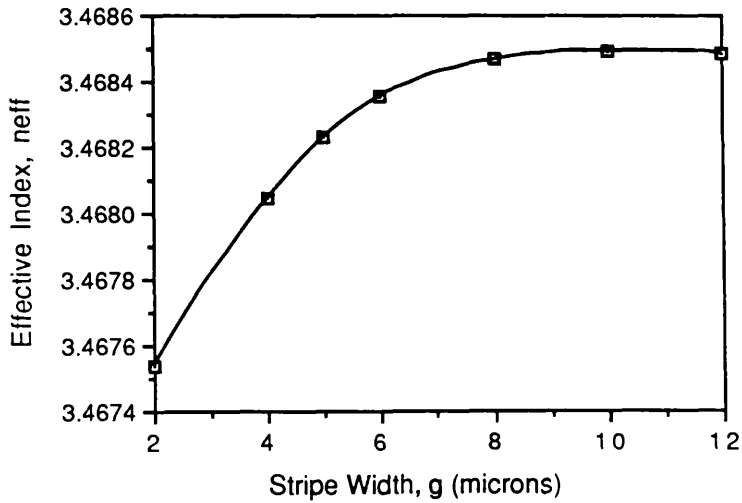


(b) With varying Stripe Width, g

(i) For Waveguide P13, $f=5.0\mu\text{m}$, $t=1.5\mu\text{m}$



(ii) For Waveguide P14, $f=5.0\mu\text{m}$, $t=1.5\mu\text{m}$



5.3 ELECTRICAL DESIGN

5.3.1 Electrical Performance

In this section are presented the theoretical calculations of: (a) the threshold voltage, V_T ; and (b) the threshold electrical power, P_T , for all of the devices of interest, both vertical and planar. The vertical devices of interest may be grouped into two categories, ie. spot contact diodes, similar to that of fig(1.2)(a), and rib (stripe) contact diodes, similar to that of fig(1.3)(b). As was previously explained, conventional Gunn diodes tend to be of the mesa (spot) type structure similar to the X-Band and J-Band diodes supplied by Plessey Microwave Ltd (see fig(3.6)(a)). The results for these diodes are shown in table(5.4).

The threshold voltage, V_T for each of the structures of interest was calculated from $V_T = E_T f$, where, $E_T =$ the threshold field $= 3.5 \times 10^5 \text{Vm}^{-1}$ for GaAs, and $f =$ the active length of the device. The electrical power consumed by the device at threshold was calculated from $P_T = I_T V_T$, where, $I_T = V_T / R$, $R = (1/Nq\mu)(f/A)$, $\mu =$ the low field mobility $= 0.800 \text{m}^2 \text{V}^{-1} \text{s}^{-1}$ for GaAs, and $A =$ the contact area of the device.

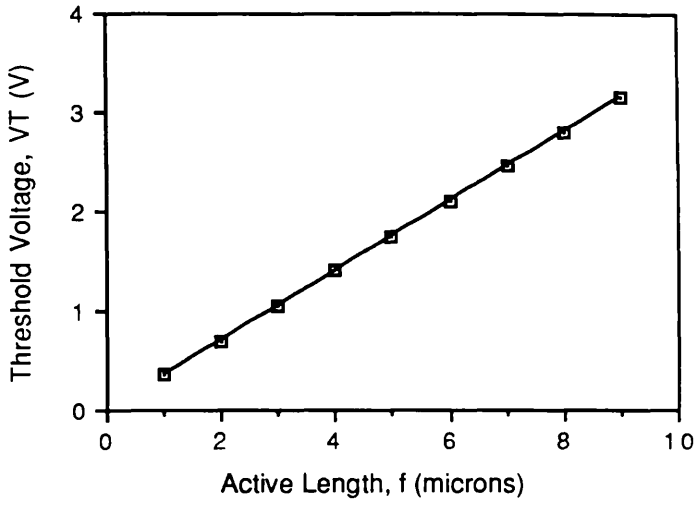
Shown in fig(5.13) are the threshold voltages for the four-layer slab guide structures given in fig(5.4), for various active layer thicknesses between 0 and $10 \mu\text{m}$. Also shown in figs(5.14)(a) and (b) are the electrical powers required for these devices, for spot contacts of diameter $20 \mu\text{m}$, $50 \mu\text{m}$ and $80 \mu\text{m}$.

The estimate of the electrical power required for the device to oscillate calculated in this way, is actually an under estimate of the power required. This is because, although the contact on the top most surface of the device is in the form of a spot contact, the contact on the bottom surface covers the whole of that surface. This means that the electric field lines within the active region of the device will not be distributed as is assumed in the above calculations, and so the effective active area of the device will not be simply that of the top contact, but somewhat larger. Consequently, the device resistance will be less than was assumed,

Table(5.4) The X-Band and J-Band Diodes supplied by Plessey

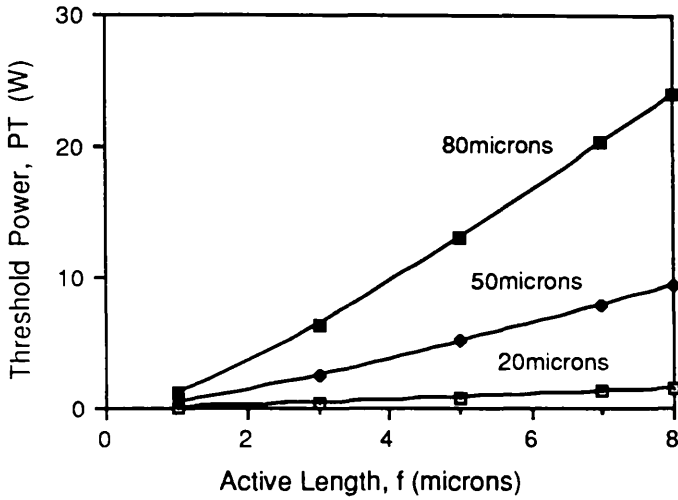
Diode	f (μm)	V _T (V)	P _T (W)
X-Band	9.2	3.22	3.95
J-Band	5.0	1.75	0.39

Fig(5.13) Threshold Voltage versus Layer Thickness for the Structures of interest

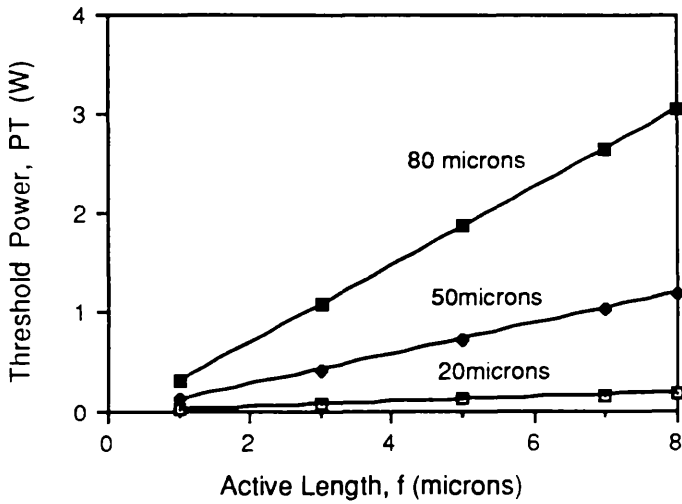


Fig(5.14) Threshold Electrical Power versus Layer Thickness for the Spot Contact Structures of interest, for various Spot Diameter sizes

(a) For Diodes S41 and S42



(b) For Diode S43



and the required threshold current, I_T , will be somewhat more. If a more accurate estimate of the electrical parameters was required, the more involved Relaxation Method [59] would have to be employed.

Shown in fig(5.15)(a) are similar results showing the variation in the required threshold electrical power for the rib structures of fig(5.6), with varying rib width, w . All of the calculations of fig(5.15)(a) were based on a rib contact length of 1.5mm. Note that from these results it can be concluded that device R1 is of no practical use as an integrated device since the current drawn by it is excessive. For example, for a rib width of $10\mu\text{m}$, and length of 1.5mm, R1 draws a current $I_T = 24.7\text{A}$. Further, for a rib width of $5\mu\text{m}$, and length of 1.5mm, R2 draws a current $I_T = 11.6\text{A}$. Although not as excessive as R1, the current drawn by R2 is still too large for the power supplies available, and also too large for the device to withstand due to thermal considerations. R3 however draws a current of only 1.6A at threshold.

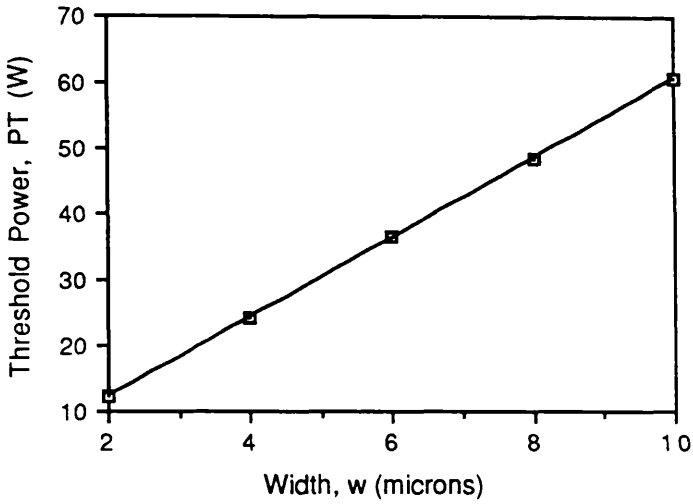
Given in fig(5.15)(b) are the results showing the variation in the required threshold electrical power for a planar structure corresponding to that of device P1 of table(5.1). Again, as for the rib guides, all the calculations were based on a device length of 1.5mm. Further, the effective area of the device was approximated to the thickness of the epilayer ($5\mu\text{m}$) multiplied by the length of the waveguide (1.5mm).

As can be seen from fig(5.15)(b), the threshold power drawn by the planar diode is much greater than that drawn by device R3. This is due to the larger active length, L , of the planar device, and the consequent higher threshold voltage. The planar diode has, however, a threshold current, $I_T=1.68\text{A}$, which is modest in comparison to that of R1 or R2.

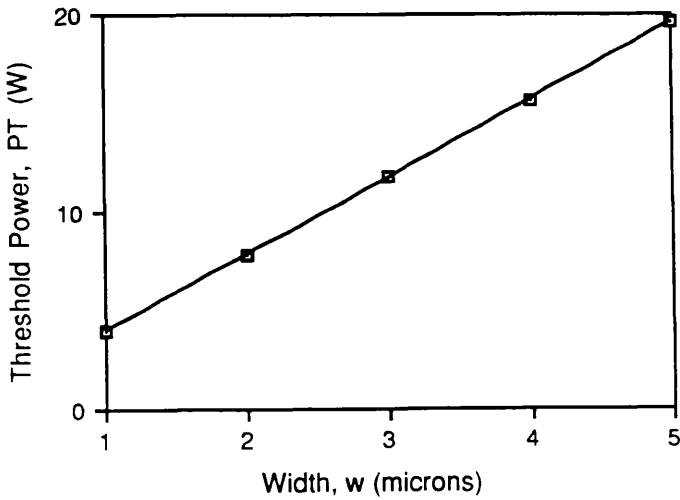
The preferred embodiment of the device incorporating a rib waveguide and a stripe contact vertical Gunn diode, provides a Schottky contact pad on the top surface of the device, as was shown in fig(1.3)(b). The Schottky contact straddles the rib guide, the purpose of the contact being to allow ease of bonding of the top ohmic contact of the device to any external circuitry, since it is not possible to

Fig(5.15)(a) Threshold Electrical Power versus Rib Width for the Rib Structures of interest (Rib Length = 1.5mm)

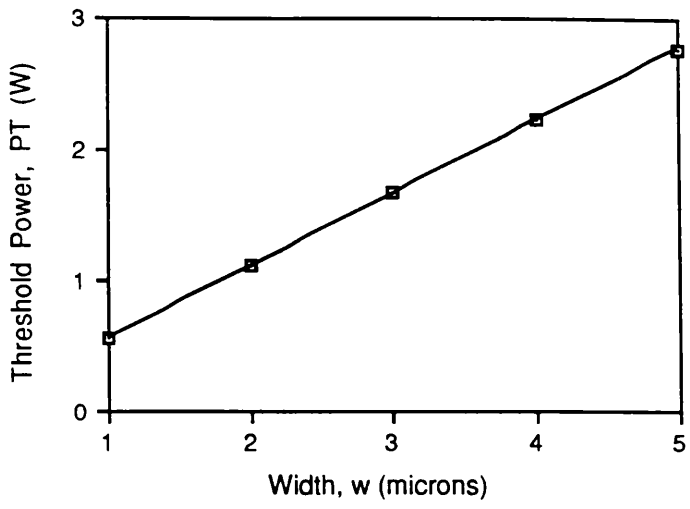
(i) For Rib R1



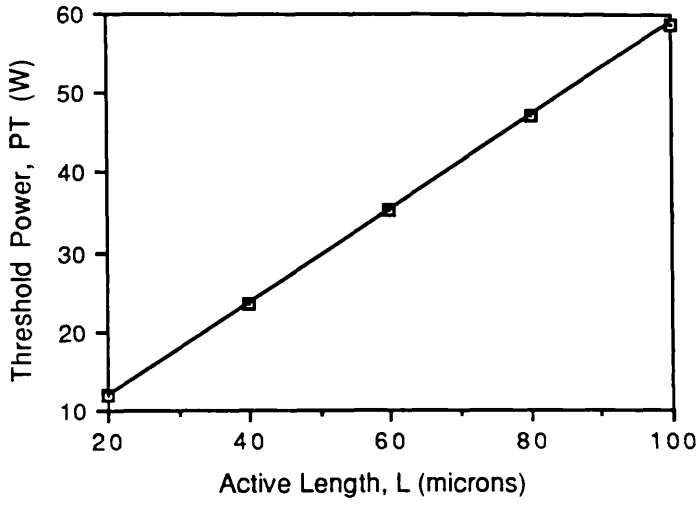
(ii) For Rib R2



(iii) For Rib R3



Fig(5.15)(b) Threshold Electrical Power versus Active Layer Length for the Planar Structures of interest



reliably bond a wire onto the top of the rib, the rib being of the order of $5\mu\text{m}$ to $10\mu\text{m}$ wide.

The inclusion of the Schottky contact does however complicate the design procedure since: (a) there will be a capacitance associated with the Schottky contact; and (b) when a negative bias is applied to the top contact, ie. the cathode, there will be a depletion of electrons under the Schottky contact. This depletion may result in a change in the refractive index of the material under the contact due to the Free Carrier Plasma effect, and hence a change in the optical propagation characteristics of the material. Each of these points is dealt with below.

Assuming that the Schottky contact acts as a parallel plate capacitor then, the device may be represented as shown in fig(5.16). Further, we have that [60]

$$C_{\text{Schottky}} = \frac{\epsilon A}{d} \quad \dots\dots 5.4$$

where, $\epsilon = \epsilon_0 \epsilon_r$

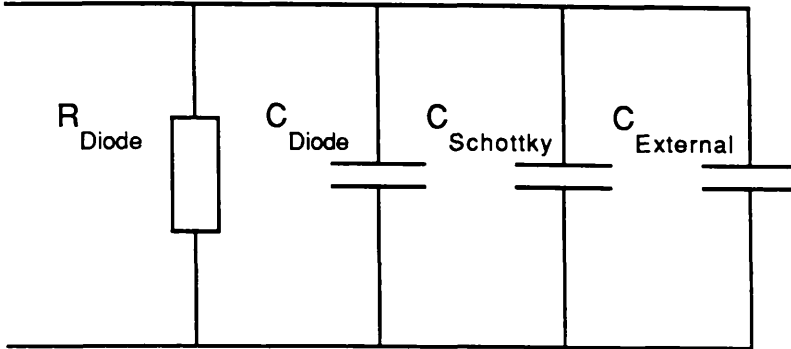
$A = \text{area of Schottky contact} = 300\mu\text{m} \times 1.5\text{mm}$

$d = t + s = 428\mu\text{m}$

The diode resistance, R_{Diode} and the capacitance of the Schottky contact, C_{Schottky} for each of the rib structures of interest are shown in table(5.5). As well as showing values of R_{Diode} and C_{Schottky} for a substrate thickness of $400\mu\text{m}$, table(5.5) also shows the corresponding values for a reduced substrate thickness of $50\mu\text{m}$. Note that these calculations were found for a rib length of 2mm . As can be seen from table(5.5), the capacitance of the Schottky contact, which varies inversely with substrate thickness, lies in the picofarad range, and is therefore of some influence in the microwave regime. The capacitance of the Schottky contact cannot therefore be ignored in the design of the device, or its associated external electrical circuitry.

The second influence on the action of the device, due to the presence of the Schottky contact, is the possible change in its optical characteristics. This change is

Fig(5.16) Equivalent Circuit representation of the Rib Guide incorporating a Vertical Diode



Table(5.5) Electrical Characteristics of the Vertical/Rib Devices

Device	s (μm)	R_{Diode} (Ω)	C_{Schottky} (pF)
R1	400	0.422	0.169
	50	0.149	1.244
R2	400	0.391	0.170
	50	0.118	1.291
R3	400	1.102	0.170
	50	0.828	1.291

due to the Free Carrier Plasma effect on the refractive index, caused when a negative bias voltage is applied to the top contact. The interface between a metal and an N-type semiconductor forming a Schottky contact may be represented as shown in fig(5.17). This model takes into account only the difference in the work functions of the metal and semiconductor, ψ_m and ψ_s , respectively, and does not address any chemical interactions on an atomic level. As can be seen from fig(5.17), for N-type material if $q\psi_m > q\psi_s$ then a Schottky contact will be formed. Further, the depletion layer width, d , in the absence of an applied field, is given by [61]

$$d = \left\{ \frac{2\epsilon V_B}{q^2 N_D} \right\}^{1/2} \dots\dots 5.5$$

where, $V_B = \text{built-in barrier voltage} = q\varphi_D = q(\varphi_m - \varphi_s)$
 $\varphi_D = \text{built-in potential}$

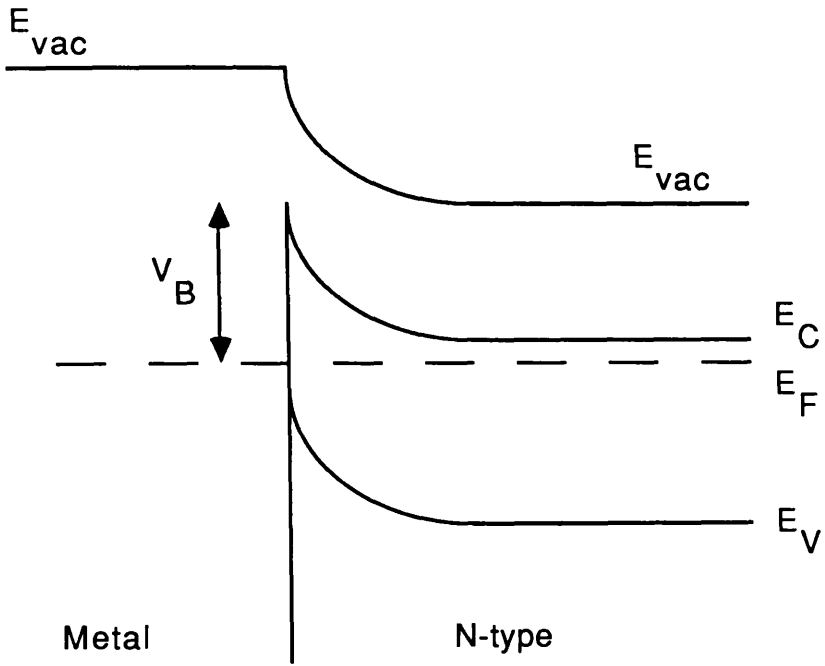
Now, consider the case of a contact made between gold, Au, having a work function, $\psi_m = 5.0\text{eV}$, and N-type GaAs ($N = 5.0 \times 10^{22} \text{m}^{-3}$) having a work function, $\psi_s = 4.1\text{eV}$. Since $\psi_m > \psi_s$ then a Schottky contact will be formed. Further, the built-in potential, $\varphi_D = 0.9\text{eV}$, which gives a depletion layer width, $d = 0.16\mu\text{m}$, in the absence of an applied bias field.

In the presence of an applied bias, d is given by [61]

$$d = \left\{ \frac{2\epsilon(\varphi_D + V_R)}{qN_D} \right\}^{1/2} \dots\dots 5.6$$

where, $V_R = \text{reverse bias voltage}$. This means that for $V_R = 2.5\text{V}$, $d = 0.314\mu\text{m}$. Assuming total depletion of carriers within the depletion region this implies that a slab layer $0.314\mu\text{m}$ thick will exist adjacent to the top surface of the device. Also, according to equation(4.21), the perturbation in the refractive index associated with the depletion region is $\Delta n(5.0 \times 10^{22} \text{m}^{-3}) = 1.353 \times 10^{-4}$, for a wavelength of $1.15\mu\text{m}$. For the case of a Schottky contact made between gold, Au and N-type GaAs ($N = 5.0 \times 10^{21} \text{m}^{-3}$), the associated depletion layer depth $d = 0.992\mu\text{m}$, and

Fig(5.17) Schematic Diagram of a Schottky Contact



$\Delta n(5.0 \times 10^{21} \text{m}^{-3}) = 1.353 \times 10^{-5}$, for a wavelength of $1.15 \mu\text{m}$.

Now, the pertinent question is whether the slab layer, produced by the application of a reverse bias voltage, will cause any appreciable change in the guiding characteristics of the device, and whether indeed the induced slab will itself support a mode. Running the three-layer slab program (already referred to in section(5.2.2)) it was found that neither of the induced slab layers associated with Schottky contacts to N-type GaAs, where, $N = 5.0 \times 10^{22} \text{cm}^{-3}$, or $N = 5.0 \times 10^{21} \text{cm}^{-3}$, supported a mode of propagation. This result was confirmed for both wavelengths of $1.15 \mu\text{m}$ and 905nm .

5.3.2 Thermal Considerations

Most Gunn diodes to date have had an electrical-to-microwave conversion efficiency of between 0.5% and 10%, most of the remaining energy being dissipated in the form of heat. This has meant that Gunn diode assemblies have necessarily incorporated some form of heat sinking. If, for the sake of simplicity, it is assumed that 100% of the electrical power, P_e , supplied to the diode is converted into heat, then

$$\epsilon = mc\Delta T = P_e t \quad \dots\dots\dots 5.7$$

where, ϵ = energy supplied

m = mass of the material = ρV

ρ = density of the material = $5.32 \times 10^3 \text{kgm}^{-3}$ for GaAs [27]

V = volume of active material

c = specific heat capacity = $0.35 \times 10^3 \text{Jkg}^{-1}\text{C}^{-1}$ for GaAs

ΔT = increase in temperature of the device

t = time for which energy is supplied

Using equation(5.7) in conjunction with the results of figs(5.14) and (5.15), the maximum time, ie. pulse length, for which electrical energy can be supplied may be

found for any given rise in temperature, ΔT . The results of such calculations for the spot contact diodes of fig(5.4) are shown in fig(5.18). As can be seen from fig(5.18), the maximum pulse length decreases with increasing active layer length, and hence volume. Further, note that for each structure the maximum pulse length, t , is independent of the area of the contact. This is because the pulse length, t , is inversely proportional to the power delivered, P_e , which is itself directly proportional to the area of the contact, as can be seen from equation(5.7).

Similarly, for the rib structures of interest the maximum electrical pulse duration is independent of the rib width. It can therefore be found that, for $\Delta T=100^\circ\text{C}$, the maximum pulse lengths for the rib structures are $t(R1)=0.868\mu\text{s}$, $t(R2)=0.960\mu\text{s}$, and $t(R3)=6.758\mu\text{s}$. It should however be remembered that the values of pulse length, t , calculated in this way are an underestimate, since the calculation assumes 100% electrical to thermal conversion, and further does not take into account any thermal dissipation.

It should also be noted that the variation in the temperature of the device when in operation may have an effect on various important optical, as well as electrical, parameters. For example, the refractive index, n , the optical absorption coefficient, α , the bandgap energy, E_g , and the threshold electric field, E_T , may all vary with temperature [46],[27].

5.4 ELECTRO-OPTICAL CONSIDERATIONS

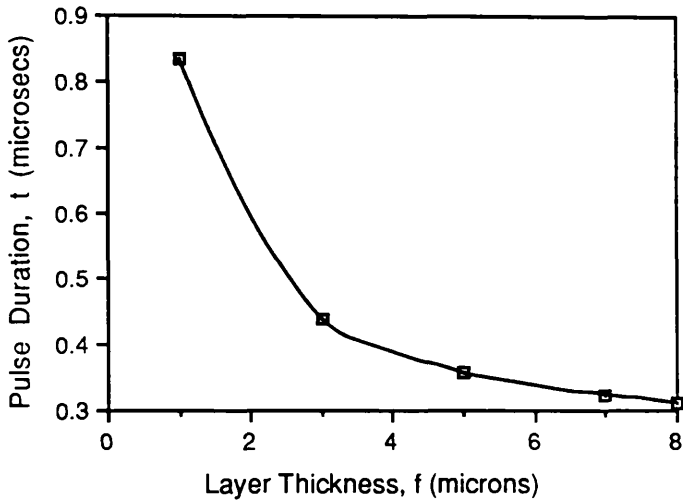
5.4.1 Calculation of Domain Characteristics

A simulation program based on the solution of Poisson's equation and the Current Continuity equation (equations(3.1) and (3.8) respectively), consistent with the boundary conditions imposed by a high field propagating Gunn domain, was written. A full listing of the program is given in Appendix B, and the documentation relating to the program in Appendix C.

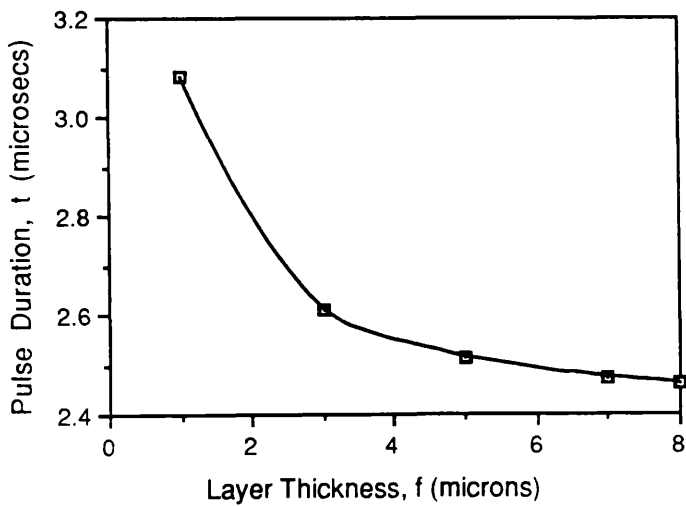
The simulation program requires to know the length and doping density of the

Fig(5.18) Maximum Electrical Pulse Duration versus Layer Thickness for the Spot Contact Structures of interest, and $\Delta T = 100K$

(a) For Diodes S41 and S42



(b) For Diode S43



contact regions and the channel (active) region of the device, along with the electric field applied across the channel region, and the structure of any doping spike, ie. domain nucleation centre, within the channel region. In return, the program calculates the carrier density profile and electric field profile associated with the propagating Gunn domain, as time progresses and the domain traverses the device. Knowing the carrier density profile and the electric field profile throughout the device, means that the associated perturbations in the index of refraction and the optical absorption, as outlined in Chapter 4, may be calculated. The program may be run using:

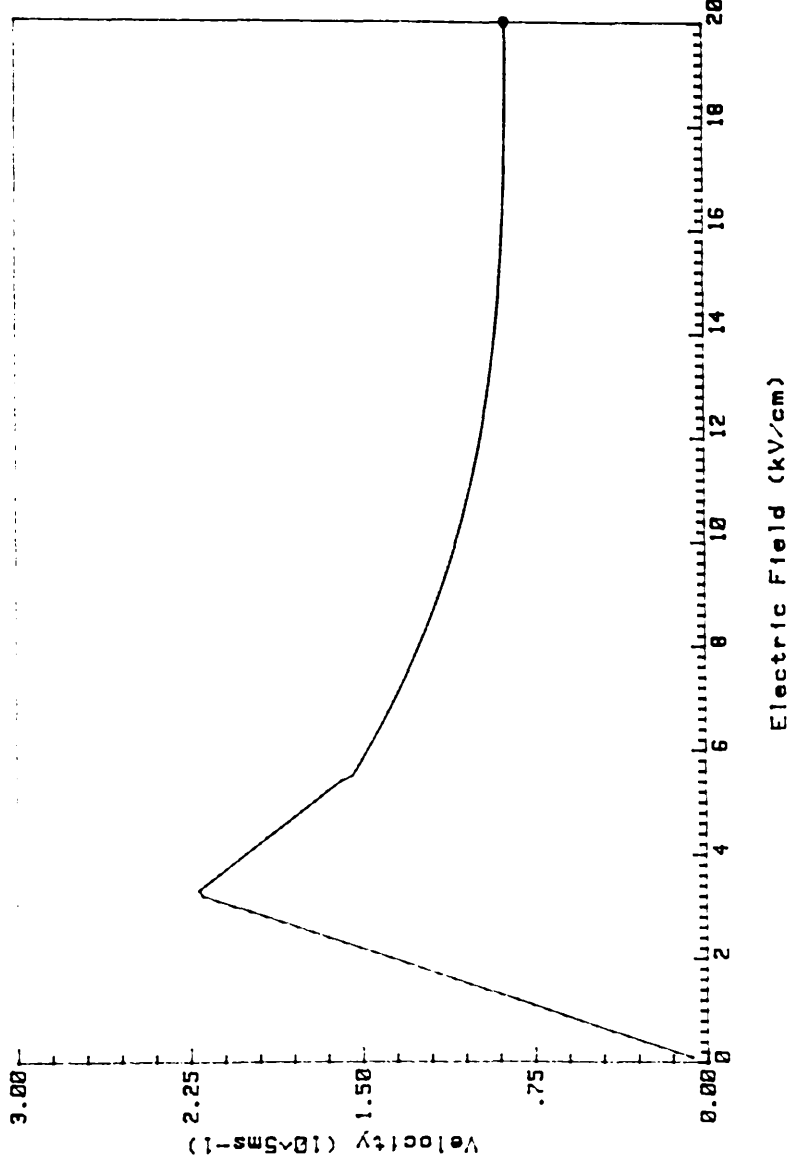
- (a) a four-line approximation to the accepted velocity-field characteristic for GaAs, and a field independent value of diffusion coefficient, $D = 0.0178\text{m}^2\text{s}^{-1}$;
- (b) an analytical velocity-field characteristic for GaAs, based on the constant temperature model [27], and a field independent D ; or
- (c) an analytical velocity-field characteristic, and a field dependent $D=D(E)$.

As will be shown, a comparison of each of the above analysis situations (a)–(c) was made for each of the various device structures of interest.

The four-line approximation to the accepted velocity-field characteristic for GaAs referred to above may be used to simplify, and therefore increase the speed of, the simulation program. The approximation has the form shown in fig(5.19), and consists of a linear section from 0 to $3.249 \times 10^5 \text{Vm}^{-1}$, peaking at a velocity of $2.229 \times 10^5 \text{ms}^{-1}$, where the mobility $\mu = v/E = 0.6860 \text{m}^2 \text{V}^{-1} \text{s}^{-1}$; an inversely linear section from $3.249 \times 10^5 \text{Vm}^{-1}$ to $5.499 \times 10^5 \text{Vm}^{-1}$, where $\mu = 0.2976 \text{m}^2 \text{V}^{-1} \text{s}^{-1}$; an inversely cubic section from $5.499 \times 10^5 \text{Vm}^{-1}$ to $20.0 \times 10^5 \text{Vm}^{-1}$; and a section of constant velocity, $v = 0.86 \times 10^5 \text{ms}^{-1}$ above $20.0 \times 10^5 \text{Vm}^{-1}$.

Now, it can be seen that rearranging the Current Continuity equation (equation(3.8)) yields

Fig(5.19) The Four-Line Approximation to the Accepted Velocity-Field Characteristic for GaAs



$$\frac{\partial E}{\partial t} = \frac{1}{\epsilon} \left[J(t) - Nqv + q \frac{\partial}{\partial x} \{DN\} \right] \quad \dots\dots\dots 5.8$$

$$\text{ie. } E(t+1) = E(t) + \frac{\Delta t}{\epsilon} \left[J(t) - Nqv + q \frac{\partial}{\partial x} \{DN\} \right] \quad \dots\dots\dots 5.9$$

$$\text{so } E^{t+1}(K) = E^t(K) + \frac{\Delta t}{\epsilon} \left[J(t) + J_C^t(K) \right] \quad \dots\dots\dots 5.10$$

where, K = any given point within the the device

$$J_C^t(K) = -Nqv + q\partial/\partial x\{DN\}$$

$E^t(k)$ = electric field at a point K at a time t

$$\text{Now, } \frac{\partial E}{\partial t} = \frac{1}{\epsilon} \left[J(t) + J_C^t(K) \right] \quad \text{and, } \int Edx = V$$

$$\text{Thus, } \int \left[\frac{\partial E}{\partial t} dx - \frac{1}{\epsilon} \right] (J(t) + J_C^t(K)) dx = 0 \quad \dots\dots\dots 5.11$$

$$\text{ie. } \frac{J(t)L_{Tot}}{\epsilon} + \frac{1}{\epsilon} \int J_C^t(K) dx = 0 \quad \dots\dots\dots 5.12$$

where, L_{Tot} = total device length

$$\text{Thus, } J(t) = - \frac{1}{L_{Tot}} \int J_C^t(K) dx \quad \dots\dots\dots 5.13$$

Substituting equation(5.13) into equation(5.10) gives,

$$E^{t+1}(K) = E^t(K) - \frac{\Delta t}{\epsilon L_{Tot}} \int J_C^t(K) dx + \frac{\Delta t}{\epsilon} J_C^t(K) \quad \dots\dots\dots 5.14$$

From Poisson's equation (equation(3.1)) we have that

$$N = - \frac{\epsilon \partial E}{q \partial x} + N_D \quad \dots\dots\dots 5.15$$

and
$$\frac{\partial N}{\partial x} = -\frac{\epsilon}{q} \frac{\partial^2 E}{\partial x^2} + \frac{\partial N_D}{\partial x} \quad \dots\dots 5.16$$

Further, substituting equations(5.15) and (5.16) into the expression for $J_c^t(K)$ yields

$$J_c^t(K) = -Nqv + q \frac{\partial}{\partial x} (DN) \quad \dots\dots 5.17$$

$$= -qv \left\{ -\frac{\epsilon}{q} \frac{\partial E}{\partial x} + N_D \right\} + qD \left\{ -\frac{\epsilon}{q} \frac{\partial^2 E}{\partial x^2} + \frac{\partial N_D}{\partial x} \right\} + qN \frac{\partial D}{\partial x}$$

Now, if $D(E)$ is taken as being independent of E then the last term in equation(5.17) is equal to zero, and so we have that

$$J_c^t(K) = -N_Dqv - \epsilon v \frac{\partial E}{\partial x} + \epsilon D \frac{\partial^2 E}{\partial x^2} + qD \frac{\partial N_D}{\partial x} \quad \dots\dots 5.18$$

Therefore from equation(5.14)

$$E^{t+1}(K) = E^t(K) - \frac{\Delta t}{\epsilon L_{Tot}} \int J_c^t(K) dx$$

$$+ \frac{\Delta t}{\epsilon} \left\{ -\epsilon v \frac{\partial E}{\partial x} - N_Dqv + \epsilon D \frac{\partial^2 E}{\partial x^2} + qD \frac{\partial N_D}{\partial x} \right\} \quad \dots\dots 5.19$$

If we define

$$J_\chi = \frac{\Delta t}{\epsilon} \left\{ -\epsilon v \frac{\partial E}{\partial x} - N_Dqv + \epsilon D \frac{\partial^2 E}{\partial x^2} + qD \frac{\partial N_D}{\partial x} \right\} \quad \dots\dots 5.20$$

then it can be seen that

$$E^{t+1}(K) = E^t(K) + J_\chi - \frac{1}{L_{Tot}} \int J_\chi dx$$

$$= E^t(K) + J_\chi - J_j \quad \dots\dots 5.21$$

where, $J_j = \frac{1}{L_{Tot}} \int J_\chi dx$

If however, D is taken as being dependent upon E , then the last term in

equation(5.17) is not equal to zero, and therefore we have that

$$J_c^t(K) = -N_D q v - \epsilon v \frac{\partial E}{\partial x} + \epsilon D(E) \frac{\partial^2 E}{\partial x^2} + q D(E) \frac{\partial N_D}{\partial x} + q N \frac{\partial D(E)}{\partial x} \dots\dots\dots 5.22$$

Inserting this into equation(5.14) shows that

$$E^{t+1}(K) = E^t(K) - \frac{\Delta t}{\epsilon L_{Tot}} \left\{ J_c^t(K) dx + \frac{\Delta t}{\epsilon} \left\{ -\epsilon v \frac{\partial E}{\partial x} - N_D q v + \epsilon D(E) \frac{\partial^2 E}{\partial x^2} + q D(E) \frac{\partial N_D}{\partial x} + q N \frac{\partial D(E)}{\partial x} \right\} \right\} \dots\dots\dots 5.23$$

Now, if we define

$$J_\chi = \frac{\Delta t}{\epsilon} \left\{ -\epsilon v \frac{\partial E}{\partial x} - N_D q v + \epsilon D(E) \frac{\partial^2 E}{\partial x^2} + q D(E) \frac{\partial N_D}{\partial x} \right\} \dots\dots\dots 5.24$$

then it can be seen that $E^{t+1}(K)$ is again given by equation(5.21).

Comparing the situations of a field independent diffusion and a field dependent diffusion, as represented by equations(5.18) and (5.22) respectively, it can be seen that in the case of $D=D(E)$ the extra term $qN\partial D(E)/\partial x$ is included in the definition of $J_c^t(K)$ and J_χ .

In the case that $D=D(E)$, the field dependence of D may be derived from the two-term Einstein relationship given by

$$D(E) = \frac{k}{q} \frac{N_1 \mu_1 T_1 + N_2 \mu_2 T_2}{N_1 + N_2} \dots\dots\dots 5.25$$

where, k = Boltzmann's constant = $1.38066 \times 10^{-23} JK^{-1}$

q = electron charge

N_1 = electron population in (000) valley

N_2 = electron population in (100) valley

μ_1, μ_2 = electron mobilities in the respective valleys

T_1, T_2 = electron temperatures in the respective valleys

Using the so-called Single-Temperature Model, which assumes that $T_1 = T_2 = T_e$, gives that [27]

$$D(E) = \frac{kT_e}{q} \frac{N_1 \mu_1 + N_2 \mu_2}{N_1 + N_2} \quad \dots\dots\dots 5.26$$

ie.
$$\frac{1}{D(E)} = \frac{q}{kT_e} \frac{N_1 + N_2}{N_1 \mu_1 + N_2 \mu_2}$$

Now, for GaAs, $\mu_1 \gg \mu_2$, and so

$$D(E) = \frac{kT_e}{q} \frac{\mu_1}{1 + \frac{N_2}{N_1}} \quad \dots\dots\dots 5.27$$

Also,

$$\frac{N_2}{N_1} = R \exp\left[\frac{-\Delta}{kT_e}\right] \quad \dots\dots\dots 5.28$$

where, R = density of states ratio = $(M_{v1}/M_{v2}) \cdot (M_{\Gamma}/M_L)^{X/2}$
 $= 94$ for GaAs in 3-D [27]

$\Delta = 0.31\text{eV}$ for GaAs

M_{v1} = number of equivalent lower valleys = 1 [62]

M_{v2} = number of equivalent upper valleys = 4

M_{Γ} = electron effective mass in Γ valley = $Mr_1 \cdot m_e$

M_L = electron effective mass in L valley = $Mr_2 \cdot m_e$

Mr_1 = Γ density of states mass

Mr_2 = L density of states mass

X = number of dimensions

Also, from the concept of energy-relaxation time [27]

$$qEv = Xk \frac{(T_e - T)}{\tau_e} \quad \dots\dots\dots 5.29$$

where, T = actual lattice temperature

τ_e = energy relaxation time $\approx 10^{-12}$ s

$$v = \frac{\mu_1 E}{1 + \frac{N_2}{N_1}} \quad \dots\dots\dots 5.30$$

$X = 3/2$ for 3-D

$= 1$ for 2-D

$= 1/2$ for 1-D

Therefore, substituting equations(5.28) and (5.30) into equation(5.29) shows that

$$qE \left\{ \mu_1 E \left[1 + \text{Rexp} \left[\frac{-\Delta}{kT_e} \right] \right]^{-1} \right\} = Xk \frac{(T_e - T)}{\tau_e} \quad \dots\dots\dots 5.31$$

Rearranging this with respect to the electron temperature, T_e gives

$$T_e = T + \frac{q\mu_1\tau_e}{Xk} E^2 \left[1 + \text{Rexp} \left[\frac{-\Delta}{kT_e} \right] \right]^{-1} \quad \dots\dots\dots 5.32$$

From equation(5.32) the electron temperature, T_e , can be computed as a function of E for any given lattice temperature, T . Further, from equations(5.27) and (5.28) the diffusion coefficient, D , may be found from

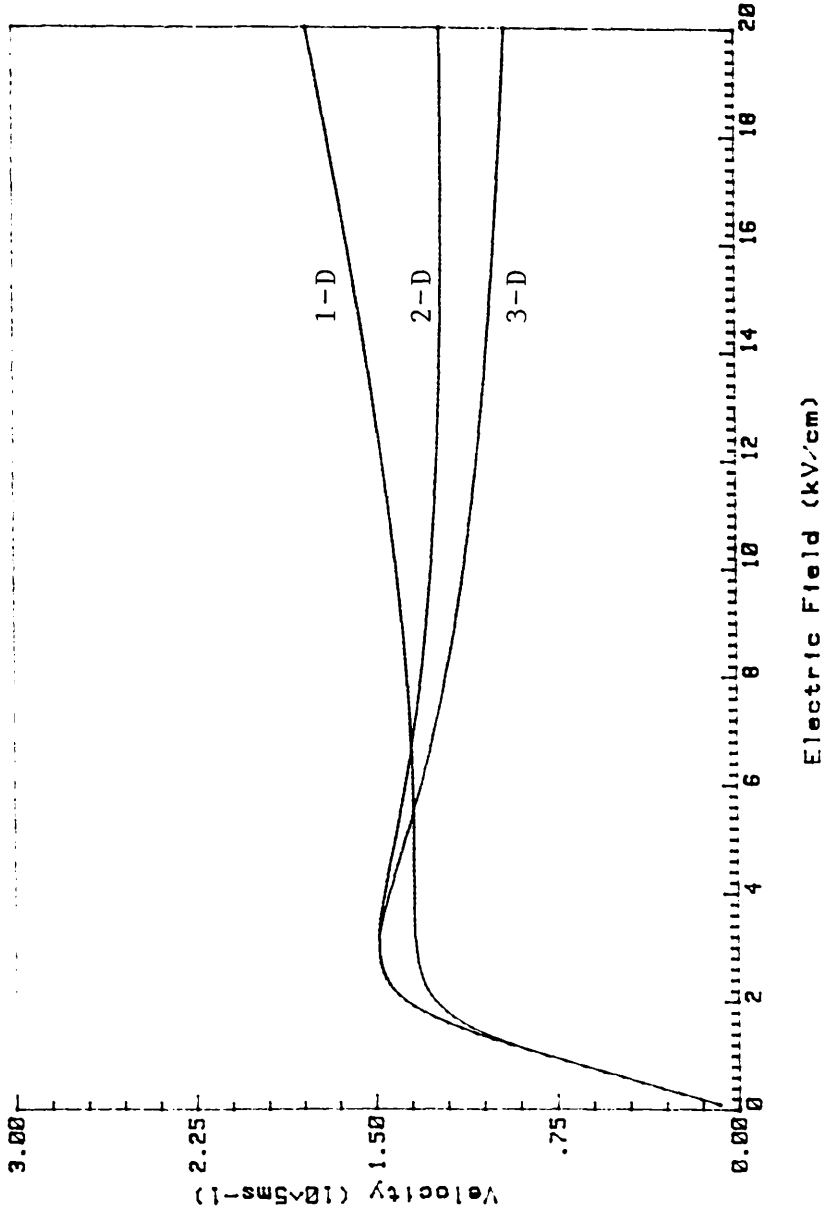
$$D(E) = \frac{kT_e\mu_1}{q} \left[1 + \text{Rexp} \left[\frac{-\Delta}{kT_e} \right] \right]^{-1} \quad \dots\dots\dots 5.33$$

Thus, since T_e may be found as a function of E from equation(5.32), by employing equation(5.33) the diffusion coefficient, D may be found as a function of E and T_e , for any given lattice temperature, T . Further, it can be seen that the electron velocity may be calculated analytically by employing equation(5.32) to find T_e , in conjunction with equations(5.28) and (5.30), for any given E and T .

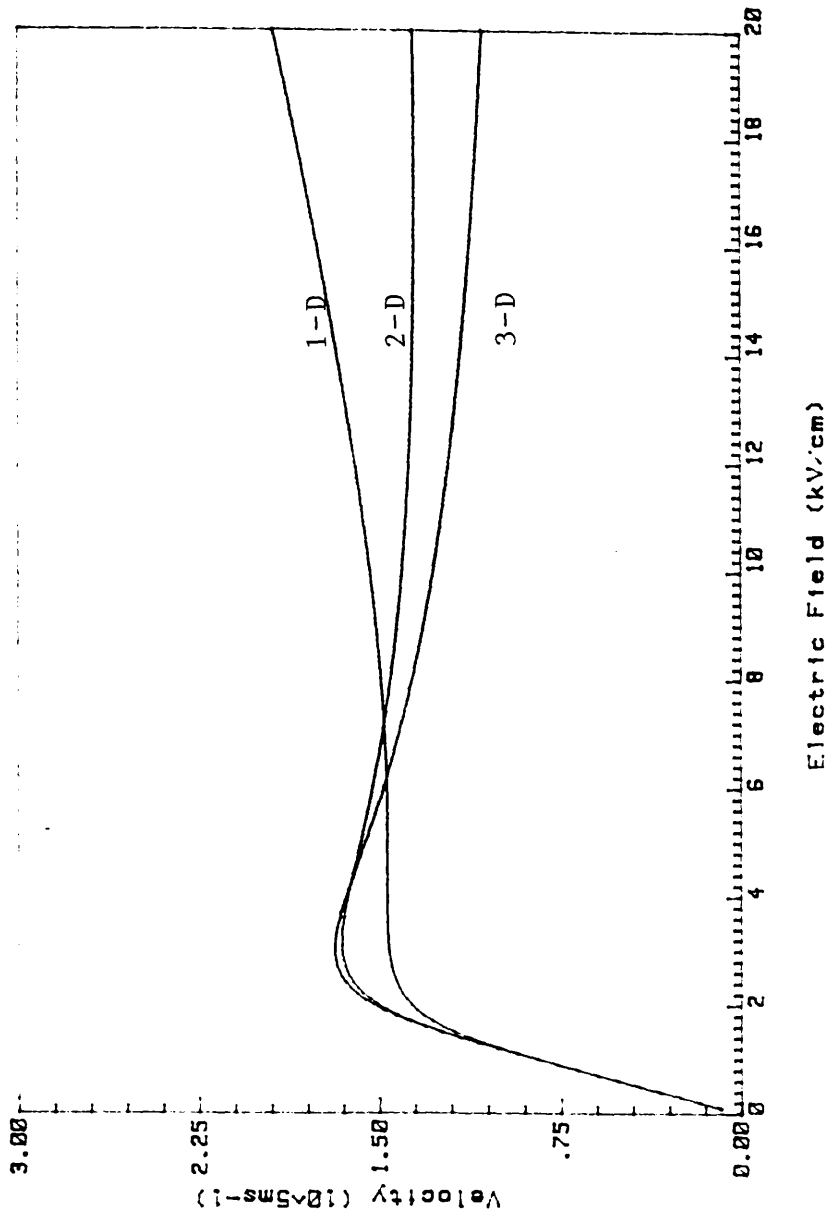
Shown in fig(5.20) are the analytical velocity–field characteristics calculated as described above for: (i) GaAs where [30], $\mu_1 = 0.800 \text{m}^2 \text{V}^{-1} \text{s}^{-1}$, $\Delta = 0.284 \text{eV}$, $M_{r1} = 0.0632$, and $M_{r2} = 0.55$; and (ii) GaAs where [27], $\mu_1 = 0.8500 \text{m}^2 \text{V}^{-1} \text{s}^{-1}$, Δ

Fig(5.20) The Analytical Velocity-Field Characteristics for 1, 2, and 3-D, for T=300K

(a) For Data Set (i)



(b) For Data Set (ii)



$= 0.31\text{eV}$, $Mr_1=0.0670$, and $Mr_2=0.55$. Figs(5.20)(a) and (b) show the characteristic for 1-D, 2-D and 3-D, for $T=300\text{K}$, for data sets (i) and (ii) respectively.

Shown in figs(5.21)(a), (b) and (c) are plots of the velocity-field characteristic for data set (ii) above for: (a) 1-D, (b) 2-D and (c) 3-D, each plot showing the velocity-field characteristic for $T=200\text{K}$, 300K and 400K . As can be seen from these plots the negative differential resistivity observed in GaAs becomes more prominent with decreasing temperature.

Also, shown in fig(5.22)(a) and (b) are the diffusion coefficient, D , versus electric field, E , characteristics for each of data sets (i) and (ii) respectively. Each plot of fig(5.22) shows the characteristic for 1-D, 2-D and 3-D, for a temperature, $T=300\text{K}$.

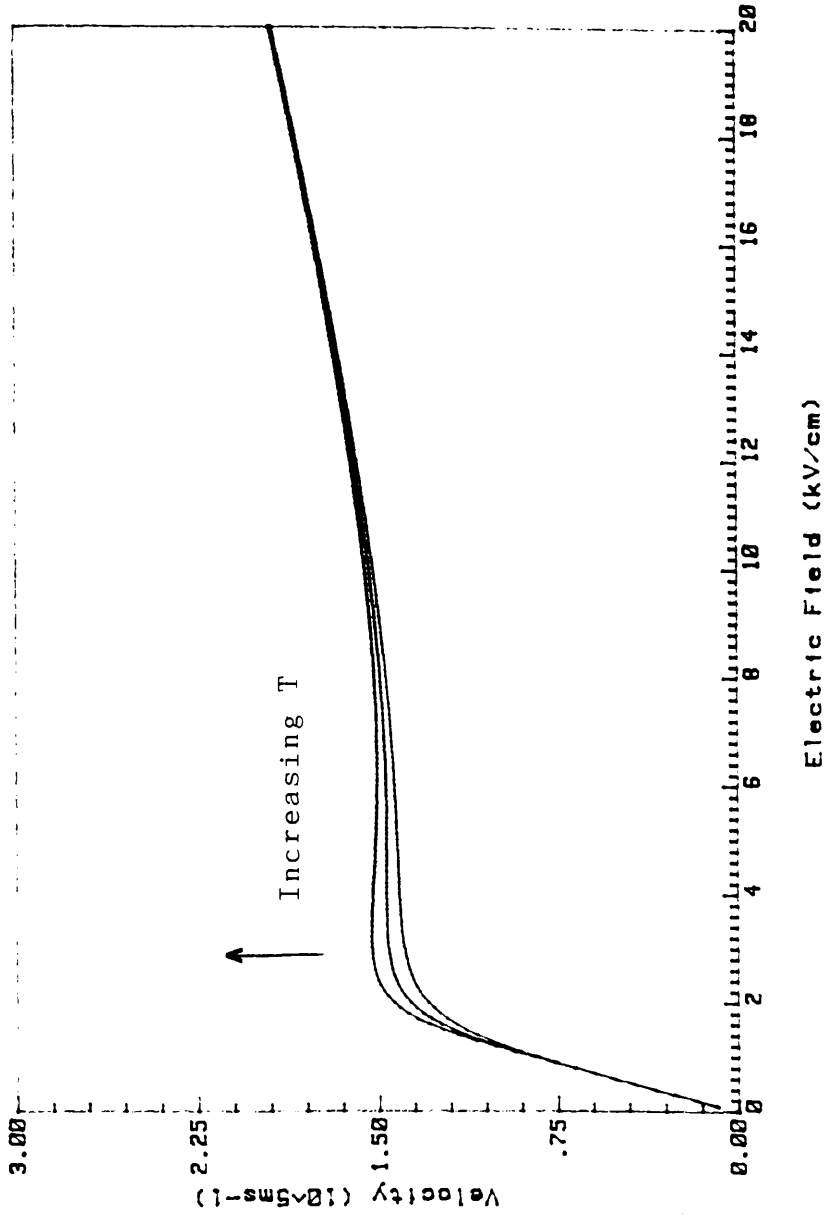
Now, for each of the preferred vertical diode/rib guide structures, the Gunn simulation program was run using the approximate velocity-field characteristic, and a constant diffusion coefficient. The results of these investigations are shown in fig(5.23). For these simulations the distance between adjacent points, $dx = 5.0 \times 10^{-8}\text{m}$, and the time step between consecutive simulations, $dt = 4.0 \times 10^{-15}\text{s}$. Also, the program assumed the active layer to have a notch, ie. domain nucleation centre, $1\mu\text{m}$ long and $0.5\mu\text{m}$ from the cathode, with a doping density of 0.9 of that of the active region.

As can be seen from these results, at low values of electric field the domain height, E_{dom} increases with increasing electric field for each of the rib structures, R1, R2 and R3. Further, at low values of electric field the domain length, L_{dom} increases with increasing electric field. This is because the total field applied across the active region tends to become increasingly dropped only across the domain. Also, all the available charge tends to be confined to the accumulation region within the dipole domain. However, as the electric field increases, both E_{dom} and L_{dom} tend to reach a peak value and then begin to decrease with increasing electric field. This is due to electron diffusion effects occurring within the domain, which can be seen to limit the maximum values of E_{dom} and L_{dom} for any given diode structure.

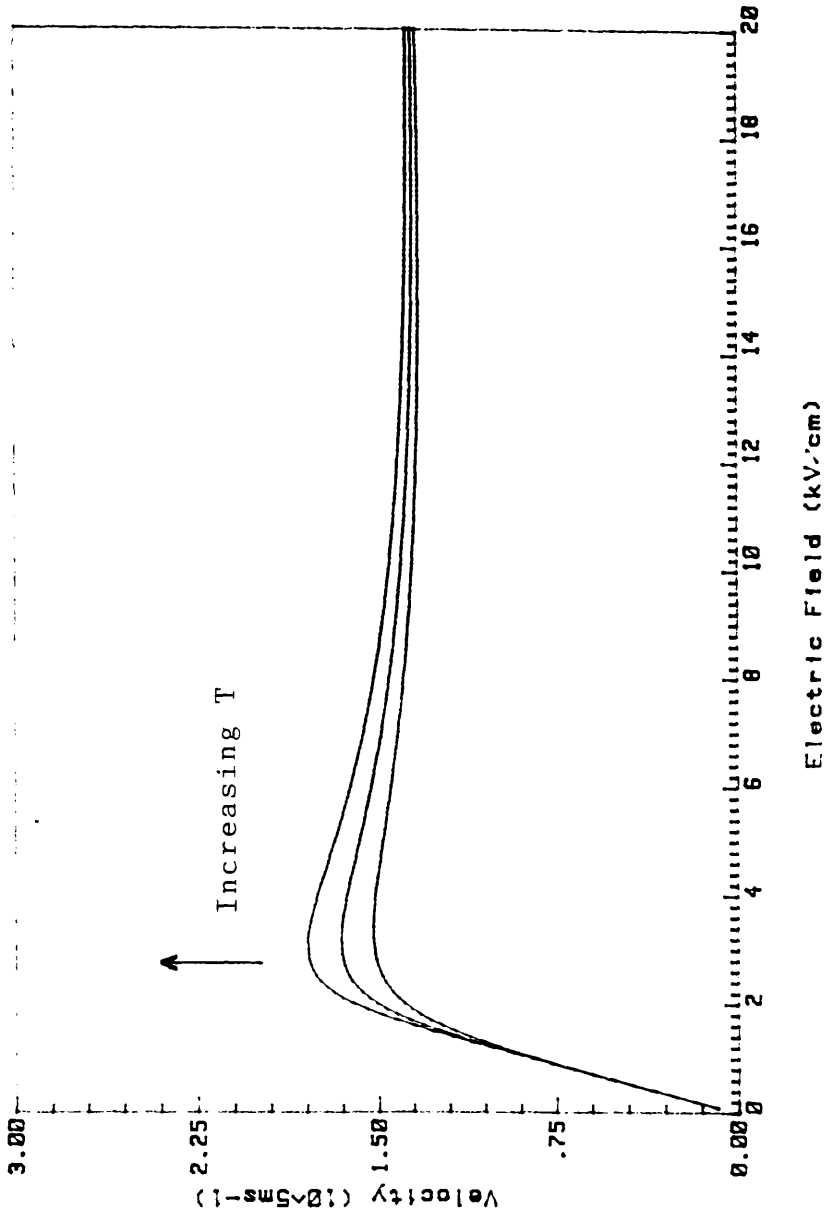
The Gunn simulation program was also run for device R3 alone for the

Fig(5.21) The Analytical Velocity-Field Characteristics for Data Set (ii), for $T = 200, 300, 400K$

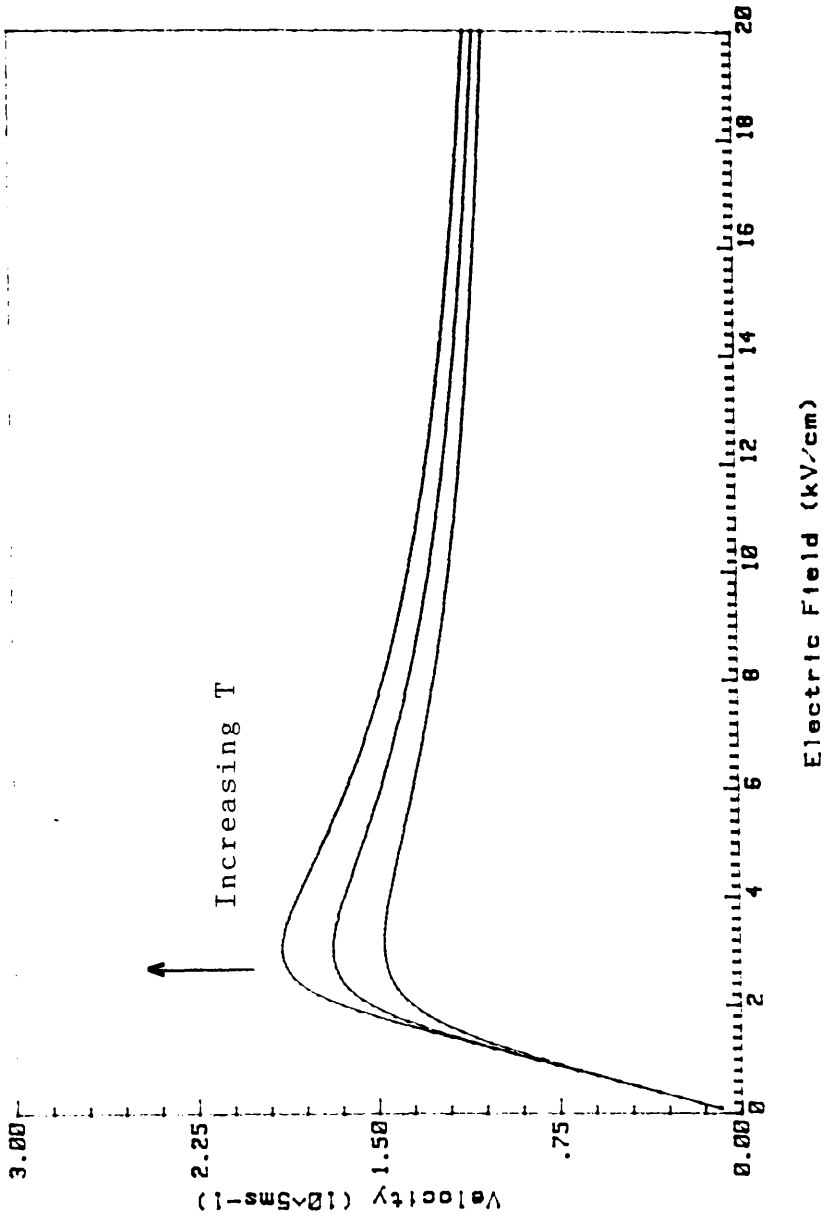
(a) For 1-D



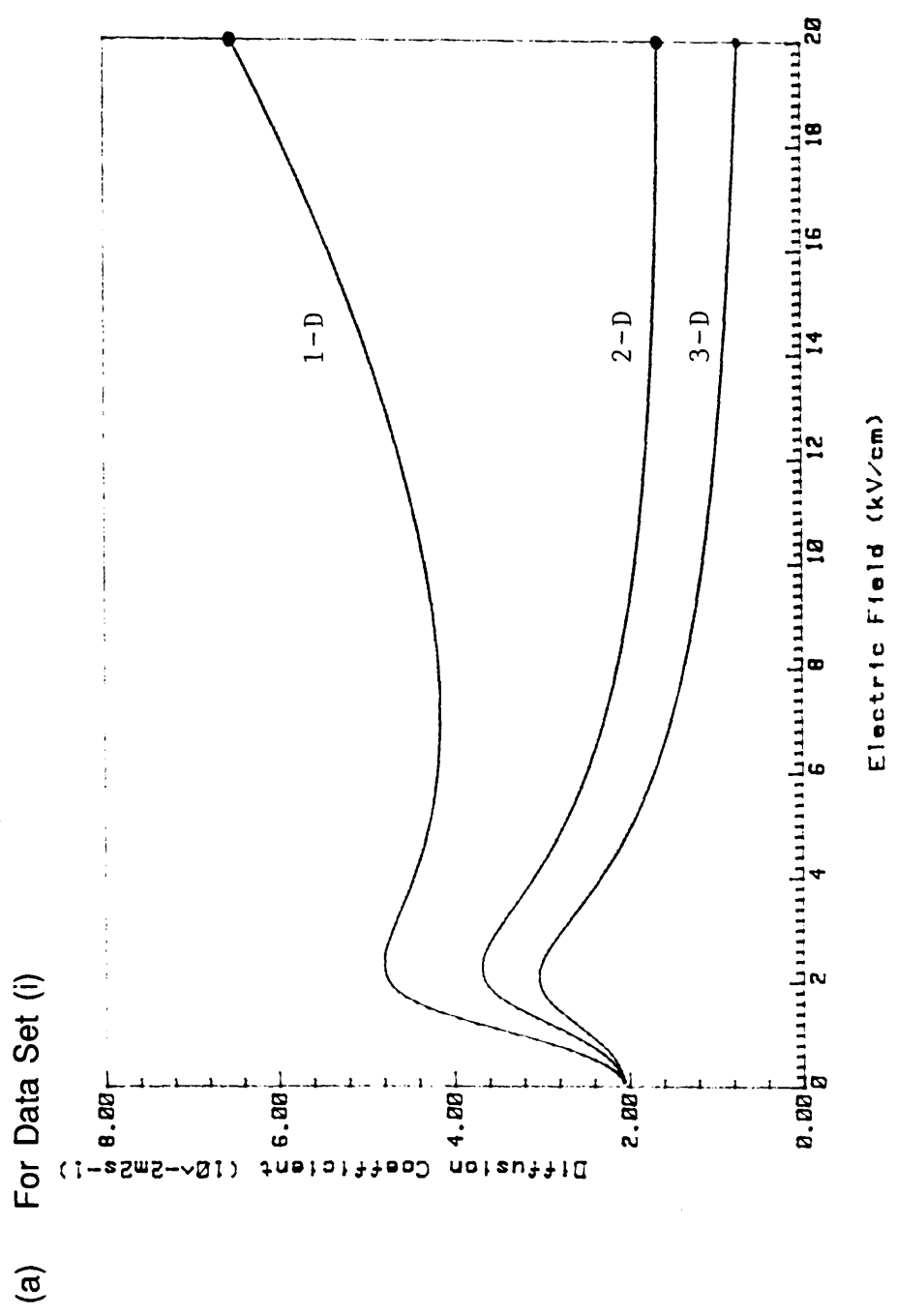
(b) For 2-D



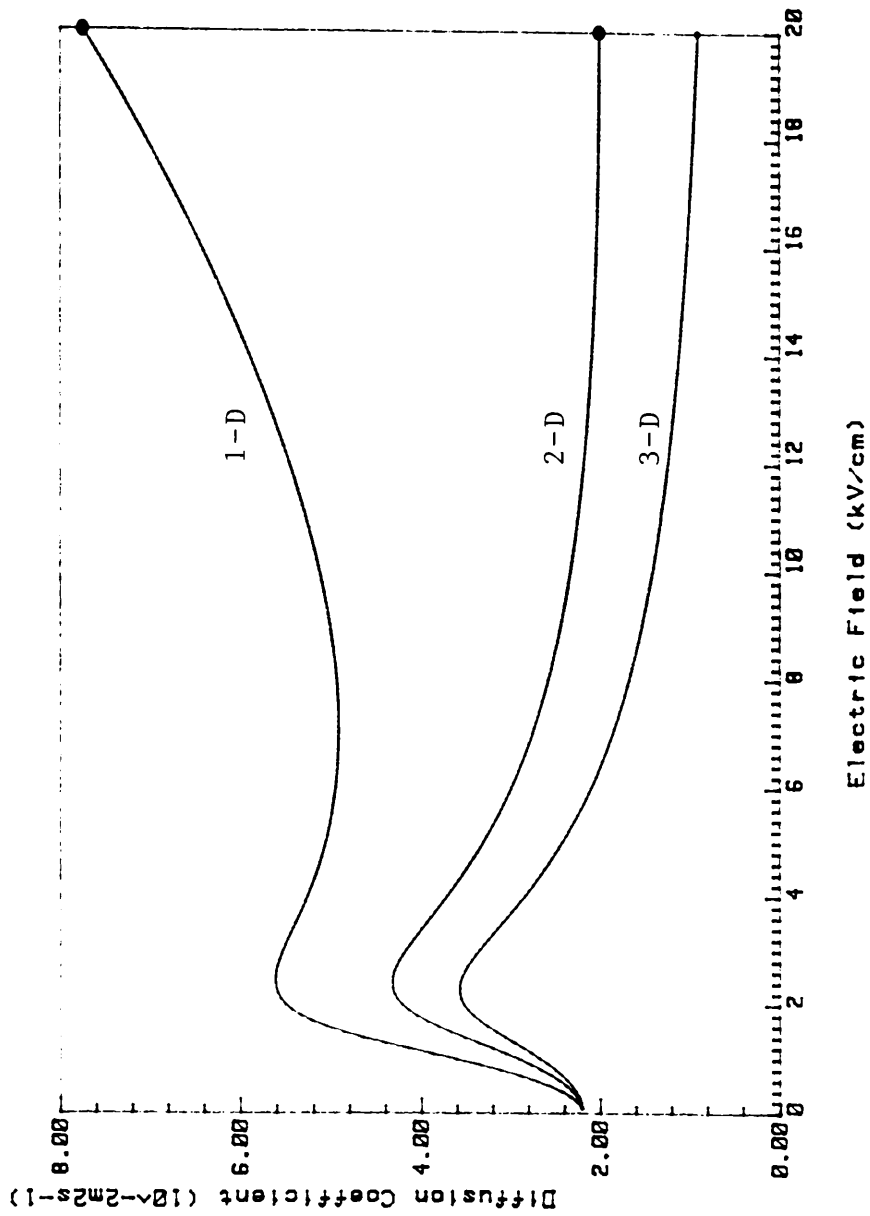
(c) For 3-D



Fig(5.22) The Diffusion Coefficient versus Electric Field Characteristics for 1, 2, 3-D,
for $T = 300K$

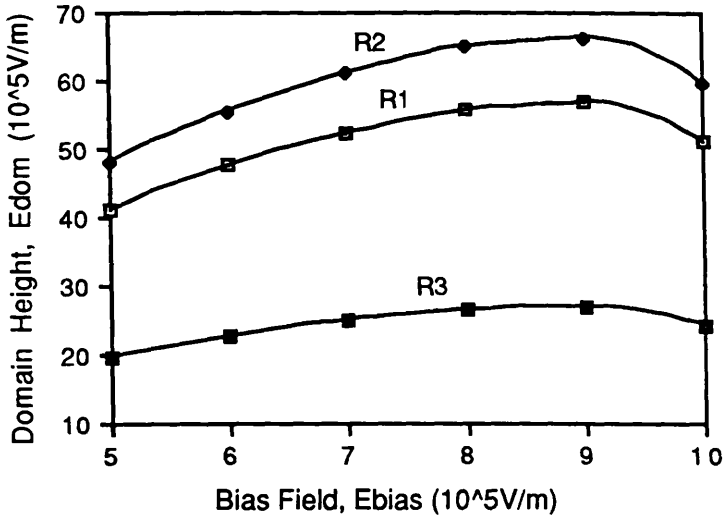


(b) For Data Set (ii)

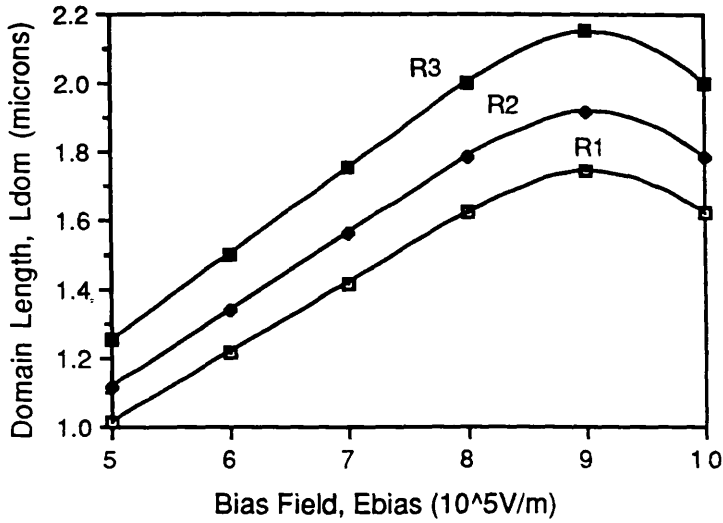


Fig(5.23) Domain Characteristics versus Bias Electric Field for an Approximate $v(E)$ and a Constant D

(a) Domain Height, E_{dom} versus Bias Field, E_{bias}



(b) Domain Length, L_{dom} versus Bias Field, E_{bias}



following situations:

- (a) an approximate $v(E)$ characteristic and constant D ;
- (b) an analytical $v(E)$ characteristic and constant D ; and
- (c) an analytical $v(E)$ characteristic and analytical $D(E)$.

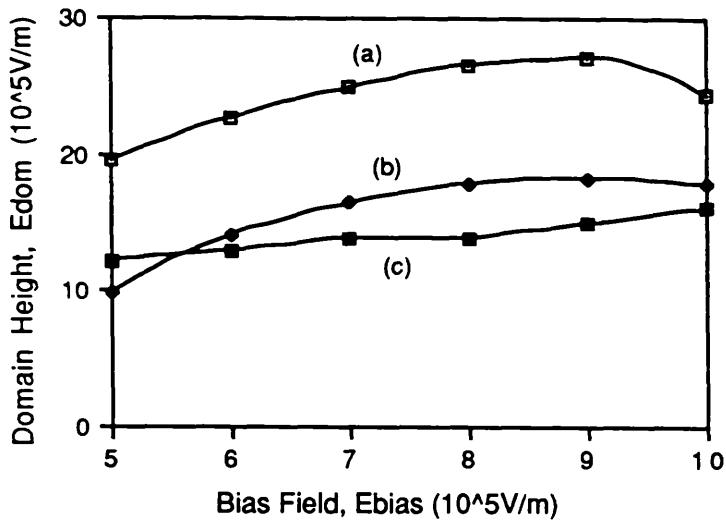
The results of these simulations, using data set (i), are shown in fig(5.24). In the same way as for the simulations of fig(5.23), $dx=5.0 \times 10^{-8}m$, and $dt=4.0 \times 10^{-15}s$, and the doping notch was taken to be $1\mu m$ long, $0.5\mu m$ from the cathode, and 0.9 of the doping density of the active region. The results of fig(5.24) were taken after: (a) 2500 time steps; (b) 1750 time steps; and (c) 1000 time steps, ie. when the domain was approximately half way across the active region. It can therefore be concluded from (a)–(c) above that the domain moves across the device faster in situation (c) than in (b), and also faster in situation (b) than in (a). This result agrees with that mentioned in section(3.2), ie. that the true domain velocity is somewhat larger than the electron velocity outwith the domain, and that the true domain velocity lies somewhat above that determined by the Equal Areas Rule.

From fig(5.24) it can be seen that simulations (a) and (b) predict the same general behaviour for the domain characteristics, and are in agreement with those of fig(5.23). However, situation (c), ie. that of an analytical diffusion coefficient, does not show (at least at such low fields) the same domain behaviour. This is because, whereas in (a) and (b), D is constant and tends to introduce diffusion effects into the domain characteristics at fields around $10.0 \times 10^5 Vm^{-1}$, in (c), D begins to decrease at fields around $2.4 \times 10^5 Vm^{-1}$. Referring to fig(5.22) it may however be seen that, at higher electric fields, the analytical value of D begins to increase again. It may therefore be concluded that at very high electric fields the decrease in E_{dom} and L_{dom} due to diffusion effects will be even more prominent in (c) than in (a) and (b).

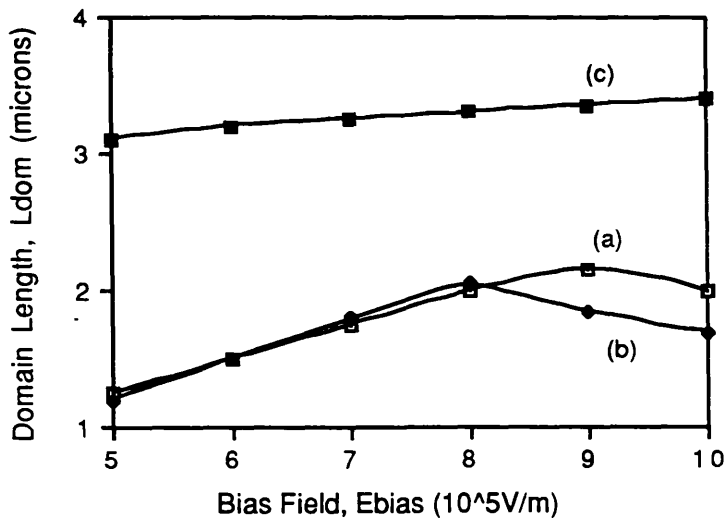
Shown in fig(5.25)(a), (b) and (c) are plots of the propagating Gunn domain of device R3 for situation (c), ie. an analytical $v(E)$ and analytical $D(E)$. The plots were taken after 500, 1000 and 1500 time steps respectively. The bias field was taken to be $E_{bias}=7.0 \times 10^5 Vm^{-1}$, ie. $V_{bias} \approx 3.9V$, for a substrate thickness of

Fig(5.24) Domain Characteristics versus Bias Electric Field for Device R3 for various cases of $v(E)$ and $D(E)$

(a) Domain Height, E_{dom} versus Bias Field, E_{bias}

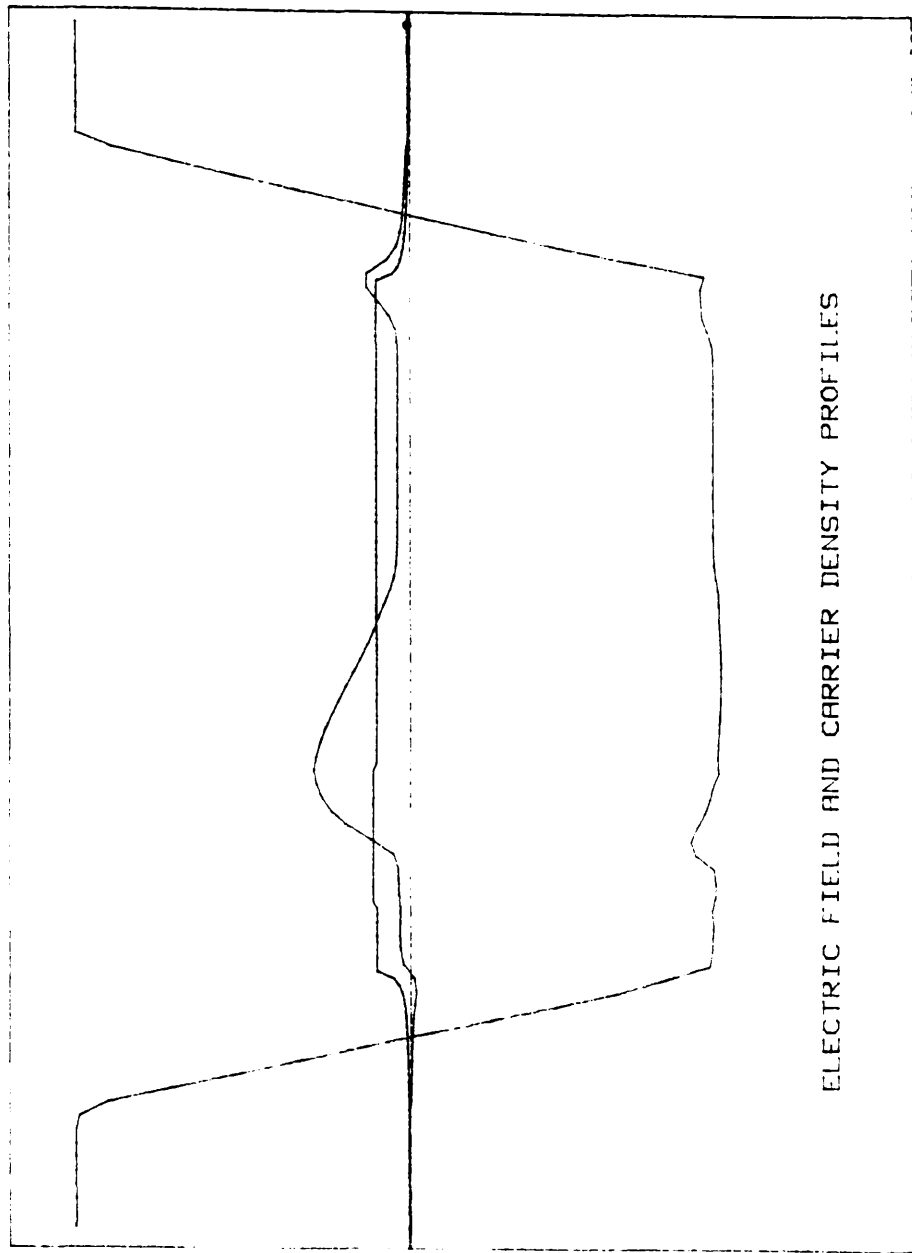


(b) Domain Length, L_{dom} versus Bias Field, E_{bias}

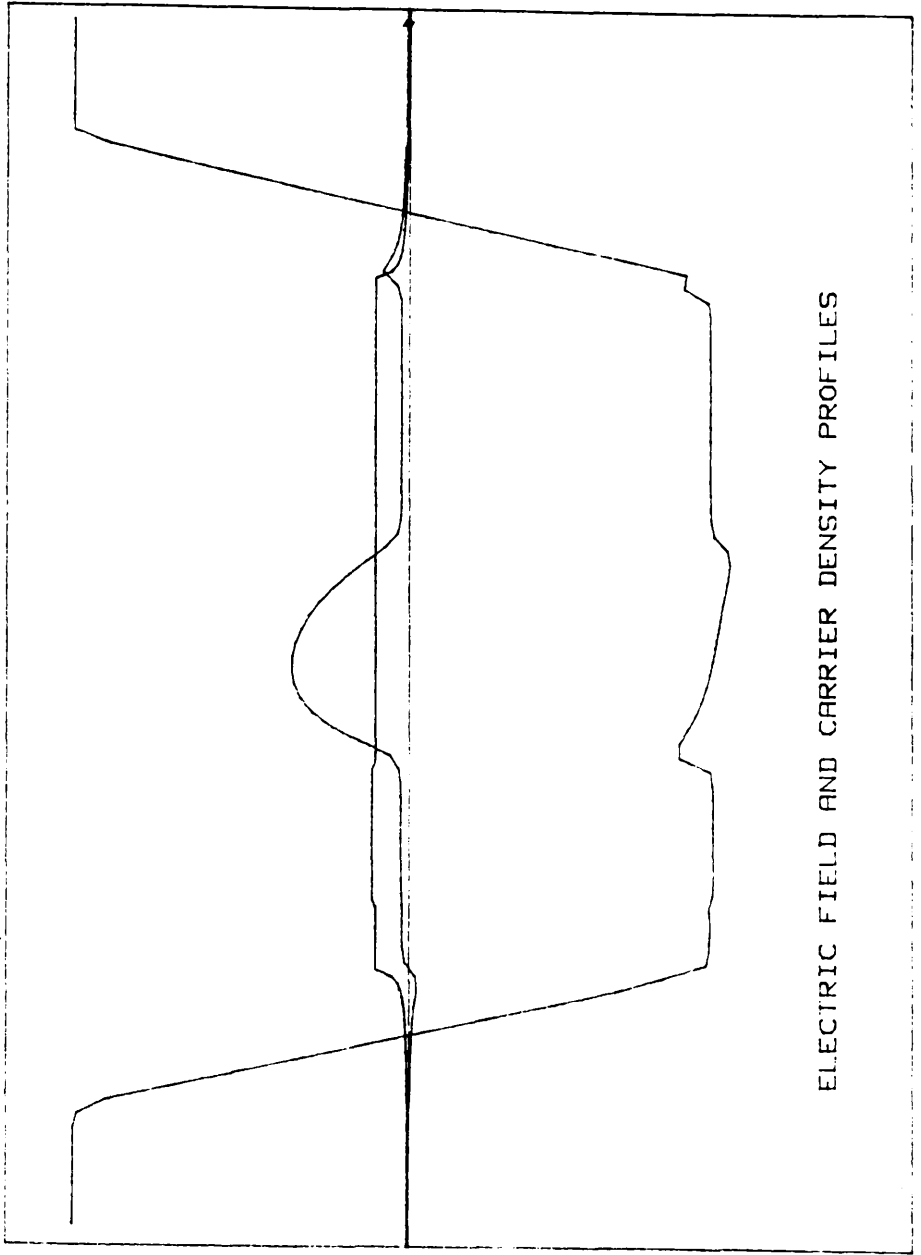


Fig(5.25) The Propagating Gunn Domain in Device R3, for $E_{bias}=7.0 \times 10^5 V/m$

(a) After 500 Simulations

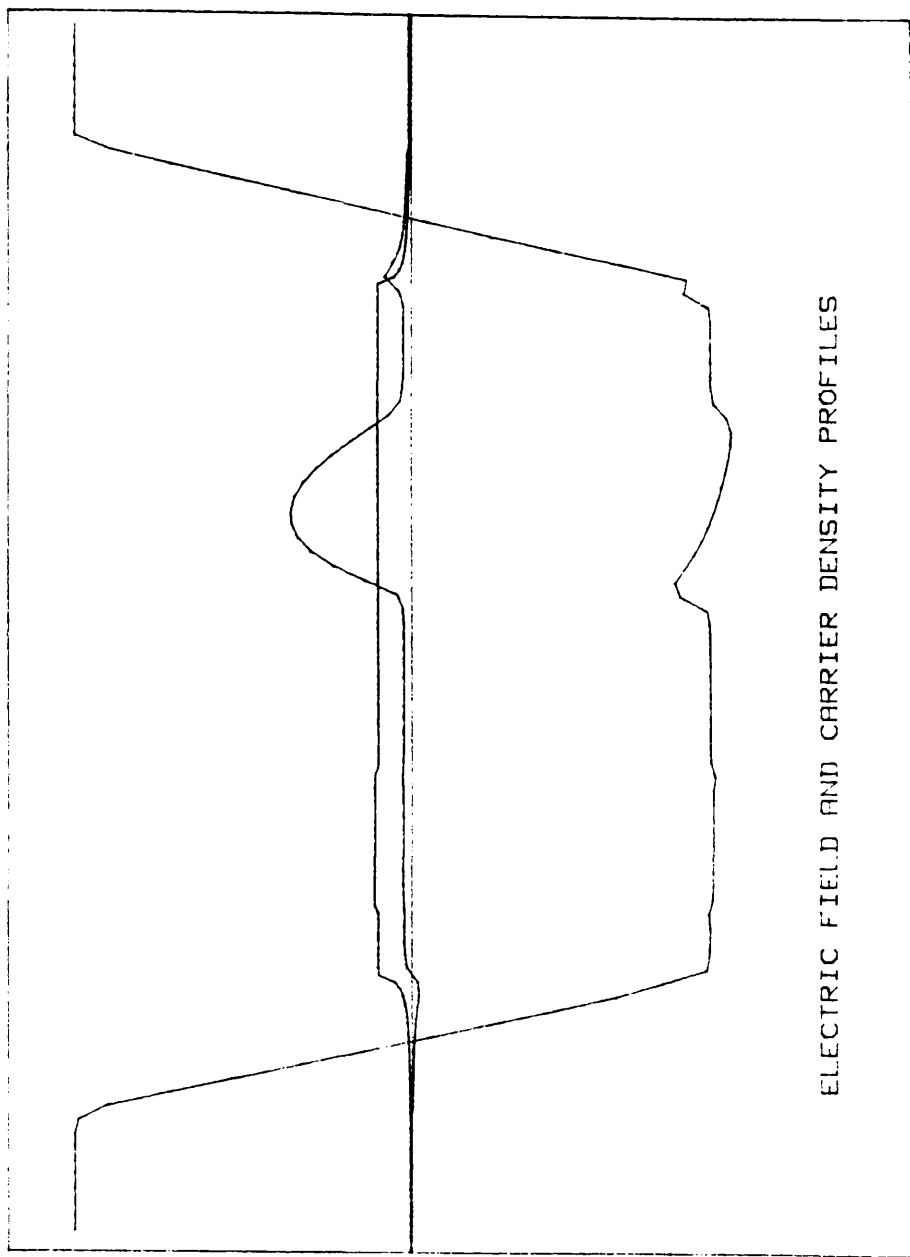


(b) After 1000 Simulations



ELECTRIC FIELD AND CARRIER DENSITY PROFILES

(c) After 1500 Simulations



ELECTRIC FIELD AND CARRIER DENSITY PROFILES

100 μm .

A 50 μm long planar device, having the structure of device P1, was also simulated using the approximate $v(E)$ characteristic and a constant value of D . The results of these simulations are shown in fig(5.26). For these simulations the space interval was $dx=20.0 \times 10^{-8} \text{m}$, the time interval, $dt=16.0 \times 10^{-15} \text{s}$, and the notch was taken to be 5.0 μm long, positioned 2.5 μm from the cathode, having a doping density equal to 0.99 of the doping density of the active region. The results were taken after 5000 simulations.

As can be seen from fig(5.26), E_{dom} and L_{dom} tend to increase as E_{bias} increases. However, unlike the results of fig(5.23), no diffusion effects can be observed, at least up to $E_{\text{bias}}=10.0 \times 10^5 \text{Vm}^{-1}$. Comparing the results of the planar device with those of device R3 (fig(5.23)), it can be seen that for the same bias field, the planar device has associated with it a domain which has a higher peak field, and which is longer, than that of the shorter vertical device. This suggests that the planar diode/photoelastic waveguide device will produce a larger optical perturbation than the vertical structures incorporating either slab or rib waveguides.

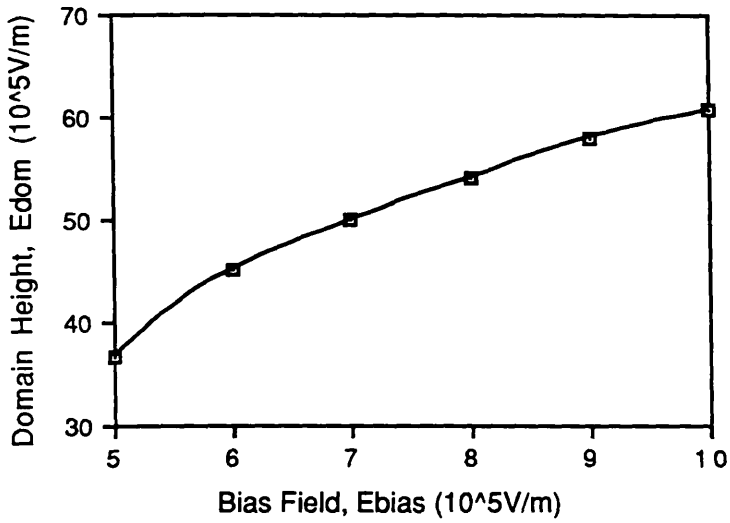
5.4.2 Influence on Optical Guiding by the Gunn Domain

In the previous section results were presented which were produced by the Gunn effect simulation program. These predicted the shape, height, and length of the propagating dipole Gunn domain present within the active layer of a Gunn diode when an electric field, greater than that of the so-called threshold field, E_T , is applied to the diode. In this section, the results presented in section(5.4.1) are used to predict the magnitude of each of the four possible perturbation mechanisms outlined in section(4.2).

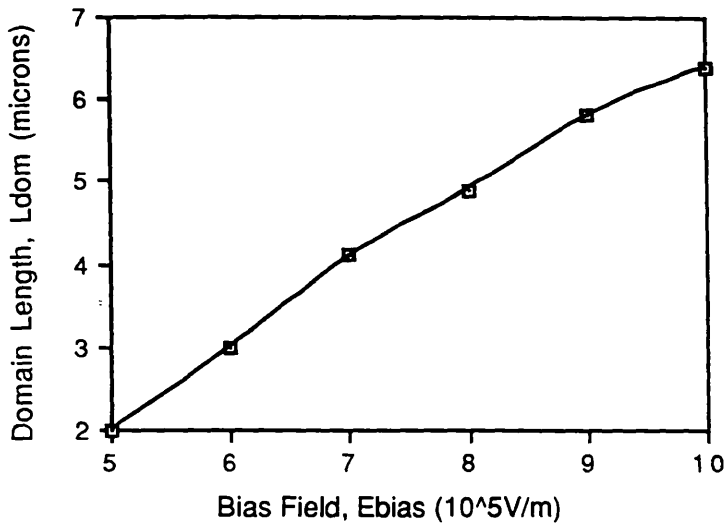
First consider the domain characteristics for each of the vertical structures, for an approximate $v(E)$ and a constant D . This situation corresponds to that of fig(5.23). Shown in table(5.6)(a) are the maximum possible perturbations introduced due to the electric field of the domain, as predicted by fig(5.23), for devices R1,

Fig(5.26) Domain Characteristics versus Bias Electric Field for Device P1, for an Approximate $v(E)$ and a Constant D

(a) Domain Height, E_{dom} versus Bias Field, E_{bias}



(b) Domain Length, L_{dom} versus Bias Field, E_{bias}



Table(5.6) Electric Field Influences on Optical Characteristics by a Propagating Gunn Domain

(a) Approximate Analysis (from Fig(5.23))

Device	E_{bias} (Vcm^{-1})	Δn_{EO} ($\lambda=1.15\mu\text{m}$)	$\Delta\alpha_{\text{EA}}$ ($\lambda=1.15\mu\text{m}$)	Δn_{EO} ($\lambda=905\text{nm}$)	$\Delta\alpha_{\text{EA}}(\text{cm}^{-1})$ ($\lambda=905\text{nm}$)
R1	9000	1.421×10^{-4}	0	1.574×10^{-4}	1475
R2	9000	1.660×10^{-4}	0	1.838×10^{-4}	3975
R3	9000	6.774×10^{-5}	0	7.501×10^{-5}	325

(b) Analysis of Device R3 (from Fig(5.24))

Analysis	E_{bias} (Vcm^{-1})	Δn_{EO} ($\lambda=1.15\mu\text{m}$)	$\Delta\alpha_{\text{EA}}$ ($\lambda=1.15\mu\text{m}$)	Δn_{EO} ($\lambda=905\text{nm}$)	$\Delta\alpha_{\text{EA}}(\text{cm}^{-1})$ ($\lambda=905\text{nm}$)
a	9000	6.774×10^{-5}	0	7.501×10^{-5}	325
b	9000	4.580×10^{-5}	0	5.072×10^{-5}	135
c	9000	4.021×10^{-5}	0	4.453×10^{-5}	105

(c) Approximate Analysis of Device P1 (from Fig(5.26))

Device	E_{bias} (Vcm^{-1})	Δn_{EO} ($\lambda=1.15\mu\text{m}$)	$\Delta\alpha_{\text{EA}}$ ($\lambda=1.15\mu\text{m}$)	Δn_{EO} ($\lambda=905\text{nm}$)	$\Delta\alpha_{\text{EA}}(\text{cm}^{-1})$ ($\lambda=905\text{nm}$)
P1	10000	1.520×10^{-4}	0	1.683×10^{-4}	3775

R2, and R3, where, Δn_{EO} = the change in the refractive index of the material due to the Linear Electro–Optic effect (table(4.1)), and $\Delta\alpha_{EA}$ = the change in the optical absorption coefficient due to the Electro–Absorption effect (equation(4.11)) [9]. As can be seen from table(5.6)(a), Δn_{EO} tends to increase with decreasing wavelength, and $\Delta\alpha_{EA}$ is negligible at wavelengths not close to the band edge. It can also be seen that both Δn_{EO} , and $\Delta\alpha_{EA}$, tend to decrease with decreasing active layer doping density, and with increasing active layer length, for a given value of electric field.

Table(5.6)(b) presents the results for device R3 for the three analysis situations presented in fig(5.24), ie. (a) an approximate $v(E)$, and constant D ; (b) an analytical $v(E)$, and constant D ; and (c) an analytical $v(E)$, and analytical $D(E)$. Again, it can be seen from table(5.6)(b) that Δn_{EO} increases with decreasing wavelength, while Δn_{EA} is negligible at wavelengths above the band edge. Table(5.6)(c) presents an estimate of the maximum electric field induced optical perturbations for the planar device P1.

Shown in table(5.7)(a) are the maximum possible perturbations introduced into devices R1, R2 and R3 due to the free carrier variation throughout the extent of the domain, where, Δn_{FC} = the change in the refractive index of the material due to the Free Carrier Plasma effect associated with the domain (equation(4.21)), and $\Delta\alpha_{FC}$ = the change in the optical absorption coefficient due to the variation in the carrier density profile across the domain (equation(4.19)). These results were again obtained from the simulation results of fig(5.23). As can be seen from table(5.7)(a), Δn_{FC} tends to decrease with decreasing wavelength, and $\Delta\alpha_{FC}$ (as for $\Delta\alpha_{EA}$) is negligible at wavelengths not close to the band edge.

Table(5.7)(b) provides a comparison of the maximum electric field induced and free carrier induced optical perturbations for the wavelengths of interest, the data being taken from tables(5.6)(a) and (5.7)(a) respectively. Note that both $\Delta\alpha_{EA}$ and $\Delta\alpha_{FC}$ are negligible at a wavelength of $1.15\mu\text{m}$. It can be seen that the ratio of Δn_{EO} to Δn_{FC} increases with decreasing wavelength, and also increases with increasing active layer doping density, and active layer length. Further, for a

Table(5.7) Free Carrier Influences on Optical Characteristics by a Propagating Gunn Domain

(a) Approximate Analysis (from Fig(5.23))

Device	E_{bias} (Vcm^{-1})	Δn_{FC} ($\lambda=1.15\mu m$)	$\Delta \alpha_{FC}$ ($\lambda=1.15\mu m$)	Δn_{FC} ($\lambda=905nm$)	$\Delta \alpha_{FC}(cm^{-1})$ ($\lambda=905nm$)
R1	9000	2.547×10^{-6}	0	1.524×10^{-6}	1.395
R2	9000	6.240×10^{-6}	0	3.734×10^{-6}	3.758
R3	9000	5.349×10^{-6}	0	3.200×10^{-6}	0.307

(b) Comparison of Electric Field and Free Carrier Influences

Device	E_{bias} (Vcm^{-1})	$\frac{\Delta n_{EO}}{\Delta n_{FC}}$	$\frac{\Delta \alpha_{EA}}{\Delta \alpha_{FC}}$	$\frac{\Delta n_{EO}}{\Delta n_{FC}}$	$\frac{\Delta \alpha_{EA}(cm^{-1})}{\Delta \alpha_{FC}(cm^{-1})}$
		($\lambda=1.15\mu m$)	($\lambda=1.15\mu m$)	($\lambda=905nm$)	($\lambda=905nm$)
R1	9000	55.79	—	103.28	1057.57
R2	9000	26.60	—	49.23	1057.60
R3	9000	12.66	—	23.44	1057.60

wavelength of 905nm, it can be seen that the ratio $\Delta\alpha_{EO}/\Delta\alpha_{FC}$ is approximately the same for each of the devices of interest.

The cyclic propagation of the Gunn domain through the rib optical waveguide was simulated by approximating the dipole domain to a slab of height, E_{dom} , and length, L_{dom} , moving through the rib in a vertical direction from cathode to anode. The .NWAVE program was run, inserting the slab into the device at various distances from the cathode. This simulation was undertaken for each of the rib structures R1, R2 and R3, the values of E_{dom} and L_{dom} which were used being the maximum values as taken from fig(5.23). The number of basis functions used in the .NWAVE program for these simulations were $f_1=7$ and $f_2=10$.

It was found, as would be expected, that when the domain was close to the cathode the perturbation introduced in the refractive index of the material, Δn_{EO} due to the presence of the domain, had no observable effect on the effective index, n_{eff} of the guide. However, as the domain passed across the position in the rib corresponding to the mode centre, an observable perturbation in n_{eff} could be observed. The observed perturbation in n_{eff} for R1, R2 and R3, for a wavelength of $1.15\mu m$, is shown in table(5.8). As can be seen from this, the perturbation Δn_{eff} is small, ie. of the order of 1.0×10^{-5} . However, in the case of device R2, Δn_{eff} can be seen to be sufficient to reduce the effective index of the guide to below the refractive index of the substrate, and therefore to cut-off the mode of the guide. The substrate refractive index, $n_s=3.464861$, and the perturbed value of $n_{eff}=3.464853$ in this case.

Note that in the above calculations it is assumed that the perturbation in the refractive index, due to the domain, is positive in value. This corresponds to the rib guides being aligned along the $[011]$ direction, and the domain introducing a waveguiding effect. If the perturbation had however been taken to be negative, ie. if the guides were aligned along the $[0\bar{1}1]$ direction, then an antiwaveguiding effect would have been introduced.

If a more precise estimate of the influence on the propagation constant, β , introduced by the presence of the propagating domain, is required, then the

Table(5.8) Perturbation in the Effective Index, Δn_{eff} due to a Domain at the Mode Centre, for $\lambda=1.15\mu\text{m}$

Device	n_{eff}	n_{eff} with Domain	Δn_{eff}
R1	3.464961	3.464956	5.0×10^{-6}
R2	3.464867	3.464853	1.4×10^{-5}
R3	3.464916	3.464898	1.8×10^{-5}

Hellmann–Feynmann Perturbation Theorem [63] could be used in conjunction with the electric field profile associated with the propagating mode as calculated by either the .NWAVE program, or the Finite Difference technique. This theorem was not, however, employed since it was not within the main aims of the project.

5.4.3 Comparison of Modulator Designs

The integrated devices of fig(1.3) have advantages over previously proposed optical modulators based on the Gunn effect [47],[7],[8] in that they: (a) provide means for optical confinement within the device; (b) require a lower electrical drive power; and (c) offer a higher frequency of optical modulation. Advantages (b) and (c) are due to the reduced active layer length of the integrated device in comparison to that of the previous bulk modulators. A quantitative comparison between the bulk modulators and the waveguide modulator structures may be obtained by comparing the average external electrical power, P_e , required to operate the modulator.

$$P_e = \frac{V^2}{R} \quad \dots\dots\dots 5.34$$

where, $V = E_{bias} \cdot f$

$$R = \frac{l}{Nq\mu} \frac{f}{A}$$

$$A = wl$$

w = modulator width = rib width

f = modulator thickness = active layer length

l = modulator length = rib length

Hence, the external drive power is given by

$$P_e = E_{bias}^2 f w l N q \mu \quad \dots\dots\dots 5.35$$

The important point to note from equation(5.35) is that the modulating power required is proportional to the active volume, $w \times f \times l$. Thus, if a comparison is made between the previously proposed bulk modulators, and the planar waveguide device of fig(1.3)(a), then it is obvious that significantly less power will be required by the planar waveguide device. Further, still greater power reduction will be obtained by employing the rib waveguide modulator of fig(1.3)(b).

5.4.4 Influence on Threshold Field of Stress due to the Photoelastic Effect

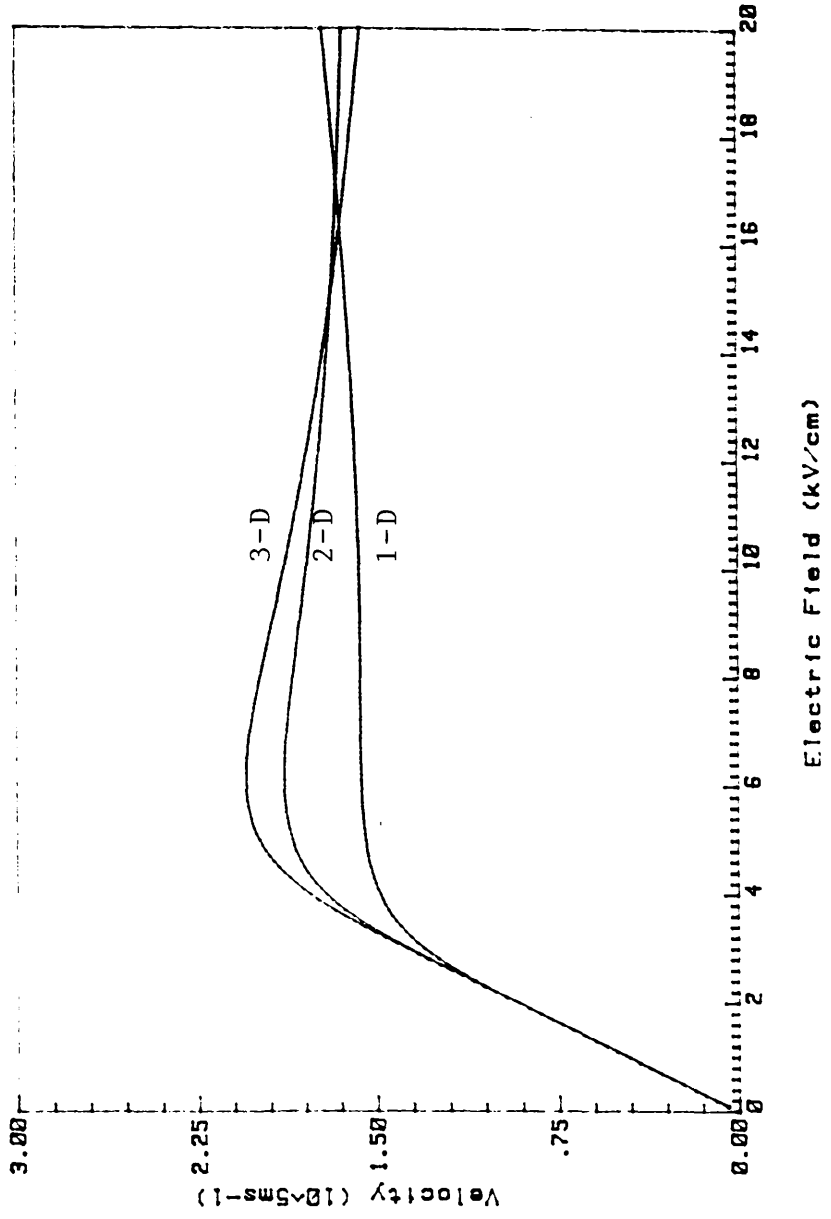
In the planar device incorporating a photoelastic waveguide, proposed in fig(1.3)(c), a stress field will exist within the epilayer below the metal stripe. The pressure experiments of Hutson *et al* [28] showed a definite decrease in the threshold voltage, V_T , and therefore the threshold field, E_T , for Gunn operation below an applied hydrostatic pressure of 15kbar= $15.0 \times 10^8 \text{Nm}^{-2}$. Further, the experiments of Westbrook *et al* [17] measured the stresses present within photoelastic waveguides to be of the order of $6.0 \times 10^8 \text{Nm}^{-2}$. Therefore it may be reasonable to expect that the presence of the photoelastic waveguide will reduce the Gunn threshold field, E_T , of the epilayer, and therefore result in a lower than expected operating voltage of the proposed planar device.

5.5 DEVICES DESIGNED IN OTHER MATERIALS

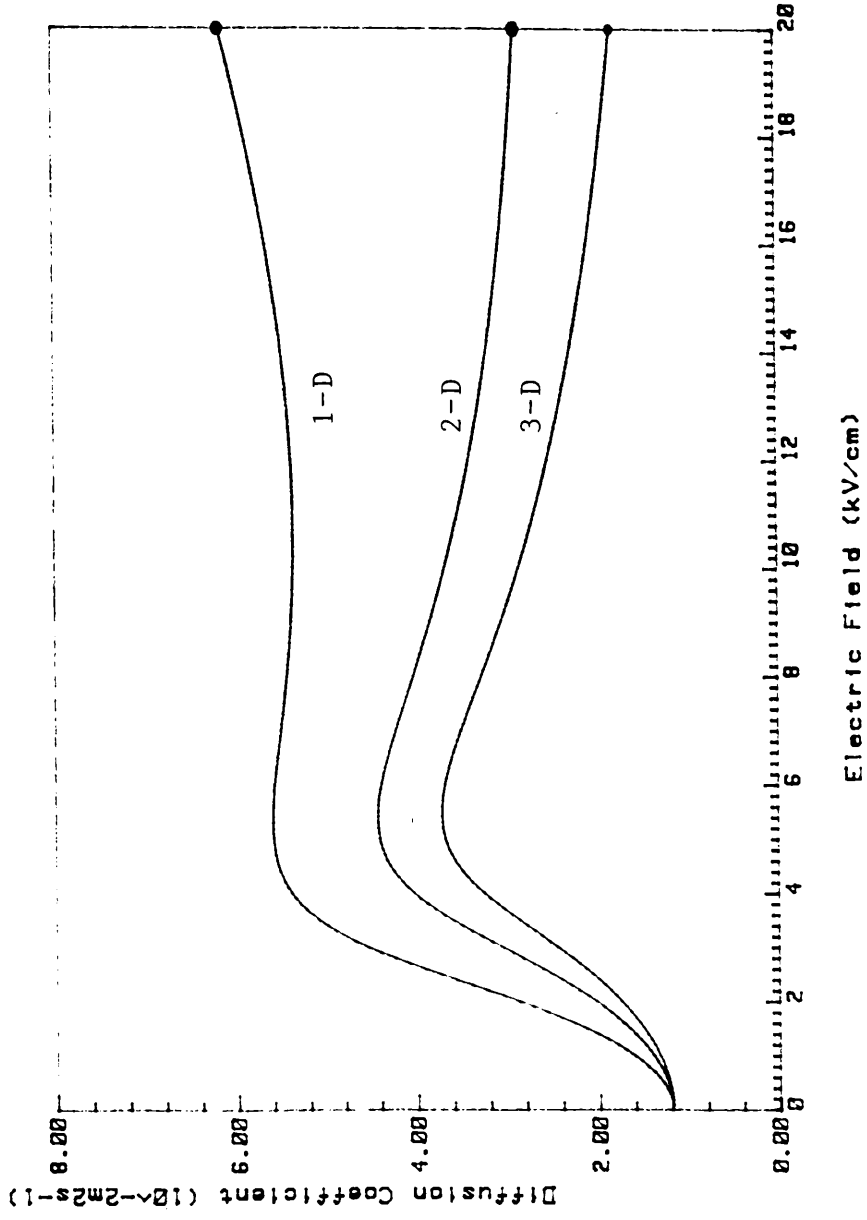
It may be envisaged that either the vertical/rib device, or the planar/photoelastic device, could be designed and fabricated in a material other than GaAs, eg. InP. The analytical $v(E)$ characteristic calculated for InP, using the same analysis as was outlined for GaAs in section(5.4.1), is shown in fig(5.27)(a). This plot shows the $v(E)$ characteristic of InP for 1-D, 2-D and 3-D, for a lattice temperature $T=300\text{K}$. The data used in the calculation of this characteristic was as follows [27]: $\mu_1=0.4600\text{m}^2\text{V}^{-1}\text{s}^{-1}$; $\Delta=0.54$; $M_{r1}=0.077$; $M_{r2}=0.55$; $M_{v1}=1$;

Fig(5.27) The Analytical Variation with Electric Field of InP, for T=300K

(a) Velocity-Field Characteristic



(b) Diffusion Coefficient - Field Characteristic



$Mv_2 = 4$.

As can be seen from fig(5.27)(a), InP offers the advantage of a higher peak electron velocity than GaAs, but has the disadvantage of a higher threshold electric field. The higher threshold field in InP suggests a correspondingly higher operating voltage in order for domains to form and propagate.

Shown in fig(5.27)(b) is the corresponding $D(E)$ characteristic for InP, when $T=300K$. As can be seen the field dependent diffusion coefficient, $D(E)$ of InP behaves in a similar manner to that of GaAs, but again, as for $v(E)$, peaks at a higher field than the GaAs characteristic. For the device structures under discussion, InP may therefore offer the advantage of an increased frequency of operation, but only at the expense of an increase in the required voltage of operation.

It may alternatively be envisaged that the devices fabricated in GaAs may additionally include tertiary or quaternary compound layers, eg. AlGaAs, to aid in optical confinement. This is what is most commonly done at present in forming rib waveguiding structures, since the heterojunction between GaAs and AlGaAs offers a greater difference in refractive index between the adjacent layers than does the homojunction formed between two differently doped GaAs layers. To date, however, no work has been done on the electrical performance of AlGaAs in relation to the Gunn effect. It should be noted that since AlGaAs has a smaller intervalley spacing, Δ , than GaAs, AlGaAs should therefore also have a correspondingly lower threshold electric field, E_T .

CHAPTER 6

DEVICES, THEIR FABRICATION AND CHARACTERISATION

6.1 PROCEDURAL ASPECTS

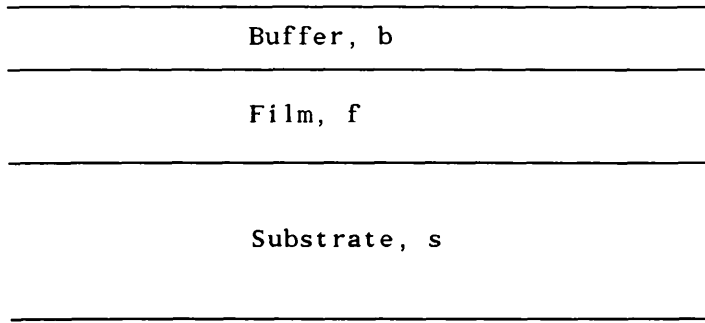
6.1.1 Material Growth

The material required for the fabrication of the proposed devices was initially supplied by the SERC III–V Semiconductor Facility in the University of Sheffield (US), and latterly by the University of Glasgow (UG) MBE (Molecular Beam Epitaxy) facility. The material designs which were required are shown in table(6.1).

Sample CPM268 was grown by VPE (Vapour Phase Epitaxy). This was because Sheffield's MBE and MOCVD (Metal Organic Chemical Vapour Deposition) [64] facilities were at the time unable to grow single layers over approximately $4\mu\text{m}$ to $5\mu\text{m}$ in thickness. Both LPE (Liquid Phase Epitaxy) and VPE [65] were attempted in growing this sample. However, it was found by the Sheffield workers that LPE was unable to produce a uniformly thick sample, and therefore VPE was chosen. The morphology of single GaAs layers grown by VPE was however a problem. The reactor was so large that a sample interlock was necessary to maintain dry conditions. A growth technique was therefore tried in order to improve the morphology. This involved the growth of AlS in the previous run to build up an Al getter in the reactor. This technique was not, however, entirely successful, and it was found that CPM268 still had an unacceptably high defect density on some areas of the sample.

Both of the remaining vertical samples, CPM351 and CPM411, were grown at the University of Sheffield by MOCVD, while the planar sample, #A31, was grown at the University of Glasgow by MBE.

Table(6.1) Material Designs Required (Grown on a (100) Crystal Plane)



Device	S41, R1	S42, R2	S43, R3	P12, P14
b (μm)	0.5	0.5	2.0	0.5
N_b (cm^{-3})	1.0×10^{18}	1.0×10^{18}	2.0×10^{17}	2.0×10^{17}
f (μm)	7.0	5.0	5.0	5.0
N_f (cm^{-3})	5.0×10^{16}	5.0×10^{16}	5.0×10^{15}	5.0×10^{15}
s (μm)	425	425	425	425
N_s (μm)	1.0×10^{18}	1.0×10^{18}	1.0×10^{18}	SI
Sample No.	CPM268	CPM351	CPM411	#A31
Source	US	US	US	UC

6.1.2 Material Characterisation

Each piece of material which was received underwent various tests in order to characterise its properties, and also to ascertain the likelihood that the material would be suitable for use in fabricating the proposed devices.

A piece of the sample would initially be cleaved to a suitable size (around 4mm x 4.5mm). The first test that this sample would undergo was a photoluminescence (PL) measurement. This is a non-destructive test which measures the spectral characteristic, and hence the bandgap, of the material. PL therefore allows one to identify whether the material is GaAs, and whether Al is present, or if carbon acceptors are present in quantity. The results of the photoluminescence measurements are shown in table(6.2). It was found that the spectral characteristics of CPM268 and CPM351 strongly showed the presence of carbon acceptors, while those of CPM411 and #A31 showed that carbon acceptors were present, but in less abundance. The measurements were taken at a reduced temperature of approximately 15K using a germanium photodetector.

The next test which was undertaken, on each of the pieces of material, was to measure the precise doping profile, ie. doping density with depth, using an electro-chemical C-V profiler, ie. a Polaron plotter [66]. The results of these tests are shown in table(6.3). For each of the samples, the magnitude of the doping density was calibrated on the $N=1.0 \times 10^{15} \text{cm}^{-3}$ to $N=1.0 \times 10^{18} \text{cm}^{-3}$ scale of the Polaron plotter by measuring the C-V curve, for any given depth within the sample, and matching this curve to a set of standard C-V curves for GaAs, supplied by Polaron Equipment Ltd.

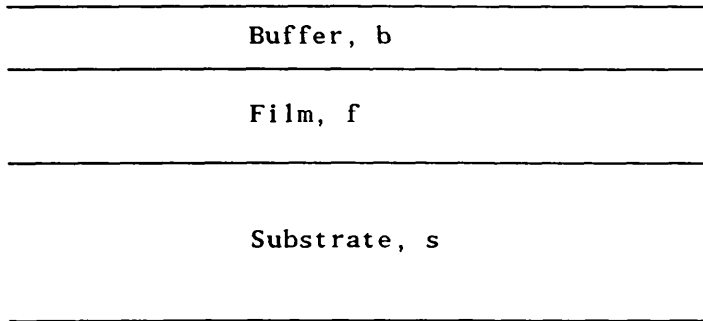
As can be seen from table(6.3), for each of the material designs, the actual material structure varied somewhat from that which was specified. However, the $N_f L$ product for the vertical structures, and the $N_f L$ product for the planar structures, was greater than 10^{12}cm^{-2} . Consequently each piece of material which was supplied was still suitable for the fabrication of a super-critical Gunn diode.

A Polaron plot was received from the University of Sheffield for sample

Table(6.2) Results of Photoluminescence Measurements

Sample	Emission Wavelength, λ (nm)	Bandgap, E_g (eV)
CPM268	819.1	1.5092
CPM351	820.3	1.5136
CPM411	819.7	1.5147
#A31	831.7	1.4928

Table(6.3) Material Designs Received (Grown on a (100) Crystal Plane)



Device	S41, R1	S42, R2	S43, R3	P12, P14
b (μm)	0.52	0.40	1.5	0.4
N_b (cm^{-3})	2.8×10^{18}	2.0×10^{18}	1.0×10^{17}	1.2×10^{17}
f (μm)	7.80	4.36	4.0	7.2
N_f (cm^{-3})	9.0×10^{16}	7.0×10^{16}	7.5×10^{15}	3.0×10^{15}
s (μm)	425	425	425	425
N_s (μm)	9.0×10^{17}	1.5×10^{18}	1.2×10^{18}	SI
Sample No.	CPM268	CPM351	CPM411	#A31

CPM411. This plot did not however tally with that found by the University of Glasgow Polaron plotter. The Sheffield plot suggested that $b=1.6\mu\text{m}$, $N_b=2.9\times 10^{17}\text{cm}^{-3}$, and $N_s=7.0\times 10^{17}\text{cm}^{-3}$, and that the active layer length $f=3.8\mu\text{m}$, and varied in doping density, almost linearly, between $N_f=2.0\times 10^{16}\text{cm}^{-3}$ and $N_f=3.7\times 10^{15}\text{cm}^{-3}$. If this was the correct structure of CPM411, then it suggested that the material would still be of use in the fabrication of Gunn diodes, since the $N_f f$ product was still above the required threshold level. However, the discrepancy between the Sheffield and Glasgow measurements may suggest a substantial variation in the structure, ie. doping density and layer depth, of the material across any given plane parallel to its surface. This would suggest that various samples of this material might therefore give substantially different experimental results.

A piece of each material was also observed under an optical microscope in order to estimate the number of defects appearing on the material surface per unit area. The results of these observations, estimated using a graticular eye piece, are shown in table(6.4). As can be seen from this table, sample CPM268 had a defect density of the order of 10^2 to 10^4 times that of the other samples. Note however that this was an averaged value over various parts of the surface of the samples, and that some parts were more free from defects, and therefore more useful for device fabrication, than others.

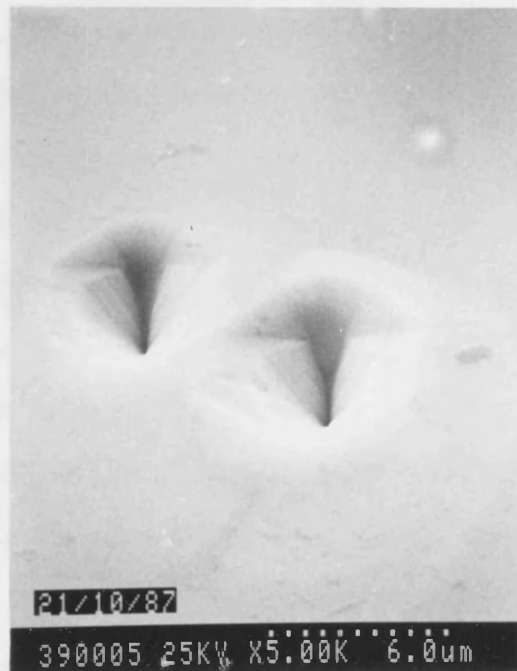
Observing the surface of the material in an SEM showed the existence of three types of defect: (a) 'eye'-shaped defects; (b) 'D'-shaped defects; and (c) elongated oval-shaped defects. The eye-shaped defect had a centre which extended into the surface of the material, therefore rendering some areas of the surface useless. A typical eye-shaped defect is shown in fig(6.1). The D-shaped defect was typically $1\mu\text{m}$ to $2\mu\text{m}$ in length, and extended into the surface of the material to a shallow depth ($\approx 0.1\mu\text{m}$). The elongated oval-shaped defect was raised ($\approx 0.05\mu\text{m}$) from the surface of the material, and had a typical length of around $0.5\mu\text{m}$.

The low field mobility, μ , of electrons within the active layer of the planar sample #A31 was measured by the Van der Pauw method [67]. This method consists

Table(6.4) Measurement of Defect Densities

Sample	Defect Density (cm^{-2})
CPM268	4.09×10^6
CPM351	3.14×10^2
CPM411	6.82×10^4
#A31	1.11×10^2

Fig(6.1) A Typical 'Eye'-Shaped Defect on the Surface of CPM268



of using a 'clover-leaf' sample. The advantages of using the clover-leaf pattern over other methods of mobility measurement are the ease of sample preparation, the relative simplicity with which the relevant voltages can be measured, and the better experimental accuracy. The principal disadvantage lies in the slightly more tedious analysis that is required on the experimental results in order to extract the Hall data, and therefore calculate the mobility.

The Van der Pauw technique applies to planar samples and yields the two-dimensional resistivity of the sample, which may then be converted to the bulk values if the sample thickness is known. For the material structures of interest, this method therefore only applies to the planar device on a semi-insulating substrate. If the same measurements were carried out for the vertical structures, on an N^{++} substrate, then the value of mobility measured would be that of the high conductivity substrate and not that of the active region.

The following procedure was carried out in order to prepare the planar sample for a Van der Pauw measurement. A sample of the material was cleaved to a suitable size ($\approx 7\text{mm} \times 7\text{mm}$) and cleaned as follows:

- ultrasonic in a beaker of soapy water for 5mins;
- rinse in deionised water for 5 mins;
- ultrasonic in a beaker of trichloroethelene for 5mins;
- ultrasonic in a beaker of methanol for 5mins;
- ultrasonic in a beaker of acetone for 5mins;
- rinse in deionised water for 5mins;
- blow dry using a nitrogen gun;
- dry off on a hot plate at 70°C for 5mins.

The cleaning procedure outlined above was that which was used in the preparation of all samples, including the vertical spot Gunn diodes, rib waveguides, and photoelastic waveguides referred to in the succeeding sections of this Chapter.

The preparation of the Van der Pauw sample was continued by etching off the capping layer using an etchant consisting of Ammonia: H_2O_2 : H_2O in the ratio 20:7:500. This etchant gave an etch rate of $0.2\mu\text{mmin}^{-1}$. The sample was then

rinsed in deionised water, blow dried, and dried off on the hotplate.

While still on the hotplate a small clover-leaf metal mask was placed on the sample, and retained on the top surface of the sample with a small quantity of wax. The sample itself was then placed on a microscope slide and retained using wax. The sample was allowed to cool, and any excess wax removed using a scalpel, such that the only wax remaining on the sample surface was that under the metal mask. An air abrasive machine was then used to powder etch the sample, ensuring that the areas of the active layer still exposed were etched away, thus forming the required clover-leaf shaped conducting structure. The sample was then placed on the hotplate and removed from the microscope slide. The metal mask was also removed from the top surface, and the sample cleaned by the same procedure as before.

The sample was then deoxidised using deionised water and ammonia in the ratio 10:1 for 30secs, and a second circular mask aligned with the clover-leaf pattern, such that each of four holes in the circular mask aligned with one leaf of the clover. The second mask was retained on the sample surface using a small piece of double sided sticky tape. The sample was then, as quickly as possible, placed in the vacuum evaporator, which was pumped down to a suitable pressure (approximately 5.0×10^{-6} mbar) before the ohmic contacts were deposited.

An ohmic contact to GaAs may be formed by creating a highly doped semiconductor layer immediately below the contact [68],[69]. The depletion width of the metal-semiconductor barrier is then sufficiently small that electrons can easily tunnel through the barrier. Fabrication of sufficiently good ohmic contacts to GaAs requires careful preparation of the contact surface before evaporation, and rapid deposition of the first metallic layer to the contact surface. The composition of the ohmic contacts for this sample, as well as for the actual devices of interest, is shown in table(6.5).

After deposition was completed, the sample was removed from the evaporator, the mask removed, and the sample cleaned by the same procedure as before. The sample was then annealed in an atmosphere of inert gas, eg. argon (Ar), at a temperature of 325°C for 1min. These annealing conditions have been found to

Table(6.5) Ohmic Contact Composition

Metal	Thickness (nm)	Proportion (%) by Weight
Au	71	88
Ge	40	12
Ni	20	25
Au	>18	—

produce low contact resistance on heavily doped material [70]. The annealing step allows the Au/Ge eutectic to alloy with the GaAs layer thus forming the required high conductivity interface. The Ni layer acts to improve the wetting, and enhances the solubility of the GaAs, but has the disadvantage of itself being a fast diffuser and compensating acceptor.

Using an HL5200 Hall System the standard Van der Pauw method for measuring conductivity was employed, ie. each of the four possible contact permutations was measured, and the resulting voltages used in turn as the inputs to the Van der Pauw equations. From these an average sheet resistivity could be calculated, and, if the thickness was known, the corresponding bulk resistivity, and hence electron mobility, could be obtained.

For a magnetic field of 0.320Tesla, and input current of $100\mu\text{A}$, the 300K value of the low field electron mobility, μ , of the $3.0 \times 10^{15} \text{cm}^{-3}$ N-doped epilayer of sample #A31 was found to be $0.3557 \text{m}^2 \text{V}^{-1} \text{s}^{-1}$. This is lower than the normally accepted value of the low field mobility of GaAs ($\mu \approx 0.800 \text{m}^2 \text{V}^{-1} \text{s}^{-1}$), and may possibly be explained as being due to deep level scattering mechanisms related to the carbon centres observed from the PL measurement [71].

6.1.3 Device Fabrication

Spot contact Gunn diodes, vertical Gunn diode/rib waveguide devices, and planar Gunn diode/photoelastic waveguide devices, have all been fabricated. The precise fabrication and characterisation procedures for each of these devices is outlined fully in sections(6.2), (6.3) and (6.4) respectively. Each of these devices was fabricated by the optical photolithographic technique commonly known as 'lift-off'. The procedural steps of this technique were as follows:

- (a) The sample was cleaned following the procedure already outlined in section(6.1.2).
- (b) In the case of the vertical structures a Au/Ge/Ni/Au ohmic contact was deposited onto the bottom of the sample, but not at this stage annealed.

- (c) Photoresist was then spun onto the top surface of the sample at a spin speed of 2000rpm for 20secs, and baked at 85°C for 30mins. The spin temperature was 25°C, and the humidity between 40% and 50%.
- (d) The sample was then exposed either on the contact printer for 4mins in the case of the spot contact diodes, or on the mask aligner for 6secs in the case of the vertical/rib or planar/photoelastic devices.
- (e) The photoresist was then developed in a mixture of 1:1, H₂O:Microposit Developer for 75secs, rinsed in deionised water, blow dried, and dried off on the hot plate.
- (f) The sample was then deoxidised using a solution of 4:1, H₂O:HCl for 20secs, rinsed quickly in running deionised water, blown dry, and loaded into the evaporator as quickly as possible to avoid regrowth of the oxide layer. The deoxidising solution of 10:1, H₂O:Ammonia could not be used with resist coated samples. A Au/Ge/Ni/Au contact similar to that of table(6.5) was then deposited onto the top surface.
- (g) The metal on top of the photoresist was lifted— off by placing the sample in a beaker of acetone for 2 to 3 hours, thus leaving the required pattern of ohmic contacts.
- (h) The sample was then annealed for 1min, at 325°C, in an atmosphere of inert gas, eg. Ar.

Following the procedure outlined above the required ohmic contacts for the devices of interest were formed.

Two types of photoresist were used. These were Shipley's AZ1350J and AZ1450J positive photoresists for spray or spin coatings between 1.5µm and 2.2µm thick [72],[73]. The advantage of AZ1450J over AZ1350J is that it should give a relatively striation free surface, and therefore better mask/resist contact during exposure.

The resist thickness versus spin speed characteristic for both AZ1350J and AZ1450J were found by spinning the resists onto clean glass slides, for a period of 20secs. The slides were then baked for 30mins at 85°C, subsequently exposed on the

contact printer for 4mins using a pattern of straight lines, and then developed in a mixture of 1:1, H₂O:Microposit Developer for 75secs.

Investigations were also made of the variation in resist thickness with spin speed for Shipley AZ1350. The AZ1350 coated slides were exposed for 3mins using the same pattern, and developed in a mixture of 1:1, H₂O:Microposit Developer for 70secs.

As can be seen from fig(6.2)(a) AZ1350J and AZ1450J give very similar characteristics, while AZ1350 gives a somewhat thinner resist layer for the same spin speed. Further, the variation in the gradient of the resist wall of AZ1450J, with developing time, was investigated. The results are shown in fig(6.2)(b).

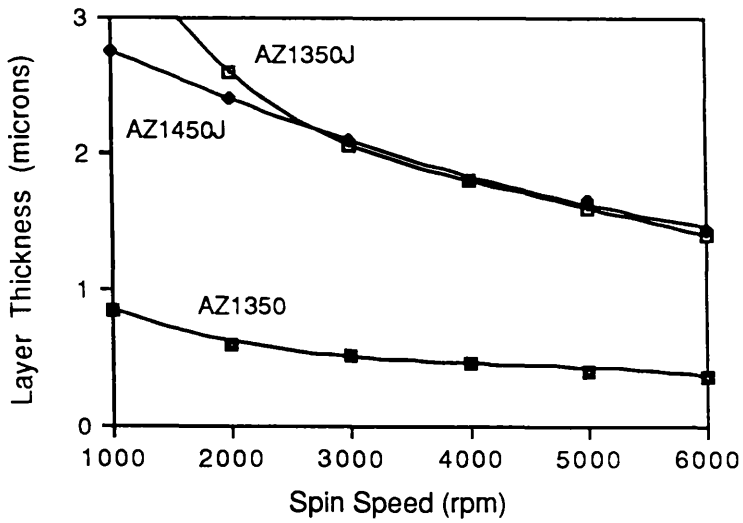
6.2 SPOT CONTACT GUNN DIODES

Spot contact Gunn diodes, of a similar structure to that of the commercial diodes shown in fig(3.6), were fabricated with spot ohmic contacts varying in diameter from 20 μ m to 90 μ m. Such spot contact Gunn diodes were fabricated from each of the pieces of vertical material, ie. CPM268, CPM351 and CPM411. The purpose of fabricating such devices was two-fold. First, one was able to ascertain if the active layer of the material oscillated, ie. whether Gunn domains formed and propagated. Second, by wet etching the spot contacts the crystallographic cleavage planes of the material could be identified from the resulting etch profile. This is important in the fabrication of the integrated devices since, as was explained in Chapter 4, the observed Linear Electro-Optic effect is different for different directions of applied electric field, and different directions of optical mode propagation.

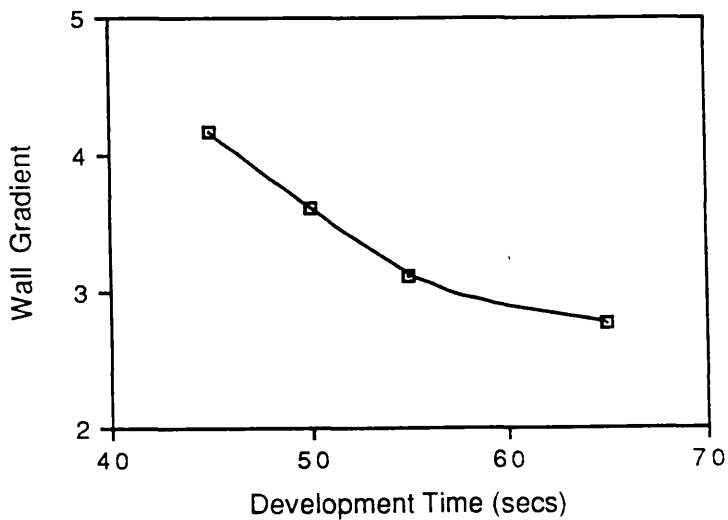
The procedure for fabricating these devices is explained schematically in fig(6.3). The sample was prepared by the fabrication procedure outlined in section(6.1.3). The samples were fabricated using a chromium mask consisting of a pattern of holes, varying in diameter in 10 μ m steps from 20 μ m to 90 μ m. A typical spot contact diode fabricated in this way, after annealing, is shown in fig(6.4). This

Fig(6.2) Characterisation of Shipley Photoresists

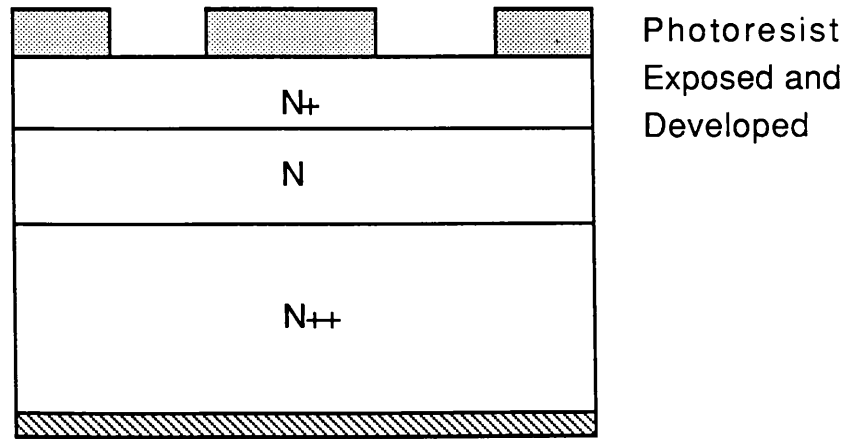
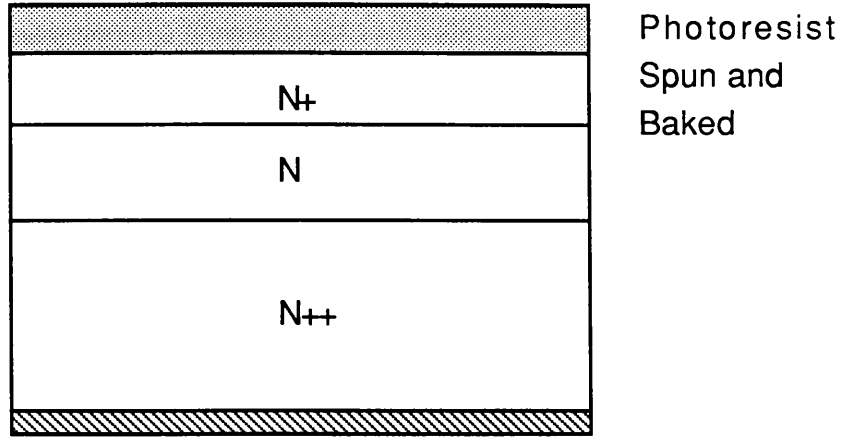
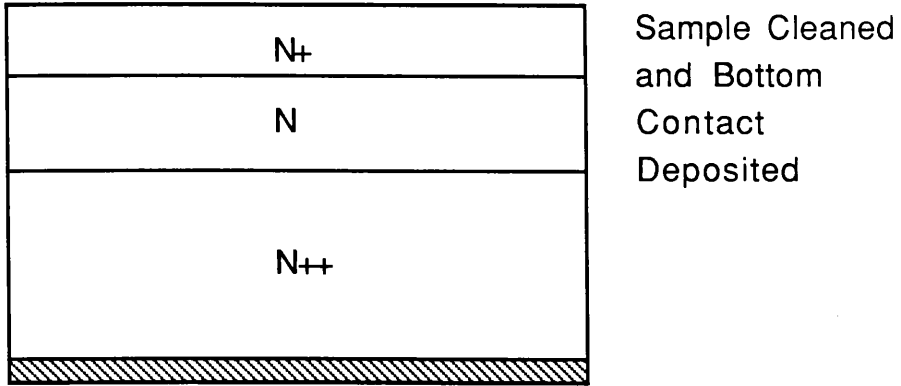
(a) Layer Thickness versus Spin Speed

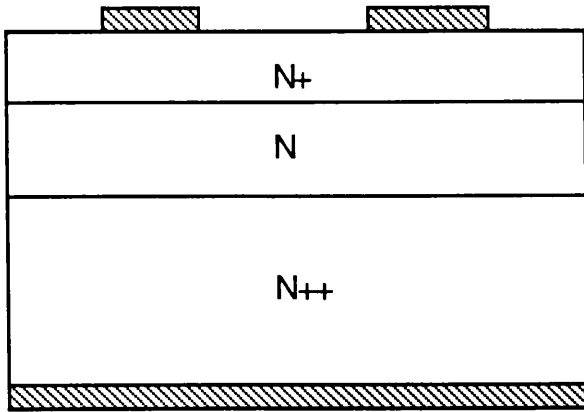


(b) Gradient of AZ1350J Wall versus Development Time (Resist Thickness = 1.8microns)



Fig(6.3) Fabrication Procedure for Spot Contact Gunn Diodes

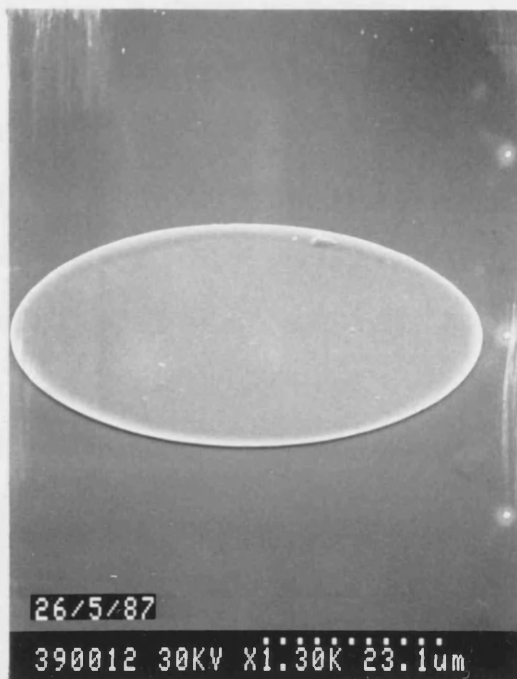




Top Contact
Deposited,
Lift-Off, and
Anneal



Fig(6.4) Typical Spot Contact Gunn Diode,
Fabricated by Lift-Off



spot contact consists of a Au/Ge/Ni/Au ohmic contact capped with a further Au bonding layer (approximately $0.8\mu\text{m}$ thick).

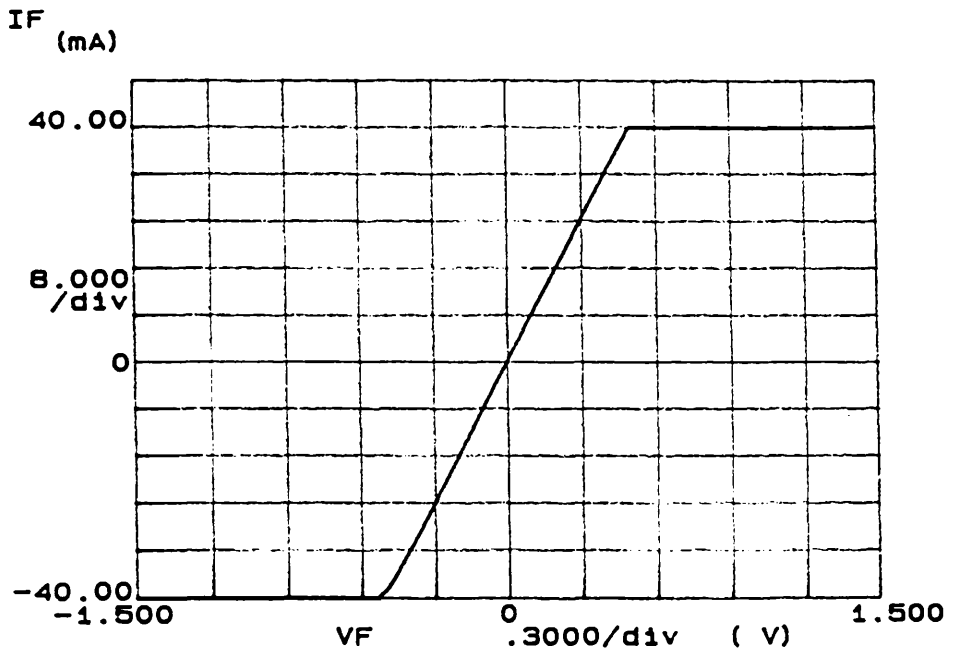
For each piece of material, each spot was probed using an Omniprobe Electrical Prober Unit, supplied by Semtek Ltd., in conjunction with an HP4145A Semiconductor Parameter Analyser. This allowed one to ensure that the Gunn diode exhibited a low-field ohmic characteristic, and that the resistance of the diode was approximately that which would be expected. For CPM411 a typical I-V characteristic for a spot size of $30\mu\text{m}$ is shown in fig(6.5). As can be seen from fig(6.5), the resistance of the $30\mu\text{m}$ spot diode is 12.5Ω . Ignoring the resistance introduced by the contacts, the theoretical resistance of the $30\mu\text{m}$ spot diode is 11.7Ω . The experimentally observed value therefore agrees well with theory, suggesting good quality ohmic contacts.

The spot contact diodes referred to above were fabricated on an unthinned substrate approximately $425\mu\text{m}$ thick. However, in order to reduce the threshold voltage, V_T of the diode, the thickness of the substrate could be reduced by, for example, mechanical polishing or wet etching. In either of these cases the ohmic contact on the rear surface was not deposited until the spot contacts on the top surface had been fabricated, and in the case of the wet etch, the top surface protected, eg. by a layer of photoresist.

The substrate of some samples was back thinned to a thickness of $150\mu\text{m}$ using silicon carbide powder, and then down to a thickness of $100\mu\text{m}$ using aluminium oxide powder. The substrate of other samples was back-thinned to a thickness of $100\mu\text{m}$ using a wet etch consisting of $\text{H}_2\text{SO}_4:\text{H}_2\text{O}_2:\text{H}_2\text{O}$ in the ratio 1:8:1. It was found, however, that when the samples were back-thinned to a thickness of around $100\mu\text{m}$, by either polishing or wet etching, they became brittle. This made further processing steps impossible with the fabrication facilities available if the sample was to remain of a useful and manageable size, ie. above $1\text{mm} \times 1\text{mm}$. The possibility of back-thinning of the substrate, leading to a reduced device operating voltage, therefore had to be abandoned.

As was pointed out earlier, the second reason for fabricating the spot diodes

Fig(6.5) I-V Characteristic for Spot Contact Diode on CPM411 (Spot Diameter = 30microns)



was that they could be used to identify the natural $\langle 011 \rangle$ cleavage planes of GaAs when treated by wet chemical etching of the top surface. To this end, each sample which was received was cleaved into rectangular samples, eg. 5mm x 5.5mm in size. In this way the two cleavage planes could be distinguished, and the orientation of the sample identified as being along one plane or the other. However, to identify the cleavage planes as either (011) or $(0\bar{1}1)$ required the use of an anisotropic wet etch, and observation of the resulting etch profile in the SEM.

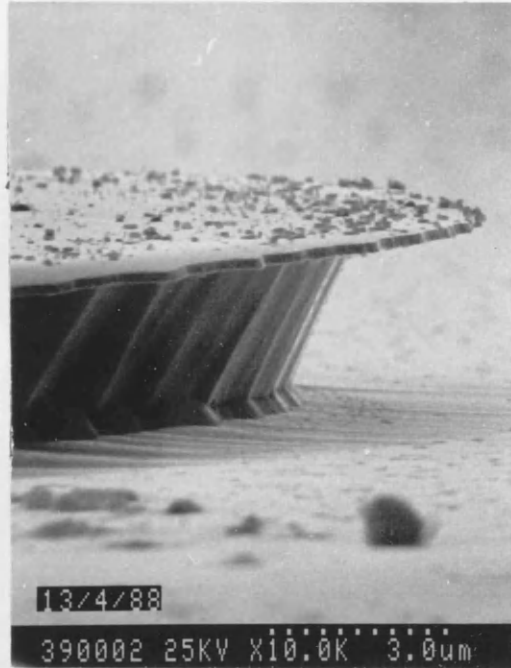
It was therefore decided to again use an acidic hydrogen peroxide solution [74], consisting of $H_2SO_4:H_2O_2:H_2O$ in the volume ratio 1:8:1 (Etch 1). This etch provides an oxidant, ie. hydrogen peroxide, H_2O_2 , and a solvent or solubilising agent, ie. sulphuric acid, H_2SO_4 , which dissolves the amphoteric oxide of GaAs.

The electron micrographs of the resulting etch profiles are shown in fig(6.6)(a), (b), and (c). As can be seen from fig(6.6)(b), the $(0\bar{1}1)$ plane yields an etch profile which connects the top of the etched surface with the upper surface by an acute-angled wall. It is also evident on closer inspection that this wall is not planar but appears to be composed of two basic surface orientations, making angles of 55° ($\{111\}$) for the portion nearest the upper surface, and approximately 40° for that nearest the etched surface. Further, from fig(6.6)(a) it can be seen that the (011) section yields a profile with obtuse-angled walls. Note also that at the extreme lower portion of the wall a small acute-angled surface exists. The etch rate of this etchant was found to be $12\mu\text{mmin}^{-1}$, which is in approximate agreement with the $14.6\mu\text{mmin}^{-1}$ which Shaw [74] found for the same etch.

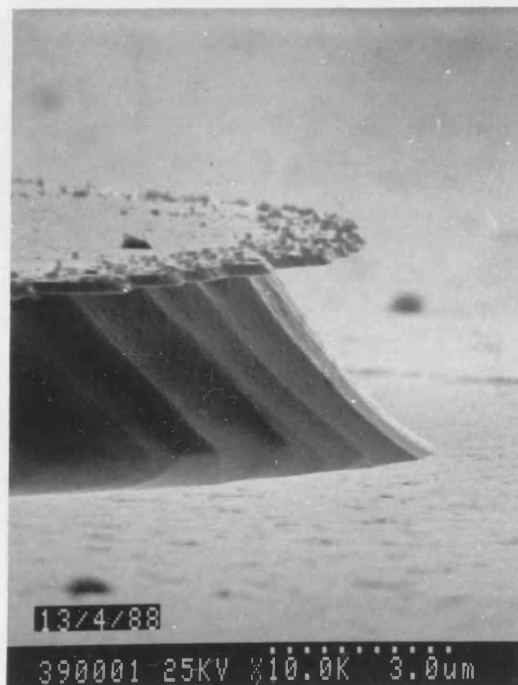
In order to investigate the variation in etch rate with temperature of an acidic hydrogen peroxide etch, a relatively more slow etch consisting of $H_2SO_4:H_2O_2:H_2O$ in the volume ratios 1:8:80 (Etch 2) was used. The results of this investigation are shown in fig(6.7). As would be expected the etch rate was found to increase with increasing temperature. It should further be noted that on observing samples etched by Etch 2 in the SEM, it was found that for the (011) section, the relative portion of the walls made up of the acute-angled surface in comparison with the obtuse one was much greater than for Etch 1. Hence, using Etch 2, it was more difficult

Fig(6.6) Electron Micrographs of Wet-Etched Spot Diodes on CPM411

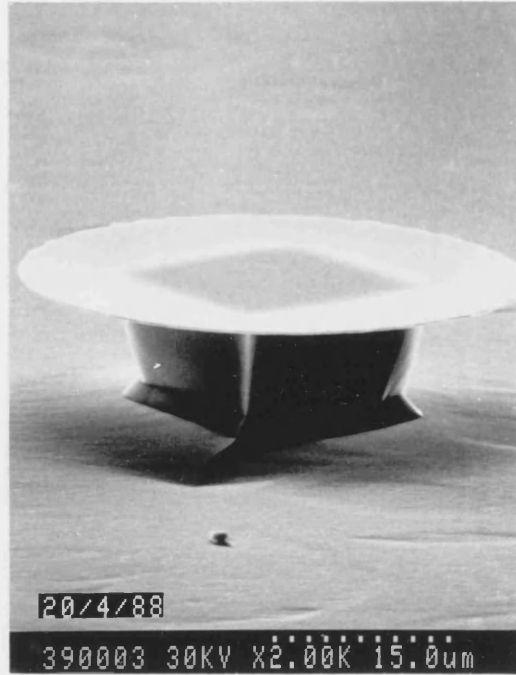
(a) (011) Section



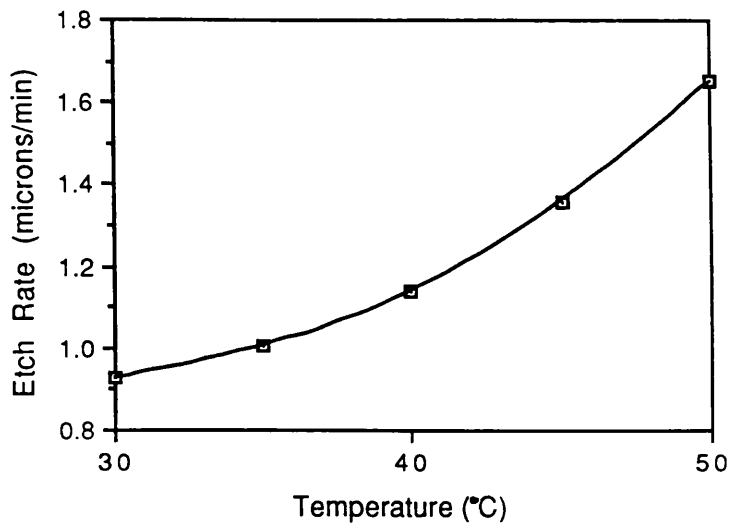
(b) (0 $\bar{1}$ 1) Section



(c) Perspective View of a Wet-Etched Spot Contact



Fig(6.7) Etch Rate versus Temperature for
H₂SO₄ : H₂O₂ : H₂O in the Volume Ratio
1 : 8 : 80 (Etch 2)



to identify the crystal orientations than by using Etch 1. This showed the importance of the correct choice of wet etch when identifying crystal orientations.

6.3 VERTICAL/RIB DEVICES

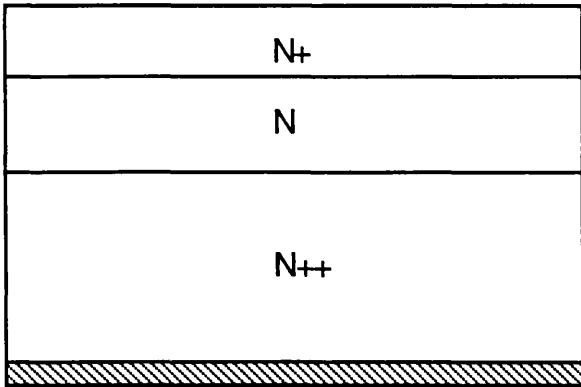
Vertical Gunn diodes incorporating a rib waveguide, as shown in fig(1.3)(b), were fabricated with ribs varying in width from $4\mu\text{m}$ to $15\mu\text{m}$. The fabrication procedure for these devices is explained schematically in fig(6.8). Again, as for the spot contact diodes, the stripe contacts were prepared by the fabrication procedure outlined in section(6.1.3). The Au/Ge/Ni/Au stripe ohmic contacts were formed using a ferric mask consisting of lines varying in width from $4\mu\text{m}$ to $15\mu\text{m}$, spaced by $350\mu\text{m}$, and 7mm long. Further, the stripe ohmic contacts were capped with a Ni layer around 125nm thick. This layer was necessary in order to form an etch mask for the next stage of fabrication, ie. SiCl_4 dry etching of the sample.

Shown in fig(6.9)(a) and (b) are the I-V characteristics for a $10\mu\text{m}$ stripe ohmic contact to CPM411 before and after annealing. As can be seen from fig(6.9), the annealing step considerably reduces the resistance of the sample, ie. from around 150Ω to 30Ω . This is due to the Au/Ge eutectic diffusing into the sample during annealing, thus forming a high conductivity region at the metal/semiconductor interface.

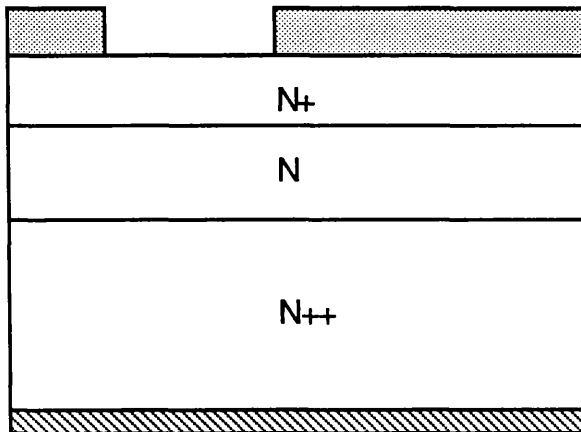
The next stage in the fabrication of these devices was the formation of the rib waveguides by etching. There are four main considerations in any etching process:

- (a) Anisotropy, ie. the extent to which wall profiles are truly vertical.
- (b) Surface and wall smoothness. These depend very much upon mask quality, substrate material, and process parameters (especially any that result in deposition as well as etching).
- (c) The extent to which etching produces surface damage. This affects the electrical performance of the device.
- (d) Etch selectivity between the various layers of the device. Etch selectivity is

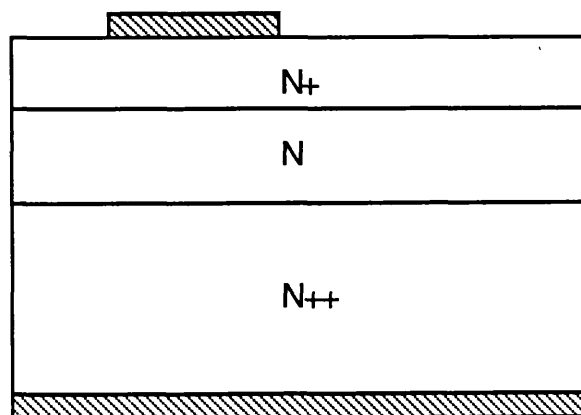
Fig(6.8) Fabrication Procedure for the Vertical / Rib Devices



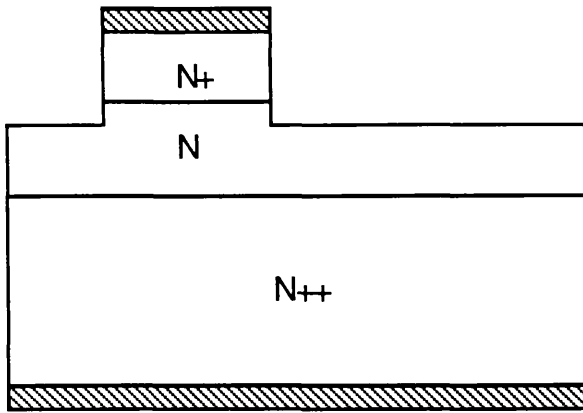
Sample Cleaned,
and Bottom
Contact
Deposited



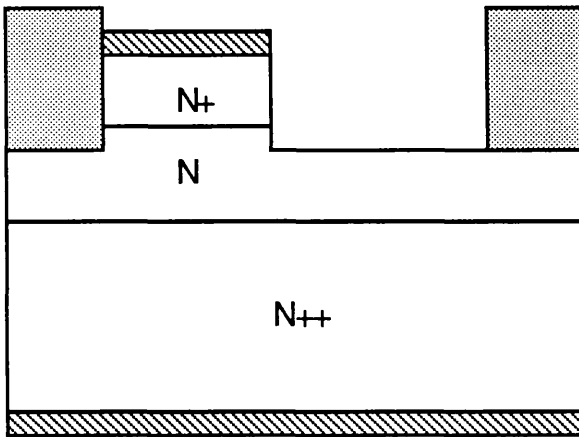
Photoresist
Spun, Baked,
Exposed and
Developed



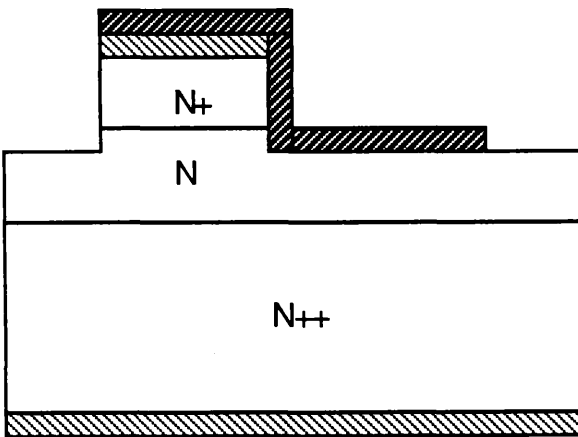
Top Contact
Deposited,
Lift-Off and
Anneal



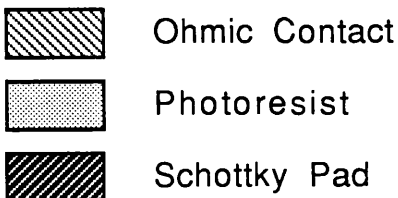
Dry Etched



Sample Cleaned,
Photoresist
Spun, Baked,
Exposed, and
Developed

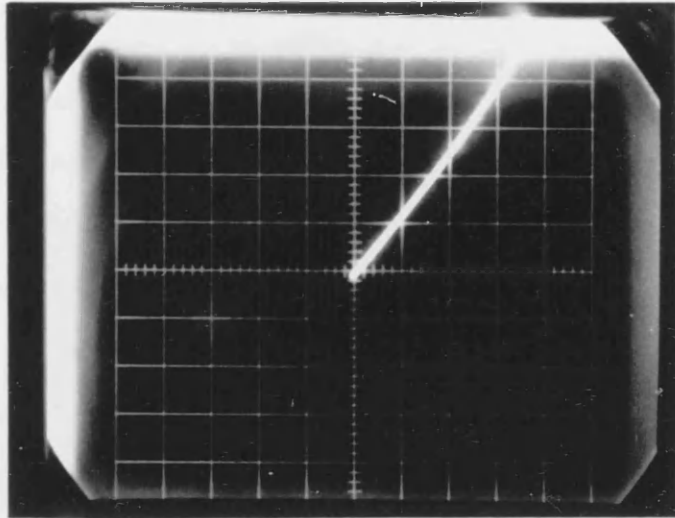


Schottky Contact
Pad Deposited,
and Lift-Off

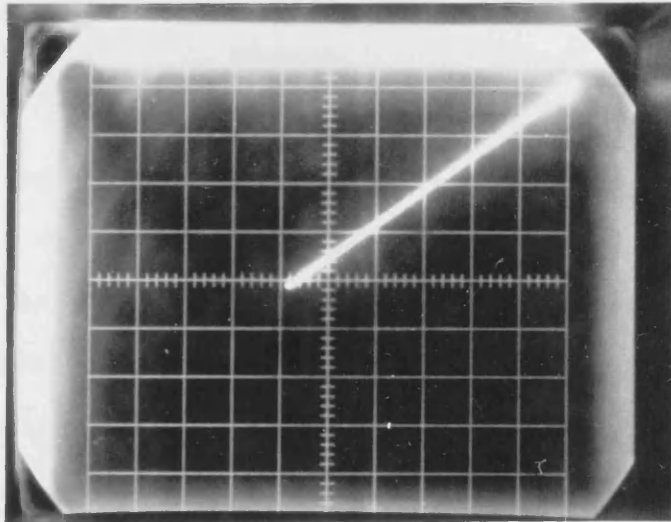


Fig(6.9) Stripe Ohmic Contact I-V Characteristics

(a) Before Anneal, $x = 0.2\text{V/div}$, $y = 1.0\text{mA/div}$



(b) After Anneal, $x = 0.01\text{V/div}$, $y = 0.5\text{mA/div}$



dependent upon the proportion and type of chemically active species used in the process.

Other considerations include the preservation of stoichiometry, a fast enough etch rate, and safety.

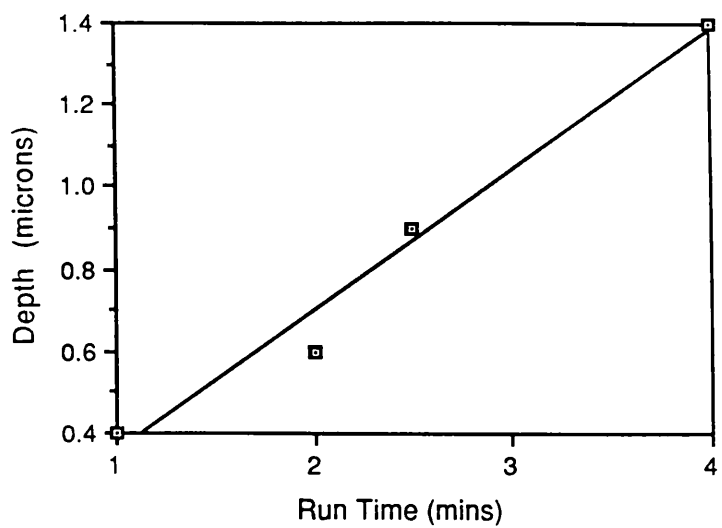
Dry etching overcomes most of the problems encountered in wet etching of fine geometrical structures, eg. due to the anisotropic nature of wet etches used for GaAs [75],[76],[77]. The regions to be etched are normally defined by photolithographically produced masks, in this case a Ni mask.

The rib devices were therefore fabricated using a Reactive Ion Etcher, RIE80, supplied by Plasma Tech Ltd., wherein the substrate was rested on the lower driven electrode, which was fed through a matching network to give a power density of around 0.5Wcm^{-2} at 13.56MHz. The upper electrode has an area around three times greater. Further, at a pressure of around 20torr = 15mbar, there was a dark space of several centimetres between the plasma and the substrate, across which the ions are accelerated directionally.

For sample CPM411, a number of samples were prepared, and the variation in etch depth with etch time observed. The results of these observations are shown in fig(6.10). This graph gives an etch rate of $0.35\mu\text{mmin}^{-1}$. Shown in fig(6.11)(a) is a stripe metal contact, consisting of an ohmic contact capped with 125nm of Ni, before etching. It was found that the minimum Ni mask thickness required was 25nm per μm of etch depth. Shown in fig(6.11)(b) is a $4\mu\text{m}$ wide rib produced by SiCl_4 RIE, having an etch depth of approximately $3.5\mu\text{m}$. A 'grass' effect can be seen on the etched surface of the sample of fig(6.11)(b). This is due to redeposition of material from either the etch mask, the electrodes, or the chamber. Fig(6.11)(c) is an end view of a cleaved edge along one of the natural cleavage planes. As can be seen from this the SiCl_4 RIE gives a substantially vertical etch wall.

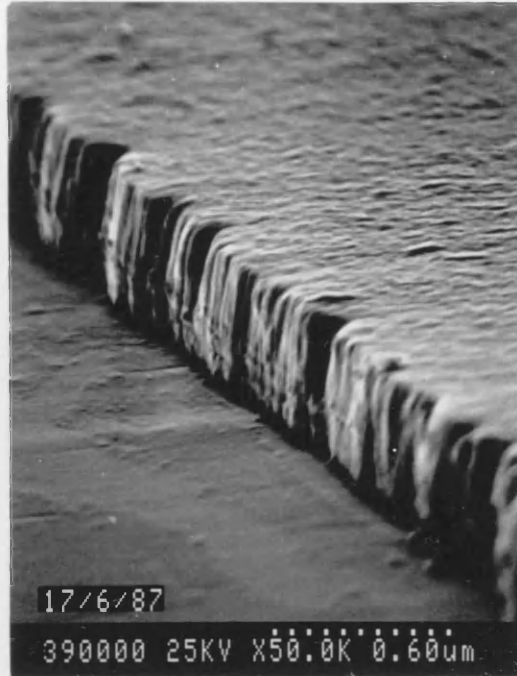
The next, and final, requirement in the fabrication of the vertical/rib devices was the formation of a rectangular Schottky contact bonding pad, this pad being positioned in such a manner as to have its longer edge running substantially parallel with the rib guide. As can be seen from fig(1.3)(c) and fig(6.8), its shorter edge is

Fig(6.10) Etch Depth versus Etch Time for CPM411

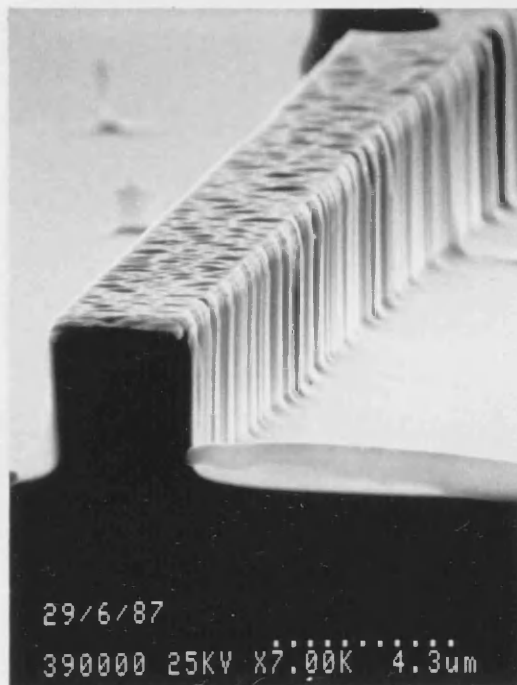


Fig(6.11) Results of SiCl_4 RIE

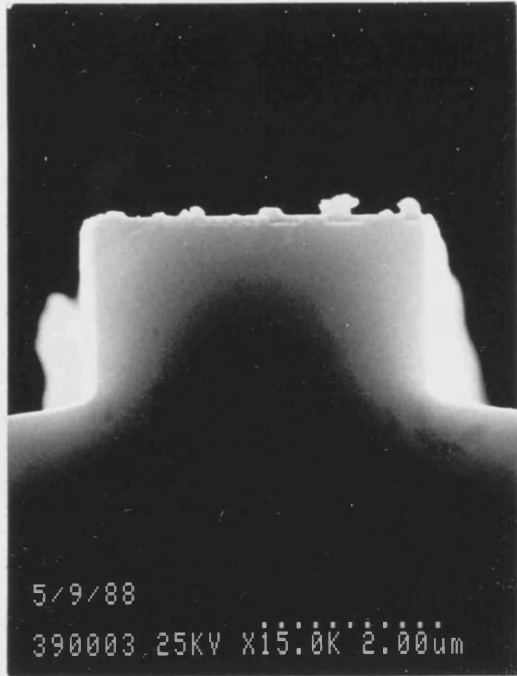
(a) Stripe Contact before Etching



(b) A Rib Produced by SiCl_4 RIE



(c) End View of a Rib Produced by SiCl_4 RIE



positioned such that the pad is adjacent to the rib, extends up one wall of the rib, and onto the top surface of the rib. In this way the Schottky pad can be used as a bonding pad to bond a wire from the device to any external circuitry. Further, for voltages below the reverse breakdown voltage of the Schottky pad, the only part of the device which will conduct will be the $N^+/N/N^{++}$ Gunn diode formed between the upper stripe ohmic contact and the ohmic contact on the base of the device.

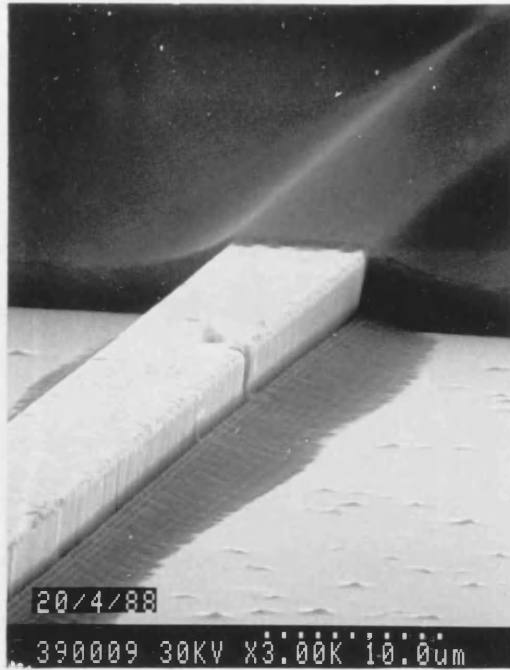
The device was again cleaned by the procedure of section(6.1.2), and photoresist spun onto the top surface. Two types of photoresist were investigated in order to define the Schottky contact pad pattern. These were Shipley AZ1450J and AZ4620A. AZ4620A was investigated since problems were encountered using AZ1450J to define the Schottky pads. These problems are explained fully below.

Samples were spun with AZ1450J at 2000rpm for 20secs, baked for 30mins at 85°C, and exposed for 6secs on the mask aligner using a ferric mask consisting of rectangles 300 μ m wide, spaced by 50 μ m, and varying in length between 1.5mm and 3.0mm. Each of the long edges of each rectangle was aligned parallel to each of the ribs already fabricated, such that the rib fell within the rectangular pattern. The rectangles were then developed away in a solution of 1:1, H₂O:Microposit Developer for 75secs, rinsed in deionised water, blow dried, and dried on the hotplate.

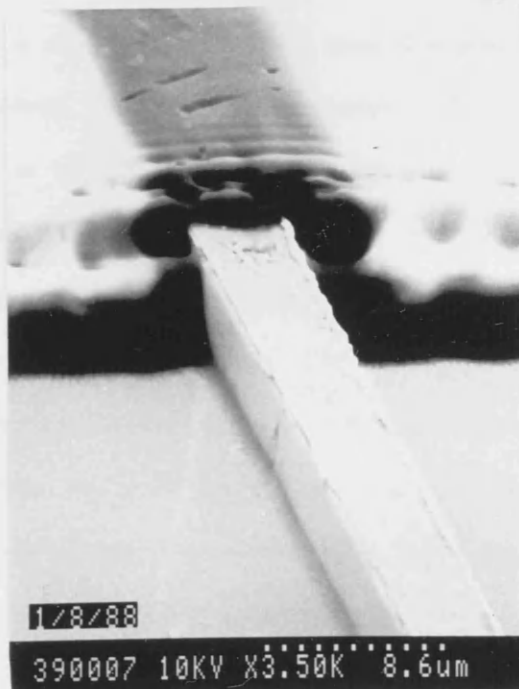
A problem however existed in the above procedure using AZ1450J. Referring to fig(6.12), viewing the sample in the SEM, it could be seen that AZ1450J succeeds in just covering the etched rib when the resist is spun on. The thickness of resist on the rib was approximately 0.56 μ m. Further, on developing the pattern of rectangular pads, it could be seen that the normal developing time of 75secs did not succeed in fully removing the thicker layer of resist built up at the sides of the rib. It was found that if the developing time was raised, eg. to 100secs, then no resist build up was left at the sides of the rib structures. However, the increase in the developing time also produced a corresponding decrease in the angle of the resist profile, and a consequently more difficult lift-off process at a later stage.

It was therefore decided to use Shipley AZ4620A positive photoresist. This resist was capable of giving a sufficiently steep resist profile as well as a very thick

Fig(6.12) AZ1450J Spun onto Etched Sample to Define Rectangular Schottky Pads



Fig(6.13) AZ4620A Spun onto Etched Sample to Define Rectangular Schottky Pads



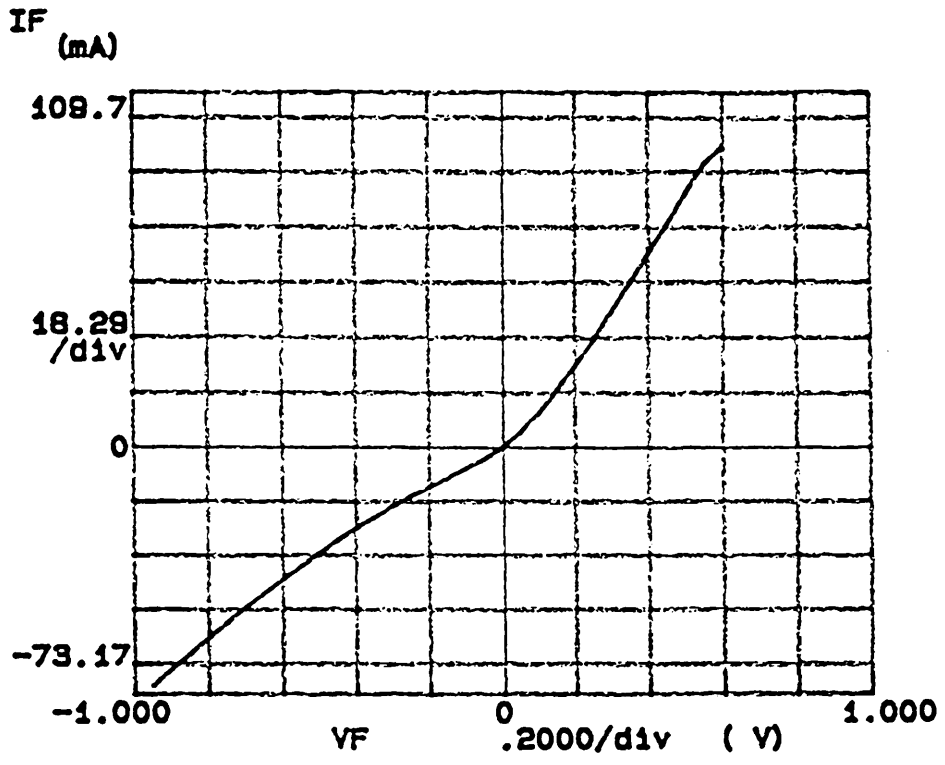
resist film (approximately $6.0\mu\text{m}$). The samples were coated with AZ4620A by spinning at 4000rpm for 20secs, then baked at 85°C for 30mins, exposed on the mask aligner using the rectangular pad pattern for 6secs, and developed for 75secs in 1:1, H_2O : MF3.2 Developer. This development time was found to give a sufficiently steep resist wall profile, as well as fully clearing any residue of resist from the side walls of the rib. This can be seen from the electron micrograph of fig(6.13). Further, a spin speed of 4000rpm was found to give a resist thickness of around $5\mu\text{m}$, ie. a resist thickness greater than the etch depth of the rib.

The sample was now ready for the deposition of the Schottky contact pads. As with ohmic contacts, the fabrication of sufficiently good Schottky contacts to GaAs requires careful preparation of the contact surface before evaporation, and rapid deposition of the first metallic layer to the contact surface. The sample surface was therefore again cleaned, and deoxidised, immediately before loading the sample into the vacuum system for deposition. The deoxidant which was used was 4:1, H_2O :HCl for 20secs, since the sample was again patterned with photoresist.

The metal systems which were used for the formation of Schottky contact pads were Ti/Au or Mo/Au. The first layer consisted of approximately 70nm of either Ti or Mo. These metals were used since either forms a good rectifying contact to GaAs. The top gold layer had a thickness of not less than 80nm in order to ensure a sufficiently thick bonding surface. Note that the Schottky pad was deposited onto the device surface at an angle of around 45° . This ensured that one of the walls of the rib was completely covered with metal. The remaining resist was then removed by the process of lift-off, ie. soaking the sample in acetone for 2 to 3 hours, rinsing in deionised water, blowing dry in nitrogen, and drying off on the hotplate. In this way the required rectangular Schottky contact pads were defined.

In order to characterise the I-V characteristic of the vertical/rib device incorporating a Schottky pad, the device was probed using the Omniprobe Electrical Prober Unit, and HP4145A Semiconductor Parameter Analyser. A typical I-V characteristic of such a device, with a Ti/Au Schottky contact, is shown in fig(6.14). The devices having a Mo/Au Schottky contact had virtually identical characteristics to

Fig(6.14) I-V Characteristic of a Typical Vertical / Rib Device Incorporating a Schottky Contact Bonding Pad



that of fig(6.14).

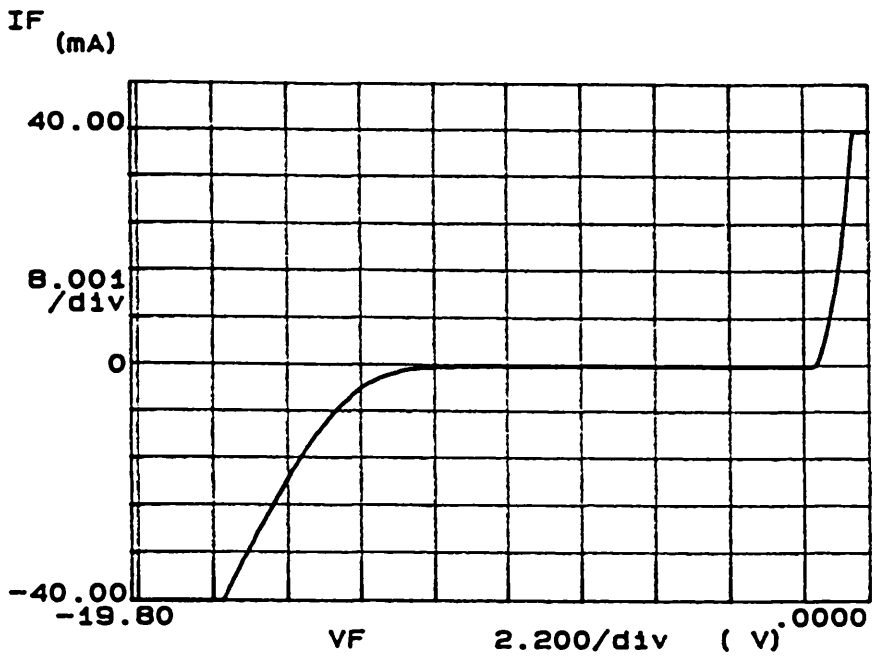
To investigate the performance of the Schottky contacts in isolation, a number of rectangular Schottky pads were fabricated on areas of the etched surface of CPM411 where no rib guides had been defined. A typical I-V characteristic of a Ti/Au Schottky contact pad is shown in fig(6.15)(a). As can be seen from this, the Schottky contact has a reverse bias breakdown voltage, V_B , of around 12.1V. Since in operation a bias voltage, V_{bias} , of around 1.75V is required for the vertical/rib device R3 to oscillate, it can be seen that when this bias voltage is applied to the cathode of the device, ie. the Schottky pad, the only region of the device which will conduct is that between the ohmic contact on the top of the rib and the ohmic contact on the base of the device. Also, it was found that if the device was annealed after the Schottky contact had been formed, the reverse bias breakdown voltage was greatly reduced. A typical characteristic of such an annealed Schottky pad is shown in fig(6.15)(b). As can be seen from this characteristic, the behaviour of the contact can no longer be said to be truly Schottky after annealing.

The vertical/rib device was viewed in the SEM after the formation of the Schottky contacts. As can be seen from fig(6.16), the electron micrograph shows that the Schottky pad extends from the etched surface adjacent the rib, up the vertical rib wall, and onto the top surface of the rib. This was confirmed by X-ray analysis of each of the surfaces, which showed that the pad on the etched surface and the sidewall consisted of Au and Ti, while the contact on the top of the rib consisted of Au, Ti, Ni and Ge.

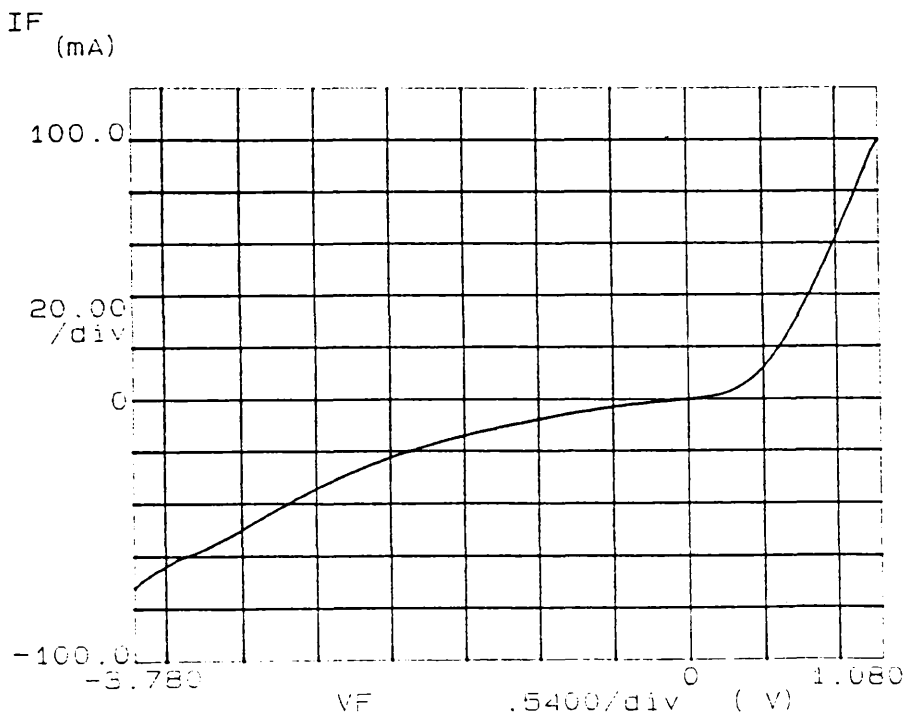
A problem which was met in the fabrication of the Schottky pads was that of adhesion between the Schottky contact and the etched surface of the GaAs. In order to optimise the adhesion, it was of the utmost importance to ensure that the surface of the GaAs was properly cleaned and deoxidised immediately before the deposition was performed. If this was not done then, it was also found that the reverse bias breakdown voltage of the Schottky pad was considerably reduced.

Fig(6.15) I-V Characteristic of a Typical Schottky Pad

(a) Unannealed, $V_B = 12.1V$



(b) Annealed



Fig(6.16) Vertical / Rib Device Incorporating a Schottky Contact Bonding Pad



6.4 PLANAR/PHOTOELASTIC DEVICES

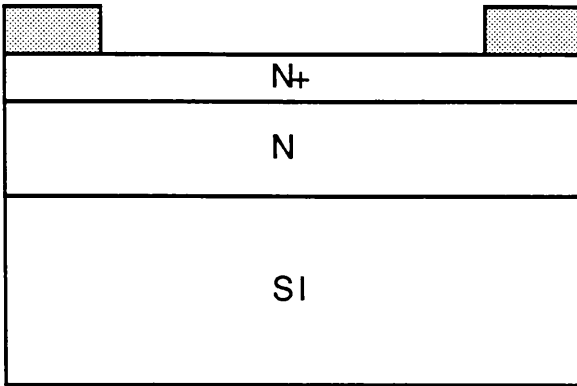
Planar Gunn diodes incorporating a photoelastic waveguide, as shown in fig(1.3)(c), were fabricated, with waveguides varying in width from $6\mu\text{m}$ to $12\mu\text{m}$. The fabrication procedure for these devices is explained schematically in fig(6.17). Rectangular holes $100\mu\text{m}$ wide, 7mm long, and spaced by $200\mu\text{m}$, were formed in a photoresist layer using a ferric mask, following procedural steps (a)–(e) of section(6.1.3). The pattern was aligned along one of the natural cleavage planes of the material.

The resist was then used as a mask for SiCl_4 RIE, or wet chemical etching, so that the N^+ contact capping layer was etched away, thus exposing the active N^- layer. Wet etching again offered the advantage of being able to identify the orientation of the sample, ie. along the (011) or $(0\bar{1}1)$ planes. The resist mask was then removed, and AZ1450J resist again spun onto the top surface of the sample. However, this time the resist was spun on at 2000rpm for 20secs, and pre-baked for 15mins at 85°C . The sample was then soaked in chlorobenzene for 15mins, rinsed in deionised water, blow dried, and post-baked for 5mins at 85°C . The sample was then exposed on the mask aligner for 6secs, using a second ferric mask which was aligned with the pattern fabricated by the first ferric mask. The second ferric mask was designed to define the resist pattern of the third step of fig(6.17).

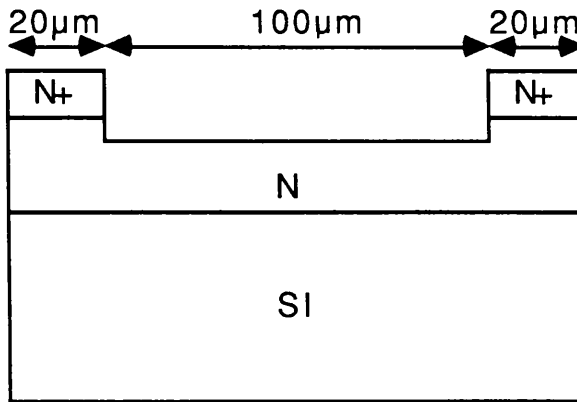
The process of chlorobenzene hardening [78] the surface of the resist was employed in order to define an overhang in the resist profile. The purpose of the overhang was to ensure lift-off of the $1.5\mu\text{m}$ of metal, deposited at the next stage, from the $1.8\mu\text{m}$ of AZ1450J resist. A schematic diagram of the resist profile is shown in fig(6.18)(a). The variation in the undercut, U, the overhang, O, and the hardened layer thickness, T, for AZ1450J, were investigated for various development times, as shown in fig(6.18)(b). A typical AZ1450J resist profile obtained by chlorobenzene hardening is shown in the electron micrograph of fig(6.19).

The next step in the fabrication process was to deposit the required metal contacts. The contact consisted of the Au/Ge/Ni/Au ohmic contact previously defined

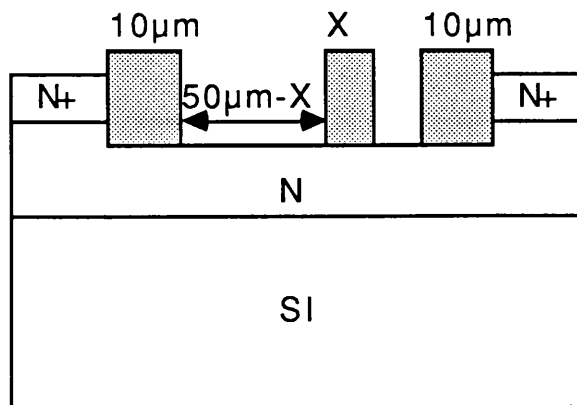
Fig(6.17) Fabrication Procedure for the Planar / Photoelastic Devices



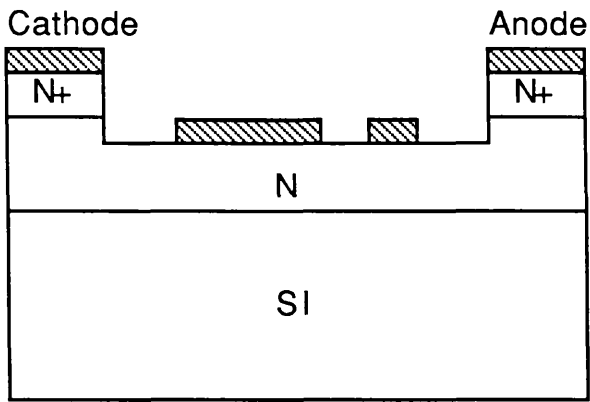
Sample Cleaned, and Photoresist Spun, Baked, Exposed and Developed



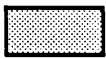
Photoresist used as Mask in Dry Etch, and then Removed



Sample Cleaned, and Photoresist Spun, Baked, Exposed and Developed;
 $X=6,8,10$ or $12\mu\text{m}$



Metal Deposited,
Lift-Off and
Anneal



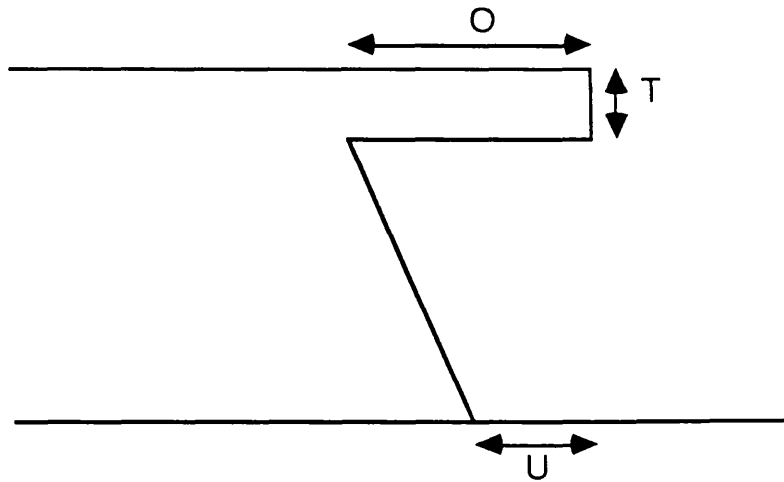
Photoresist



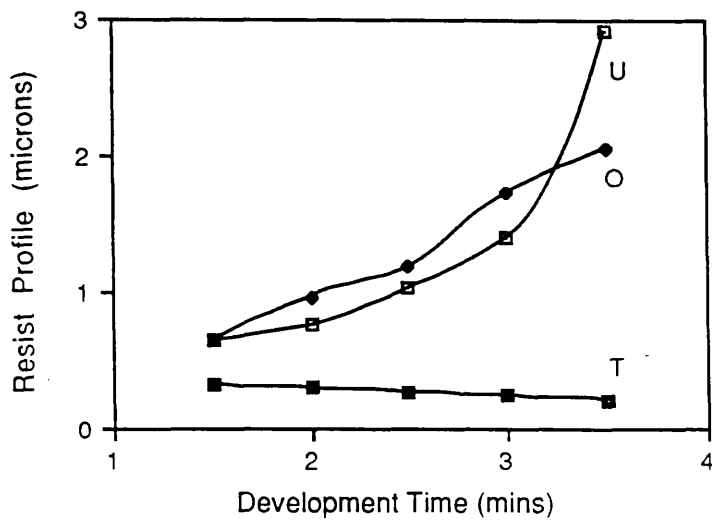
Ohmic Contact

Fig(6.18) Chlorobenzene Hardening of AZ1450J

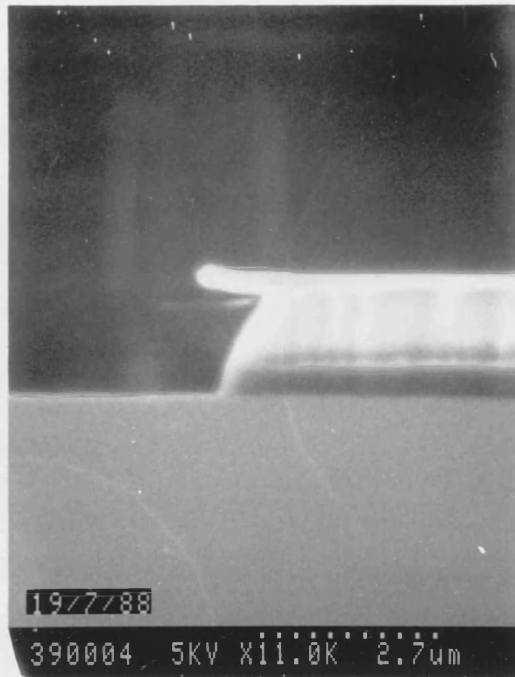
(a) Schematic Diagram of Resist Profile



(b) Variation of Resist Profile with Developing Time



Fig(6.19) Electron Micrograph of Chlorobenzene
Hardened AZ1450J



in table(6.5) (the total thickness of which is approximately 168nm), capped with around $1.332\mu\text{m}$ of Au, thus making a total contact thickness of around $1.5\mu\text{m}$. The pattern was then lifted-off in the normal way, leaving a planar Gunn diode with three photoelastic guides between cathode and anode, one guide near the cathode, one near the anode, and one positioned between the two contacts, as shown in fig(6.17).

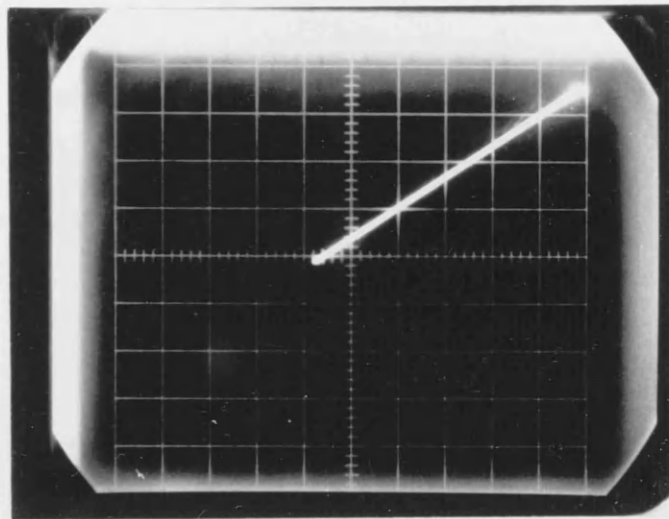
The third fabrication step of fig(6.17) was also undertaken using the thicker AZ4620A resist. However, despite the much thicker layer depth offered by this resist, it was found that unless the resist was also chlorobenzene soaked, there was difficulty in lifting-off the pattern. This was due to the thick metallic layer being resilient to the lift-off process, and resulted in many of the guide lines not being cleared out, and also in some of the metal deposited onto the surface of the sample being pulled off.

After lift-off was completed, the sample was annealed by the process previously outlined in procedural step (g) of section(6.1.3). Electrical measurements were then carried out on the sample. A typical I-V characteristic of a planar sample, after annealing, is shown in fig(6.20).

In order to measure the magnitude of the stress produced within the sample, due to the presence of the $1.5\mu\text{m}$ metal layer, samples were back thinned to a thickness of approximately $100\mu\text{m}$. A sodium-interference-microscope [10] was then used to investigate the interference fringes associated with the sample. The process used to back thin the sample was as follows. First the sample was mounted on a jig using a small amount of wax to stick it down. The sample was then polished down from $425\mu\text{m}$ to around $150\mu\text{m}$, using a glass flat cover, and a mix of Buehler 600 Silicon Carbide Powder and water. The sample was further thinned from $150\mu\text{m}$ to $100\mu\text{m}$ using a mix of bleach, $3\mu\text{m}$ alumina powder, and water. The alumina acted as a physical etch, while the bleach, which contains Cl, acted as a chemical etch. This thinning process differed from that previously outlined in section(6.2) since in this case a polished rear surface was required.

By placing the thinned sample under a sodium-interference-microscope the

Fig(6.20) I-V Characteristic of a Typical Planar / Photoelastic Device,
 $x = 0.05\text{V/div}$, $y = 4\text{mA/div}$



deflection, δ , over the sample length could be calculated from [79]

$$\delta = \frac{D\lambda}{2a} \quad \dots\dots\dots 6.1$$

where, D = lateral shift in the fringe pattern

λ = wavelength of sodium light = 580nm

a = fringe separation

Both D and a could be measured from photographs of the fringe pattern taken from the sodium-interference-microscope. Over a sample length, S , the radius of curvature, ρ , may be found from

$$\rho = \frac{S^2}{2\delta} \quad \dots\dots\dots 6.2$$

Further, using this value of ρ the product of the film stress, σ_f , and the film thickness, t , is given by

$$\sigma_f t = \frac{E' d^2}{6\rho(1-\nu)} \quad \dots\dots\dots 6.3$$

where, d = substrate thickness

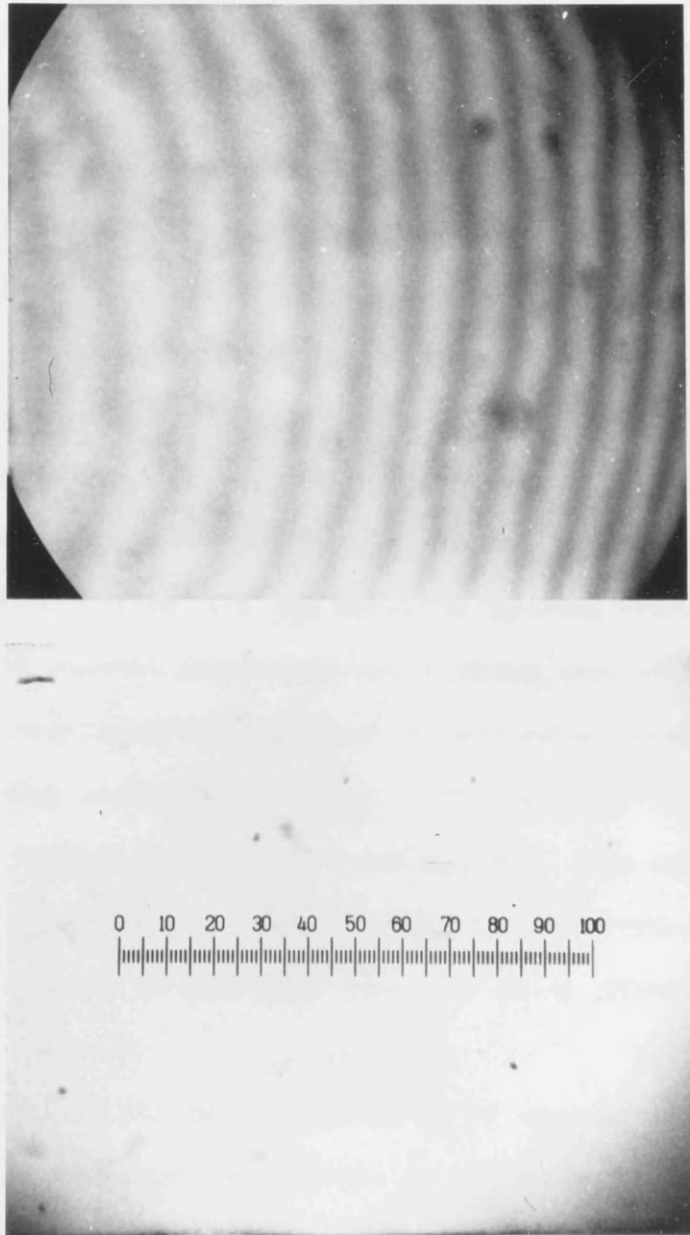
E' = Young's modulus

ν = Poisson's ratio

$$\frac{E'}{1-\nu} = 1.23 \times 10^{12} \text{ dyn cm}^{-2}$$

A typical fringe pattern observed under the sodium-interference-microscope is shown in fig(6.21). Using equations(6.1), (6.2) and (6.3) in conjunction with the observed fringe pattern, it was found that for a film thickness, $t=1.5\mu\text{m}$ the product of film stress and thickness, $\sigma_f t = 7.76 \times 10^6 \text{ dyn cm}^{-1} = 77.6 \text{ Nm}^{-1}$, ie. the film stress, $\sigma_f = 5.17 \times 10^7 \text{ Nm}^{-2}$.

Fig(6.21) Typical Fringe Pattern Observed Under the Sodium Interference Microscope ($D = 1.6\text{cm}$, $a = 1.4\text{cm}$)



6.5 CLEAVING, MOUNTING, AND BONDING OF DEVICES

As was previously explained, on receipt of a sample the majority of it was cleaved into rectangular samples, eg. 5mm x 5.5mm in size. This allowed the two cleavage planes to be distinguished, although not identified.

A mechanical scribing machine was used to scribe the samples, which were always scribed from the back surface. This was particularly important in the case of completed devices incorporating waveguides in which one desired a good, unbroken, and unchipped cleavage edge in order to ensure good optical input to, and output from, the device. The scribed sample was then sandwiched between two glass slides with the scribe running colinearly with one of the longer edges of each of the two slides. A third slide was then placed on top of the portion of the sample protruding from the first two slides, and pressure applied to the third slide by hand. This applied pressure caused it to cleave along the scribe line.

For optical experiments the sample did not need to be securely mounted. Indeed sticking it down was of a distinct disadvantage in loss measurements carried out by the method of sequential cleaving. The best method of mounting samples for purely optical experiments was therefore found to be simply placing them on top of the device mount, the device mount consisting of a long, thin rectangular, horizontally mounted aluminium mount (approximately 1.5mm x 1.5mm x 2cm), retained by a grub screw in relation to a goniometer, and x, y stage. This mounting arrangement allowed optical access to the sample. A small piece of double sided sticky tape was also placed on top of the device mount to aid in retaining the device, but also allowing easy removal.

For electrical experiments the device required to be mounted within a microstrip circuit. The analysis and fabrication procedure for this circuit is explained in section(7.2.1). For the vertical devices the sample had to be mounted on a copper clad ground plane on the top surface of the microstrip circuit, the base contact, ie. the anode of the device, being in electrical contact with the ground plane. To this end the device was mounted on the ground plane using either quick

drying silver dag, or an electrically conductive epoxy such as the silver filled epoxy H20E, supplied by Alpha Metals Ltd.. The disadvantage of the epoxy was that in order to obtain optimum electrical conductivity of the adhesive it required to be cured at an elevated temperature of around 150°C for 5mins. This high temperature curing process however degrades the performance of the annealed ohmic contacts of all of the devices, and also destroys the Schottky performance of the contact pads of the vertical/rib devices.

The top contact, ie. the cathode, of the device was connected to the microstrip circuit via a gold bonding wire of 25 μ m in diameter. If the cathode contact was sufficiently large, two or more bonding wires were used in order to cut down parasitic reactances within the circuit. The bonding wire could be positioned by either of two techniques. The first of these techniques was to use an ultrasonic bonder. This technique did however have a number of disadvantages. For example, spot contacts of less than 70 μ m in diameter could not be observed through the microscope of the bonder when the bonder wedge was positioned above the contact. This therefore prevented bonding of such spots. A further disadvantage occurred due to the force exerted on the contact during bonding. If the adhesion of the contact to the semiconductor surface was not sufficient, then it was often found that the process of attempting to make a bond would actually lift the metal contact off the semiconductor surface. This was a particular problem in the case of the rectangular Schottky contact pads in the vertical/rib devices.

The second technique made use of two linear probe movements, such as the OMP242 stages supplied by Semtek Ltd., and a binocular microscope. The probing tip of one of these stages was replaced by a bonder wedge, having a hole at the pointed end to feed the bonding wire through. The probing tip of the other stage was replaced by a sharpened match stick. A small amount of either silver dag or conductive epoxy was then loaded onto the end of the match stick, and dispensed onto the bonding pad. The first stage was then used to position the bonding wire within the pool of adhesive, and left to dry. In the case of the epoxy this process had to be carried out *in situ* on a hotplate, in order that the epoxy could be

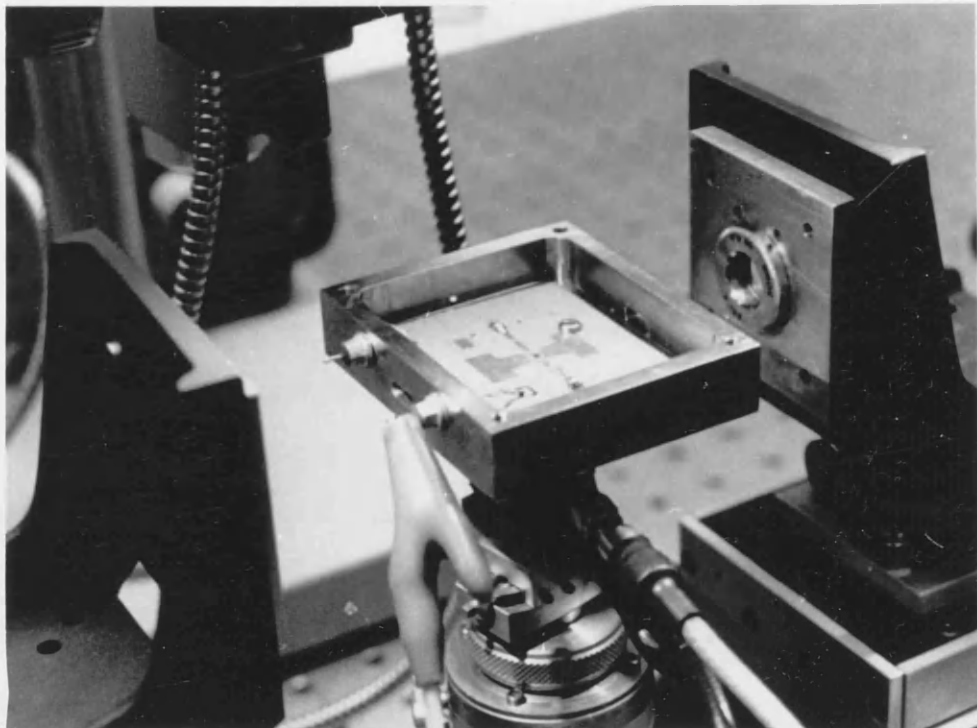
properly cured.

A second pool of adhesive was then dispensed onto the second bonding surface, and the first stage drawn away from the first bond, allowing the wire to feed through the hole in the bonder tip, and fall into the second pool of adhesive. When the second pool of adhesive had dried the first stage was drawn away from it, and the bonding wire cut with a scalpel.

For the planar device the sample had again to be mounted on the copper clad ground plane on the top surface of the microstrip circuit. The base of the device did not however need to be in electrical contact with the ground plane. However, it was found to be more convenient to mount the planar device using either silver dag or epoxy. Two bonds therefore had to be formed, one from the microstrip circuit to the cathode, and one from the anode to the ground plane. These bonds were formed by either of the techniques already described for the vertical devices.

The microstrip circuit was then mounted, and secured by means of grub screws, within a rectangular stainless steel cavity, as shown in fig(6.22). The cavity both shielded the microstrip circuit, and provided a ground plane for it. Two such cavities were available, one for purely electrical experiments, and one for Electro-Optic experiments. The two cavities were identical, except that the one used for Electro-Optic experiments had a slit in the centre of each of its longer sides to allow for optical input and output of the waveguiding sample mounted on the circuit board. In the case of the integrated devices the sample therefore had to be mounted with the waveguides running substantially parallel to the shorter edges of the cavity.

Fig(6.22) Device Mounted within Microstrip Circuit and Retained within Stainless Steel Cavity



CHAPTER 7

EXPERIMENTAL RESULTS AND DISCUSSION

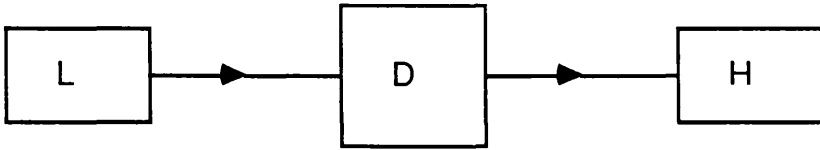
In this Chapter are presented the experimental results for the devices already described in previous Chapters. The experiments which were carried out may be divided into three different types. Firstly, purely optical experiments carried out on each of the slab, rib, and photoelastic waveguiding structures. Secondly, purely electrical experiments carried out in order to test the microwave performance of the devices. These experiments were carried out on the vertical spot contact diodes, as well as the vertical/rib devices incorporating a Schottky contact bonding pad, and the planar/photoelastic devices. The third type of experiment, which were carried out only on the integrated vertical/rib device structures, were Electro-Optic experiments. These experiments were performed in order to observe whether any interaction was present between the optical guided wave and the propagating Gunn domain, and also in order to quantify such observations.

7.1 OPTICAL EXPERIMENTS

7.1.1 Guiding Characteristics

All purely optical experiments were carried out at a wavelength, λ , of $1.15\mu\text{m}$, using an NEC He:Ne gas laser with a CW output of approximately 10mW. The experimental set up is shown in fig(7.1). As was explained in section(6.5), for optical experiments the sample was mounted on a device mount comprising a long, thin rectangular mount (approximately $1.5\text{mm} \times 1.5\text{mm} \times 2.0\text{cm}$) retained horizontally by a grub screw in relation to a goniometer and x, y stage. Using this, any given waveguide sample could be placed on top of the mount, and retained by a piece of double sided sticky tape. A pair of x40 objective lenses, having a focal length, $F=0.65\text{mm}$, could then be used to couple light into and out of the sample by the end fire method. Both of the lenses were mounted on x, y, z stages in

Fig(7.1) Experimental Apparatus for Optical Experiments



L = Laser ; D = Mounted Device ; H = Hamamatsu IR Camera

order that they could be precisely aligned to the guiding sample.

Each of the optical waveguide samples were cleaved to a length of between 1.5mm and 4mm. Optical waveguiding was observed in all of the waveguides under consideration, ie. the slab waveguides S41, S42, and S43; the rib waveguides R1, R2, and R3, with and without the Schottky bonding pads; and the photoelastic waveguiding samples P11, and P12. The mode profiles of each of the waveguiding samples could be observed, and digitally stored, using the Hamamatsu IR Camera and controller, linked to an IBM PC via an IEEE 488 Interface.

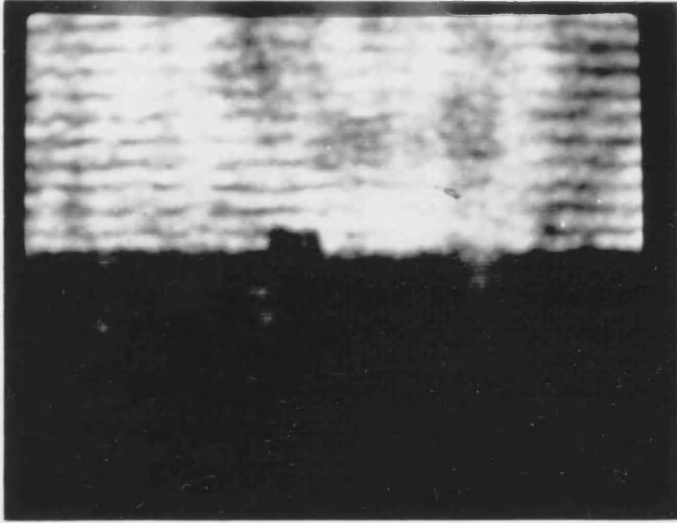
It was found that slab guide S41 supported two vertical modes, ie. the fundamental mode, and the first order even mode. This was in agreement with the results of the four-layer vertical slab program, referred to in section(5.2.2). It was further found that slab guides S42, and S43, supported only the fundamental mode as theory predicted.

Rib waveguide samples were similarly tested, and it was observed that rib guide R1 supported three modes, ie. the TE_{00} , TE_{01} , and TE_{10} modes, while rib guides R2 and R3 supported only the fundamental TE_{00} mode. Fig(7.2)(a) shows rib guide R3 exhibiting a characteristic pattern of Lloyd fringes. By raising the sample slightly from this position end-fire coupling was achieved. The profile of the vertical component of the fundamental mode of R3, as stored by the computer, is shown in fig(7.2)(b). As can be seen from this, the horizontal (y) component of the mode had a half width of around $8.3\mu\text{m}$. This compares well to that found by the .NWAVE program, as shown in fig(5.9), which predicts a half width of around $8.0\mu\text{m}$. Shown in fig(7.2)(c) is a photograph of the output of the rib guide R3.

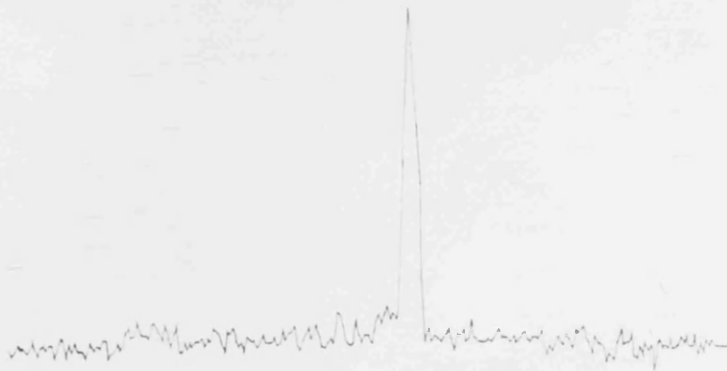
To ensure that photoelastic waveguides, consisting of a thick gold layer on top of an ohmic contact, could be formed, photoelastic guides equivalent in structure to device P12 were fabricated directly onto a semi-insulating substrate. Other samples, having no ohmic contact beneath the thick gold layer, were also fabricated on a semi-insulating substrate. As expected, it was found that the samples with the ohmic contact performed in substantially the same way as those without, and that the thin ohmic contact layer had no significant effect on the optical guiding characteristic of

Fig(7.2) Experimentally Observed Mode Profiles

- (a) Lloyds Fringes Exhibited by a $5\mu\text{m}$ Wide Rib Waveguide R3



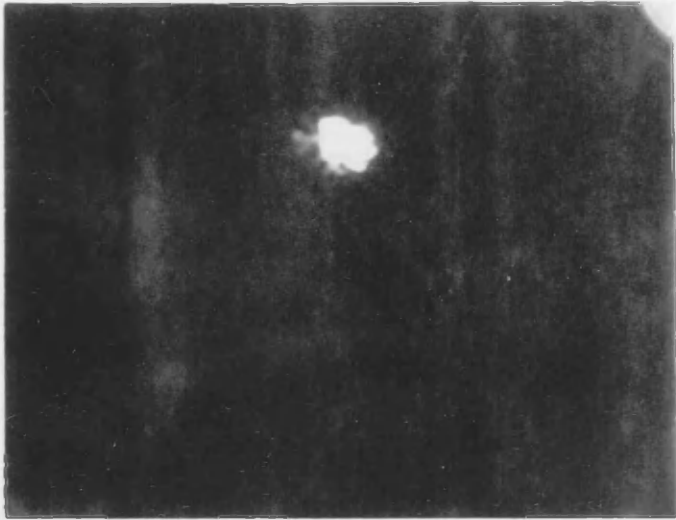
- (b) Horizontal Component of TE₀₀ Mode for a $5\mu\text{m}$ Wide Rib Waveguide R3



H

$10\mu\text{m}$

(c) Near Field Intensity Pattern at the Output of a $5\mu\text{m}$ Wide Rib Waveguide R3



$10\mu\text{m}$

the sample.

Photoelastic waveguide samples of the structure of device P12, incorporating ohmic contacts, were fabricated and tested. These samples were found to guide optical radiation at a wavelength of $1.15\mu\text{m}$, as was predicted by the Finite Difference calculations presented in section(5.2.4). These guides were also found to be monomode, which is in agreement with theoretical predictions.

7.1.2 Loss Measurements

An important feature of any optical waveguide is the loss, L (dBcm^{-1}) suffered by an optical signal propagating through the guide [11],[80],[81]. The basic method of measuring waveguide loss is to launch a known optical power into the waveguide, and measure the optical power emerging from the other end. However, a number of disadvantages exist in such a simple approach, eg. coupling losses at the input and output are unknown. Also, in a multimode guide, losses due to each mode cannot be individually measured. A number of methods have therefore been proposed in order to obviate the above mentioned disadvantages [82],[83],[84].

One of the simplest, and most accurate, of these methods is known as the method of Sequential Cleaving. This method comprises end-fire coupling of light of the desired wavelength directly onto the cleaved input face of the waveguide, and measurement of the total power transmitted. This measurement is repeated for a number of samples of different lengths, these samples being obtained, for example, by repeatedly shortening an initially relatively long sample. For each measurement the observed output power is maximised by careful alignment of the coupling system. In this way coupling losses are kept approximately constant. It is therefore the case that the loss coefficient, α , can be found from the gradient of the semilog transmitted power versus sample length graph. Hence, the optical loss, L (dBcm^{-1}) may be found since, $L = 4.3\alpha(\text{cm}^{-1})$.

This procedure of sequential cleaving was carried out for each of the two dimensional guiding structures under consideration, ie. the rib guides R1, R2, and

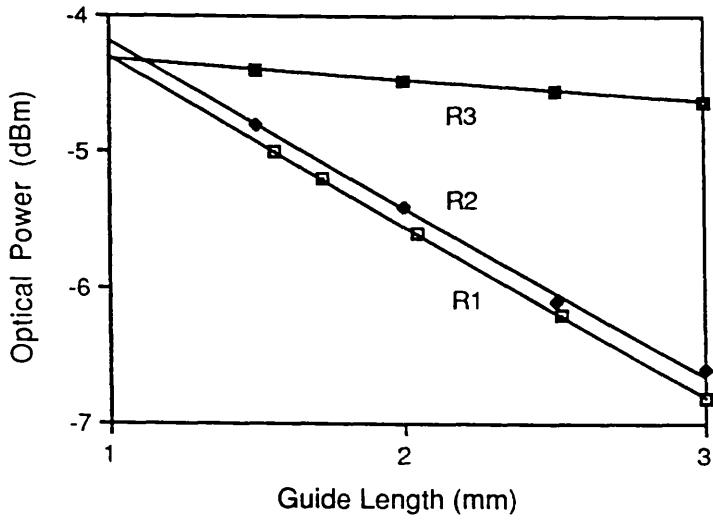
R3, and the photoelastic guides P11, and P12. The optical power transmitted by the guiding structures was measured using a Photodyne Model 22XLA Fiber Optic Power Meter, inserted between the mounted device and the Hamamatsu IR Camera of fig(7.1). Calibration considerations relevant to the Power Meter are explained in Appendix D.1.

The results obtained for various sample lengths for each of the rib guiding structures are presented in fig(7.3). From this graph it can be calculated that the optical loss, L of the rib guides are $L(R1)=12.5\text{dBcm}^{-1}$, $L(R2)=12.3\text{dBcm}^{-1}$, and $L(R3)=1.5\text{dBcm}^{-1}$. It was suspected that the major loss mechanism present in these guides was Free Carrier loss, due to the relatively high doping densities of the guiding regions. From theory, the loss due to Free Carriers in the rib structures is of the order of 0.215dBcm^{-1} for R1, and R2, and 0.022dBcm^{-1} for R3 [11]. Comparing these theoretical values to the experimental values shows, however, that the contribution to optical loss within these guides due to Free Carrier losses was not as large as was initially suspected, and that other loss mechanisms, such as scattering, are predominant. However, the values of L found for R1, R2, and R3 are reasonable in comparison to one another in that R2 has a shorter active length than R1, and therefore closer optical confinement. Further, R3 has an active layer doping density of the order of ten times less than that of R2, and R3, and therefore has a significantly lower optical loss.

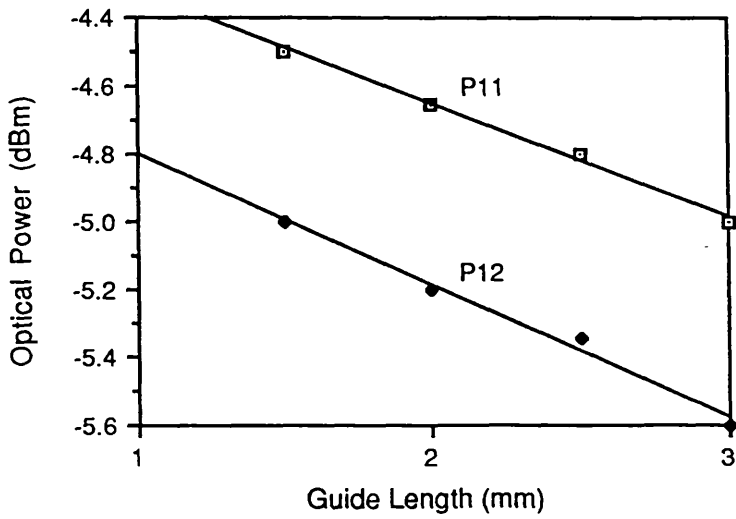
These results are also in good agreement with previously reported values of the optical loss of homojunction rib waveguides formed in GaAs [85], wherein it was noted that the two major contributions to propagation loss were due to Free Carrier absorption, and scattering due to imperfections. Note further that the optical loss of samples of device R3, with and without a Schottky bonding pad, was measured. It was found through these measurements that the presence of the pad had no observable effect on the optical loss of the device.

Fig(7.4) shows similar experimental results for the photoelastic waveguides P11 and P12. From these graphs it can be seen that the losses in these structures are $L(P11)=3.2\text{dBcm}^{-1}$, and $L(P12)=4.0\text{dBcm}^{-1}$. The higher loss of the P12 samples,

Fig(7.3) Optical Losses Measured by Sequential Cleaving for Rib Guides R1, R2, and R3



Fig(7.4) Optical Losses Measured by Sequential Cleaving for Photoelastic Guides P11 and P12



in comparison to the P11 samples, is again probably due to the higher doping density of the guiding region of P12.

7.2 MICROWAVE EXPERIMENTS

7.2.1 Microstrip Circuit Design and Fabrication

Microwave tests could have been carried out in either rectangular metallic waveguide, or in microstrip or coplanar waveguide circuits [86]. With recent developments in monolithic microwave integrated circuit (MMIC) technology [87] it was decided however to carry the experiments out in microstrip. Microstrip has a number of advantages over coplanar transmission structures, eg. the mode of propagation in microstrip is almost TEM, allowing an easy approximate analysis and fabrication of wide band circuits. Further, simple transitions to and from coaxial circuits are feasible.

The configuration of microstrip waveguide is shown in fig(7.5). W is the strip width, and h the substrate thickness. The simplest method of microstrip analysis is the Quasi-Static approach in which the mode of wave propagation is assumed to be pure TEM [87]. Values of the characteristic impedance, Z_{om} of the microstrip line, and the phase constant, β can then be written as

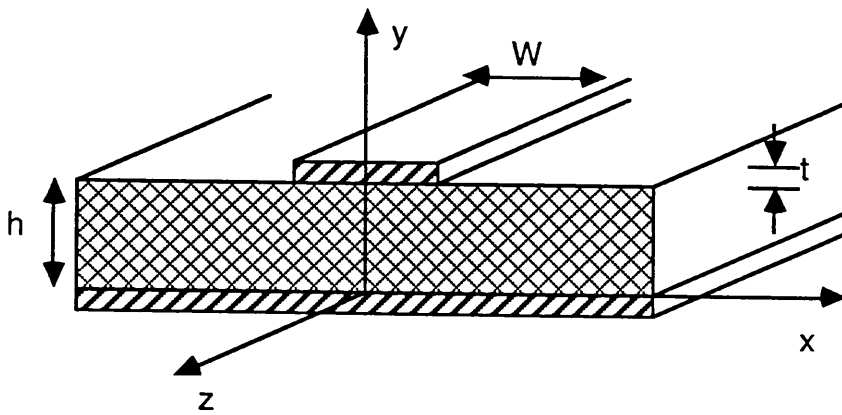
$$Z_{om} = Z_{om}^a \left[\frac{C_a}{C} \right]^{1/2} \quad \dots\dots 7.1$$

$$\text{and } \beta = \beta_o \left[\frac{C}{C_a} \right]^{1/2} \quad \dots\dots 7.2$$

where, C_a = capacitance per unit length of the microstrip configuration with the dielectric substrate replaced by air

C = capacitance per unit length of the microstrip configuration with the dielectric substrate present

Fig(7.5) Configuration of Microstrip Waveguide



$$Z_{Om}^a = \frac{1}{cC_a}$$

$$\beta_o = \frac{\omega}{c}$$

Formulaes for the impedance can thence be derived via a Modified Conformal Transformation method [88], explicitly relating both Z_{Om} in terms of W/h and ϵ_r (ie. analysis), and W/h in terms of Z_{Om} and ϵ_r (ie. synthesis), for both $W/h > 2$ and $W/h < 2$.

For the narrow strips (ie. $W/h < 2$) of interest here, it can be shown that [86]

$$\frac{2h}{W} = \frac{1}{4} e^{h'} - \frac{1}{2} e^{-h'} \quad \dots\dots\dots 7.3$$

where,

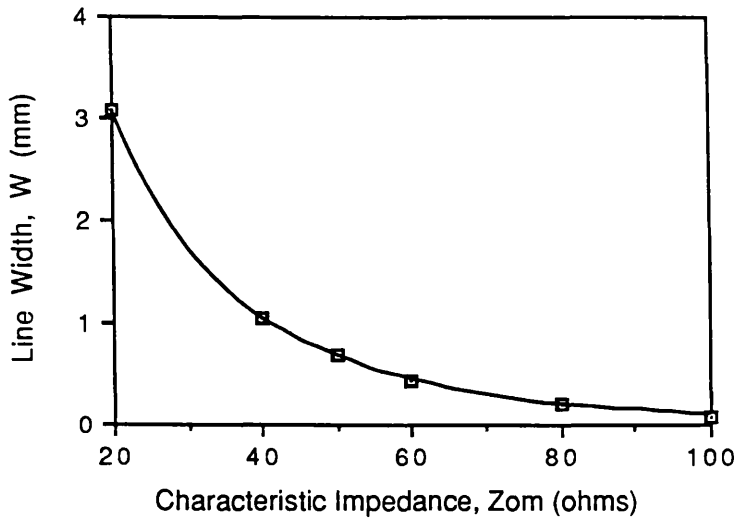
$$h' = \left[\frac{\epsilon_r + 1}{2} \right]^{1/2} \frac{Z_{Om}}{60} + \frac{\epsilon_r - 1}{\epsilon_r + 1} \left[0.226 + \frac{0.120}{\epsilon_r} \right] \quad \dots\dots\dots 7.4$$

It should be pointed out that in the Modified Conformal Transformation method discussed above, the thickness of the microstrip conductor is ignored, and the analysis is restricted to an open microstrip without any enclosure.

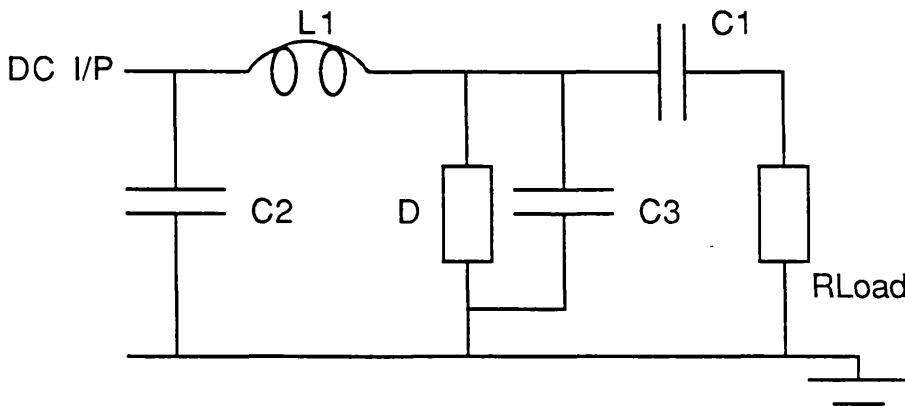
For the fabrication of the microstrip circuit 3M Copper Clad PTFE, Microwave Substrate was used. This substrate had a dielectric constant, $\epsilon_r = 11$, a substrate thickness, $h = 780 \mu m$, and a metal thickness, $t = 30 \mu m$. Using this data in conjunction with equations(7.3) and (7.4), the required strip width, W , for any given characteristic impedance, Z_{Om} , could be found. The results of such calculations are shown in fig(7.6). Note that for $Z_{Om} = 50 \Omega$, $W = 0.68 mm$

The circuit diagram of the required microstrip circuit is shown in fig(7.7). This circuit allowed the diode to be operated in Transit Time Mode. The purpose of the capacitor C_1 is to block DC from being applied to the microwave output, since a DC signal applied to the input of the spectrum analyser will damage it. Further, the

Fig(7.6) Width of Microstrip Line, W versus Characteristic Impedance, Z_{om} for 3M Copper Clad, PTFE Microwave Substrate



Fig(7.7) Circuit Diagram of Microstrip Circuit for Microwave Experiments



$C1 = 3.6\text{pF}$; $C2 = 1\text{nF}$; $C3 = \text{Gunn Diode Capacitance}$; $L1 = 3.6\text{pH}$; $R_{Load} = 50 \Omega$;
 $D = \text{Gunn Diode}$

inductor L_1 prevents the microwave output from reaching the DC input terminals. C_1 is a surface mounted, chip type capacitor, and L_1 is a spiral inductor fabricated on the surface of the microstrip substrate [4]. C_2 is a filtering capacitor, the purpose of which is to remove any high frequency components from the input signal.

The procedure for fabricating the microstrip boards was as follows. First, the boards were chopped to the correct size (ie. approximately 5cm x 4cm) using a guillotine. Next, each board was ultrasonically cleaned in genklene, methanol, acetone, and finally deionised water, for 5mins each. Each board was then etched in a solution of 4:1, H_2O :Ammonia for 1min, rinsed in deionised water, blow dried in nitrogen, and then dried on a hotplate. Next, each board was coated on one side with AZ1350J which was spun on at 4000rpm for 20secs, and baked for 30mins at $85^{\circ}C$. The other side of each board was then similarly coated with AZ1350J. One side of each board was then exposed on the contact printer for 5mins, using a chromium mask to define the required microstrip pattern. The boards were then developed in a mixture of 1:1, H_2O :Microposit Developer for approximately 75secs. In this way a photoresist mask was defined which corresponded to the desired copper pattern.

Next, each board was placed in an ultrasonic bath of ferric chloride, ie. copper etch, at a temperature of $45^{\circ}C$. It was found that a board required around 6mins in the ferric chloride bath in order to etch away the unwanted copper. The boards were then rinsed in water to remove any excess ferric chloride, and placed in a beaker of acetone to remove the photoresist mask on the top surface, and also to remove the photoresist which had been protecting the bottom copper surface. Each board was then rinsed in deionised water, blow dried in nitrogen, and dried on a hotplate.

To complete the fabrication of the microstrip circuit, the surface mounted capacitor, C_1 , had to be soldered into place. This was done by first tinning the microstrip lines on each side of the position in which C_1 was to be placed. Silver loaded solder was recommended for use with these surface mounted capacitors. Next,

C_1 was held in position using a pair of tweezers, and with the aid of a binocular microscope, it was ensured, using a soldering iron, that the end metallic contacts of C_1 were covered with the solder which had already been used to tin the microstrip lines.

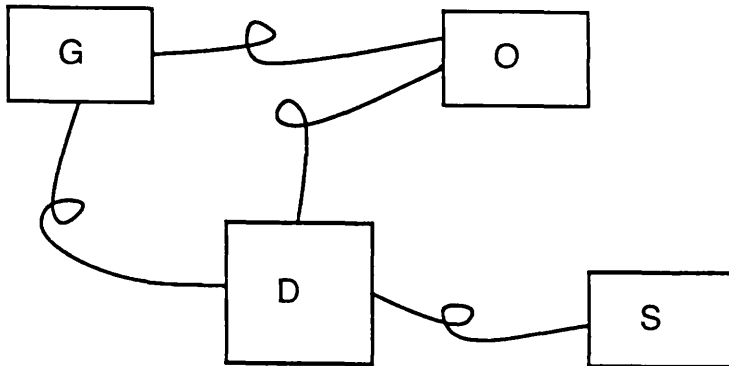
7.2.2 Experimental Results

The experimental apparatus used for the microwave experiments is shown in fig(7.8). The pulsed DC input to the device was supplied via an HP214A Pulse Generator. This generator could deliver a maximum of 5amps. The microwave output was monitored by a spectrum analyser. Two spectrum analysers were available. These were a Tektronix 492 Spectrum Analyser with a frequency range of 50KHz to 21GHz, and a Tektronix 7L18 Spectrum Analyser with a potential frequency range of 1.5GHz to 60.5GHz. The 7L18 was a plug in unit for the Tektronix 7000 Series. An oscilloscope was used to monitor the output from the pulse generator, and also the input to the microstrip circuit after filtering capacitor C_2 .

Microwave experiments were carried out on spot contact diodes fabricated on each of CPM268, CPM351, and CPM411, in order to ascertain whether each of these pieces of material was suitable for the fabrication of Gunn diodes, ie. whether the material oscillated. Microwave experiments were also carried out on the vertical diode/rib waveguide device R3, with Schottky contact bonding pads, as well as on the planar diode/photoelastic waveguide device P12. The results for each of these devices is presented below.

The procedure for the microwave experiments was as follows. A signal having a pulse length of $10\mu\text{sec}$, and a duty ratio of 0.1 (to prevent thermal runaway), was applied to the microstrip circuit. The amplitude of the pulse was varied from 0V to around twice the expected threshold voltage, V_T , in 0.5V steps. The experimental results for each of the pieces of vertical material are shown in table(7.1). The Tektronix 492 Spectrum Analyser was used to test CPM268, and CPM351, while the Tektronix 7L18 Spectrum Analyser was used to test CPM411, due to the higher

Fig(7.8) Apparatus used in the Microwave Experiments



D = Device Mounted on Microstrip Board within Stainless Steel Cavity ; G = Pulse Generator ; S = Spectrum Analyser ; O = Oscilloscope

Table(7.1) Results of Microwave Experiments carried out on Vertical Spot Contact Diodes

Material	Threshold Voltage, V_T (V)	Oscillation Frequency, f_r (GHz)	Domain Velocity, v_{dom} (ms^{-1})
CPM268	2.8	12.7	0.99×10^5
CPM351	1.9	19.5	0.85×10^5
CPM411	1.6	24.0	0.96×10^5

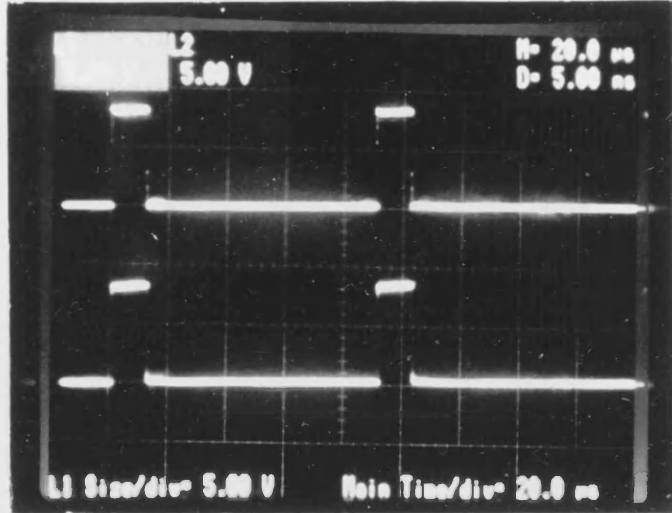
oscillation frequency, f_T , of CPM411. As can be seen from these results, the threshold voltage, V_T , for oscillation of each of these materials is in relatively good agreement with the theoretical threshold voltages presented in fig(5.13), bearing in mind the variation in the active layer length, as found by the Polaron measurement, from that of the design specification. Further, taking the active layers to be as found by the Polaron measurement, ie. $7.8\mu\text{m}$, $4.36\mu\text{m}$, and $4.0\mu\text{m}$, for CPM268, CPM351, and CPM411 respectively, then the corresponding domain velocities, $v_{\text{dom}}=f.f_T$ can also be found, as shown in table(7.1), where, f = the active layer length, and f_T = the Transit Time Mode oscillation frequency.

Shown in figs(7.9)(a) and (b) are: (a) the filtered input to the microstrip circuit; and (b) the corresponding output of the Gunn diode, as observed on the Tektronix 492 Spectrum Analyser, for an $80\mu\text{m}$ spot contact diode formed on CPM351. The electrical to microwave conversion efficiency, H , of this device may thus be calculated from the data of fig(5.14) when used in conjunction with the data of fig(7.9). The conversion efficiency, H , is given by the ratio of the microwave power, P_m out, to the electrical power, P_e in. From fig(7.9)(a), $P_e=0.1 \times V^2/R$, (where, $V=7.0\text{V}$, and $R=0.234\Omega$), and $P_m=0.398\text{W}$. This gives that $H \approx 1.9\%$. The factor of 0.1 is included in the calculation of the electrical power since the bias signal is pulsed with a duty cycle of 0.1

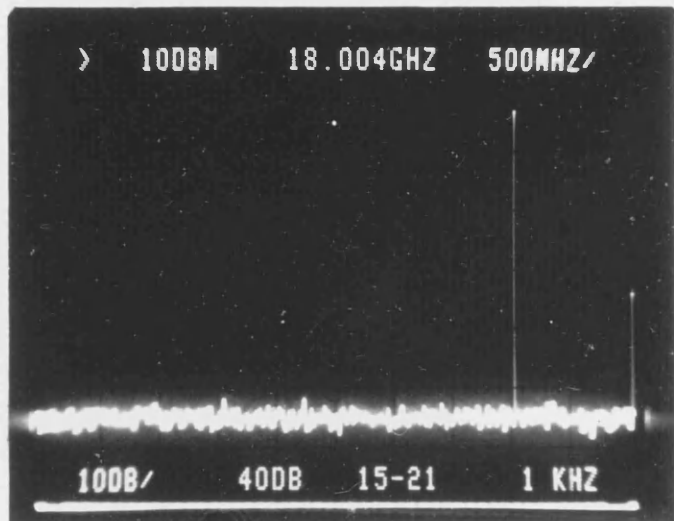
Microwave tests were similarly carried out on the vertical diode/rib waveguide device R3 (fabricated on CPM411), incorporating a Schottky bonding pad. Again the device was supplied with a signal having a pulse length of $10\mu\text{sec}$, and a duty ratio of 0.1. As for the vertical spot diodes fabricated on CPM411, the vertical/rib device was found to have a threshold voltage, $V_T=1.6\text{V}$, and oscillate in Transit Time Mode at a frequency, $f_T=24\text{GHz}$. The microwave output of the stripe contact diode for an input voltage, $V_{\text{bias}}=1.8\text{V}$, is shown in fig(7.10) (where the RF attenuation of the analyser is 90dB). Again, the electrical to microwave conversion efficiency, H , may be calculated. From fig(7.10), the microwave output power, $P_m=10\text{mW}$. Also, the electrical input power, $P_e=1.76\text{W}$, since $V_{\text{bias}}=1.8\text{V}$, and the resistance of the device, $R=1.84\Omega$. Hence, $H \approx 5\%$. This value of H should, however, be viewed with

Fig(7.9) Operation of 80 μ m Spot Diode on CPM351
in Pulsed Transit Time Mode

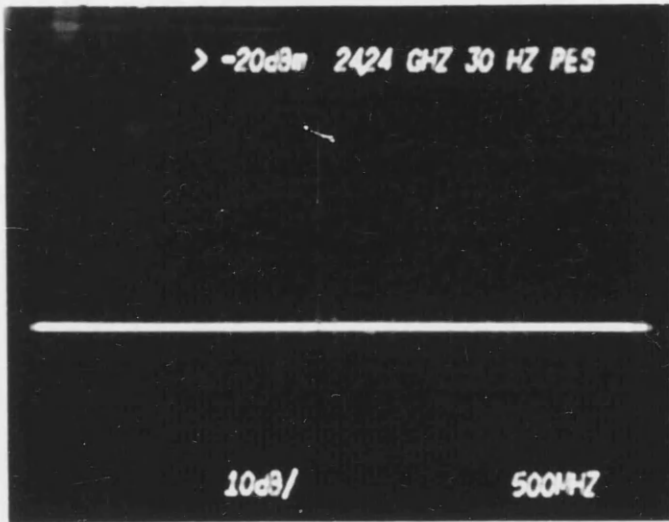
- (a) Electrical Input Signal to Microwave Circuit ;
Rep. Rate = 10kHz ; Pulse Width = 10 μ sec ;
Pulse Height = 8.0V



- (b) Microwave Output as Observed on the Tektronix
492 Spectrum Analyser ; f_r = 19.5GHz ; Centre
Frequency = 18GHz ; Resolution Bandwidth =
1kHz ; Frequency Span/Div = 500MHz ; Ref.
Level = 10dBm ; RF Attenuation = 40dB



Fig(7.10) Microwave Output as Observed on the Tektronix 7L18 Spectrum Analyser for the Vertical / Rib Device R3 ; $f_r = 24\text{GHz}$; Centre Frequency = 24.24GHz ; Resolution Bandwidth = 30Hz ; Frequency Span/Div = 500MHz ; Ref. Level = -20dBm



some suspicion since the 24GHz oscillation signal was observed and measured using the Tektronix 7L18 Spectrum Analyser. This analyser should only be used in conjunction with an external mixer above a frequency of 18GHz. No compatible external mixer was however available. It should be noted that this is the first report of oscillations observed in such a vertical, stripe contact, Gunn diode.

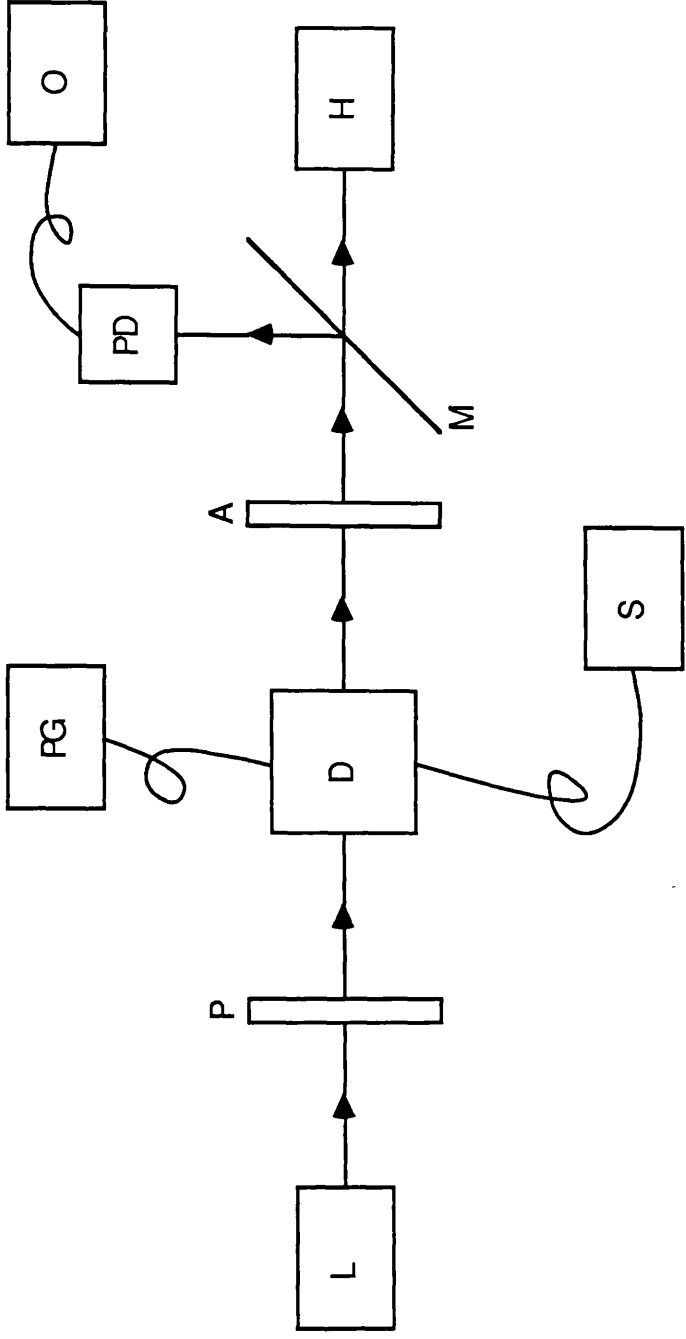
Microwave tests were also carried out on the planar diode device, P12 fabricated from A#31. This device should have had a threshold voltage, V_T , of around 35V. However, no oscillations were observed from this sample. This could be explained as being a result of the formation of a shorting channel between the cathode and the anode, ie. the creation of current filaments resulting from impact ionisation associated with the passage of the high-field domain across the diode [89]. This was substantiated by observing that a discolouration of the material near the anode region appeared after the testing of these devices, implying partial melting near the anode region.

7.3 ELECTRO-OPTIC EXPERIMENTS

The purpose of the experiments described in this section was to investigate the potential of the device R3 as an integrated optical modulator. Presented in this section, therefore, are experimental modulation results for the vertical diode/rib waveguide device R3, incorporating a Schottky contact bonding pad. Results are presented for wavelengths, λ , of $1.15\mu\text{m}$ and 905nm. Also presented is an estimate of the effective Electro-Optic coefficient, r_{41} , of GaAs, at $\lambda=1.15\mu\text{m}$ and $\lambda=905\text{nm}$, at a frequency of 24GHz, as well as an estimate of the effective Electro-Absorption coefficient, α , at $\lambda=905\text{nm}$.

A block diagram of the experimental apparatus is shown in fig(7.11). As in purely microwave experiments, the device was mounted and bonded on a microstrip circuit fabricated on 3M PTFE Cu Clad Microwave Substrate. The circuit diagram was already shown in fig(7.7). This circuit allowed the device to be operated in Transit Time Mode. As was shown in fig(6.22), the circuit itself was mounted within

Fig(7.11) Block Diagram of the Experimental Apparatus used in Electro-Optic Experiments



L = Laser ; P = Polariser ; D = Mounted Device ; PG = Pulse Generator ; S = Spectrum Analyser ; A = Analyser ; M = Partially Reflecting Mirror ; H = Hamamatsu IR Camera ; PD = Photodiode ; O = Oscilloscope or Spectrum Analyser

a stainless steel box, identical to that which was used for microwave experiments, except that the box used for integrated experiments provided slits in the centre of the longer sides of the box. Optical access to the mounted device was provided by means of these slits.

As can also be seen from fig(6.22), the laser beam was end-fired into and out of the sample by means of Flat Mounted Refracting Microscope Objective lenses. These lenses had a focal length, $F=51\text{mm}$ and a numerical aperture, $NA=0.08$, therefore giving a resolution, $S=1.22\lambda/2NA \approx 8.7\mu\text{m}$ at $1.15\mu\text{m}$.

For all experiments a precision IR linear polariser/analyser unit was used. This unit had an effective wavelength operating range of approximately 800nm to $2.2\mu\text{m}$, and an average transmittance of about 35% over that spectral range. For all experiments the polariser was set at an angle of 45° to the domain field, ie. to the vertical. The analyser was set perpendicular to the polariser for Electro-Optic measurements, and parallel to the polariser for Electro-Absorption measurements.

This experimental arrangement was used since it avoids the complication of having to employ a phase coherent detection system. This is because the polariser allows the linearly polarised optical beam to be introduced into the rib guide at 45° to the x and y axes of the guide. Because the phase change for Electro-Optic modulation occurs only for waves polarised in the y direction (ie. parallel to the material surface), and not for those polarised in the x direction, a rotation of the polarisation vector will occur as the waves propagate along the z direction. This change of polarisation due to Electro-Optic modulation can then be detected by a polarisation sensitive detector, or by placing the analyser, ie. polarisation-sensitive filter, ahead of the detector.

In a similar way, for Electro-Absorption modulation the input beam may be introduced into the guide at an angle of 45° to the x and y axes. However, for this type of modulation no polarisation rotation occurs, only a change in the intensity of the beam polarised along the direction in which the polariser is set. The analyser was consequently set parallel to the polariser in this case.

The partially reflecting mirror, or beam splitter, which was used was of the

pellicle (extra thin construction) type, having an estimated transmission/reflectance ratio at $\lambda=1.15\mu\text{m}$ of 30:45. The major advantage of such a beam splitter was the elimination of second surface reflections, or 'ghost images'. This is because the beam splitter is fabricated from an elastic membrane of cellulose nitrate, mounted on an optically flat aluminium alloy frame. Reflections from the front and back of the membrane are therefore essentially superimposed.

In order to detect the modulated optical signal emerging from the output of the device, either a fast diode, having a typical rise time of the order of 50ps, or a slow diode, having a typical rise time of the order of 200ns, may be used. The fast diode may be used in conjunction with a spectrum analyser to directly detect and measure the modulation. The slow diode may, however, alternatively be used in conjunction with an oscilloscope to detect the averaged optical modulation, and hence to estimate the magnitude of the Electro-Optic modulation depth, η_{EO} . The analysis required to extract the modulation depth from the average signal detected by the slow diode is somewhat involved, and is explained in detail in Appendix E. From Appendix E it can be seen that for Electro-Optic modulation the modulation depth

$$\eta_{EO} = \frac{4\pi I_{\perp}}{I_0} \quad \dots\dots\dots 7.5$$

where, I_{\perp} = average signal received with the polariser and analyser in the perpendicular arrangement

I_0 = input optical intensity

Further, for Electro-Absorption modulation the modulation depth is

$$\eta_{EA} = \cos \left\{ 2 \left[1 - \frac{2I_{\parallel}}{I_0} \right]^{1/2} \right\} \quad \dots\dots\dots 7.6$$

where, I_{\parallel} = average signal received with the polariser and analyser in the parallel arrangement

From equation(7.5) it can be seen that the modulation depth, η_{EO} of the Electro-Optic modulation signal can be calculated, provided that the averaged modulation signal, with the polariser and analyser in the perpendicular arrangement, I_{\perp} , can be measured, and the input intensity, I_O , is known. Similarly, from equation(7.6) it can be seen that the modulation depth, η_{EA} of the Electro-Absorption modulation signal can be calculated, if the averaged modulation signal with the polariser and analyser set parallel, I_{\parallel} , can be measured, and I_O is known.

A suitable fast diode which was found was the HSD30 supplied by Instrument Technology Ltd. (ITL). A suitable slow diode which was found was the GM8 supplied by Rofin-Sinar UK Ltd.. The required data for these diodes is given in Appendix D.2.

7.3.1 Experiments at a Wavelength of $1.15\mu\text{m}$

There are three aspects to the operation of the integrated vertical/rib device to be considered. These are: the purely optical behaviour of the device acting as an optical waveguide, the purely microwave (electrical) behaviour of the device acting as a Gunn diode, and the interaction between the microwave and optical actions. In the experiments of this section these aspects were addressed consecutively

Considering the device first as an optical waveguide, at $\lambda=1.15\mu\text{m}$ an NEC He:Ne laser with a CW output of approximately 10mW was used. The beam was focussed by means of the Flat Refracting Microscope Objective lenses to a spot size of approximately $20\mu\text{m}$. The Hamamatsu IR Camera, controller and video monitor were then aligned to the optical beam. The device, mounted within the microwave cavity, was then placed between the two lenses. The position of the device was then adjusted, using the x, y stage, in order that the beam was end-fired into and out of the device by means of the objective lenses. The Hamamatsu IR Camera was then used in order to monitor the output guided optical beam from the rib device.

Next, considering the device as a Gunn diode, the device was again electrically

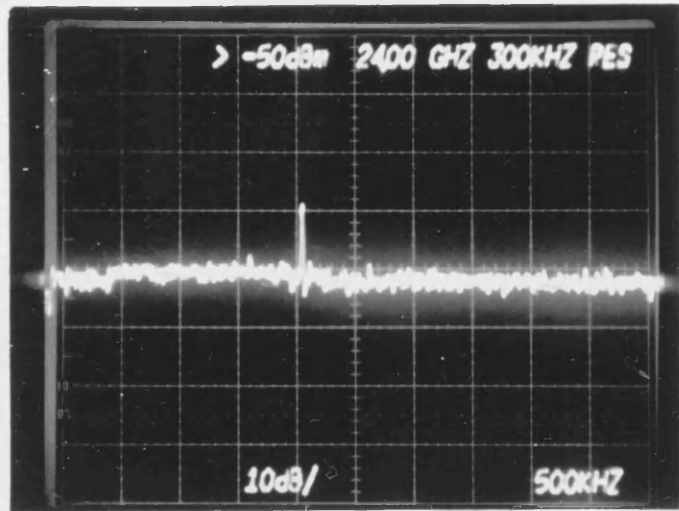
biased using the HP214A Pulse Generator. A negative going rectangular pulse of $10\mu\text{s}$ duration was applied to the cathode, ie. top surface, of the vertical/rib device. The electrical signal again had a duty cycle of 0.1 to prevent thermal runaway. The input pulse height was adjusted from 0V in 0.1V steps. Monitoring the output of the microstrip circuit, using the Tektronix 7L18 Spectrum Analyser, the device was found to oscillate at a frequency of 24GHz, and have an input threshold voltage of 1.6V. This was already explained in the results of section(7.2).

The device was at this stage acting both as an optical waveguide and as a Gunn diode. It was therefore now possible to monitor and measure the interaction between the electrical and the optical actions of the device. The modulated optical signal was observed using the fast photodiode in conjunction with the Tektronix 7L18 Spectrum Analyser. With the polariser and analyser in the perpendicular arrangement modulation was successfully observed at a frequency of 24GHz. The modulation signal detected by the fast photodiode and spectrum analyser, in the perpendicular polariser/analyser arrangement, is shown in fig(7.12). This is the first reported observation of Electro–Optic modulation due to propagating Gunn domains within an integrated optical waveguide.

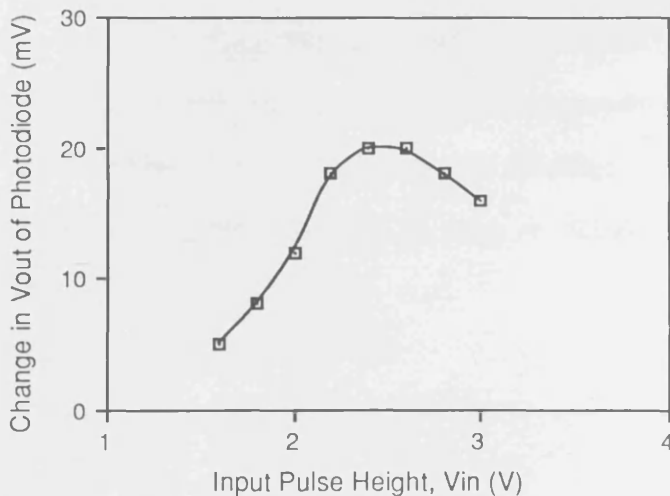
At this wavelength, with the polariser and analyser set in the parallel arrangement, no modulation was observed. This is in agreement with the calculations of section(5.4.2) which suggest that no Electro–Absorption modulation should be seen at such a long wavelength. In view of the original calculations of section(5.4.2), the experimental results also substantiate that electric field induced effects outweigh Free Carrier effects, and that Free Carrier effects are indeed negligible. This may be concluded since such effects should be crystallographically independent and should therefore, if present, be observed in the parallel polariser/analyser arrangement.

Although the above results clearly show the presence of Electro–Optic modulation due to propagating Gunn domains, using this detection system no reliable measurements of the magnitude of the received modulation signal could be made. This is because, as was explained in section(7.2.2), the Tektronix 7L18 Spectrum Analyser should in fact be used with an external mixer above a frequency of

Fig(7.12) Electro-Optic Modulation Signal for $\lambda = 1.15\mu\text{m}$, Detected by an ITL HSD30 Photodiode, and Tektronix 7L18 Spectrum Analyser ; $V_{in} = 1.8\text{V}$; Centre Frequency = 24GHz ; Resolution Bandwidth = 300kHz ; Frequency Span/Div = 500kHz ; Ref. Level = -50dBm



Fig(7.13) Averaged Modulation Signal, Detected by a GM8 Photodiode and Oscilloscope, for Electro-Optic Modulation, $\lambda = 1.15\mu\text{m}$



18GHz.

In order to measure and quantify the Electro–Optic modulation effect due to Gunn domains, the slow Ge photodiode, type GM8, and oscilloscope were used to measure the averaged received intensity. The results obtained using the slow diode are shown in fig(7.13). As can be seen from this, the Electro–Optic modulation effect at $\lambda=1.15\mu\text{m}$, due to propagating domains, tends to increase with increasing bias voltage up to a bias voltage, V_{bias} , of approximately 2.3V. This behaviour was predicted by the approximate simulation results of section(5.4.1) (using an approximate velocity–field characteristic and a constant diffusion coefficient), and by the semi–analytical simulation results (using an analytical velocity–field characteristic and a constant diffusion coefficient). This tendency may be explained as being due to diffusion effects occurring within the domain, causing charge held within the domain to diffuse out, therefore leading to a reduction in the peak domain field.

Using the Photodyne 22XLA Fibre Optic Power Meter, the input optical power, P_{in} , to the rib guide was measured to be $P_{\text{in}}=-10.7\text{dBm}=0.08\text{mW}$. Since the responsivity of the diode was 0.425AW^{-1} at $\lambda=1.15\mu\text{m}$, and since the impedance of the photodiode receiver circuit was set to $47\text{k}\Omega$, then the corresponding unmodulated input voltage, V_{O} , to the oscilloscope was equal to 1.8V. This input voltage is directly proportional to the input optical intensity, I_{O} . Similarly, the average change in the output voltage, V_{Out} , of the photodiode due to domain modulation is directly proportional to the average modulated signal, I_{\perp} . From fig(7.13), the maximum change in V_{Out} was measured to be 20mV. Consequently, using these results in conjunction with equation(7.5), the corresponding value of the peak rotation factor is $A=0.138$. Hence, the maximum Electro–Optic modulation depth, η_{EO} , may be found since, from Appendix E, $\eta_{\text{EO}} = I_{\text{EO}}/I_{\text{O}} = |\sin A| = 13.8\%$, when A is small.

7.3.2 Experiments at a Wavelength of 905nm

In the same way as for a wavelength of $1.15\mu\text{m}$, experiments were carried out at a wavelength of 905nm, in both the perpendicular and parallel polariser/analyser arrangements. An RCA Type SG2001 GaAs laser diode was used. The laser diode was mounted on a head unit which also housed a capacitor–discharge SCR current pulser circuit. The current pulser was fed with a variable DC voltage of 0–300V, and was triggered by a 1KHz fixed–frequency oscillator. The manufacturers published data for the diode indicated a minimum total peak radiant power of 1W, and a peak forward current of 10A.

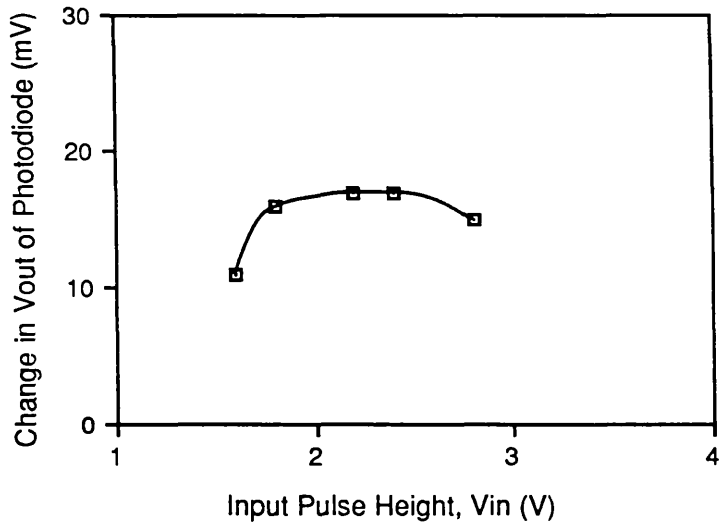
Using the fast photodiode and the spectrum analyser, Electro–Optic modulation was observed at $\lambda=905\text{nm}$, with the polariser and analyser in the perpendicular arrangement. Further, with the analyser set parallel to the polariser, modulation was detected due to the Electro–Absorption effect. Both of these modulation signals were observed to have the same frequency as the Transit Time oscillation frequency of the Gunn diode, ie. 24GHz.

Again, the slow Ge photodiode, type GM8, and oscilloscope were used to measure the averaged perturbation in the received intensity due to domain modulation. The results obtained using this diode are shown in fig(7.14)(a) and (b) for Electro–Optic and Electro–Absorption modulation respectively. Again, it may be noticed that each of these modulation signals peaks at an input bias voltage of around 2.3V

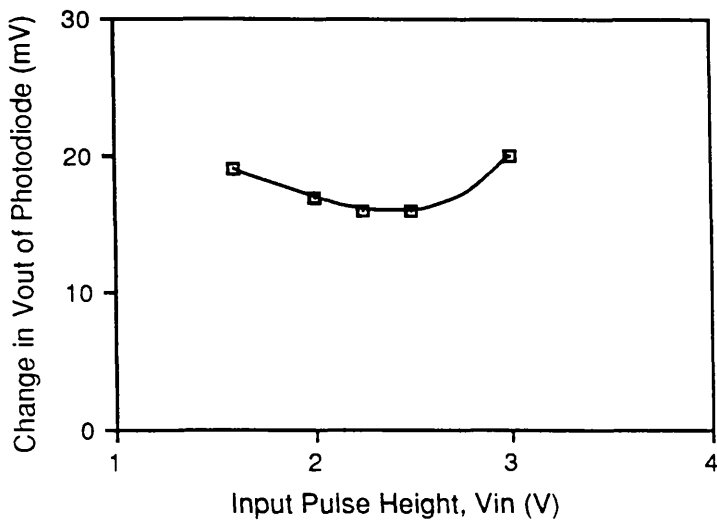
Using the Photodyne 22XLA Fibre Optic Power Meter the input optical power, P_{in} , to the rib guide was measured to be $P_{\text{in}} = -7.9\text{dBm} = 0.16\text{mW}$. The responsivity of the diode was 0.225AW^{-1} at $\lambda=905\text{nm}$, and the impedance of the photodiode circuit was again $47\text{k}\Omega$. Using this data in the same way as for $\lambda=1.15\mu\text{m}$, and observing from fig(7.14)(a) that the maximum change in the output voltage of the photodiode in the perpendicular polariser/analyser arrangement was 17mV, the corresponding value of the peak rotation factor, A , may be calculated to be $A=0.118$ using equation(7.5). Further, the corresponding maximum modulation depth

Fig(7.14) Averaged Modulation Signal, Detected by a GM8 Photodiode and Oscilloscope, $\lambda = 905\text{nm}$

(a) For Electro-Optic Modulation



(b) For Electro-Absorption Modulation



for Electro-Optic modulation, for $\lambda=905\text{nm}$, is therefore given by $\eta_{EO}=11.8\%$, since A is small.

Also, it can be seen from fig(7.14)(b) that the maximum change in the output voltage of the photodiode in the parallel arrangement was 4mV . Hence, using equation(7.6) in conjunction with the above data, the peak rotation factor is $A=1.146$. Thus, the maximum modulation depth, η_{EA} due to Electro-Absorption modulation, may be found, since from Appendix E, $\eta_{EA} = I_{EA}/I_O = \cos A = 41.2\%$.

Electro-Optic modulation, giving rise to polarisation rotation, is observed only in the perpendicular polariser/analyser arrangement. Further, Electro-Absorption modulation can only be observed and measured in the parallel polariser/analyser arrangement, where Electro-Absorption is the only modulation mechanism present. Electro-Absorption modulation is however also present in the perpendicular arrangement. For this reason, a quantitative correction to the observed Electro-Optic effect can be made using the Electro-Absorption results.

The value of the modulation depth, η_{EO} for the Electro-Optic effect, for $\lambda=905\text{nm}$, should therefore be corrected by taking the magnitude of the Electro-Absorption effect into account. After this correction, the value of η_{EO} becomes higher by an amount equal to η_{EA} , ie. since $\eta_{EA}=41.2\%$, then the corrected value of $\eta_{EO}=16.7\%$. This correction indicates that the experimental values of η_{EO} are in agreement with the theoretical predictions of table(5.6) which suggest a stronger influence due to the Linear Electro-Optic effect at $\lambda=905\text{nm}$ than at $\lambda=1.15\mu\text{m}$.

It should be noted that the sample used for the above experiments, at $\lambda=1.15\mu\text{m}$ and at $\lambda=905\text{nm}$, was 2.5mm long, and was oriented along the (011) crystal direction. Samples oriented along the $(0\tau1)$ crystal direction were observed to have a similar behaviour, in that at $\lambda=1.15\mu\text{m}$ only Electro-Optic modulation was observed, whereas at $\lambda=905\text{nm}$ both Electro-Optic and Electro-Absorption modulation were observed. Further, the Electro-Optic effect produced by the $(0\tau1)$ samples was substantially the same as that produced by samples oriented along

(011). This was because the only difference in the operation of the samples oriented along different directions is that those oriented along (011) will give a positive phase change, whereas those oriented along (0 $\bar{1}$ 1) will give a negative phase change. This difference in the effect was not however observable by the detection system which was used.

7.3.3 Calculation of Electro-Optic and Electro-Absorption Coefficients

According to the theory of the Electro-Optic effect, the modulation depth is given by [8]

$$\eta_{EO} = \frac{I_{EO}}{I_O} = \sin^2 \left[\frac{1}{2} \Gamma \right] \quad \dots\dots\dots 7.7$$

where, Γ = the retardation [43]

$$= \left[\frac{\pi}{\lambda} \right] n^3 r_{41} E_{dom} l$$

$$n = 3.467554 \quad \text{at } \lambda = 1.15 \mu\text{m}$$

$$= 3.587480 \quad \text{at } \lambda = 905 \text{nm}$$

$$l = \text{length of the sample} = 2.5 \text{mm}$$

E_{dom} = peak domain field

$$\text{ie. } \frac{1}{r_{41}} = \left[\frac{\pi}{\lambda} \right] n^3 E_{dom} l \frac{1}{\Gamma} \quad \dots\dots\dots 7.8$$

Thus, it can be seen that an estimate can be made of the Electro-Optic coefficient, r_{41} , of the material, for any given wavelength, λ , if the retardation, Γ , is known and an estimate can be made of the peak field, E_{dom} within the domain. No direct measurement of E_{dom} could be made in the short vertical diode under consideration.

However, an estimate of E_{dom} could be obtained via the theoretical simulation results of section(5.4.1). The estimated values of r_{41} , at a modulation frequency of

24GHz, are shown in table(7.2). The results are presented for: (a) the approximate simulation results; (b) the semi-analytical simulation results; and (c) the analytical simulation results. Note that for $\lambda=905\text{nm}$ the corrected value of η_{EO} ($=16.7\%$) was used. Note also that the calculations presented in table(7.2) assume a constant value of electric field, equal to E_{dom} , across the length of the domain. The values of r_{41} given in table(7.2) agree well with those given by Walsh [93], who reported a variation in r_{41} from $1.2 \times 10^{-12} \text{mV}^{-1}$ to $1.6 \times 10^{-12} \text{mV}^{-1}$ over the wavelength range $1\mu\text{m}$ to $3\mu\text{m}$.

An estimate of the value of the absorption coefficient, α , of the observed Electro-Absorption effect, at $\lambda=905\text{nm}$, may also be made since

$$\eta_{\text{EA}} = \frac{I_{\text{EA}}}{I_0} = e^{-\alpha l} = 41.2\% \quad \dots\dots\dots 7.9$$

Using equation(7.9) the effective absorption coefficient, $\alpha = 355\text{cm}^{-1}$. This compares favourably with the values of α calculated from the simulation results presented in table(5.6)(b).

Table(7.2) Calculated Values of r_{41} of GaAs at 24GHz

Wavelength	Simulation Method	E_{dom} (kVcm ⁻¹)	η_{EA} (%)	$r_{41} \times 10^{-12}$ (mV ⁻¹)
1.15 μ m	Approximate	27.079	13.8	0.9872
	Semi-analytical	18.307	13.8	1.4602
	Analytical	16.074	13.8	1.6631
905nm	Approximate	27.079	16.7	0.9860
	Semi-analytical	18.307	16.7	1.4585
	Analytical	16.074	16.7	1.6612

CHAPTER 8

SUMMARY OF RESULTS, AND FUTURE WORK

8.1 CONCLUSIONS

The project was successful in meeting the initial aims outlined in section(1.2), since the investigations of section(7.3), and the results presented therein, clearly indicate for the first time modulation of a guided optical carrier wave due to effects introduced by the electric field associated with a propagating Gunn domain.

Whereas at a wavelength, $\lambda=1.15\mu\text{m}$ modulation was observed to arise solely from the Linear Electro-Optic effect, at $\lambda=905\text{nm}$ modulation was observed due to both the Linear Electro-Optic effect and the Electro-Absorption effect, Electro-Absorption modulation being particularly strong. At $\lambda=1.15\mu\text{m}$ the modulation depth of the optical guided wave, due to the Linear Electro-Optic effect, η_{EO} , was found to be 13.8%, whereas at $\lambda=905\text{nm}$, η_{EO} was found to be 11.8%.

It was further found that at $\lambda=905\text{nm}$ the modulation depth due to the Electro-Absorption effect, η_{EA} , was 41.2%. A quantitative correction could thence be made to the observed Electro-Optic effect at $\lambda=905\text{nm}$. Taking into account this correction, η_{EO} at $\lambda=905\text{nm}$ becomes 41.2% higher, ie. 16.6%.

Since direct measurement of the electric field within the domain of the vertical device was not possible, the results of the computer simulation program, GUNNSIM, were used in conjunction with the experimental results to obtain an estimate of the Electro-Optic coefficient, r_{41} , at $\lambda=1.15\mu\text{m}$ and $\lambda=905\text{nm}$. These values were shown in table(7.2). The values found were in agreement with previously reported results at lower frequencies. Further, an estimate of the Electro-Absorption coefficient, α , was calculated and found to be equal to 355cm^{-1} . This was in reasonable agreement with the estimated theoretical values presented in section(5.4.2).

Previous work relating to optical devices operating in association with Gunn diodes have, for example, demonstrated the mutual phase-locking of a coupled laser diode and Gunn diode, oscillating at a frequency of 1.249GHz [94].

Another previous work integrated a laser diode and a Gunn diode on a semi-insulating substrate, the two devices being integrated in series, such that the laser acted as one of the Gunn oscillator electrodes [95]. In this device oscillating current pulses, coming from the Gunn device, formed the injection current of the laser diode, such that the laser light was modulated at the frequency of the Gunn diode, ie. 1GHz.

Each of the above examples differs, however, from the device examined in the work presented herein. This is because the device R3 comprises a Gunn diode and an optical waveguide, not only operating in association with one another, but which are also combined within the same device structure.

The device also differs from those which have been considered in previously reported experiments investigating the interaction between propagating domains and an optical signal, since the device provides means for guiding the optical radiation within a rib optical waveguide. This obviates the disadvantages of the prior work, eg. by Cohen *et al* [7], and Ohta *et al* [8], which showed the mechanism of optical modulation due to propagating domains in bulk GaAs samples, but wherein the interaction was found to be weak in comparison to other Electro-Optic modulators, and of little practical value. Further, these samples required high bias voltages. It was found, by the experiments of section(7.3), that a much stronger interaction was obtained when the domain propagated through an integrated optical waveguide, and also that a much smaller operating voltage was required.

The results of section(7.3) did however substantiate previous work in that it was found that at a wavelength, $\lambda=1.15\mu\text{m}$, only Linear Electro-Optic modulation was observed, whereas at $\lambda=905\text{nm}$, Electro-Absorption as well as Linear Electro-Optic modulation was observed. It was also concluded from the experimental observations that, as was expected from the theoretical calculations of section(5.4.2), electric field induced perturbations in the optical characteristics of the device (ie. due to the Linear Electro-Optic or Electro-Absorption effects) far outweighed those due to Free Carrier effects (ie. the Free Carrier Plasma or Free Carrier Absorption effects).

If the device is compared with previously proposed Electro–Optic waveguide modulators, then it can be seen that the vertical diode/rib waveguide device, R3, differs from previous devices in that R3 depends for its operation not only on the presence or absence of a local perturbation in the optical characteristics, but also that this perturbation will propagate and may be controlled with regard to its magnitude by variation of the bias voltage [96],[97],[98],[99].

For example, the Electro–Optic modulator of Campbell *et al* [99] comprised an N^+ GaAs substrate, having a $2.5\mu\text{m}$ thick N^- type epilayer, with a narrow Schottky barrier stripe contact on the top surface. Light was thus confined underneath the contact when the Schottky contact was reverse biased. Campbell *et al* demonstrated: a modulation depth due to the Linear Electro–Optic effect of 95% at $\lambda=1.15\mu\text{m}$, and at $\lambda=1.06\mu\text{m}$, for a bias voltage of 40V; a detection limited modulation rate of 150MHz, with a potential maximum operating frequency and bandwidth of 1.2GHz; and a power requirement of around $3\mu\text{WMHz}^{-1}$.

It can therefore be seen that the vertical diode/rib waveguide device, R3, offers a considerably lower Electro–Optic modulation depth than the device of Campbell *et al*. R3 also has the disadvantage of a somewhat higher power requirement of around $115.6\mu\text{WMHz}^{-1}$ for a rib width of $5\mu\text{m}$, rising to $346.8\mu\text{WMHz}^{-1}$ for a rib width of $15\mu\text{m}$. This disadvantage of high electrical power consumption, and also the subsequent low electrical to microwave conversion efficiency, leading to the production of heat, is of course one of the major disadvantages of all Gunn diode devices.

The vertical/rib device does, however, have the advantages of having a considerably smaller operating voltage ($\approx 1.6\text{V}$), and a Transit Time Mode operating frequency of 24GHz. Further, if the Gunn diode is operated in Delayed Domain Mode, then the modulator could be used in conjunction with a received microwave signal of between 12GHz and 24GHz. The device thus offers a potential bandwidth of 12GHz.

8.2 FUTURE INVESTIGATIONS

As was explained in section(3.4), a Gunn diode may be operated in either a Constant Voltage or a Constant Current Mode. For the experiments of Chapter 7 the diodes were operated in the Constant Voltage Mode known as Transit Time Mode. In Transit Time Mode when a field, E_{bias} , higher than the required threshold voltage, E_T , is applied between the anode and the cathode of the device, a dipole domain forms, and the electric field outwith the domain falls below that of E_T to some quasi-DC level, E_R . The field outwith the domain will remain at this level until the domain is destroyed at the cathode, at which time the electric field throughout the device redistributes itself to the bias level which it was at before the domain originally nucleated. Another domain will then form and propagate, and the process repeat itself.

The important point to note here is that for one complete domain cycle the electric field at any given point within the diode will originally be E_{bias} , fall to E_R when the domain forms, peak at E_{dom} when the domain passes by, fall back to E_R when the domain is passed, and rise to E_{bias} when the domain is destroyed. This sequence then repeats itself when the next domain forms. The sequence is true for all Constant Voltage Modes, not only Transit Time Mode.

This means that there are essentially two occasions when the electric field at a given point changes. These are first when the domain passes over the point, and second when the domain is destroyed and renucleates. Both of these instances will give rise to electric field induced modulation effects occurring within the device. Both will also occur at the same microwave frequency, and can therefore not be distinguished. It can be seen from the simulation results of section(5.4.1) that E_R is of the order of two to three times less than E_{bias} , which is itself of the order of 1.5 to 4 times less than E_{dom} .

It is therefore obvious that for Constant Voltage Modes, although the change in electric field at any given point due to the domain propagating is greater than that due to the domain being destroyed, there are still two individual, but

indistinguishable, contributions to electric field induced optical modulation.

In order however that the only electric field induced modulation occurring within the device is produced by the propagating Gunn domain, the device may be operated in Constant Current Mode [21]. As was previously explained in section(3.4.2), in this mode of operation no redistribution of the electric field occurs throughout the diode when a domain is destroyed at the anode and renucleated at the cathode. This means that, for any given point, the sole perturbation in the electric field, and hence contribution to electric field induced optical modulation, will be due to the propagating domain. Further, in the Constant Current Mode of operation more than one domain can exist within the diode at any time. This mode may therefore offer even higher operating frequencies, and potential bandwidths, than the Constant Voltage Modes.

Any future work directed towards the planar diode/photoelastic waveguide device must of course repeat the experiments of section(7.3) in observing the interaction between the high-field domain and the guided light via the Linear Electro-Optic and Electro-Absorption effects. For the planar diode the electric field of the domain is directed along the surface of the material, ie. along the (100) crystal plane. The electric field is, therefore, perpendicular to the (011) plane if the guides are aligned along (011), or the (0 $\bar{1}$ 1) plane if the guides are aligned along (0 $\bar{1}$ 1). Accordingly, the theory of the Electro-Optic effect in zinc-blende crystals [43] suggests that the maximum phase retardation, along the direction of the guides, observed in the planar device, will be twice that observed in the vertical device for the same value of domain field.

It can be envisaged that the planar device could be biased by a DC electric field just below threshold. Domain formation could then be triggered by a pulse of light [100], as explained in section(4.3.2). The light could have photon energies either above or below the band gap energy of the material. This suggests that the Gunn diode could be controlled directly by optical pulses, or that the diode could be used as a high-speed detector.

If, however, the optical triggering of Gunn domains, and the Electro-Optic

interaction of these domains, are combined within the one device, then other potential applications emerge. For example, a domain could be triggered by a first pulsed light beam, and the Electro-Optical effects induced by the domain used to modulate a second guided light beam. The device would thus effectively have an all-optical switching function, the switching information being carried by the first light pulse. The device would resemble the planar diode/photoelastic waveguide device of fig(1.3)(c).

In operation, a first picosecond light pulse from a mode-locked laser would be input into the photoelastic guide on the inner edge of the cathode. This pulse would then trigger formation of a Gunn domain, which would propagate from cathode to anode, traversing the photoelastic guide on the inner edge of the anode. The field associated with the domain would alter the optical properties of the anode guide via the Linear Electro-Optic and Electro-Absorption effects. This alteration would then be detected by a second picosecond pulse input into the anode guide, this pulse being derived from the same laser as the first pulse, but being controllably delayed with respect to the first. The mechanism for modulation of the second pulse would again be dependent upon the wavelength of operation, eg. for light of wavelength larger than that of the bandgap the Linear Electro-Optic effect, giving rise to a refractive index perturbation and consequent polarisation modulation of the light pulse, would predominate. Alternatively, for light of wavelength close to the material bandgap Electro-Absorption modulation would be much greater, and might predominate.

A further consideration which should be addressed in the construction of the planar devices is that of the stress within the active epilayer. The pressure experiments of Hutson *et al* [28] demonstrated a decrease in the threshold field for Gunn domain formation, E_T , below an applied hydrostatic pressure of $15.0 \times 10^8 \text{Nm}^{-2}$. Further, stresses within photoelastic guides have been measured to be of the order of $6.0 \times 10^8 \text{Nm}^{-2}$ [17]. It can therefore reasonably be expected that the presence of the photoelastic guide may affect the threshold field, and therefore possibly reduce the threshold voltage of the planar device.

The planar device may also find application in the area of optoelectronic microwave switching [101], where a microwave signal would be generated by illuminating the device with light pulses of energy greater than the bandgap energy. In this way, the effective length of the Gunn diode may be varied, thus varying the corresponding output microwave frequency. This effect could therefore be used in either the optical control of a microwave signal, or in the microwave processing of an optical signal.

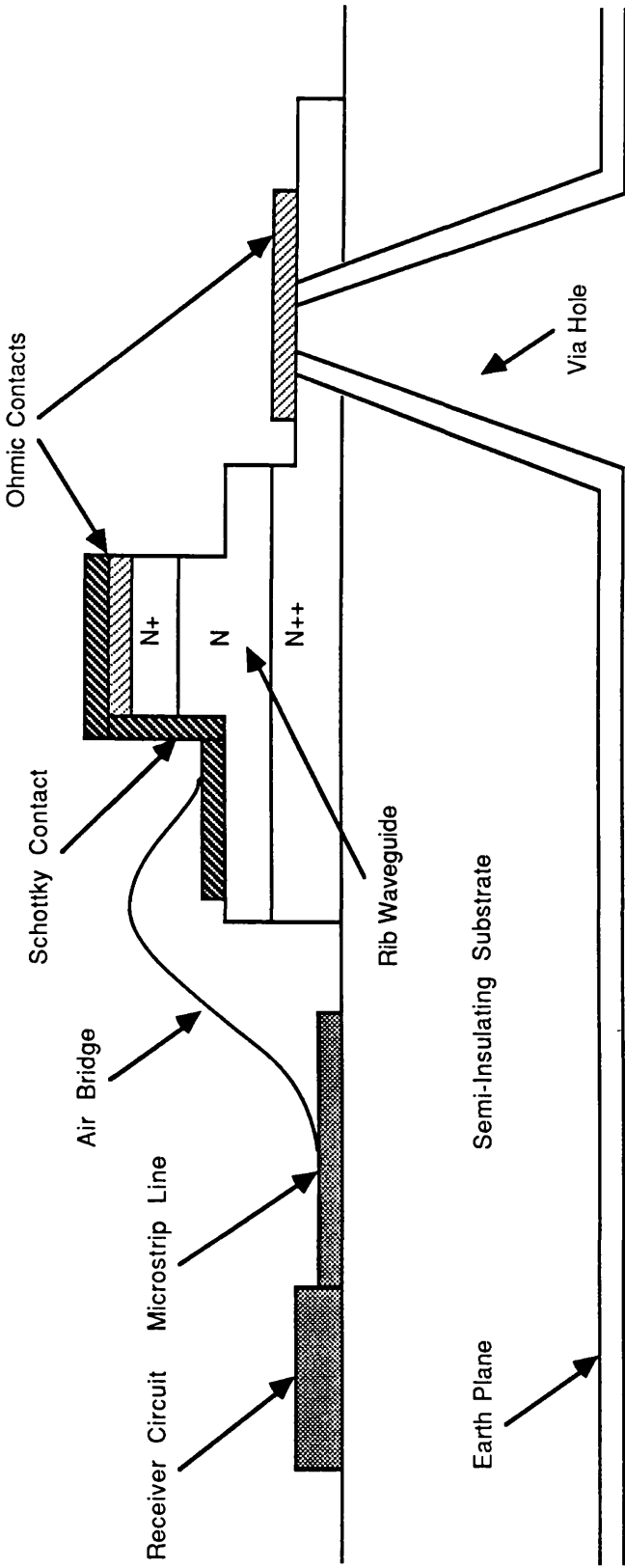
8.3 INTEGRATED DEVICES

As was previously mentioned in section(1.2), the original aim of this work was to design an integrated active optoelectronic microwave receiver, wherein a radiant microwave signal would be received and used to directly modulate a guided optical wave. The experiments of section(7.3) have shown the feasibility of optical modulation within an integrated optical waveguide due to propagating Gunn domains. Therefore, it can now be envisaged, using known microstrip antenna array technology [102],[103], that an integrated active optoelectronic microwave receiver could be fabricated by connecting the output of such an antenna array receiver to either the vertical/rib or planar/photoelastic device. The diode device could then be operated in Delayed Domain Mode, and used to encode the received microwave signal onto the guided optical wave through domain induced Electro– Optical effects.

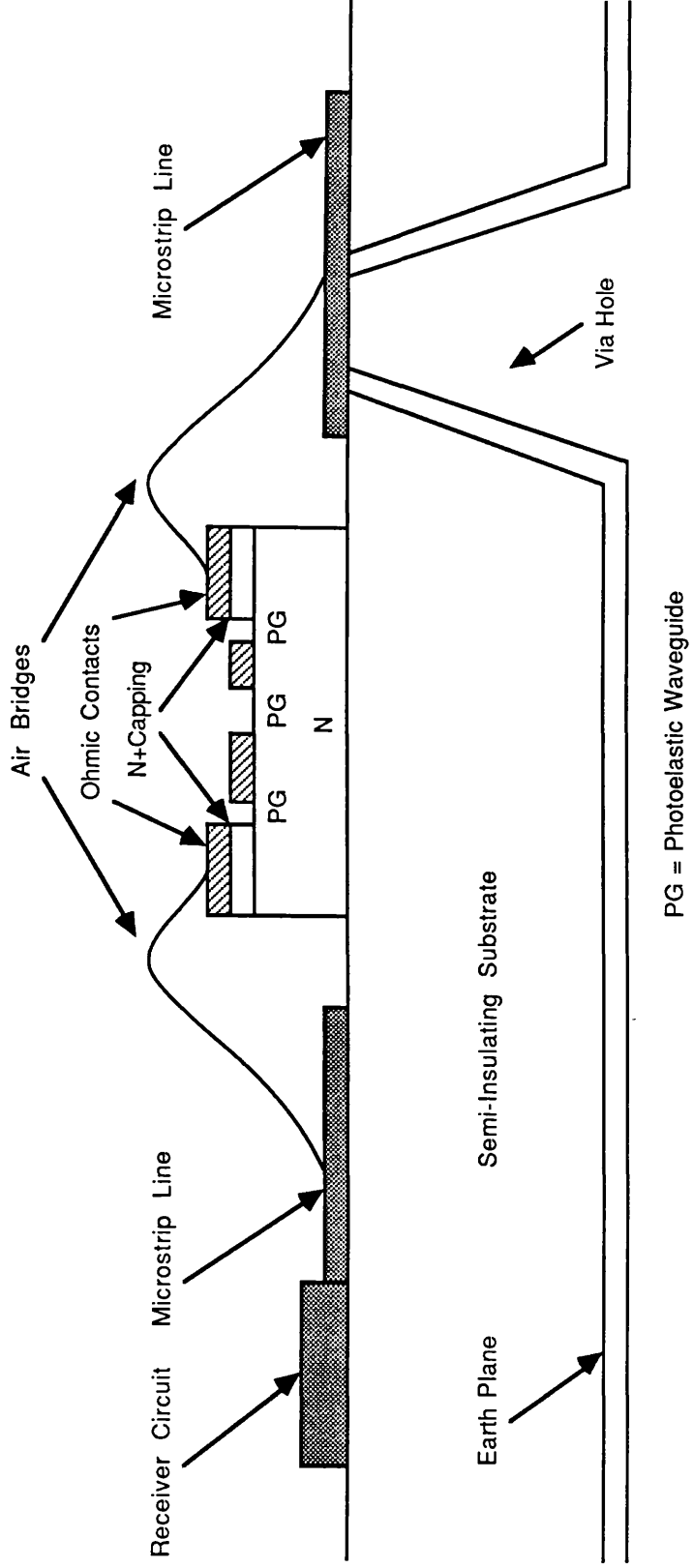
It could further be envisaged that the integrated device might not only be mounted in association with an antenna receiver fabricated on conventional copper clad microstrip board, but that the whole receiver could be fabricated on the same semi–insulating GaAs substrate. Such a monolithic integrated active optoelectronic microwave receiver would constitute a complete radar receiver on a single chip, and could be fabricated using special design features such as air bridges and through–substrate vias. Schematic diagrams of possible embodiments of such a device are shown in figs(8.1)(a) and (b) for: (a) the vertical diode/rib waveguide design; and (b) the planar diode/photoelastic waveguide design.

Fig(8.1) Monolithic Integrated Active Optoelectronic Microwave Receivers

(a) The Vertical Diode / Rib Waveguide Device



(b) The Planar Diode / Photoelastic Waveguide Device



As can be seen from fig(8.1)(a), in the case of the vertical diode, a microstrip line extends from the antenna array receiver circuit carrying the received microwave signal to the modulator device via an air bridge. The modulator device can be seen to be similar in construction to the device investigated in section(7.3), ie. R3, with the obvious difference that the device of fig(8.1)(a) is fabricated on a semi-insulating substrate. The anode of the device, therefore, is not formed by an ohmic contact on the base of the N-type substrate, but is rather formed by the first N^+ epilayer grown on top of the substrate, and is connected to the earth plane by a via-hole.

The planar device of fig(8.1)(b) can be seen to be analagous to the vertical device design, except that only two epilayers are required. Further, the anode of the device, situated on the top-most surface, is connected to the earth plane by an air bridge and via-hole.

It can be seen that the monolithic integrated active optoelectronic microwave receivers described above may be used to detect a radiant microwave signal, and consequently use this signal as the modulation signal to control an optical guided wave. These receivers may therefore find application in such areas as the optical processing of a microwave signal used in a satellite up or down-link.

APPENDIX A THE EQUAL AREAS RULE

The following gives an outline of the calculation of the steady-state properties of a stable, uniformly propagating, high field domain observed in the Gunn effect. The equations to be satisfied are [33] the Current Continuity equation

$$J(t) = Nqv(E) + \epsilon \frac{\partial E}{\partial t} - q \frac{\partial}{\partial x} [D(E)N] \quad \dots\dots A.1$$

and Poisson's equation

$$\epsilon \frac{\partial E}{\partial x} = (N - N_D)q \quad \dots\dots A.2$$

where, $J(t)$ = total current density

N = electron density

N_D = donor density

$D(E)$ = diffusion coefficient

It is assumed in this calculation that the diffusion coefficient, D , is independent of the electric field E , and that the drift velocity $v(E)$ follows the form shown in fig(3.4).

For a freely propagating stable domain, as shown in fig(3.3), the boundary condition is that

$$E \rightarrow E_R \text{ (= a constant) as } x \rightarrow \pm\infty$$

thus $N \rightarrow N_D, \partial N/\partial x \rightarrow 0, \text{ and } \partial E/\partial t \rightarrow 0 \text{ as } x \rightarrow \pm\infty$

and so, $J(t) = qN_D v_R \quad \dots\dots A.3$

where, $v_R = v(E_R)$

We therefore seek a non-trivial solution of equations(A.1) and (A.2) for which

$$E = E(x - v_D t) \quad \dots\dots A.4$$

$$N = N(x - v_D t) \quad \dots\dots A.5$$

where, v_D is the domain velocity. Now from equation(A.4)

$$\frac{\partial E}{\partial t} = -v_D \frac{\partial E}{\partial x} \quad \dots\dots A.6$$

$$\frac{\partial N}{\partial x} = \frac{dN}{dE} \frac{\partial E}{\partial x} \quad \dots\dots A.7$$

Substituting equations(A.3), (A.6) and (A.7) into equation(A.1), and rearranging, gives

$$q \left\{ N_D v_R - N v(E) \right\} = \left\{ qD \frac{\partial N}{\partial E} + \epsilon v_D \right\} \frac{\partial E}{\partial x}$$

and substituting for $\partial E/\partial x$ from equation(A.2) gives

$$\left\{ N_D v_R - N v(E) \right\} = - \left\{ qD \frac{\partial N}{\partial E} + \epsilon v_D \right\} \frac{(N - N_D)}{\epsilon} \quad \dots\dots A.8$$

Rearranging equation(A.8) shows that

$$(N - N_D) \frac{dN}{dE} = \frac{\epsilon}{qD} \left\{ N v(E) - N_D v_R - v_D (N - N_D) \right\} \quad \dots\dots A.9$$

Rearranging this and multiplying by $1/NN_D$ gives

$$\left[\frac{1}{N_D} - \frac{1}{N} \right] \frac{dN}{dE} = \frac{\epsilon}{qN_D D} \left\{ (v(E) - v_D) - \frac{N_D}{N} (v_R - v_D) \right\} \quad \dots\dots A.10$$

Integrating equation(A.10) from the conditions at infinity to any point within the domain

$$\int_{N=N_D}^{N=N} \left[\frac{1}{N_D} - \frac{1}{N} \right] dN = \frac{\epsilon}{qN_D D} \int_{E_R}^E \left\{ (v(E) - v_D) - \frac{N_D}{N} (v_R - v_D) \right\} dE \quad \dots\dots A.11$$

Therefore,

$$\frac{N}{N_D} - 1 - \ln \left[\frac{N}{N_D} \right] = \frac{\epsilon}{qN_D D} \int_{E_R}^E \left\{ (v(E) - v_D) - \frac{N_D}{N} (v_R - v_D) \right\} dE \quad \dots\dots A.12$$

Now, the depletion and accumulation branches of the domain must come together when $N=N_D$ at $E=E_D$, as well as at $E=E_R$. Since the left-hand side of equation(A.12) vanishes when $N=N_D$, then the right-hand side must vanish at $E=E_D$, when N in the integrand takes values on either the depletion branch, where $N < N_D$, or the accumulation branch, where $N > N_D$. From equation(A.12) this can be seen to be impossible unless $v_D=v_R$ since the first term in the integrand is independent of N , whereas the second term will differ in both cases.

It can therefore be concluded that equation(A.12) is solvable only if $v_D=v_R$, ie. that the domain drifts at the same velocity as the electron drift velocity outside the domain, if it is assumed that D is independent of E . Therefore,

$$\frac{N}{N_D} - 1 - \ln \left[\frac{N}{N_D} \right] = \frac{\epsilon}{qN_D D} \int_{E_R}^E \left\{ v(E) - v_R \right\} dE \quad \dots\dots A.13$$

At the peak point of the domain $E=E_D$ and $N=N_D$, and so equation(A.13) becomes

$$0 = \int_{E_R}^{E_D} \left\{ v(E) - v_R \right\} dE \quad \dots\dots A.14$$

This suggests that E_D is determined by the simple geometrical condition that the two shaded areas in fig(3.4) should be equal. This is the so called Equal Areas Rule. The solid line in fig(3.4) represents the static $v(E)$ characteristic, whereas the dashed line represents the locus of points (E_D, v_R) determined by the Equal Areas Rule, ie. the dynamic characteristic. The dynamic characteristic extends from the peak of the $v(E)$ characteristic to the point (E_{DM}, v_{RM}) , for which the areas bounded by the line $v=v_{RM}$ above and below the characteristic are equal. The domain shape may be found by integration of equation(A.14).

APPENDIX B LISTING OF GUNNSIM, THE GUNN EFFECT SIMULATOR

```

10 !
20 ! GUNN EFFECT SIMULATOR
30 !
40 ! DEPARTMENT OF ELECTRONICS AND ELECTRICAL ENGINEERING
50 ! UNIVERSITY OF ALABAMA
60 !
70 !
90 !
100 ! LAST MODIFIED: 14 JUNE 1988
110 !
120 ! THIS PROGRAM CAN BE RUN TO PLOT EITHER ELECTRIC FIELD
130 ! AND CARRIER DENSITY PROFILES OR REFRACTIVE INDEX AND
140 ! CARRIER DENSITY PROFILES USING EITHER AN APPROXIMATE
150 ! OR ANALYTICAL FORM FOR  $V(x)$  AND A CONSTANT OR FIELD
160 ! DEPENDENT DIFFUSION COEFFICIENT.
170 OPTION BASE 0
180 DIM E(2001),F(2001),Eb(2001),G1dc(2001),Nawc(2001),X(2001)
190 DIM H(2001),Hd(2001),G1cn(2001),Nawc(2001)
200 DIM R(10),Te(2001),Nratio(2001),V(2001),D(2001)
210 DIM Profile$(1),Vex(1)
220 !
230 GINIT
240 GRAPHICS ON
250 GCLEAR
260 GOSUB Questions
270 GOSUB Data
280 GOSUB Velfield
290 GOSUB Initial
300 GOSUB Core
310 !
320 END
330 !
340 !
350 Questions: ! INPUTS AND SCREEN DATA
360 !
370 STANDARD
380 INPUT "ENTER BIAS FIELD (V/CM) ",Ebias
390 INPUT "ENTER CHANNEL LENGTH (MICRONS) ",Lc
400 INPUT "ENTER CONTACT LENGTH (MICRONS) ",Lcc
410 ! CONVERT TO CORRECT UNITS IN METERS
420 L=Lc*1E-6
430 C=Lcc*1E-6
440 Eb=Ebias*100 ! Eb=FIELD ACROSS CHANNEL, V/m
450 RETURN
460 !
470 Data: ! DATA STATEMENTS ARE HERE
480 !
490 ! DOING LEVELS AND DEVICE PARAMETERS
500 N1=5.0E22 ! CHANNEL DOPING
510 N2=1.0E24 ! CONTACT DOPING
520 Lt=L+2*C ! TOTAL DEVICE LENGTH
530 Nmax=N2*4 ! SCALING FACTOR FOR PLOT
540 Emax=20*Eb ! SCALING FACTOR FOR PLOT
550 ! DEFINING NOTCH
560 Notchfactor=0.9
570 Notchwidth=1E-6
580 Notchpos=C+L/10
590 ! DEFINING GRADIENT OF POSITIVE PROFILE
600 H2=2
610 ! INCREMENTS
620 Dt=4E-15 !
630 ! NOTE: MAX. VALUE OF Dx=4E-9 FOR C=1 $\mu$ m & L=7 $\mu$ m SINCE S<2001
640 Dx=5E-8 !
650 Dxx=Dx ! Dxx=Dx/2 FOR HALF SCREEN PLOT

```

```

660 S=INT((L+2*C)/Dx) ! NUMBER OF POINTS
661 Cathode=INT(C/Dx)
662 Anode=INT((L+C)/Dx)
663 Notch=INT(Notchpos/Dx)
670 ! DIFFUSION COEFFICIENT
680 !
690 D=0.0178
700 !
710 ! OTHER CONSTANTS
720 Eq=1.6021E-19 ! Coulombs
730 Es=(8.854E-12)*13.5
740 A1=Dt*D/(Dx*Dx)
750 A2=Dt*Eq*D/(Es*Dx)
760 A3=Es/(Dx*Eq)
770 A4=Eq*Dt/(Es*Dx)
780 C2=Dt*Eq/Es
790 Fthreshold=3ES
800 Repeat=50 ! Repeat = NO. OF SIMS. BETWEEN OUTPUTS.
810 Tmax=10000 ! Tmax = NO. OF TIMES CALC. LOOP REPEATED.
820 Value=4000 ! Value = NO. OF SIMS. BEFORE CALLING DOMAIN.
830 ! OPTICAL CONSTANTS
840 Rio=3.467567 ! BY ADACHI, REF. LAB BK.1, P151 (LAMBDA=1.15um)
850 Lambda=1.15E-6
860 R41=1.2E-12 ! REF. GHIA, 1974 ELECTRO-OPTIC COEFF. OF GaAs.
870 Pi=3.1415926
880 M=9.1091E-31 ! kg
890 Me=0.0632*M
900 Vel=2.99792E8 ! Vel=VELOCITY OF LIGHT
910 Constant=Eq*Eq*Lambda*Lambda
920 Constant=(8*Pi*Pi*Es*Ric*Me*Vel*Vel)/Constant
930 Constant=1/Constant
940 Rcl=Rio-(N1*Constant)
950 Rct=Rio-(N2*Constant)
960 Drcl=0.5*Rcl*Rcl*Rcl*R41*Eb
970 Drct=0.5*Rct*Rct*Rct*R41*Eb
980 ! DEVICE INFORMATION SCREEN
990 WINDOW -10,110,-0.8,1.1
1000 FRAME
1010 PEN 3
1020 MOVE 0,1
1030 LABEL " DEVICE INFORMATION SCREEN"
1040 PEN 1
1050 MOVE 0,0.8
1060 LABEL " Channel length (microns) = "&VAL$(Lc)
1070 MOVE 0,0.7
1080 LABEL " Contact length (microns) = "&VAL$(Lcc)
1090 MOVE 0,0.6
1100 FLOAT 2
1110 LABEL " Channel doping density = "&VAL$(N1)&" cm^3"
1120 MOVE 0,0.5
1130 LABEL " Contact doping density = "&VAL$(N2)&" cm^3"
1140 MOVE 0,0.3
1150 PEN 2
1160 LABEL " Time step, Dt (secs) = "&VAL$(Dt)
1170 MOVE 0,0.2
1180 STANDARD
1190 LABEL " Repeat interval = "&VAL$(Repeat)
1200 MOVE 0,0.1
1210 LABEL " Space intervals = "&VAL$(INT(S))
1220 PEN 5
1230 MOVE 0,-0.1
1240 LABEL " Bias electric field, Eb = "&VAL$(Ebias)&" V/
cm"
1250 MOVE 0,-0.2
1260 FLOAT 4
1270 LABEL " Ref. index change at 1.15um due to Eb, Drcl = "&VAL$(Drcl)

```

```

1280 STANDARD
1290 PEN 3
1300 MOVE 0,-0.4
1310 LABEL " Notch factor      = "%VAL1(Notchfactor)
1320 MOVE 0,-0.5
1330 LABEL " Notch width      = "%VAL1(Notchwidth/1E-6)
1340 MOVE 0,-0.6
1350 LABEL " Notch pos'n     = "%VAL1(Notchpos/1E-6)
1360 DISP "CONTINUE"
1370 PAUSE
1380 DISP " "
1390 GCLEAR
1400 RETURN
1410 !
1420 Velfield: ! *****DRAW GRAPH*****
1430 !
1440 INPUT "Do you wish Approx or Exact V-E ? (A/E)",Ves
1450 PEN 1
1460 LABEL "REMEMBER TO CHANGE THE SUB. VELOCITY ACCORDINGLY !!!"
1470 DISP "CONTINUE"
1480 PAUSE
1490 DISP " "
1500 GINIT
1510 !
1520 T=300.0 ! K
1530 Tmax=100*T ! K
1540 Vmax=3.0E5 ! ms-1
1550 Dmax=10*0.0178 ! m2s-1
1560 !
1570 ! *****DRAW GRAPH*****
1580 GCLEAR
1581 !
1582 !PLOTTER IS 405,"HPGL";DISTGR1
1583 !
1590 MOVE 50,95
1600 PEN 2
1610 CSIZE 4
1620 LABEL "GaAs Characteristic"
1630 MOVE 2.5,35
1640 CSIZE 3
1650 DEG
1660 LDIR 90
1670 LABEL "Velocity (10^5ms-1)"
1680 LDIR 0
1690 MOVE 45,0
1700 LABEL "Electric Field (kV/cm)"
1710 VIEWPORT 10,125,10,90
1720 PEN 1
1730 FRAME
1740 WINDOW 0,200,0,1.0
1750 AXES 2,0.05,0,0,10,5,3
1760 CLIP OFF
1770 CSIZE 3,0.5
1780 FOR I=0 TO 200 STEP 20
1790     MOVE I,(-0.04)
1800     LABEL USING "#,K";(I/10)
1810 NEXT I
1820 LORG 3
1830 FOR I=0 TO 1.0 STEP 0.25
1840     MOVE -1.0,I
1850     LABEL USING "#,DD.DD";(I*3)
1860 NEXT I
1870 DISP "CONTINUE"
1880 PAUSE
1890 DISP " "
1900 ! *****DRAW GRAPH*****

```

```

1910 Emin1=0.0 ! kV/cm
1920 Emax1=20.0 ! kV/cm
1930 Ecount=200
1940 Eminve=Emin1*1.0E5 ! Convert to V/e
1950 Emaxve=Emax1*1.0E5
1960 Eincr=(Emaxve-Eminve)/Ecount
1970 IF Ve#="E" THEN
1980 GOSUB Exact
1990 ELSE
2000 GOSUB Approx
2010 END IF
2020 DISP "CONTINUE"
2030 PAUSE
2040 DISP " "
2041 !
2042 !PLOTTER IS "INTERNAL",7
2043 !
2050 GCLEAR
2060 RETURN
2070 !
2080 Approx: ! ***** CALCULATES APPROXIMATE *****
2090 !
2100 ! ***** CONSTANTS FOR GaAs CHARACTERISTICS *****
2110 Mob1=0.686
2120 Mob2=-0.2976
2130 Ra=2.23E-14
2140 Vf1at=86000
2150 Vpeak=222900
2160 Low=324900
2170 High=549900
2180 Fv=20000000
2190 PEN 7
2200 MOVE 0,0
2210 FOR K=1 TO Ecount
2220 F=Eminve+K*Eincr
2230 GOSUB Velocity
2240 PLOT K,Val/Vmax
2250 NEXT K
2260 !
2270 RETURN
2280 !
2290 !Velocity: ! ***** GET VELOCITY FROM F FOR GaAs *****
2300 !
2310 SELECT F
2320 CASE <Low
2330 Val=Mob1*F
2340 CASE <High
2350 Val=Mob2*(F-Low)+Vpeak
2360 CASE <Fv
2370 Val=Vf1at+Ra*((Fv-F)*(Fv-F)*(Fv-F))
2380 CASE ELSE
2390 Val=Vf1at
2400 END SELECT
2410 Vov=Val*C2 ! USED IN ALGORITHM, SEE SUBROUTINE CORE.
2420 IF K*Dx<C OR K*Dx>L+C THEN Vov=C2*Mob1*F*N1/(2*N1)
2430 RETURN
2440 !
2450 Exact: ! ***** CALCULATE EXACT VELOCITY *****
2460 !
2470 STANDARD
2480 PRINT " N = Newest data for GaAs"
2490 PRINT " S = Sze's data for GaAs"
2500 PRINT " I = Data for InP"
2510 INPUT " Which data do you want ?",D3
2520 IF (D3="N") THEN
2530 Mob1=0.800 ! 8000cm2V-1s-1 Gamma Valley

```

```

2540 !Mob2=0.2500 ! 2500cm2V-1s-1 L valley !!! Don't use !!!
2550 Mr1=0.0632 ! Gamma density of states mass
2560 Mr2=0.55 ! L density of states mass
2570 Deltae1=0.284 ! Gamma-L energy separation in eV
2580 Mu1=1 ! Number of equivalent lower valleys
2590 Mu2=4 ! Number of equivalent upper valleys
2591 Tau=1.0E-12 ! Energy relaxation time (seconds)
2600 END IF
2610 IF (Ds="S") THEN
2620 Mob1=0.8500
2630 Mr1=0.0670
2640 Mr2=0.55
2650 Deltae1=0.31
2660 Mu1=1
2670 Mu2=4
2671 Tau=1.0E-12
2680 END IF
2690 IF (Ds="I") THEN
2700 Mob1=0.4600
2710 !Mob2=????
2720 Mr1=0.077
2730 Mr2=0.55 ! ??????
2740 Deltae1=0.53
2750 Mu1=1
2760 Mu2=4
2761 Tau=0.30E-12 ! ??????
2770 END IF
2780 M1=Mr1*M
2790 M2=Mr2*M
2800 Kb=1.38054E-23 ! JK-1
2820 ! *****CALCULATE*****
2830 Accuracy=1.0 ! K
2840 INPUT "How many dimensions ? (1,2 or 3)",Dimm
2850 !IF Dimm<>1 OR 2 OR 3 THEN GOTO 1129
2860 GOSUB Assigndata
2870 Te=T
2880 Nrat=Nratioinitial
2881 Vp=0
2890 FOR K=1 TO Ecount
2900 F=Eminve+K*Eincr
2910 GOSUB Velocity
2920 Te(K)=Te
2930 DISP " Te = ";Te(K); " K = ";K
2940 Nratio(K)=Nratio
2950 V(K)=V
2960 D(K)=D
2961 IF V>Vp THEN
2962 Vp=V
2963 Ep=F
2964 END IF
2970 NEXT K
2980 DISP "CONTINUE"
2990 PAUSE
3000 DISP " "
3010 GOSUB Plotresults
3020 RETURN
3030 !
3040 Assigndata: ! *****CALCULATE*****
3041 !
3050 Kbt=Kb*T
3060 Dele=Deltae1*Eq
3070 Prefactor=0.5*Dimm ! For kinetic energy - T relation
3080 R=(Mu2/Mu1)*((M2/M1)^Prefactor)
3090 Nratioinitial=R*EXP(-Dele/Kbt)
3100 !E=Eminve !!!!!!!!!!!!!!!!!!!!!!!!!!!!!!!
3110 Afront=(Eq*Tau*Mob1)/(Prefactor*Kb)

```

```

3120 RETURN
3130 !
3140 Velocity: ! ***** CALCULS ANALYTICAL V FOR ANY E *****
3150 !
3160 Afrontterm=Afront*F*F
3170 ! TWO METHODS OF FINDING ANAL. V (E)
3180 GOSUB Rtbis
3190 !GOSUB Finddiff
3200 !
3210 Te=Rtb
3220 Kbte=Kb*Te
3230 Nratio=R*EXP(-Dele/Kbte)
3240 ! CALCULATE V (E) FIND (E)
3250 V=Mob1*F/(1+Nratio)
3251 ! (E) (E) COMMENT OUT NEXT LINE
3260 I=(Kbte*Mob1/Eq)/(1+Nratio)
3270 !
3280 Vvv=V*C2
3290 RETURN
3300 !
3310 Rtbis: ! ***** FINDS T (E) (E)
3311 !
3320 Z1=T
3330 Z2=T+Afrontterm/(1.0) ! Highest expected value
3340 Zacc=Accuracy
3350 Jmax=40
3360 Tt=Z2
3370 GOSUB Ffx
3380 Fmid=Fx
3390 Tt=Z1
3400 GOSUB Ffx
3410 Ff=Fx
3420 IF ((Ff*Fmid)>=0.0) THEN
3430 PRINT " OUT OF ROOTS"
3440 END IF
3450 IF (Ff<0.0) THEN
3460 Rtb=Z1
3470 Ddx=Z2-Z1
3480 ELSE
3490 Rtb=Z2
3500 Ddx=Z1-Z2
3510 END IF
3520 FOR J=1 TO Jmax
3530 Ddx=Ddx*0.5 ! Take mid point
3540 Zmid=Rtb+Ddx
3550 Tt=Zmid
3560 GOSUB Ffx
3570 Fmid=Fx
3580 IF (Fmid<=0.0) THEN Rtb=Zmid
3590 IF ((ABS(Ddx)<Zacc) OR (Fmid=0.0)) THEN GOTO 3610
3600 NEXT J
3610 RETURN
3620 !
3630 Ffx: ! ***** FINDS F (E) (E)
3631 !
3640 Kbtt=Kb*Tt
3660 Nrat=R*EXP(-Dele/Kbtt) !!!!!!!!!!!!!!!
3690 Fx=Tt-T-Afrontterm/(1+Nrat)
3700 RETURN
3710 !
3720 Finddiff: ! ***** FINITE DIFF. METHOD OF FINDING Te *****
3721 !
3730 Jmax=100
3740 Te2=T
3750 FOR J=1 TO Jmax
3760 Nrat=R*EXP(-Dele/(Kb*Te2)) !!!!!!!!!!!!!!!

```

```

3770     Tel=T+frontterm/(1+Nrat)
3780     Zacc=ABS(Te1)-ABS(Te2)
3790     IF (ABS(Zacc)<=Accuracy) THEN GOTO 3820
3800     Te2=Te1
3810 NEXT J
3820 Rtb=Te1
3830 RETURN
3840 !
3850 Plotresults: ! ***** PLOTS N2/Nmax AND D vs E *****
3860 !
3870 PEN 2
3880 MOVE 0,0
3890 FOR K=1 TO Ecount
3900     PLOT K,Te(K)/Tmax
3910 NEXT K
3920 PEN 3
3930 MOVE 0,0
3940 FOR K=1 TO Ecount
3950     PLOT K,Nratio(K)/100
3960 NEXT K
3970 PEN 4
3980 MOVE 0,0
3990 FOR K=1 TO Ecount
4000     PLOT K,V(K)/Vmax
4010 NEXT K
4020 PEN 5
4030 MOVE 0,0
4040 FOR K=1 TO Ecount
4050     PLOT K,D(K)/Dmax
4060 NEXT K
4070 PEN 2
4071 DISP " Ep = ";Ep;" Vp = ";Vp
4072 PAUSE
4080 RETURN
4090 !
4100 Initial: ! ***** PLOTS ORIGINAL PROFILES *****
4110 !
4120 ! ***** DEFINE GRAPHICS WINDOW *****
4130 GINIT
4140 GCLEAR
4150 INPUT " Do you wish E-field or ref. index profile ? (E/R) ",Profile$
4160 WINDOW 0,S=Dx,-.25,1.1
4170 PEN 1
4180 MOVE (S=Dx)/10,-0.15
4190 IF Profile$="E" THEN
4200     LABEL " INITIAL ELECTRIC FIELD AND DOPING PROFILES"
4210 ELSE
4220     LABEL " INITIAL REFRACTIVE INDEX AND DOPING PROFILES"
4230 END IF
4240 FRAME
4250 MOVE 0,0.5
4260 DRAW S=Dx,0.5
4270 PEN 2
4280 MOVE 0,N2/Hmax
4290 ! ***** CALCULATE AND PLOT N2/Nmax DOPING AND E/R PROFILES *****
4300 FOR I=1 TO S
4310     X=Dx*I
4320     X(I)=Dxx*I
4330     IF X<C/2 THEN P=N2
4340     IF X>C/2 AND X<C THEN P=N2-(N2-N1)*(X-C/2)*(1/(C-C/2))
4350     IF X=C THEN P=N1
4360     IF X=Notchpos AND X<Notchpos+Notchwidth THEN P=Notchfactor*N1
4370     IF X=C+L AND X<C+L+(C-C/2) THEN P=N1+(N2-N1)*(X-L-C)*1/(C-C/2)
4380     IF X=L+C+C-C/2 THEN P=N2
4390     Nd(I)=P
4400     Eb(I)=Eb*N1/Nd(I)

```

```

4410     E(I)=Eb(I)
4420     PLOT X,Nd(I)/N2
4430  NEXT I
4440  PEN 5
4450  MOVE 0,Eb*N1/N2/Emax
4460  FOR I=1 TO S
4470     X=I*Dx
4480     PLOT X,Eb(I)/Emax+0.5
4490     F(I)=E(I)
4500  NEXT I
4510  E(S)=E(S+1)
4520  E(0)=E(S)
4530  Nd(0)=Nd(S)
4540  DISP "CONTINUE"
4550  PAUSE
4560  DISP " "
4570  RETURN
4580  !
4590  Core: ! ***** MAIN PROGRAM BLOCK *****
4600  !
4610  GOSUB Outline
4620  ! ***** CALCULATE INITIAL VALUES OF PLOTTED OUTPUT *****
4630  FOR K=1 TO S
4640     O1de(K)=(E(K)/Emax+0.5
4650     O1dn(K)=(Es*(E(K+1)-E(K))/(Eq*Dx)+Nd(K))/N2
4660     ! POISSON'S EQUATION NORMALISED TO N2
4670     Newe(K)=O1de(K)
4680     Newn(K)=O1dn(K)
4690  NEXT K
4700  ! ***** PLOT INITIAL DISTRIBUTION OF FIELD AND CURRENT *****
4710  F=Eb
4720  GOSUB Velocity
4730  J1=V00*N1
4740  J3=-Jj/(10*J1)-0.125
4750  T1=0
4760  GOSUB Replot
4770  ! ***** MAIN CALCULATION *****
4780  FOR T1=0 TO Tmax
4800     FOR Rep=1 TO Repeat
4810         Time=(T1*Repeat+Rep)*Dt
4820         !DISP T1*Rep+Rep,Time
4830         Sum=0
4840         FOR K=2 TO S-1
4850             !
4860             F=E(K+1)
4870             GOSUB Velocity
4880             D(K+1)=D
4890             !
4900             F=E(K)
4910             GOSUB Velocity
4920             D(K)=D
4930             Jchi=-V00*(Nd(K)+A3*(E(K+1)-F))+A1*(E(K+1)+E(K-1)-2*F)+A2*(Nd(K
+1)-Nd(K))
4940             Jchi=Jchi+A4*((A3*(E(K+1)-F))+Nd(K))* (D(K+1)-D(K))
4950             F(K)=F+Jchi
4960             Sum=Sum+Dx*Jchi
4970         NEXT K
4980         ! ***** DEAL WITH ENDED NODES *****
4990         !
5000         F=E(2)
5010         GOSUB Velocity
5020         D(2)=D
5030         !
5040         F=E(1)
5050         GOSUB Velocity
5060         D(1)=D

```

```

5070      Jchi=-V00*(Nd(1)+F3*(E(2)-F))+A1*(E(2)+E(S)-2*F)+A2*(Nd(2)-Nd(1))
5080      Jchi=Jchi+A4*((A3*(E(2)-F))+Nd(2))*(D(2)-D(1))
5090      F(1)=F+Jchi
5100      Sum=Sum+Dx*Jchi
5110      !
5120      F=E(1)
5130      GOSUB Velocity
5140      D(1)=D
5150      !
5160      F=E(S)
5170      GOSUB Velocity
5180      D(S)=D
5190      Jchi=-V00*(Nd(K)+F3*(E(1)-F))+A1*(E(1)+E(S-1)-2*F)+A2*(Nd(1)-Nd(S))
)
5200      Jchi=Jchi+A4*((A3*(E(1)-F))+Nd(S))*(D(1)-D(S))
5210      F(S)=F+Jchi
5220      Sum=Sum+Dx*Jchi
5230      Jj=Sum/(2*C+L)
5240      FOR K=1 TO S
5250          F(K)=F(K)-Jj
5260      NEXT K
5270      FOR K=1 TO S-1
5280          E(K)=F(K)
5290          N(K)=(Es*(E(K+1)-E(K)))/(Eq*Dx)+Nd(K))
5300          ! POISSON'S EQUATION REARRANGED
5310      NEXT K
5320      E(S)=F(S)
5330      NEXT Rep
5340      FOR K=1 TO S-1
5350          Nnew(K)=E(K)/Emax+0.5
5360          Nnew(K)=N(K)/N2
5370      NEXT K
5380      PEN 1
5390      GOSUB Replot
5400      ! CALL FOR SUBROUTINE DOMAIN
5410      IF (T1*Repeat)=Value THEN GOSUB Domain
5420      !GOSUB Domain
5430      NEXT T1
5440      RETURN
5450      !
5460      Outline: ! ***** DRAW SCREEN FOR OUTPUT *****
5470      !
5480      !PLOTTER IS 405,"HPGL";BISTORT
5490      WINDOW 0,S*Dx,-.25,1.1
5500      GCLEAR
5510      PEN 1
5520      MOVE (S*Dx)/10,-0.15
5530      IF Profile#="E" THEN
5540          LABEL " ELECTRIC FIELD AND CARRIER DENSITY PROFILES"
5550      ELSE
5560          LABEL " REFRACTIVE INDEX AND CARRIER DENSITY PROFILES"
5570      END IF
5580      FRAME
5590      MOVE 0,0.5
5600      DRAW S*Dx,0.5
5610      !PLOTTER IS "INTERNAL",7
5620      !PAUSE
5630      RETURN
5640      !
5650      Replot: ! ***** ERASE OLD VALUES AND PLOTS NEW *****
5660      !
5670      ! DRAW BIAS LINE
5680      PEN 1
5690      MOVE 0,Eb(1)/Emax+0.5
5700      FOR I=1 TO S
5710          X=I*Dx

```

```

5760     PLOT X,Eb(I)/Emax+0.5
5770 NEXT I
5780 ! ***** PLOT OUTPUT *****
5790 PEN 2
5800 FOR I=3 TO S-1 STEP 2
5810     PEN -2
5820     MOVE X(I-2),O1dn(I-2)
5830     DRAW X(I),O1dn(I)
5840     PEN 2
5850     MOVE X(I-2),Neun(I-2)
5860     DRAW X(I),Neun(I)
5870 NEXT I
5880 PEN 5
5890 FOR I=3 TO S-1 STEP 2
5900     PEN -5
5910     MOVE X(I-2),O1de(I-2)
5920     DRAW X(I),O1de(I)
5930     PEN 5
5940     MOVE X(I-2),Neue(I-2)
5950     DRAW X(I),Neue(I)
5960 NEXT I
5970 FOR K=1 TO S
5980     O1dn(K)=Neun(K)
5990     O1de(K)=Neue(K)
6000 NEXT K
6010 !GOSUB Current
6020 DISP T1*Repeat ! NO. OF SIMULATIONS SO FAR.
6030 RETURN
6040 !
6050 ! Current: ! ***** CURRENT *****
6051 !
6060 ! J2=-Jj/(10*J1)-.25
6070 ! PEN 6
6080 ! Pz=(T) MOD (S+10)
6090 ! MOVE (Pz-1)*Dxx/4,J3
6100 ! DRAW Pz*Dxx/4,J2
6110 ! J3=J2
6120 ! IF Pz=0 THEN
6130 !     MOVE -10*Dx,-0.25
6140 !     AREA PEN 1
6150 !     RECTANGLE 10*Dx+X(S-1)+Dxx,0.25,FILL
6160 ! END IF
6170 ! RETURN
6180 !
6190 Domain: ! ***** CALCULATE DOMAIN HEIGHT AND WIDTH *****
6191 !
6194 Edow=0
6195 FOR K=Notch TO Anode
6196     IF E(K)>Eb THEN
6197         IF E(K)>Edow THEN
6198             Edow=E(K)
6199             Peak=K
6200         END IF
6201     END IF
6202     IF E(K)<Edow THEN
6203         GOTO 6206
6204     END IF
6205 NEXT K
6206 FOR K=(Peak-1) TO Cathode STEP -1
6210     IF ((E(K)-E(K-1))/E(K))<0.10 THEN
6220         IF E(K)<=Eb THEN
6230             Kmin=K
6240             Emin=E(K)
6250             GOTO 6250
6260         END IF
6270     END IF

```

```

6280 NEXT K
6290 FOR K=(Peak+1) TO Anode
6300 IF ((E(K)-E(K+1))/E(K))<0.10 THEN
6310 IF E(K)<=Eb THEN
6320 Kmin2=K
6330 Emin2=E(K)
6340 GOTO 6380
6350 END IF
6360 END IF
6370 NEXT K
6380 Almin1=Kmin1*Dx/1E-6
6390 almin2=Kmin2*Dx/1E-6
6400 Aldom=Almin2-Almin1
6410 GCLEAR
6420 WINDOW -10,110,-0.1,1.1
6430 PEN 1
6440 FRAME
6450 PEN 3
6460 MOVE 0,1.0
6470 LABEL " DOMAIN CHARACTERISTICS"
6480 PEN 1
6490 MOVE 0,0.8
6500 LABEL " DOMAIN HEIGHT, Edom = "&VAL$(Edom)
6510 IF Profile=E THEN GOTO 6550
6520 Dridom=0.5*Rcl*Rcl*Rcl*R41*Edom
6530 MOVE 0,0.7
6540 LABEL " DOMAIN HEIGHT, Iridom = "&VAL$(Dridom)
6550 MOVE 0,0.6
6560 LABEL " DOMAIN WIDTH = "&VAL$(Aldom)&" microns "
6570 PEN 2
6580 MOVE 0,0.5
6590 LABEL " END POINTS : TRAILING EDGE = "&VAL$(Almin1)&" microns "
6600 MOVE 0,0.4
6610 LABEL " TRAILING FIELD = "&VAL$(Emin1/100)&" V/cm"
6620 MOVE 0,0.3
6630 LABEL " LEADING EDGE = "&VAL$(Almin2)&" microns "
6640 MOVE 0,0.2
6650 LABEL " LEADING FIELD = "&VAL$(Emin2/100)&" V/cm"
6660 MOVE 0,0.1
6670 PEN 5
6680 LABEL " NO. OF SIMULATIONS = "&VAL$(I!*Repeat)&" PEAK = "&VAL$(Pea
k)
6690 !PEN 3
6700 !DISP "CONTINUE"
6710 !PAUSE
6720 !DISP " "
6730 !DUMP GRAPHICS TO PRT
6740 PAUSE
6750 GCLEAR
6760 !PLOTTER IS 405,"HPGL";ISTORY
6770 !GOSUB Outline
6780 !GOSUB Greplot
6790 !PLOTTER IS OFF
6800 PLOTTER IS 1,"GRAPHICS"
6810 GOSUB Outline
6820 GOSUB Replot
6830 !DUMP GRAPHICS TO PRT
6840 IF Value=150000 THEN Value=200000
6850 IF Value=100000 THEN Value=150000
6860 IF Value=75000 THEN Value=100000
6870 IF Value=62500 THEN Value=75000
6880 IF Value=50000 THEN Value=62500
6890 IF Value=37500 THEN Value=50000
6900 IF Value=25000 THEN Value=37500
6910 IF Value=10000 THEN Value=25000
6920 IF Value=10000 THEN Value=25000

```

```

6921 IF Value=6000 THEN Value=10000
6930 IF Value=5000 THEN Value=6000
6940 IF Value=4000 THEN Value=5000
6941 IF Value=1750 THEN Value=4000
6943 IF Value=1500 THEN Value=1750
6944 IF Value=1250 THEN Value=1500
6950 IF Value=1000 THEN Value=1250
6960 RETURN
6961 Grepot: ! *****DUMP FOR PHYSICS TO S4PGL*****
6962 !
6963 PEN 1
6964 MOVE 0,Eb(1)/E#ax+0.5
6965 FOR I=1 TO S
6966     X=I#Dx
6967     PLOT X,Eb(I)/E#ax+0.5
6968 NEXT I
6969 MOVE 0,Eb(1)/E#ax+0.5
6970 PEN 1
6971 FOR I=3 TO S-1 STEP 2
6972     PLOT X(I),Hewn(I)
6973 NEXT I
6974 MOVE 0,Eb(1)/E#ax+0.5
6975 PEN 1
6976 FOR I=3 TO S-1 STEP 2
6977     DRAW X(I),Hewe(I)
6978 NEXT I
6979 RETURN
6981 END

```

The GUNNSIM program (listed in Appendix B) simulates the action of a super-critical Gunn device. The program displays the carrier density profile, and either the electric field or the refractive index profiles, associated with the propagating Gunn domain, as time progresses and the domain traverses the device. The program therefore requires to know the length, and the doping density, of the contact and channel regions of the device, along with the electric field applied across the channel region, and the structure of any doping spike (ie. domain nucleation centre) within the device. The program is divided into the following subroutines:

Questions: The channel and contact lengths are input in microns, along with the bias field, $E_{\text{bias}} = E_B$, applied across the channel region. The variables are then converted to the required units.

Data: The doping levels of the channel and contact regions, and the total device length, are defined along with the structure of the doping spike, and the gradient of the doping profile between the channel and contact regions. The time interval between successive simulations, Dt is also defined, and the device divided into S equal parts of length Dx . Further, the optical constants necessary for the conversion of the electric field profile into the corresponding refractive index profile are given, along with all other constants necessary for the required calculations. Included also is the repeat interval, ie. the number of simulations between outputting consecutive results to the screen.

Velfield: Allows the user to select either the approximate, or analytical, velocity-field characteristic, and either a constant, or field dependent, diffusion coefficient, depending on the analysis method desired. This is done by selecting either subroutine Approx, or subroutine Exact.

Approx: This subroutine defines all the constants necessary for the approximate four-line velocity-field characteristic, and displays this characteristic on the screen.

Velocity: For any given value of electric field this subroutine calculates the corresponding value of velocity. Two subroutines named Velocity exist. One calculates the velocity, $v(E)$ given by the four-line approximation. The other calculates the analytical $v(E)$ characteristic given by either the root bisection method, or the finite difference method.

Exact: Allows selection of data from one of a number of various sources, and then calculates, and plots, the corresponding analytical $v(E)$ characteristic.

Assigndata: Calculates various constants required in the running of the subroutines for the analytical $v(E)$ characteristic.

Rtbis: Calculates the electron temperature, T_e , as a function of electric field, E , by the root bisection method.

Ffx: Calculates the conversion factor of consecutive results of the subroutine Rtbis.

Findiff: Calculates the electron temperature, T_e , as a function of electric field, E , by the Finite Difference method. This subroutine was found, however, to bifurcate at electric fields greater than the threshold field.

Plotresults: Plots the analytical variation with electric field, E , of all, or some of the following: the electron temperature, T_e ; the upper to lower valley electron population ratio, N_2/N_1 ; the electron velocity, v , and the electron diffusion coefficient, D .

Initial: This subroutine requires to know whether the user wishes to view the carrier

density profile, along with either the electric field profile, or the refractive index profile, associated with the propagating domain. On answering this prompt the program goes on to plot the initial profile shapes within the device.

Core: This constitutes the main program block, based on the solution of Poisson's equation and the Current Continuity equation given in the algorithm presented in section(5.4). The initial values of the variables used for the plotted output are assigned, and plotted on the screen. The algorithm is then employed to calculate the profiles associated with the propagating domain as time progresses. After a number of simulations, equal to the repeat interval, the new profiles are plotted to the screen using the subroutine Replot. The position of the peak field within the domain is also found, as this information is required when the subroutine Domain is called.

Outline: Draws a frame around the output domain profiles, labels the output profiles, and draws the line corresponding to the bias value of the electric field or refractive index.

Replot: The old output is erased from the screen, and the new plotted. The new output values are then assigned to the array holding the old output values. The number of simulations carried out so far is also displayed.

Domain: This subroutine may be called at regular intervals during the running of the program in order to calculate the width, and the maximum electric field and/or maximum refractive index change, associated with the propagating domain. The program is paused, allowing the information printed to the screen to be dumped to the printer, along with the corresponding domain profile if so desired.

Greplot: May be selected in order to dump the domain profile, selected by subroutine Domain, to the HP Graphics Plotter.

D.1 PHOTODYNE MODEL 22XLA FIBRE OPTIC POWER METER

A Photodyne Model 22XLA Fibre Optic Power Meter was used to measure all the relevant optical powers in the experiments presented in Chapter 7. This meter incorporated a general purpose germanium detector head (Model 550). Such heads each have a unique behaviour with varying wavelength, λ , and are calibrated by the US National Bureau of Standards. The responsivity (Amps/Watt) for the head used for these experiments is shown in fig(D.1)(a).

The head was calibrated to a set point of 1300nm. This suggested a dB add-on factor had to be added to each measurement which was taken, this factor being dependent upon wavelength. The variation in the dB add-on factor with wavelength is shown in fig(D.1)(b).

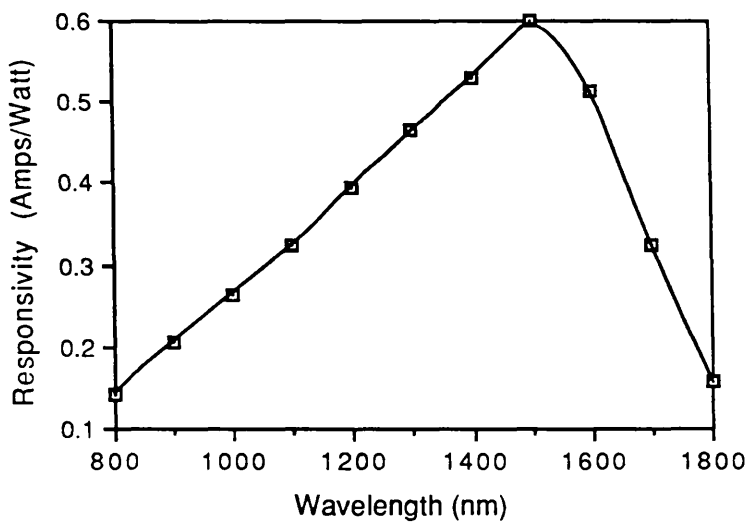
D.2 PHOTODIODE DATA

Two photodiodes were used in the Electro-Optic experiments of section(7.3). The first of these was the ITL InGaAs HSD30 High Speed Photodetector. This detector was used in conjunction with a spectrum analyser to directly detect Electro-Optic, or Electro-Absorption, modulation. The characteristics of this diode are shown in table(D.1).

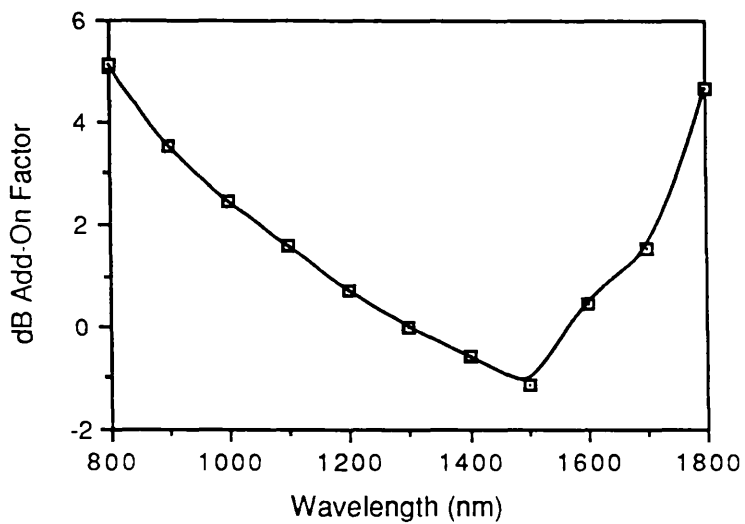
The second photodiode which was used in these experiments was the Rofin-Sinar UK Ltd., GM8 Ge Photodiode. This was a relatively slow photodetector which could be used, in conjunction with an oscilloscope, to measure the averaged modulated intensity received. Hence, using the analysis outlined in Appendix E, the modulation depth of the modulated signal could be calculated. The characteristics of this diode are also shown in table(D.1).

Fig(D.1) Spectral Analysis Data for Ge Detector Head

(a) Responsivity versus Wavelength



(b) dB Add-On Factor versus Wavelength



Table(D.1) Photodiode Characteristics

Photodiode	HSD30	GM8
Material	InGaAs	Ge
Typical Pulse Rise Time	45ps	200ns
Active Diameter	100 μ m	5.0mm
Peak Sensitivity Wavelength	1600nm	1500nm
-10dB Spectral Range	950nm-1650nm	500nm-1800nm
Responsivity (Amps/Watt)		
at $\lambda=1.15\mu$ m	—	0.425
at $\lambda=905$ nm	—	0.225

APPENDIX E SLOW DIODE ANALYSIS

If an optical detector, ie. a 'slow' diode with a rise-time far below that of the microwave modulated optical signal (ie. the microwave drive signal), is used to average the optical intensity, then the change in the average intensity can be related to the actual modulation depth.

Considering first modulation due to the Linear Electro-Optic effect. It can be seen that the output amplitude, I_{EO} with the polariser and analyser in the perpendicular arrangement, is given by

$$I_{EO} = I_0 |\sin \Phi_{EO}| \tag{E.1}$$

where, I_0 = input intensity

Φ_{EO} = polarisation rotation factor

Now, assuming that the polarisation rotation factor is a sinusoidally dependent function, ie. $\Phi_{EO} = A |\sin \omega t|$, then we have that the averaged received signal, over one modulation cycle, is given by

$$I_{\perp} = \frac{\omega}{2\pi} \int_0^T I_0 |\sin(A |\sin \omega t|)| dt \tag{E.2}$$

Now, it can be shown for Bessel functions of the first kind, $J_{\nu}(z)$, that when ν is fixed, and $z \rightarrow 0$, then [90]

$$J_{\nu} \approx \frac{(\frac{1}{2} z)^{\nu}}{\Gamma(\nu+1)} \tag{E.3}$$

where, $\nu \neq -1, -2, -3, \dots$

$\Gamma(n+1) = n!$ for integer values

It can therefore be seen that $J_{\nu}(z) = 1$, for $\nu = 0$. It can also be shown that [91]

$$\begin{aligned}
J_\nu(z) &= \sum_{k=0}^{\infty} (-1)^k \frac{z^{2k}}{2^{2k}(k!)^2} \\
&= 1 + \left[-\frac{z^2}{4} \right] + \left[\frac{z^4}{64} \right] + \dots \\
&= 1 - \frac{z^2}{4} \quad \text{for small } z \quad \dots\dots\dots E.4
\end{aligned}$$

Now, it can further be shown that the following serial expansions are correct [92]

$$\begin{aligned}
\sin(x\sin\theta) &= 2 \sum_{k=0}^{\infty} J_{2k+1}(x) \sin[(2k+1)\theta] \quad \dots\dots\dots E.5 \\
&= 2J_1(x)\sin\theta + 2J_3(x)\sin3\theta + 2J_5(x)\sin5\theta + \dots\dots\dots
\end{aligned}$$

and,

$$\begin{aligned}
\cos(x\cos\theta) &= J_0 + 2 \sum_{k=1}^{\infty} (-1)^k J_{2k}(x) \cos(2k\theta) \quad \dots\dots\dots E.6 \\
&= J_0(x) - 2J_2(x)\cos2\theta + 2J_4(x)\cos4\theta + \dots\dots\dots
\end{aligned}$$

Thus, approximating the modulation effect of the propagating domain to a half-wave rectified sinusoidal influence, we have that

$$I_{\perp} = \frac{\omega}{2\pi} \int_0^{T/2} I_0 \sin(A\sin\omega t) dt \quad \dots\dots\dots E.7$$

And, using equation(E.5) we have that

$$I_{\perp} \approx \frac{I_0 J_1(A)}{\pi} \quad \dots\dots\dots E.8$$

Further, assuming A to be small, and employing equation(E.3), it can be seen that $J_1(A) = A/4$. Thus,

$$I_{\perp} \approx \frac{AI_0}{4\pi} \quad \dots\dots\dots E.9$$

Therefore, rearranging equation(E.9), we have that the modulation depth, η_{EO} for

Electro-Optic modulation, is given by

$$\eta_{EO} = \frac{I_{EO}}{I_O} \approx A \approx \frac{4\pi I_{\perp}}{I_O} \quad \dots\dots E.10$$

In an analogous way, the modulation depth, η_{EA} observed due to Electro-Absorption modulation, may be calculated using the averaged output amplitude, I_{\parallel} observed with the polariser and analyser in the parallel arrangement. The output amplitude in the parallel arrangement, I_{EA} , is given by

$$I_{EA} = I_O \cos \Phi_{EA} \quad \dots\dots E.11$$

where, Φ_{EA} = polarisation rotation factor

$$= A |\cos \omega t|$$

Thus, the averaged received signal, over one modulation cycle, is given by

$$I_{\parallel} = \frac{\omega}{2\pi} \int_0^T I_O \cos(A \cos \omega t) dt \quad \dots\dots E.12$$

Assuming that the propagating domain produces an approximately half-wave rectified modulation influence it can be seen, using equation(E.6), that

$$\begin{aligned} I_{\parallel} &= \frac{\omega}{2\pi} \int_0^{T/2} I_O \cos(A \cos \omega t) dt \\ &\approx \frac{I_O J_0(A)}{2} \quad \dots\dots E.13 \end{aligned}$$

Further, employing equation(E.4)

$$I_{\parallel} \approx \frac{I_O}{2} \left[1 - \frac{A^2}{4} \right] \quad \dots\dots E.14$$

Thus, it can be seen that the modulation depth, η_{EA} , of the modulated signal due to the Electro-Absorption effect is given by

$$\eta_{EA} = \frac{I_{EA}}{I_0} \approx \cos A \approx \cos \left\{ 2 \left[1 - \frac{2I_{11}}{I_0} \right]^{1/2} \right\} \quad \dots\dots\dots E.15$$

REFERENCES

1. LADBROOKE, P.H.: 'GaAs Mesfet's and High Electron Mobility Transistors (HEMT)', *Gallium Arsenide for Devices and Integrated Circuits*, 1986, Proc. GaAs School, UWIST, Cardiff
2. DUMKE, W.P.: 'Intraband Transitions and Maser Action', *Phys. Rev.*, 1962, 127, 5, pp.1559-1563
3. ALFEROV, Zh.I., ANDREEV, V.H., KOROL'KOV, V.I., PORTNOI, E.L., and YAKOVENKO, A.A.: 'Spontaneous Radiation Sources Based on Structures with AlAs-GaAs Heterojunctions', *Sov. Phys. Semicond.*, 1970, 3, pp.1107-1110
4. COMBES, P.F., GRAFFEUIL, J., and SAUTEREAU, J.F.: 'Microwave Components, Devices and Active Circuits', 1987, Wiley, Chichester
5. YARIV, A.: 'The Beginning of Integrated Optoelectronic Circuits', *IEEE Trans. Elect. Dev.*, 1984, 31, 11, pp.1656-1661
6. SOBOL, H.: 'The Application of Microwave Techniques in Lightwave Systems', *J. Lightwave Technology*, 1987, 5, 3, pp.293-299
7. COHEN, M.G., KNIGHT, S., and ELWARD, J.P.: 'Optical Modulation in Bulk GaAs using the Gunn Effect', *Appl. Phys. Lett.*, 1966, 8, 11, pp.269-271
8. OHTA, K., KAWASHIMA, M., and KATAOKA, S.: 'Electro-Optic Modulation of a Laser Beam by a Travelling High-Field Domain in a GaAs Gunn Diode', *J. Appl. Phys.*, 1975, 46, 3, pp.1318-1321
9. KOGELNIK, H., RAMASWAMY, V.: 'Scaling Rules for Thin-Film Optical Waveguides', *Appl. Optics*, 1974, 13, 8, pp.1857-1862
10. BENSON, T.M.: 'Integrated Optical Components Produced in GaAs and InP Epitaxial Layers using the Photoelastic Effect', 1982, Ph.D Thesis, University of Sheffield
11. HUNSPERGER, R.G.: 'Integrated Optics: Theory and Technology', 1985, Springer-Verlag, New York

12. RAMASWAMY, V.: 'Strip-Loaded Film Waveguide', *Bell Sys. Tech. J.*, 1974, 53, 4, pp.697-703
13. HEWAK, D.W., LIT, J.W.Y.: 'Generalised Dispersion Properties of a Four-Layer Thin-Film Waveguide', *Appl. Optics*, 1987, 26, 5, pp.833-841
14. KOSHIBA, M., SUZUKI, M.: 'Equivalent Network Analysis of Dielectric Thin-Film Waveguides for Optical Integrated Circuits and it's Applications', *Radio Sci.*, 1982, 17, 1, pp.99-107
15. MacFADYEN, D.N.: 'Components for GaAs Integrated Optics Fabricated by Wet Chemical Etching', 1980, Ph.D Thesis, University of Glasgow
16. CAMPBELL, J.C., BLUM, F.A., and SHAW, D.W.: 'GaAs Electro-Optic Channel-Waveguide Modulator', *Appl. Phys. Lett.*, 1975, 26, 11, pp.640-642
17. WESTBROOK, L.D., ROBSON, P.N., and MAJERFELD, A.: 'Strain-Induced Optical Waveguiding in GaAs Epitaxial Layers at $1.15\mu\text{m}$ ', *Elect. Lett.*, 1979, 15, 3, pp.99-100
18. KIRBY, P.A., SELWAY, P.R., and WESTBROOK, L.D.: 'Photoelastic Waveguides and their Effect on Stripe-Geometry GaAs/Ca_{1-x}Al_xAs Lasers', *J. Appl. Phys.*, 1979, 50, 7, pp.4567-4579
19. WESTBROOK, L.D., FIDDYMENT, P.F., and ROBSON, P.N.: 'Photoelastic Channel Optical Waveguides in Epitaxial GaAs Layers', *Elect. Lett.*, 1980, 16, 5, pp.169-170
20. GUNN, J.B.: 'Microwave Oscillation of Current in III-V Semiconductors', *Solid State Commun.*, 1963, 1, pp.88-91
21. GUNN, J.B.: 'Instabilities of Current in III-V Semiconductors', *IBM J. Res. Dev.*, 1964, 8, pp.141-159
22. GUNN, J.B.: 'Instabilities of Current and of Potential Distribution in GaAs and InP', *Proc. Sym. Plasma Effects in Solids*, 1964, pp.199-207

23. KROEMER, H.: 'Theory of the Gunn Effect', *Proc. IEEE*, 1964, 52, p.1736
24. RIDLEY, B.K., WATKINS, T.B.: 'The Possibility of Negative Resistance Effects in Semiconductors', *Proc. Phys. Soc. Lond.*, 1961, 78, pp.293-304
25. HILSUM, C.: 'Transferred Electron Amplifiers and Oscillators', *Proc. IRE*, 1962, 50, pp.185-189
26. HILSUM, C.: 'Historical Background of Hot Electron Physics', *Solid State Electron.*, 1978, 21, pp.5-8
27. SZE, S.M.: 'Physics of Semiconductor Devices', 2nd Edition, 1981, Wiley, Chichester
28. HUTSON, A.R., JAYARAMAN, A., and CHYNOWETH, A.G.: 'Mechanism of the Gunn Effect from a Pressure Experiment', *Phys. Rev. Lett.*, 1965, 14, pp.639-641
29. ALLEN, J.W., SHYAM, M., CHEN, Y.S., and PEARSON, G.L.: 'Microwave Oscillations in $\text{GaAs}_{1-x}\text{P}_x$ Alloys', *Appl. Phys. Lett.*, 1965, 7, 4, pp.78-80
30. BLAKEMORE, J.S.: 'Semiconducting and Other Major Properties of Gallium Arsenide', *J. Appl. Phys.*, 1981, 53, 10, pp.R123-R181
31. PICKERING, C., ADAMS, A.R., PITT, G.D., and VYAS, M.K.R.: 'The Effect of Pressure on High Electric Field Instabilities in n-type GaAs', *J. Phys.*, C8, 1975, pp.129-137
32. BUTCHER, P.N.: 'Theory of Stable Domain Propagation in the Gunn Effect', *Phys. Lett.*, 1965, 19, 7, pp.546-547
33. BUTCHER, P.N., FAWCETT, W.: 'A Simple Analysis of Stable Domain Propagation in the Gunn Effect', *Brit. J. Appl. Phys.*, 1966, 17, pp.841-850
34. BUTCHER, P.N., FAWCETT, W.: 'Calculation of the Velocity-Field Characteristic for Gallium Arsenide', *Phys. Lett.*, 1966, 21, 5, pp.489-490

35. BUTCHER, P.N., FAWCETT, W.: 'Stable Domain Propagation in the Gunn Effect', *Brit. J. Appl. Phys.*, 1966, 17, pp.1425-1432
36. BUTCHER, P.N., FAWCETT, W., and OGG, N.R.: 'Effect of Field-Dependent Diffusion on Stable Domain Propagation in the Gunn Effect', *Brit. J. Appl. Phys.*, 1967, 18, pp.755-759
37. BUTCHER, P.N.: 'The Gunn Effect', *Rep. Prog. Phys.*, 1967, 30, 1, pp.97-148
38. CARROLL, J.E.: 'Hot Electron Microwave Generators', 1970, Edward Arnold, London
39. HOBSON, G.S.: 'The Gunn Effect', 1974, Clarendon Press, Oxford
40. BOSCH, B.G., ENGELMANN, R.H.W.: 'Gunn-Effect Electronics', 1975, Pitman Publishing, London
41. SHAW, M.P., GRUBIN, H.L., and SOLOMON, P.R.: 'The Gunn-Hilsum Effect', 1979, Academic Press, London
42. TAYLOR, H.F., YARIV, A.: 'Guided Wave Optics', *Proc. IEEE*, 1974, 62, 8, pp.1044-1060
43. NAMBA, S.: 'Electro-Optical Effect of Zincblende', *J. Opt. Soc. Amer.*, 1961, 51, 1, pp.76-79
44. YARIV, A.: 'Introduction to Optical Electronics', 2nd Edition, 1976, Holt, Rinehart and Winston, London
45. NYE, J.F.: 'Physical Properties of Crystals', 1957, Clarendon Press, London
46. PANKOVE, J.I.: 'Optical Processes in Semiconductors', 1971, Prentice Hall, Englewood Cliffs
47. GORDON, E.I.: 'Gunn-Effect Light Modulator', 1965, US Patent No. 3,475,078
48. GUETIN, P., BOCCON-GIBOD, D.: 'Franz-Keldysh Effect with Gunn Domains in Bulk GaAs', *Appl. Phys. Lett.*, 1968, 13, 5, pp.161-163
49. SANDOMIRSKII, V.B., SHEVEREV, A.V.: 'Doppler Effect from a Gunn Domain', *Sov. Tech. Phys. Lett.*, 1983, 9, 12, p.608

50. MYERS, F.A., McSTAY, J., and TAYLOR, B.C.: 'Variable-Length Gunn Oscillator', *Elect. Lett.*, 1968, 4, 18, pp.386-387
51. ADAMS, R.F., SCHULTE, H.J.: 'Optically Triggered Domains in GaAs Gunn Diodes', *Appl. Phys. Lett.*, 1969, 15, 8, pp.265-267
52. HAYDL, W.H., SOLOMON, R.: 'The Effect of Illumination on Gunn Oscillations in Epitaxial GaAs', *IEEE Trans. Elect. Dev.*, 1968, 15, 11, pp.941-942
53. SEWELL, K.G., BOATHER, L.A.: 'Multimode Operation in GaAs Oscillators Induced by Cooling and Illumination', *Proc. IEEE*, 1967, 55, 7, pp.1228-1229
54. AFROMOWITZ, M.A.: 'Refractive Index of $\text{Ga}_{1-x}\text{Al}_x\text{As}$ ', *Solid State Commun.*, 1974, 15, pp.59-63
55. ILEGEMS, M., PEARSON, G.L.: 'Infrared Reflection Spectra of $\text{Ga}_{1-x}\text{Al}_x\text{As}$ Mixed Crystals', *Physical Rev. B1*, 1970, 1, 4, pp.1576-1582
56. ADACHI, S.: 'Refractive Indices of III-V Compounds: Key Properties of InGaAsP Relevant to Device Design', *J. Appl. Phys.*, 1982, 53, 8, pp.5863-5869
57. ADACHI, S.: 'GaAs, AlAs, and $\text{Al}_x\text{Ga}_{1-x}\text{As}$: Material Parameters for use in Research and Device Applications', *J. Appl. Phys.*, 1985, 58, 3, pp.R1-R29
58. ROBERTSON, M.J., RITCHIE, S., and DAYAN, P.: 'Semiconductor Waveguides: Analysis of Optical Propagation in Single Rib Structures and Directional Couplers', *IEE Proc., Pt. J*, 1985, 132, 6, pp.336-342
59. LORRAIN, P., CORSON, D.: 'Electromagnetic Fields and Waves', 2nd Edition, 1970, Freeman, San Fransisco
60. RAMO, S., WHINNERY, J.R., and VAN DUZER, T.: 'Fields and Waves in Communication Electronics', 2nd Edition, 1984, Wiley, Chichester
61. BUBE, R.H.: 'Electrons in Solids An Introductory Survey', 1981,

Academic Press, London

62. KITTEL, C.: 'Introduction to Solid State Physics', 5th Edition, 1976, Wiley, Chichester
63. ARNAUD, J.A.: 'Beam and Fiber Optics', 1976, Academic Press, London
64. HERRENDEN-HARKER, W.G., WILLIAMS, R.H.: 'Epitaxial Growth of GaAs : MBE and MOCVD', *Gallium Arsenide for Devices and Integrated Circuits*, 1986, Proc. GaAs School, UWIST, Cardiff
65. HOUSTON, P.A.: 'Liquid Phase and Vapour Phase Epitaxy of GaAs and Related Compounds', *Gallium Arsenide for Devices and Integrated Circuits*, 1986, Proc. GaAs School, UWIST, Cardiff
66. THOMAS, H.: 'Characterisation of GaAs I: Electrical Techniques', *Gallium Arsenide for Devices and Integrated Circuits*, 1986, Proc. GaAs School, UWIST, Cardiff
67. VAN DER PAUW, L.J.: 'A Method of Measuring Specific Resistivity and Hall Effect of Discs of Arbitrary Shape', *Philips Research Reports*, 1958, 13, 1, pp.1-9
68. PIOTROWSKA, A., GUIVARC'H, A., and PELOUS, G.: 'Ohmic Contacts to III-V Compound Semiconductors: A Review of Fabrication Techniques', *Solid State Elect.*, 1983, 26, 3, pp.179-197
69. LAKHANI, A.A., OLVER, L.C., DVORSKY, E.F., and HEMFLING, E.U.: 'Passivation of Ohmic Contacts to GaAs', *IEEE Elect. Dev. Letts.*, 1985, 11, pp.586-588
70. PATRICK, W., MACKIE, W.S., BEAUMONT, S.P., and WILKINSON, C.D.W.: 'Low Temperature Annealed Contacts to Very Thin GaAs Epi-Layers', *Appl. Phys. Lett.*, 1986, 48, pp.986-988
71. BENZAQUEN, M., MAZURUK, K., WALSH, D., SPRINGTHORPE, A.J., and MINER, C.: 'Determination of Donor and Acceptor Impurity Concentrations in n-InP and n-GaAs', *J. Elect. Mats.*, 1987, 16, 2, pp.111-117

72. DILL, F.H: 'Optical Lithography', *IEEE Trans. Elect. Dev.*, 1975, 22, 7, pp.440-444
73. PACANSKY, J., LYERLA, J.R.: 'Photochemical Decomposition Mechanisms for AZ-Type Photoresists', *IBM J. Res. Dev.*, 1979, 23, 1, pp.42-55
74. SHAW, D.W: 'Localised GaAs Etching with Acidic Hydrogen Peroxide Solutions', *J. Electrochem Soc.: Solid-State Sci. and Tech.*, 1981, 128, 4, pp.874-880
75. WOODWARD, J.: 'Wet and Dry Processing of GaAs', *Gallium Arsenide for Devices and Integrated Circuits*, 1986, Proc. GaAs School, UWIST, Cardiff
76. LI, J.Z., ADESIDA, I., and WOLF, E.D.: 'Evidence of Crystallographic Etching in (100) GaAs using SiCl₄ Reactive Ion Etching', *J. Vac. Sci. Tech. B*, 1985, 3, 1, pp.406-409
77. HU, E.L., HOWARD, R.E.: 'Reactive-Ion Etching of GaAs and InP using CCl₂F₂/Ar/O₂', *Appl. Phys. Lett.*, 1980, 37, 11, pp.1022-1024
78. CANAVELLO, B.J., HATZAKIS, M., and SHAW, J.M.: 'Process for Obtaining Undercutting of a Photoresist to facilitate Lift-Off', *IBM Tech. Dis. Bull.*, 1977, 19, 10, p.4048
79. HOFFMAN, R.W.: 'The Mechanical Properties of Thin Condensed Films', *Phys. Thin Films*, 1966, 3, pp.211-273
80. MIYAGI, M., NISHIDA, S.: 'Bending Losses of Dielectric Rectangular Waveguides for Integrated Optics', *J. Opt. Soc. Am.*, 1978, 68, 3, pp.316-319
81. DERI, R.J., KAPON, E., and SCHIAVONE, L.M.: 'Bend Losses in GaAs/AlGaAs Optical Waveguides', *Elect. Lett.*, 1987, 23, 16, pp.845-847
82. NOURSHARGH, N., STARR, E.M., FOX, N.I, and JONES, S.G.: 'Simple Technique for Measuring Attenuation of Integrated Optical

- Waveguides', *Elect. Lett.*, 1985, 21, 18, pp.818-820
83. WALKER, R.G.: 'Simple and Accurate Loss Measurement Technique for Semiconductor Optical Waveguides', *Elect. Lett.*, 1985, 21, 13, pp.581-583
 84. MERZ, J.L., LOGAN, R.A., and SERGENT, A.M.: 'Loss Measurements in GaAs and $\text{Al}_x\text{Ga}_{1-x}\text{As}$ Dielectric Waveguides between 1.1eV and the Energy Gap', *J. Appl. Phys.*, 1976, 47, 4, pp.1436-1450
 85. CARENCO, A.: 'Semiconductor Waveguides in III-V Materials for Integrated Optics', 4th European Conference on Integrated Optics, Glasgow, 1986, pp.1-7
 86. GUPTA, K.C., GARG, R., and BAHL, I.J.: 'Microstrip Lines and Slotlines', 1979, Artech, Dedham
 87. PENGELLY, R.S.: 'Gallium Arsenide Monolithic Microwave Integrated Circuits', *Gallium Arsenide for Devices and Integrated Circuits*, 1986, Proc. GaAs School, UWIST, Cardiff
 88. WHEELER, H.A.: 'Transmission Line Properties of Parallel Strips Separated by a Dielectric Sheet', *IEEE Trans. Microwave Theory Tech.*, 1965, 13, pp.172-185
 89. CHIGOGIDZE, Z.N., KHUCHUA, N.P., GUTNIK, L.M., KHARATI, R.G., VARLAMOV, I.V., BEKIREV, U.A., and TYUTYUN, A.A.: 'Mechanism of Failure of Gunn Diodes', *Sov. Phys. Semicond.*, 1973, 6, 9, pp. 1443-1447
 90. ABRAMOWITZ, M., STEGUN, I.A.: 'Handbook of Mathematical Functions', 1970, Chap.9, Dover Publications, New York
 91. GRADSHTEYN, I.S, RYZHIK, I.M.: 'Table of Integrals, Series and Products', 1980, Academic Press, London
 92. SPIEGEL, M.R.: 'Advanced Mathematics for Engineers and Scientists', Schaum's Outline Series, 1980, McGraw-Hill, London
 93. WALSH, T.E.: 'Gallium Arsenide Electro-Optic Modulators', *RCA Review*, 1966, pp.323-335

94. IZADPANAH, S.H., RAV-NOY, Z., MUKAI, S., MARGALIT, S., and YARIV, A.: 'Mutual Phase Locking of a Coupled Laser Diode-Gunn Diode Pair', *Appl. Phys. Lett.*, 1984, 45, 6, pp.609-610
95. LEE, C.P., MARGALIT, S., URY, I., and YARIV, A.: 'Integration of an Injection Laser with a Gunn Oscillator on a Semi-Insulating GaAs Substrate', *Appl. Phys. Lett.*, 1978, 32, 12, pp.806-807
96. HALL, D., YARIV, A., and GARMIRE, E.: 'Optical Guiding and Electro-Optic Modulation in GaAs Epitaxial Layers', *Optics Commun.*, 1970, 1, 9, pp.403-405
97. ALFERNESS, R.C.: 'Waveguide Electro-Optic Modulators', *IEE Microwave Theory Tech.*, 1982, 30, 8, pp.1121-1135
98. CROSS, P.S., SCHMIDT, R.V.: 'A 1Gbit/s Integrated Optical Modulator', *IEEE J. Quantum Elect.*, 1979, 15, 12, pp.1415-1418
99. CAMPBELL, J.C., BLUM, F.A., and SHAW, D.W.: 'GaAs Electro-Optic Channel-Waveguide Modulator', *Appl. Phys. Lett.*, 1975, 26, 11, pp.640-642
100. CARRUTHERS, T.F.: 'Picosecond Optical Control of TEDs', ed. LEE, C.H., 1984, Academic Press, London
101. PLATTE, W., -ING, Dr.: ' Optoelectronic Microwave Switching', *IEE Proc., Pt. J*, 1985, 132, 2, pp.126-132
102. CARVER, K.R., MINK, J.W.: 'Microstrip Antenna Technology', *IEEE Trans. Ant. Prop.*, 1981, 29, 1, pp.2-24
103. MAILLOUX, R.J., McILVENNA, J.F., and KERNWEIS, N.P.: 'Microstrip Array Technology', *IEEE Trans. Ant. Prop.*, 1981, 29, 1, pp.25-37

